Visualizing the membrane confinement, trafficking, and structure of the GABA transporter, GAT1

Thesis by

Princess Izevbua Ikhianosen Uerenikhosen Imoukhuede

In Partial Fulfillment of the Requirements

for the Degree of

Doctor of Philosophy

California Institute of Technology

Pasadena, California

2008

(Defended February 8, 2008)

ACKNOWLEDGEMENTS

I would like to thank Henry Lester for being a great mentor and scientific advisor. I've learned so much from you. I appreciate the intellectual freedom you've given me over my work. I would also like to thank you for fostering a collaborative, diverse, and intellectually stirring lab environment through which I have learned and grown tremendously as a scientist. As I move forward in my career, I can only hope to live up the example you have set of scientific rigor, ethical leadership and compassionate mentoring.

I would like to thank my committee. First, my collaborator Robert Chow; it has been an honor to work with you at USC, and to learn from both you and Darren Michael. Our collaboration opened a new area of science to me, which I have been able to share with others. Your thoughtful comments on my work have given focus of my studies and have helped to mold me into an excellent scientist.

I'd like to thank Professor Fraser, from whom I first learned optical principles. Through him I met the microscopy czars Mary Dickinson and Chris Waters both of whom I must thank for helping me troubleshoot experiments. In addition to serving on my committee, I'd like to thank Professor Fraser for being an advocate for social progress.

I'd like to thank Professor Yang who helped to unify my understanding of microscopy. Through his courses, I learned the mathematical principles governing optics. I appreciate greatly your taking the time to explain concepts to me, discuss topics in microscopy, offer scientific and career advice, and serve on my committee.

I would like to thank **ALL** the members of the Lester lab. **EACH** of you has had a significant impact on my graduate training! I would especially like to thank the members of the 10AM, sometimes 9AM, fluorescence and transporter clubs. You folks have kept me on my toes with challenging questions and rousing scientific discussions. I would especially like to thank Fraser Moss and Joanna Jankowsky. Everything I know about experimental biology, I've learned from you! Thanks for your patience, thanks for your advice, and thanks for your support! I am also grateful to Raad Nashmi and Rigo Pantoja for your help and guidance. I'd like to offer lots of thanks to Purnima Deshpande, Eloisa Imel, and Kathleen Hamilton; you've each been so kind to me and you've looked out for me throughout my time here. Finally, I'd like to thank Bruce Cohen, Ryan Drenan, Herwig Just, Cagdas Son, and Sheri McKinney for your support.

I must thank my church communities: All Saints Episcopal Church in Pasadena, CA and the Church of the Holy Family in Park Forest, IL. First, I'll give a special shout-out to the clergy, who despite ministering to thousands, still send prayers my way. I'd like to thank my Indaba peeps for stimulating theological discussion, for being so accepting and culturally sensitive, and for being true friends when I've really needed you! I'd also like to offer thanksgiving to the Canterbury Choir and music director. I'll forever remember my time with you, lifting our voices in joyous praise to God.

I would also like to thank Andrew Medina-Marino, Holly Beale, Dennice Gayme, Tara Gomez, Tosin Otitoju, and Tashica Williams for your support throughout grad school. When I think back to the fun times and positive interactions, you're the folks that come to mind. Your sincerity, kindness, and good naturedness have made Caltech a more welcoming environment for me and others.

I truly appreciate the encouragement and advice of my mentors, Dr. Paula Hammond, Dr. Linda Griffith, Dr. Erica O'Neal, Dr. Elaine Bearer, Dr. Heather Pinkett, and Dean Blanche Staton.

I would especially like to express my gratitude to Brandi Jones, Janice Black, Candice Rypsi, C.L., and Milton Mitchell. From my first day on campus until now, you have each made me feel welcome, offered much needed advice, provided resources, and done so much to help me negotiate a very demanding environment. Thank you.

Finally, I would like thank my family. It's absolutely impossible to list everything they've done. If I did, this section would be longer than the body of my thesis. But I will mention a few highlights. Since leaving for boarding school at 15, my dad has had an open door policy. Anytime I felt like coming home, day or night he'd pick me up, no questions asked. Similarly, anytime I've needed to call him: 2AM, 4AM, 6AM….he's always answered. Good news, bad news, he's the first to hear. Having my dad's unconditional love and support has been a tremendous comfort and blessing in every step of my journey. Therefore, I want to thank him so much for always being there for me.

Next, I'd like to thank my mom. Her patient words and guidance have calmed my fears. She has infused me with hope and optimism when things have seemed to go horribly wrong. She has inspired me in countless ways. I am immensely grateful for all that she's done for me. It would be no less fitting than to thank my mom's clone: Mommy Odion (thanks to one is thanks to both). You've supported me when I've been home-sick, nervous, tired, hungry, happy, excited, joyful, and even when I couldn't walk. I sincerely thank you for your prayers, I thank you for your love, and I thank you for your support.

And of course, I reserve a heap of thanks to my most learned and esteemed comrade, Big Brother Chief! Yours is by far the hardest acknowledgement to write, because you've encouraged me in so many ways! When I think to how you've supported me through Caltech, I remember all the emails and essays you proofread, pep-talks you've given me, the non-billable legal/academic/social/political advice you've offered. I also remember the times you've encouraged me to sleep in, relax, or just have fun. All your advice and support has made me better off today than I was two days ago. So I must say that, I'm much obliged, much obliged!

Altogether, I thank God for such a loving family, and it is with great humility that I dedicate this thesis to you. Without your support, I would not be one of the first African-American women to earn an engineering doctorate from Caltech.

ABSTRACT

Transporter trafficking regulators can play an important role in maintaining the transporter density necessary for effective function. I determine interactions that confine GAT1 at the membrane by investigating GAT1 lateral mobility through fluorescence recovery after photobleaching (FRAP). I find that the mobility of GAT1 can be increased by depolymerizing actin or by blocking the GAT1 PDZ interacting domain. I also identify ezrin as the GAT1 adaptor to actin. Through fluorescence resonance energy transfer (FRET), the distance between GAT1-YFP and Ezrin-CFP is calculated as 64--68 Å, and it can be significantly increased by disrupting the actin cytoskeleton. Altogether, my data reveals that actin confines GAT1 to the plasma membrane via ezrin, an interaction mediated through the GAT1-PDZ interaction domain.

Discoveries in the field of vesicle fusion provide direct ties to translational research. While the study of vesicle fusion classically has been applied to neurotransmitter and neuropeptide containing vesicles; there is evidence that secretory vesicles physiologically differ from vesicles trafficking membrane protein. For instance, GAT1 resides on a vesicle lacking neurotransmitter but containing some v-SNARE proteins. These differences in the vesicle composition suggest inherent differences in trafficking mechanisms, which can only be confirmed through further study of membrane protein trafficking. To this end, I apply total internal reflection fluorescence microscopy (TIRFM) to quantify the number of GAT1 molecules on vesicles and to observe the movement of vesicles containing fluorescently tagged GAT1 into the plasma membrane. I determine that these vesicles contain 3--7 molecules of GAT1 and uncover a population of GAT1 vesicles with ATP-dependent lateral displacement.

The protein-protein interactions, trafficking, and oligomerization of mouse GAT1 were studied using fourteen different fusions of mGAT1 with fluorescent protein. We determine that a natural PDZ-interacting motif is minimally required for wild-type GAT1 behavior. Fusions with wild-type function yielded up to 21% FRET efficiency, indicating efficient GAT1 oligomerization. Additionally, 45% FRET was observed between a GAT1 construct and YFP-syntaxin-1A. Inserting XFP between R565 and L566, resulted in 33% FRET but impaired function, which indicated the “RL” motif in the proximal C-terminus governs export from the endoplasmic reticulum but not transporter oligomerization.

TABLE OF CONTENTS

Chapter 1: Introduction

This chapter contains three sections. The first section gives an overview of what is known about GAT1 function, subtypes in the brain, structure, trafficking, and ties to epilepsy. The second section describes the optical approaches used to study the GABA transporter. The chapter concludes with a summary of the subsequent chapters of the thesis.

Background

GAT1 Function

Synapses help translate information in order for us to learn, recall, think, and exhibit emotion. Every action is governed by synaptic networks. Many neurological and psychiatric disorders stem from problems with chemical and/or electrical signal transmission at the synapse. Hence several drugs used to treat these conditions target synaptic transporters and receptors. For example, the antiseizure drug, carbamazapine, binds to the postsynaptic $GABA_A$ receptor, resulting in modulations in chloride conduction. Even drugs prescribed for treatment of depression, anxiety, and attention deficit hyperactivity disorder (also known as "ADHD") block synaptic transporters---the serotonin and norepinephrine transporters to be exact. Therefore any insight gained into the structure of synapses can result in significant improvements in clinical medicine and human health.

A study of the synapse typically focuses on the proteins that facilitate and regulate synaptic transmission. Figure 1 displays a representative synapse. Synaptic transmission occurs when vesicles containing neurotransmitter fuse with the presynaptic membrane, thereby releasing neurotransmitter into the synaptic cleft. The neurotransmitter diffuses throughout the synapse and binds to a postsynaptic ion channel, resulting in channel opening. The opening of an ion channel allows ions to move through the channel pore. Hence, synaptic transmission involves the conversion of a chemical signal into an electrical signal. Synaptic transmission is terminated by the action of neurotransmitter transporters which pump neurotransmitter from the synaptic cleft back into the presynaptic neuron. Figure 2 displays the process of synaptic transmission, where the neurotransmitter is GABA; the postsynaptic ion channel is the GABA$_A$ receptor; the ion permeating the channel pore is chloride; and the neurotransmitter transporter is the GABA transporter, GAT1.

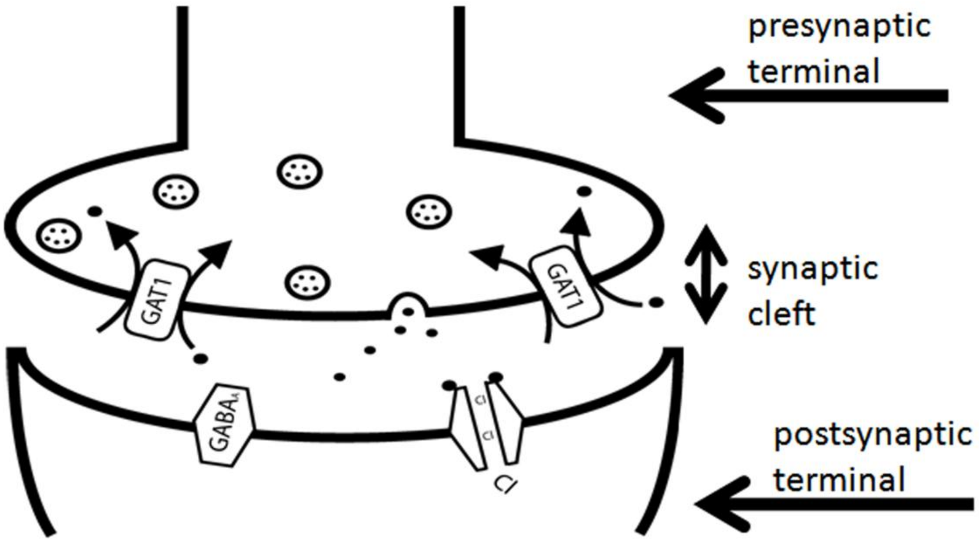

Figure 1. The image shows fusion of GABA-containing vesicles with the plasma membrane. The binding of GABA to a GABA$_A$ *receptor results in the opening of receptor and the movement of chloride ions through the pore of the receptor. This process of inhibitory synaptic transmission is terminated by the transport of GABA from the synaptic cleft into the presynaptic terminal via the action of GAT1. This process is considered inhibitory, because chloride ions are negatively charged, and upon entering the postsynaptic terminalmthey decrease in the membrane voltage (hyperpolarization), thereby inhibiting neuronal excitation.*

The GABA transporter, GAT1 is the focus of the studies in this thesis. It is a member of the solute carrier 6 (SLC6) family of transporters. Included in this family are the norepinephrine transporter (NE), serotonin transporter (SERT), dopamine transporter (DAT), and GABA transporters (GAT) (1). In addition to terminating synaptic transmission, these transporters are also involved in maintaining a low neurotransmitter concentration throughout the brain and preventing excessive activation of synaptic receptors (2, 3). The removal of neurotransmitter from the synapse requires energy, which is harnessed from the difference in intracellular and extracellular ion concentrations. Table 1 specifies the intracellular and extracellular concentrations of Na^+, Cl^-, and K^+.

Table 1. Intracellular and extracellular ion concentrations adapted from Alberts (4)

Ion	**Intracellular Concentration**	**Extracellular Concentration**
Na^+	5--15 mM	145 mM
Cl^-	5--15 mM	110 mM
K^+	140 mM	5 mM

Since ions move from regions of high concentration to low concentration, the difference in ion concentration (concentration gradient) can be used to drive the movement of molecules that cannot diffuse across the plasma membrane into the neuron. GAT1 applies this principle by transporting GABA into the neuron through co-transport of 2 Na^+ and 1 Cl^- down their concentration gradients.

It must be noted that GAT1 can also reverse, transporting GABA out of the neuron either under depolarizing conditions (increased plasma membrane voltage) or due to a significant increase in intracellular Na^+ or Cl^- concentrations. Figure 3 displays GAT1 transport reversal. Drugs that raise the intracellular concentration of Na^+ (for example, glutamate) can also cause transport reversal. Studies of GAT reversal have been performed in a range of model systems including: toad and catfish retina, human hippocampus, rat brain synaptosomes, mouse cerebral cortex, human embryonic kidney cells, and *Xenopus* oocytes (frog eggs) (5, 6). Wu and Richerson have found that physiologically relevant increases in extracellular K^+ concentration (11--17 mM) can induce transport reversal in rat hippocampus (7). Transport reversal is believed to have great importance during high-frequency neuronal excitation. It is thought that transporter reversal and vesicular release of GABA work in tandem to inhibit neuronal firing.

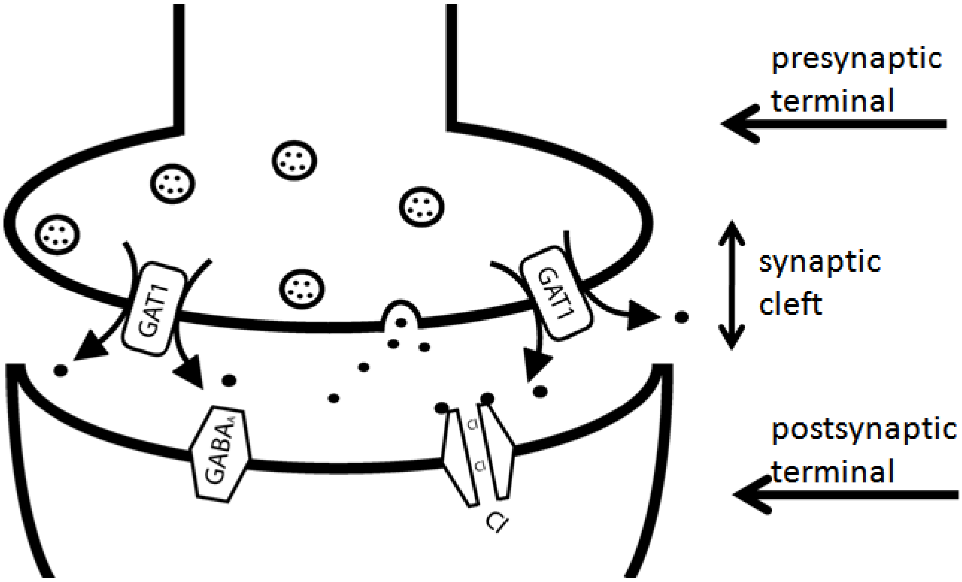

Figure 2. GAT1 can reverse transport under certain conditions, including: depolarizing conditions or upon significant increase in the sodium or chloride concentrations in the presynaptic terminal. Therefore, rather than transporting GABA into the presynaptic terminal, GAT1 can transport GABA into the synapse.

GABA Transporter Subtypes and Distribution

There are four known subtypes of the GABA transporter: GAT1, GAT2, GAT3, and BGT1. GAT1 is the predominant GAT in the central nervous system (CNS).

Through *in situ* hybridization, immunocytochemistry, and fluorescence microscopy it has been found that GAT1 is found in high concentration in the cerebellum, hippocampus, and thalamic reticular nucleus (8). GAT1 is expressed in astrocytes but primarily on axons and presynaptic terminals (boutons) of GABAergic inhibitory neurons. Figure 3 displays the localization of GAT1 in such a neuron. This image was acquired from the cerebellum of a pre-natal mouse (E18) expressing a fusion of GAT1 to the green fluorescent protein (GFP).

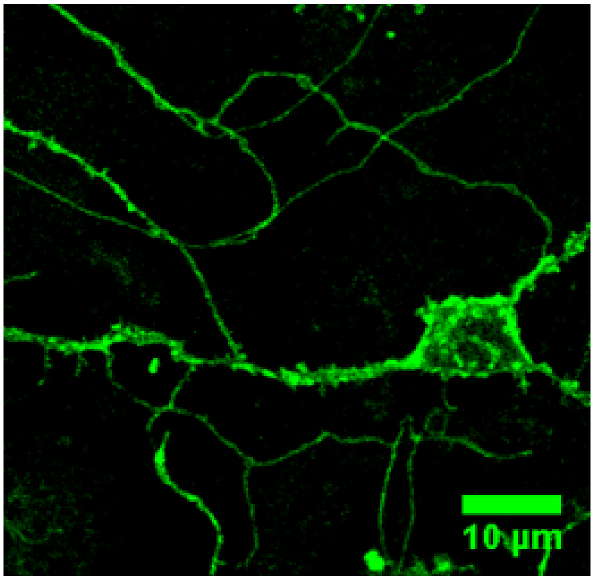

Figure 3.GAT1 localization in a neuron. This image shows the localization of the GABA transporter, GAT1, in a neuron and its processes. The localization of GAT1 is visualized through emission of a green fluorescent protein (GFP) molecule fused to GAT1. The image represents primary cultures from the cerebellum of pre-natal (E18) mice expressing GAT1-GFP after 14 days of culture.

GAT3 is also specific to the central nervous system, being preferentially located on astrocytes and found in the olfactory bulb, cerebral cortex, thalamus, hippocampus, superior and inferior colliculus, substantia nigra, cerebellum, and brain stem (9-11).

GAT3 is believed to be developmentally regulated, being found in higher concentrations in the brains of post-natal mice versus adult animals (12). Both GAT2 and BGT1 are preferentially found on astrocytes (non-neuronal support cells) in the CNS, and they are also found in the liver and the kidney (10, 11). BGT1 is distinct from the other transporters, because it can transport sodium, chloride, and GABA in ratios of 3:2:1 or 3:1:1 (13), in contrast to the previously described GAT ratio of 2 Na^+ to 1 Cl^- to 1 GABA. BGT1 is also distinct because its role in the kidney and liver is to maintain the intracellular osmotic balance under hypertonic conditions (under increased extracellular solute concentrations), by transporting the osmolyte, betaine (13, 14). Despite the fact that it can also transport betaine, BGT1 actually has a higher affinity for GABA than for betaine. Given the role that BGT1 plays in maintaining osmolarity in peripheral tissues, it is believed that both BGT1 and GAT2 play a similar role of maintaining the osmotic balance within the CNS (1, 9).

GAT1 Structure

GAT1 contains twelve transmembrane (TM) domains with both the amino and carboxy termini located intracellularly (15). Figure 4 displays a schematic of the transporter. The membrane topology of GAT1 had been predicted through hydropathy plots and N-linked glycosylation scanning mutagenesis (16). Another distinguishing characteristic of GAT1 is a large extracellular loop between TM 3--4 that contains three N-glycosylation sites. Structurally, the SLC6 transporters form oligomers. This hypothesis has been supported by fluorescence resonance energy transfer (FRET) studies with GAT, SERT, and DAT (17-19).

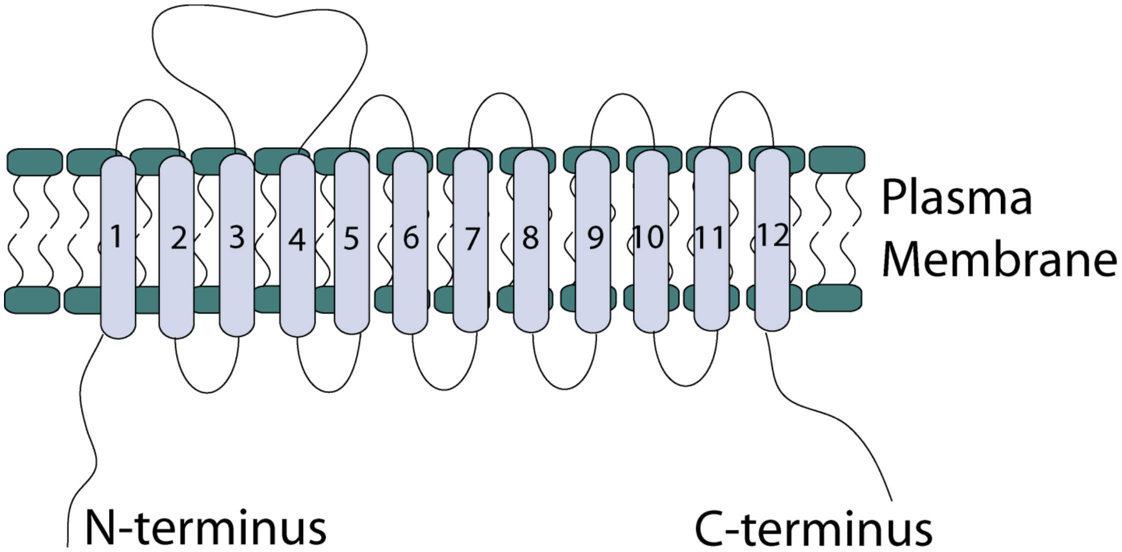

Figure 4. Schematic diagram of GAT1 membrane topology. GAT1 contains 12 transmembrane domains numbered from left to right with both the N-terminus and the C-terminus found in the cytosol. Although the figure is not drawn to scale, the transporter does contain a large second extracellular loop.

In 2005, the crystal structure of the leucine transporter was solved to a 1.65 Å resolution (20). The leucine transporter is bacterial in origin and shares 20--25% sequence identity to the transporters of the SLC6 family; hence, it is considered a homologue of SLC6 transporters. The X-ray crystal structure showed 12 TM domains; thereby confirming the predicted membrane topology. The structure also confirmed that the transporter formed homodimers and determined that the dimerization interface was just following TM12. Prior to the crystal structure it was believed that transporter oligomerization was driven by a series of four repeated leucines (leucine heptad repeat) found within the TM2 (17-19). Although the dimerization interface has now been confirmed to follow TM12, the previous work points to TM2 as a region significant to transporter structure and trafficking.

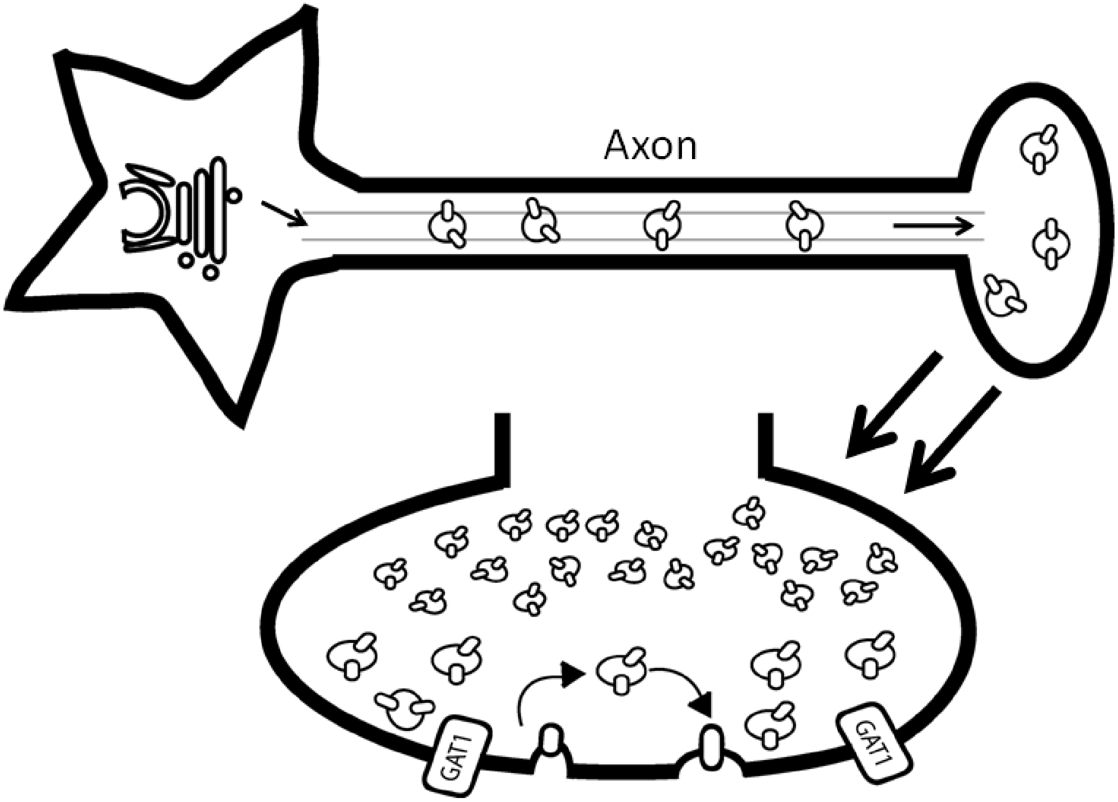

Figure 5. Schematic of GAT1 vesicle trafficking. GAT1 trafficking involves the movement of vesicles containing GAT1 from the Golgi along the axon and into the presynaptic terminal. Although there is no change in GAT1 vesicle size at the presynaptic terminal, the size difference seen in the schematic is used to differentiate the two different GAT1 vesicle populations. The first pool of vesicles, represented by the larger vesicles, is termed the readily releasable pool. These vesicles actively insert GAT1 into the plasma membrane through the process of exocytosis and remove GAT1 from the plasma membrane through the process of endocytosis, as indicated by the arrows. The second pool is termed the reserve pool; they are represented by the smaller vesicles in the schematic. As the name suggests, these vesicles are not actively involved in vesicle fusion, and they comprise a majority of the GAT1vesicle population, accounting for 70% of GAT1 vesicles.

GAT1 Trafficking

GAT1 trafficking refers to the steps from GAT1 translation and processing in the endoplasmic reticulum (ER) and Golgi apparatus to GAT1 arrival on the plasma membrane. It also includes the retrieval of GAT1 from the membrane through the process of endocytosis and the recycling of GAT1 back to the membrane. Figure 5 displays the movement of vesicles containing the transporter from the Golgi, along the axon, and finally arriving at the presynaptic terminal where the GAT1 vesicles fuse to place GAT1 on the plasma membrane. Many of the steps depicted in the schematic are regulated; therefore, what follows describes the protein interactions and GAT1 structural elements that control GAT1 trafficking.

The first steps in GAT1 trafficking involves export from the ER. This step requires oligomerization of GAT1. GAT1 mutants that are unable to oligomerize are therefore retained in the ER. Additionally, GAT1 ER export and subsequent movement through the Golgi occurs through the action of COPII-coated vesicles, requiring the interaction between the RL motif on the GAT1 C-terminus (amino acids 566 & 567) and the COPII vesicle component, Sec24D (21, 22). In contrast, a transporter with a mutated RL sequence is retained in the ER.

Once the transporter has met the necessary conditions for ER and Golgi export, the vesicle containing GAT1 is translocated to the plasma membrane by traversing microtubules along the axon to finally arrive at the presynaptic plasma membrane (Figure 5). Here, it is stationed either in a readily releasable pool (RRP) of vesicles, which actively inserts the transporter into the plasma membrane at a rate of 1.1 min^{-1}, or it is part of the reserve pool of vesicles, which represents 70% of the total GAT1 pool (23). As the name implies, this pool does not actively traffic GAT1 onto the membrane;

however, if its role mirrors that the role of the synaptic vesicle reserve pool, then it can be recruited for vesicle fusion upon depletion of the RRP.

Vesicle fusion involves the interaction of vesicle SNARES (V-SNARES) with tethering SNARES (T-SNARES) on the plasma membrane. The vesicle that traffics the transporter to the plasma membrane contains the V-SNARE, VAMP. Additionally, it contains rab3A, a G-protein that aids exocytosis; rab11, a GTPase involved in vesicle recycling; and Syntaxin 1A, a T-SNARE that mediates vesicle fusion when on the plasma membrane (24). This vesicle does not contain vGAT; therefore it is distinct from the synaptic vesicle that contains GABA. It also does not contain synaptotagmin, which is the calcium sensor on neurotransmitter-containing vesicles (synaptic vesicles) that prompts vesicle fusion, nor does it contain synaptophysin, which is another marker of synaptic vesicles (24, 25).

The fusion of the GAT1 vesicle to the plasma membrane requires the interaction of the last 3 amino acids of GAT1 (alanine, tyrosine, and isoleucine) termed the postsynaptic density 95/Discs large/Zona occludens1 (PDZ) interacting motif, with a PDZ protein. The mutation, truncation, or disruption of this motif results in impaired GAT1 trafficking, with 70% of the GAT1 that should be on the plasma membrane remaining in GAT1 vesicles (8). Other proteins that increase GAT1 membrane localization include protein kinase C (PKC) (26-28), syntaxin 1A (29, 30), and tyrosine kinases (31, 32).

Once GAT1 has been delivered to the plasma membrane, it can also be retrieved from the plasma membrane through the process of endocytosis. The average GAT1 internalization rate is $0.7\ \text{min}^{-1}$ (23). As previously mentioned, tyrosine kinases increase the exocytosis of GAT1; likewise, reduced phosphorylation of GAT1 by tyrosine phosphatases or by the inhibition of tyrosine kinase activity increases the GAT1 internalization rate (31, 32). This increase in GAT1 internalization by extension reduces the number of GAT1s that can transport GABA (33), thereby reducing GAT1 transport activity (31).

GAT1 and Epilepsy: Current Therapeutic Approaches

GABA is the main inhibitory neurotransmitter in the CNS and when released into the synaptic cleft, it binds to $GABA_A$, $GABA_B$, and $GABA_C$ receptors (GABA binding to $GABA_A$ receptors is shown in Figure 1). The binding of GABA to $GABA_A$ receptors in mature neurons results in the opening of the receptor and the movement of chloride ions through the receptor pore. This movement of negative charge is defined as an inhibitory postsynaptic current, and it hyperpolarizes the cell; thereby reducing the ability of the neuron to fire excitatory currents (34). Therefore, when GAT1 removes GABA from the synaptic cleft it terminates inhibitory signaling. Since epilepsy is defined by abnormal neuronal excitation, drugs that target and inhibit GAT1 function should prolong neuron inhibition, thus serving as potent antiepileptics.

Tiagabine is currently the only FDA-approved drug that blocks GAT1. Its side effects include: tremor, ataxia, dizziness, nervousness, sedation, and asthemia (3). In order to determine whether these side effects are related to the block of GAT1 and not due to non-specific tiagabine interactions, complete knockout of the GAT1 gene was studied in a mouse. The GAT1 knockout mouse neither changes the expression pattern of the major proteins involved in GABA transmission in the cerebellum nor in the hippocampus. However, rotorad behavioral tests show that the mice exhibit loss of muscular coordination (ataxia). Additionally, open-field and exploratory cage tests reveal mouse anxiety and nervousness. Tremor measurements show that the knockout mice exhibit constant 25--32 Hz tremor in their limbs and tails. Electrophysiology performed on brain slices from the knockout mice, show an increased $GABA_A$ receptor-mediated tonic conductance in both cerebellar granule and Purkinje cells, a slower decay of spontaneous inhibitory postsynaptic currents in cerebellar granule cells. These results all indicate that knockout of GAT1 increases the extracellular GABA concentration. GAT1 knockout also produces behavioral and physiological effects that are similar to the side effects of tiagabine treatment. This indicates that the tiagabine side effects are actually due to the blocking of the transporter, rather than from interactions with unintended targets. In turn, this shows that a drug that exclusively blocks GAT1 may not be the most advantageous therapeutic agent, if tremor, ataxia, nervousness, and anxiety are to be avoided.

Since the GAT1 knockout resulted in pronounced behavioral and physiological effects, an alternative treatment approach is necessary, which can confer fewer adverse drug effects. One such approach would target one or more of the less predominant neuronal GABA transporters such as BGT1 (11, 35). This has been tested with the anticonvulsant EF1502, which non-competitively blocks both GAT1 and BGT1. EF1502 blocks GAT1 at lower levels than tiagabine with IC50s for EF1502 and tiagabine of 4 µM and 0.8 µM, respectively, and it blocks BGT1 at higher levels than tiagabine with IC50s for EF1502 and tiagabine of 22 µM and 300 µM, respectively (36). Additionally, EF1502 has a significant effect on partial seizures as probed with animal seizure models (35). These promising findings represent a new approach to the treatment of epilepsy.

In addition to the insight gained from the knockout mouse and EF,1502, research into transport reversal has gained a spotlight into the treatment of epilepsy. The importance of transport reversal in the treatment of epilepsy is supported by recent work which finds that two anticonvulsants, gabapentin and vigabatrin enhance GAT transport reversal (6). Additionally, in temporal lobe epilepsy (TLE) there is a decrease in transporter number (probed by ^{3}H-nipecotic acid binding in rat hippocampus); such a decrease would reduce the contribution of transporter reversal on seizure inhibition. TLE is also characterized by a decrease in glutamate-induced transport reversal (probed by human microdialysis probes of GABA concentration); since seizures are marked by elevated glutamate concentrations, a reduction in GAT ability to reverse in this state would again reduce the contribution of transporter reversal on seizure inhibition (6).

Altogether, the drugs that target and treat epilepsy can function on a number of GAT1 processes. Consequently, continued research into GAT1 protein interactions and structure may lead to the discovery of additional therapeutics targeting GAT1 function.

Applying Fluorescence Microscopy to the Study of GAT1

Studying GAT1 Vesicle Trafficking with Total Internal Reflection Fluorescence Microscopy

Discoveries in the field of vesicle fusion provide direct ties to translational research. Studies of exocytosis have led to an understanding of the role of insulin secretion in type 2 diabetes (37) and to determining the mechanism of action of the antiepileptic drug levetiracetam (Keppra), which binds to the synaptic vesicle protein SV2A (38). The foci of exocytosis studies have been to sensitively measure the time-scale, protein recruitment, and regulation of each step in vesicle trafficking. Vesicle fusion events have been visualized using the vesicular stomatitis virus glycoprotein (39).

The kinetics of docking and fusion has been established through the use of proteoliposomes containing vesicle fusion proteins (SNARES) (40). Although the SNARE proteins are well studied, only recently has fluorescence imaging been applied to understand the formation of the SNARE complex in fusion events (41).

To this end, I use total internal reflection fluorescence microscopy (TIRF) to study the dynamics of the GAT1 vesicle. TIRF is a powerful technique, because it offers a better optical slice than confocal microscopy (~100 nm vs. ~500 nm). The fiber optic cables used by the telecommunications industry also apply the principle of TIRF. The laws of reflection and refraction establish that when light travels from one medium into another, a portion may be reflected back into the starting medium and a portion may be transmitted into the second medium. The index of refraction, *(n)*, gives the ratio of the speed of light in a vacuum to the speed of light in a medium. Snell's law gives the relationship between indices of refraction of the mediums through which light travels (n_1, n_2), the angle of incidence of the light (θ_1), and the angle of refraction of the light (θ_2) (42):

$$n_1 \sin\theta_1 = n_2 \sin\theta_2 \, .$$

Furthermore, when a ray of light passes from a medium of high refractive index (for instance a glass coverslip) to one of lower refractive index (such as a neuron) a critical angle of incidence exists where no light is transmitted through the sample and 100% of the light is reflected with no loss in intensity or frequency of the reflected light. This phenomenon is termed total internal reflection, and the critical angle (θ_c) is given by:

$$n_1 \sin\theta_1 = n_2 \sin 90^\circ$$

$$\theta_c = \sin^{-1}\frac{n_2}{n_1}$$

$n_1 = 1.52$ index of refraction of glass

$n_2 = 1.38$ index of refraction of cell cytosol

$$\theta_c = \left(\sin^{-1}\frac{1.38}{1.52}\right)\left(\frac{180}{\pi}\right) = 65.2^\circ$$

Figure 6 displays the phenomenon of total internal reflection.

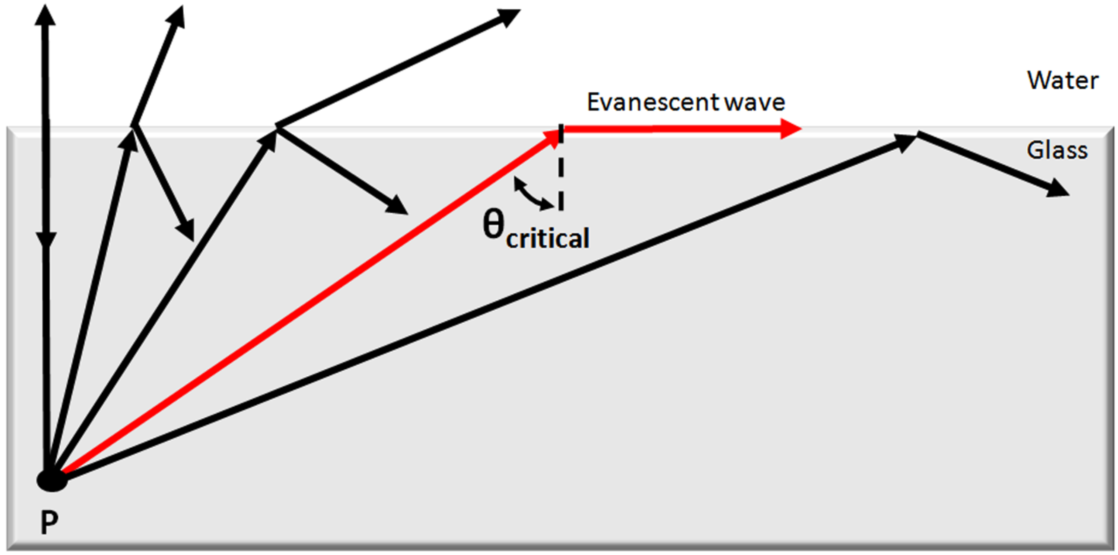

Figure 6. Total internal reflection. Point P is the light source with the light traveling from the high refractive index medium (glass) to the lower refractive index medium, (water). With increasing angle of incidence, less refraction is seen until a critical angle, $\theta_{critical}$*, where there is total internal reflection of the light.*

In TIRF, energy is transmitted across the reflection plane via an evanescent wave. As the name suggests, this wave decays exponentially and allows for imaging within approximately 100 nm of the incident plane (43). The advantage of this technique is the ability to excite fluorescent molecules near the coverslip. In the case of cell cultures, TIRF would excite molecules on or near cell membranes adhering to the coverslip.

Figure 7 displays a cell illuminated such that the laser illuminates the entire sample (widefield fluorescence), and the same cell illuminated by a laser that is introduced at the TIR critical angle (TIRF). The montage clearly shows that changing the laser angle reveals details on the cell membrane that were not visible under widefield fluorescence.

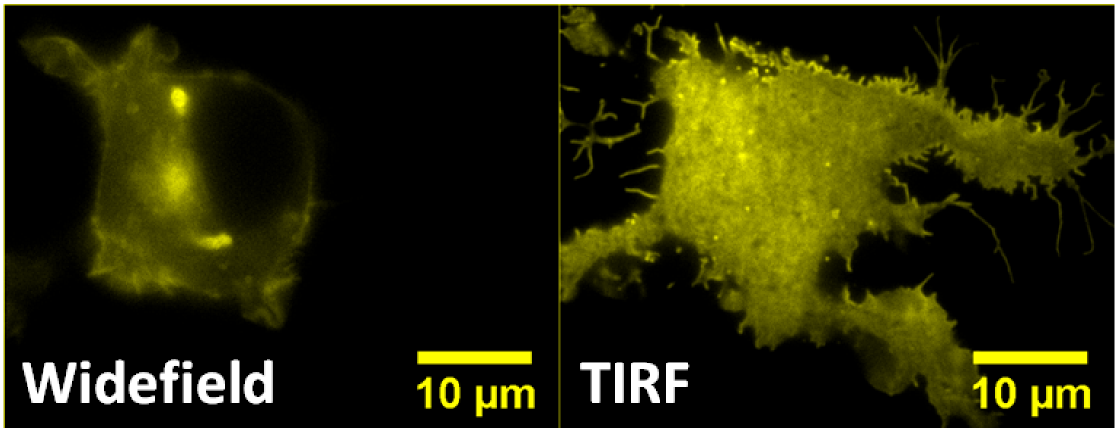

Figure 7. Comparison of widefield fluorescence to TIRF. The left panel shows a cell that has been illuminated with a laser that is introduced normal to the coverslip, resulting in illumination of the entire cell. In contrast, the right panel shows the same cell, illuminated by a laser that is introduced at the TIRF critical angle. Because the plasma membrane of the cell is adhered to the coverslip, the TIRF view reveals the cellular details at the plasma membrane more clearly.

Achieving TIRF through a microscope objective lens requires that the maximal half-angle that the objective can collect photons is greater than the TIRF critical angle. This property of the lens is termed the numerical aperture (NA), and is defined by the relation: $NA = n\sin\theta$. A 1.45 NA objective is the minimum acceptable NA used in TIRF illumination, because it can obtain a maximal illumination and collection half angle of 68.4º, a value that allows achievement of the TIRF critical angle of 65.2º. In contrast, a standard 100X 1.4 NA objective can only obtain a maximum illumination half angle of 63.8º; this value falls below the TIRF critical angle condition.

$$\begin{aligned}
&\text{n} = 1.56\text{, index of refraction of lens medium (oil immersion objective)}\\
&\text{NA} = 1.45\text{, minimum acceptable 100X TIRF objective}\\
&\theta_{1.45NA} = \sin^{-1}\left(\frac{1.45}{1.56}\right)\left(\frac{180}{\pi}\right) = 68.4^\circ\\
&\theta_{1.4NA} = \sin^{-1}\left(\frac{1.4}{1.56}\right)\left(\frac{180}{\pi}\right) = 63.8^\circ
\end{aligned}$$

Studying GAT1 Structure through Fluorescence Resonance Energy Transfer

As previously mentioned, the GAT1 exists as an oligomer on the plasma membrane. Fluorescence resonance energy transfer (FRET) is typically employed to probe the oligomerization state of a protein. This technique allows for the determination of distances between neighboring molecules, essentially serving as a molecular ruler. There are certain conditions required for FRET to occur, which include the following:

- the absorption spectrum of an acceptor fluorophore must overlap the emission spectrum of a donor fluorophore,
- the donor and the acceptor molecules must be located within a distance of 10--100 Å of one another, and

- the dipole moments of both fluorophores must be parallel.

There are four primary methods of studying FRET. These include: the three-cube method, donor photobleaching, fluorescence lifetime imaging, and donor recovery after acceptor photobleaching (DRAP). In the DRAP method, the donor is excited, a wavelength stack of x-y images is collected and the acceptor is photobleached (44). This iteration of image acquisition and photobleaching continues until complete photobleach of the acceptor is reached. Figure 8 displays a representative DRAP FRET experiment. In this figure, cyan fluorescent protein (CFP) is the donor fluorophore and yellow fluorescent protein (YFP) is the acceptor fluorophore; therefore, CFP is dequenched with YFP photobleach.

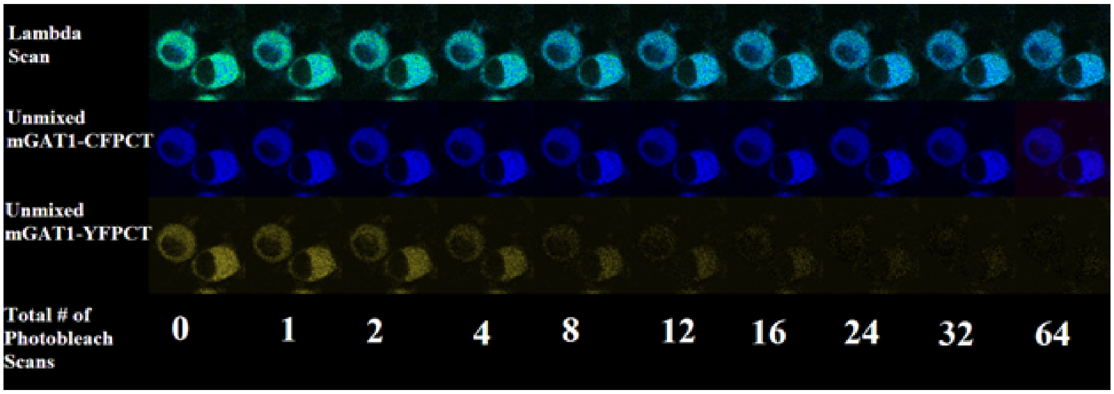

Figure 8. Donor recovery after acceptor photobleach (DRAP) protocol for measuring FRET. In this FRET approach, YFP is fully photobleached after 64 scans by the laser. The image also shows that as YFP is photobleached, there is an increase in CFP fluorescence, indicating FRET occurs between the two molecules. (Explanation: When CFP is within 10--100 Å of a YFP molecule, it donates its energy to YFP, rather than emitting photons; however, when YFP is photobleached, CFP can emit photons, as indicated by the increase in CFP fluorescence.) Please note: The increase in CFP fluorescence is hard to discern by eye when looking at the "unmixed mGAT1-CFPCT image panels." A clearer view of this increase is seen in the "lambda scan" images, where the cells clearly move from a green color (blue + yellow) to a deep blue color.

FRET data is analyzed by normalizing fluorescence intensities to the initial fluorescence, and determining FRET efficiency using the following relation: $E = 1 - \frac{I_{DA}}{I_D}$, where E corresponds to the FRET efficiency. I_{DA} represents the intensity of the donor in the presence of the acceptor, this corresponds to donor fluorescence intensity prior to photodestruction of the acceptor. I_D represents the donor fluorescence intensity without the acceptor, corresponding to the dequenched donor fluorescence following photodestruction of the acceptor (45). From the FRET efficiency, the distance between the donor and acceptor fluorophores can be obtained from the following relation:

$E = \frac{R_o^6}{R_o^6 + R^6}$, where R_o is the Förster distance and is specific to the donor and acceptor used in the FRET experiment; it corresponds to the distance where the FRET efficiency is half maximal.

Studying GAT1 Membrane Confinement with Fluorescence Recovery after Photobleaching

The lateral mobility of a protein on the plasma membrane is now accepted as a form of protein trafficking (23). Lateral diffusion of the AMPA receptor is not only faster than trafficking by exocytosis, but it also accounts for a significant amount of AMPA receptor exchange in dendrites (46). Fluorescence recovery after photobleaching (FRAP) allows for the measurement of molecular lateral mobility and diffusion (47). In this technique, a region of interest is exposed with a high-intensity laser to irreversibly bleach fluorophores in the region. After bleaching, diffusion of fluorescent molecules into the bleached region is monitored by acquisition of images with an attenuated laser. Raw data are corrected for the photobleaching that occurs during image acquisition and normalized by taking a ratio of the fluorescence in the observed region to the initial fluorescence value as follows: $\frac{f(t) - b(t)}{\left(f_{NB}(t) - b(t)\right) \times \left(f(t_o) - b(t_o)\right)}$. Here, the background fluorescence is represented by b(t), the fluorescence in a region not bleached is given by f_{NB} (t), and the pre-bleach fluorescence intensity is represented by $f(t_o)$. A recovery curve is obtained from the data, and from this we can determine the fraction of molecules, M_f, that are free to diffuse, vs. those that are immobilized. In the following equation, F_{bo} is the is the initial fluorescence following photobleach and F_∞ is the asymptote of the recovery curve (48): $M_f = \frac{F_\infty - F_{bo}}{1 - F_{bo}}$. The diffusion coefficient is obtained by first determining the half time for fluorescence recovery using the following equations: $F_h = \frac{F_\infty + F_{bo}}{2}$, $t_{\frac{1}{2}} = t_h - t_{bo}$, where F_h is the value for fluorescence when half the recovery has occurred; t_h is the corresponding time for F_h; t_{bo} is the time, following photobleaching, when the first recovery image is obtained; and $t_{\frac{1}{2}}$ is the half time of equilibration (49). Finally, the diffusion coefficient is related to the recovery half-time by the following relation: $t_{\frac{1}{2}} = \frac{\gamma\omega^2}{D_{eff}}$, where γ is a constant that describes a circular Gaussian beam, ω is the radius of the bleach spot, and D_{eff} is the effective diffusion coefficient (50).

Summary of Thesis

In the following chapters, I visualize GAT1 membrane confinement, vesicle trafficking, and structure using the microscopy techniques outlined above. In Chapter 2 I apply FRAP, FRET, and TIRF to determine the interactions that confine GAT1 at the membrane. In Chapter 3 I apply TIRF to fluorescently resolve the vesicle that traffics GAT1 onto the plasma membrane, and to explore the kinematics of the GAT1 vesicle. I also quantify the number of GAT1 molecules on a vesicle. Chapter 4 applies FRET to determine the oligomerization state of the GAT1 mutants, and confocal microscopy to determine the localization of GAT1 on the plasma membrane. Appendix I is a review of the structure, oligomerization, trafficking, and pharmacology of GABA transporter.

Finally, in Appendix II I apply TIRF to characterize the distribution of subunits of the neuronal nicotinic acetylcholine receptor on the plasma membrane.

References

1. Chen, N.-H., M. A. Reith, and M. Quick. 2004. Synaptic uptake and beyond: the sodium- and chloride-dependent neurotransmitter transporter family SLC6. Pflügers Archiv European Journal of Physiology 447:519-531.

2. Giros, B., M. Jaber, S. R. Jones, R. M. Wightman, and M. G. Caron. 1996. Hyperlocomotion and indifference to cocaine and amphetamine in mice lacking the dopamine transporter. Nature 379:606-612.

3. Chiu, C. S., S. Brickley, K. Jensen, A. Southwell, S. McKinney, S. Cull-Candy, I. Mody, and H. A. Lester. 2005. GABA transporter deficiency causes tremor, ataxia, nervousness, and increased GABA-induced tonic conductance in cerebellum. J Neurosci 25:3234-3245.

4. Alberts, B., D. Bray, K. Hopkin, A. Johnson, J. Lewis, M. Raff, K. Roberts, and P. Walter. 2004. Essential cell biology. Garland Science, New York.

5. Hoogland, G., H. A. Spierenburg, C. W. van Veelen, P. C. van Rijen, A. C. van Huffelen, and P. N. de Graan. 2004. Synaptosomal glutamate and GABA transport in patients with temporal lobe epilepsy. J Neurosci Res 76:881-890.

6. Richerson, G. B., and Y. Wu. 2004. Role of the GABA transporter in epilepsy. Adv Exp Med Biol 548:76-91.

7. Wu, Y., W. Wang, and G. B. Richerson. 2001. GABA Transaminase Inhibition Induces Spontaneous and Enhances Depolarization-Evoked GABA Efflux via Reversal of the GABA Transporter. J. Neurosci. 21:2630-2639.

8. Chiu, C. S., K. Jensen, I. Sokolova, D. Wang, M. Li, P. Deshpande, N. Davidson, I. Mody, M. W. Quick, S. R. Quake, and H. A. Lester. 2002. Number, density, and surface/cytoplasmic distribution of GABA transporters at presynaptic structures of

knock-in mice carrying GABA transporter subtype 1-green fluorescent protein fusions. J Neurosci 22:10251-10266.

9. Cohen-Kfir, E., W. Lee, S. Eskandari, and N. Nelson. 2005. Zinc inhibition of {gamma}-aminobutyric acid transporter 4 (GAT4) reveals a link between excitatory and inhibitory neurotransmission. Proceedings of the National Academy of Sciences 102:6154-6159.

10. Ana Gadea, A. M. L.-C. 2001. Glial transporters for glutamate, glycine, and GABA: II. GABA transporters. Journal of Neuroscience Research 63:461-468.

11. Schousboe, A., A. Sarup, O. M. Larsson, and H. S. White. 2004. GABA transporters as drug targets for modulation of GABAergic activity. Biochemical Pharmacology 68:1557-1563.

12. Liu, Q. R., Lopez-Corcuera, B., Mandiyan, S., Nelson, H., Nelson, N. 1993. Molecular Characterization of Four Pharmacologically Distinct alpha-aminobutyric acid transporters in mouse brain. The Journal of Biological Chemistry 268:2106-2112.

13. Matskevitch, I., C. A. Wagner, C. Stegen, S. Broer, B. Noll, T. Risler, H. M. Kwon, J. S. Handler, S. Waldegger, A. E. Busch, and F. Lang. 1999. Functional Characterization of the Betaine/gamma -Aminobutyric Acid Transporter BGT-1 Expressed in Xenopus Oocytes. J. Biol. Chem. 274:16709-16716.

14. Kempson, S. A., and M. H. Montrose. 2004. Osmotic regulation of renal betaine transport: transcription and beyond. Pflügers Archiv European Journal of Physiology 449:227-234.

15. Guastella, J., N. Brecha, C. Welgmann, H. A. Lester, and N. Davidson. 1992. Cloning, expression, and localization of a rat brain high-affinity glycine transporter.

Proceedings of the National Academy of Sciences of the United States of America 89:7189-7193.

16. Bennnett, E. R., Kanner, B.I. 1997. The Membrane Topology of GAT-1, a (Na+ + Cl-)-coupled gamma-Aminobutyric Acid Transporter from Rat Brain. The Journal of Biological Chemistry 272:1203-1210.

17. Farhan, H., Korkhov, V.M., Paulitschke, V., Dorostkar, M.M., Scholze, P., Kudlacek, O., Freissmuth, M., Sitte, H. 2004. Required for Membrane Targeting of the Rat gamma-Aminobutyric Acid Transporter-1 (GAT1). The Journal of Biological Chemistry 279:28553-28563.

18. Hastrup, H., Karlin, A., Javitch, J.A. 2001. Symmetrical dimer of hte human dopamine transporter revealed by cross-linking Cys-306 at the extracellular end of the sixth transmembrane segmetn. Proccedings of the National Academy of Acience USA 98:10055-10060.

19. Schmid, J. A., Scholze, P., Kudlacek, O., Freissmuth, M., Singer, E.A., Sitte, H.H. 2001. Oligomerization of the Human Serotonin Transporter and fo the Rat GABA Transporter 1 Visualized by Fluorescence Resonance Energy Transfer Microscopy in Living Cells. The Journal of Biological Chemistry 276:3805-3810.

20. Yamashita, A., S. K. Singh, T. Kawate, Y. Jin, and E. Gouaux. 2005. Crystal structure of a bacterial homologue of Na+/Cl--dependent neurotransmitter transporters. Nature 437:215-223.

21. Farhan, H., V. Reiterer, V. M. Korkhov, J. A. Schmid, M. Freissmuth, and H. H. Sitte. 2007. Concentrative Export from the Endoplasmic Reticulum of the {gamma}-

Aminobutyric Acid Transporter 1 Requires Binding to SEC24D. J. Biol. Chem. 282:7679-7689.

22. Farhan, H., V. M. Korkhov, V. Paulitschke, M. M. Dorostkar, P. Scholze, O. Kudlacek, M. Freissmuth, and H. H. Sitte. 2004. Two Discontinuous Segments in the Carboxyl Terminus Are Required for Membrane Targeting of the Rat {gamma}-Aminobutyric Acid Transporter-1 (GAT1). J. Biol. Chem. 279:28553-28563.

23. Wang, D., and M. W. Quick. 2005. Trafficking of the Plasma Membrane g-Aminobutyric Acid Transporter GAT1. Size and rates of an acutely recycling pool. J. Biol. Chem. 280:18703-18709.

24. Deken, S. L., D. Wang, and M. W. Quick. 2003. Plasma Membrane GABA Transporters Reside on Distinct Vesicles and Undergo Rapid Regulated Recycling. J. Neurosci. 23:1563-1568.

25. Lodish, H., A. Berk, L. S. Zipursky, P. Matsudaira, D. Baltimore, and J. Darnell. 1999. Molecular Cell Biology. W.H. Freeman, New York.

26. Quick, M. W., J. L. Corey, N. Davidson, and H. A. Lester. 1997. Second messengers, trafficking- related proteins, and amino acid residues that contribute to the functional regulation of the rat brain GABA transporter GAT1. J. Neurosci. 17:2967-2979.

27. Wang, D., S. L. Deken, T. L. Whitworth, and M. W. Quick. 2003. Syntaxin 1A Inhibits GABA Flux, Efflux, and Exchange Mediated by the Rat Brain GABA Transporter GAT1. Mol Pharmacol 64:905-913.

28. Deken, S. L., Beckman, M.L., Boos, L., Quick, M.W. 2000. Transport rates of GABA transporters: regulation by the N-terminal domain and syntaxin 1A. Nature Neuroscience 3:998-1003.

29. Purves, D., G. J. Augustine, D. Fitzpatrick, L. C. Katz, A.-S. LaMantia, J. O. McNamara, and S. M. Williams. 2001. Neuroscience. Sinauer Associates, Sunderland. 681.

30. White, H. S., W. P. Watson, S. L. Hansen, S. Slough, J. Perregaard, A. Sarup, T. Bolvig, G. Petersen, O. M. Larsson, R. P. Clausen, B. Frolund, E. Falch, P. Krogsgaard-Larsen, and A. Schousboe. 2005. First Demonstration of a Functional Role for Central Nervous System Betaine/{gamma}-Aminobutyric Acid Transporter (mGAT2) Based on Synergistic Anticonvulsant Action among Inhibitors of mGAT1 and mGAT2. J Pharmacol Exp Ther 312:866-874.

31. Clausen, R. P., E. K. Moltzen, J. Perregaard, S. M. Lenz, C. Sanchez, E. Falch, B. Frolund, T. Bolvig, A. Sarup, O. M. Larsson, A. Schousboe, and P. Krogsgaard-Larsen. 2005. Selective inhibitors of GABA uptake: synthesis and molecular pharmacology of 4-N-methylamino-4,5,6,7-tetrahydrobenzo[d]isoxazol-3-ol analogues. Bioorganic & Medicinal Chemistry 13:895-908.

32. Michael, D. J., R. A. Ritzel, L. Haataja, and R. H. Chow. 2006. Pancreatic {beta}-Cells Secrete Insulin in Fast- and Slow-Release Forms. Diabetes 55:600-607.

33. Lynch, B. A., N. Lambeng, K. Nocka, P. Kensel-Hammes, S. M. Bajjalieh, A. Matagne, and B. Fuks. 2004. The synaptic vesicle protein SV2A is the binding site for the antiepileptic drug levetiracetam. PNAS 101:9861-9866.

34. Toomre, D., J. A. Steyer, P. Keller, W. Almers, and K. Simons. 2000. Fusion of Constitutive Membrane Traffic with the Cell Surface Observed by Evanescent Wave Microscopy. J. Cell Biol. 149:33-40.

35. Liu, T., W. C. Tucker, A. Bhalla, E. R. Chapman, and J. C. Weisshaar. 2005. SNARE-Driven, 25-Millisecond Vesicle Fusion In Vitro. Biophys. J. 89:2458-2472.

36. An, S. J., and W. Almers. 2004. Tracking SNARE Complex Formation in Live Endocrine Cells. Science 306:1042-1046.

37. Halliday, D., Resnick, R., Krane, K.S. . 1992. Physics. John Wiley & Sons, Inc., New York.

38. Axelrod, D. 2003. Total Internal Reflection Fluorescence Microscopy in Cell Biology. Methods in Enzymology 361:1-33.

39. Dickinson, M. E., G. Bearman, S. Tilie, R. Lansford, and S. E. Fraser. 2001. Multi-spectral imaging and linear unmixing add a whole new dimension to laser scanning fluorescence microscopy. Biotechniques 31:1272, 1274-1276, 1278.

40. Nashmi, R., M. E. Dickinson, S. McKinney, M. Jareb, C. Labarca, S. E. Fraser, and H. A. Lester. 2003. Assembly of a4b2 nicotinic acetylcholine receptors assessed with functional fluorescently labeled subunits: effects of localization, trafficking, and nicotine-induced upregulation in clonal mammalian cells and in cultured midbrain neurons. J Neurosci 23:11554-11567.

41. Triller, A., and D. Choquet. 2005. Surface trafficking of receptors between synaptic and extrasynaptic membranes: and yet they do move! Trends in Neurosciences 28:133-139.

42. Wells, K. S., Sandison, D.R., Strickler, J., Webb, W.W. 1990. Quantitative Fluorescence Imaging with Laser Scanning Confocal Microscopy. In Handbook of Biological Confocal Microscopy. J. B. Pawley, editor. Plenum Press, New York and London. 27-39.

43. Axelrod, D., Koppel, D.E., Schlessinger, J., Elson, E., Webb, W.W. . 1976. Mobility measurement by analysis of fluorescence photobleaching recovery kinetics. Biophysical Journal 16:1055-1069.

44. Rabut, G., Ellenberg, Jan. 2005. Photobleaching Techniques to Study Mobility and Molecular Dyanmics of Proteins in Live Cells: FRAP, iFRAP, and FLIP. In Live Cell Imaging: A Lab Manual. D. S. Robert D. Goldman, editor. Cold Spring Harbor Laboratory Press, Cold Spring Harbor, New York. 101-126.

45. Wey, C. L., Cone, R.A., Edidin, M.A. 1981. Lateral Diffusion of Rhodopsin in Photoreceptor Cells Measured by Fluorescence Photobleaching and Recovery. Biophysical Journal 33:225-232.

Chapter 2: Ezrin mediates tethering of the γ-aminobutyric acid transporter, GAT1, to actin filaments via a C-terminal PDZ domain

This chapter has been submitted for publication. We determine interactions that confine GAT1 at the membrane by investigating the lateral mobility of GAT1-YFP8 expressed in neuroblastoma 2a (N2a) cells. I performed the FRAP, TIRF, and FRET experiments along with the analysis. Fraser Moss performed the molecular biology, creating GAT1-YFP8.

Ezrin mediates tethering of the γ-aminobutyric acid transporter GAT1 to actin filaments via a C-terminal PDZ domain

Princess I. Imoukhuede[1,2], Fraser J. Moss[2], Darren J. Michael[3], Robert H. Chow[3], and Henry A. Lester[2*]

[1]Bioengineering and [2]Division of Biology, California Institute of Technology, Pasadena, CA 91125, USA
[3]Zilkha Neurogenetic Institute and Department of Physiology and Biophysics, Keck School of Medicine, University of Southern California, Los Angeles, CA 90089, USA
**Corresponding author: Henry A. Lester, 1200 E California Blvd., M/C 156-29, Pasadena, CA 91125-2900, Phone: (626)395-4946, Fax: (626)564-8709, Email: lester@caltech.edu*

Running Title: GAT1 interacts with actin via PDZ domain & ezrin

Total character count: 49,075

A high density of neurotransmitter transporters on axons and presynaptic boutons is required for efficient clearance of neurotransmitter from the synapse. Therefore, regulators of transporter trafficking (insertion, retrieval, and confinement) can play an important role in maintaining the transporter density necessary for effective function. We determine interactions that confine GAT1 at the membrane by investigating the lateral mobility of GAT1-YFP8 expressed in neuroblastoma 2a (N2a) cells. Through fluorescence recovery after photobleaching (FRAP) we find that a significant fraction (~ 50%) of membrane-localized GAT1 is immobile. The mobility of the transporter can be increased by depolymerizing actin or by interrupting the GAT1 PDZ-interacting domain. Microtubule depolymerization, in contrast, does not affect GAT1 membrane mobility. We also identify ezrin as a major GAT1 adaptor to actin. Förster resonance energy transfer (FRET) determines that the distance between GAT1-YFP8 and ezrin-CFP is 64--68 Å. This distance can be increased by disrupting the actin cytoskeleton. Altogether, our data reveal that actin confines GAT1 to the plasma membrane via ezrin, and this interaction is mediated through the GAT1-PDZ interaction domain.

Key Words: GABA, transporter, GAT1, lateral mobility, trafficking, FRAP, actin, cytoskeleton, PDZ-interacting motif, fluorescent protein

The γ-aminobutyric acid (GABA) transporter GAT1 (51), a member of the SLC6 family of neurotransmitter transporters, is a 12-transmembrane domain protein that aids in terminating GABAergic synaptic signaling by transporting GABA into cells. GAT1 is the predominant GABA transporter in the brain and is localized primarily on axons and presynaptic terminals of GABAergic inhibitory neurons; it is also expressed on astrocytes (52, 53).

The uptake of each GABA molecule is coupled to co-transport of two Na^+ ions and one Cl^- ion (54-56). The complete time for one transport cycle is ~ 100 ms, which is longer than the ~ 10 ms decay time constant of GABAergic postsynaptic currents (57). This implies that each transporter functions at most only once per synaptic event. To accommodate such functional constraints, a GAT1 density on the order of 1000 transporters/μm^2 is required (33). The actual measured density of GAT1 molecules on several membranes, including presynaptic boutons and axons, is 800--1300 transporters/μm^2 (33). Therefore, a high membrane density of GAT1 underlies the efficient clearance of GABA from the synaptic cleft and from nearby extrasynaptic compartments. Knowing that a high density of GAT1 on the membrane aids in clearance, one may ask how GAT1 trafficking is regulated and how GAT1 is restricted among membrane compartments.

Some aspects of GAT1 trafficking have been studied, and GAT1 insertion and retrieval time constants of 1.1 and 0.7 min^{-1}, respectively, have been obtained through biotinylation studies (23). Previous studies have also revealed that that 30% of the GAT1 cellular pool exists within the plasma membrane. The remaining 70% of GAT1 is found in vesicles adjacent to the membrane surface. The trafficking rates and the high number of reserve GAT1 vesicles have the potential to affect GAT1 membrane density and effectively increase GABA turnover.

We seek an understanding of the restriction of GAT1 mobility at the membrane and by analogy the restriction of other SLC6 family transporters. To this end we apply FRAP to measure GAT1 movement at the plasma membrane. FRAP reveals both the time course and the mobile fraction for protein movement, which are governed by passive diffusion, by active processes, and by tethering within and near the plane of the membrane. Furthermore, lateral mobility is now accepted as a form of protein trafficking as revealed through recent work on postsynaptic receptors (α-amino-3-hydroxy-5-methyl-4-isoxazolepropionic acid receptor [AMPAR], *N*-methyl-D-aspartic acid receptor [NMDAR], $GABA_A$ subunits, and glycine receptor) (23). Lateral diffusion of the AMPAR is not only faster than trafficking by exocytosis, but it also accounts for a significant amount of AMPAR exchange in dendritic spines (46).

Since membrane protein mobility can be reduced or restricted by linkage to the cytoskeleton (58, 59), we apply cytoskeleton disruptors to determine how interactions with actin and/or microtubules impact GAT1 mobility.

Membrane confinement often occurs through a cytoskeleton adapter protein such as gephyrin, which serves as a scaffold between the glycine receptor and microtubules (60) or ezrin, which tethers the cystic fibrosis transmembrane conductance regulator (CFTR) to actin (61). Therefore, we utilize FRET to determine the proximity of an adaptor that may be involved in GAT1 restriction.

Altogether, the data reveal novel interactions between GAT1, ezrin, and the actin cytoskeleton, and these interactions require the GAT1 C-terminal PDZ-interacting domain.

Results

In this study, we used an optimized fusion protein between mouse GAT1 and, at the C-terminus, YFP, followed by an additional eight residues that incorporate a PDZ domain binding site. This construct, GAT1-YFP8, produces the same maximal GABA uptake and has the same GABA concentration dependence as the wild type transporter. We report elsewhere that the GAT1-YFP8 transporter dimerizes correctly and is correctly trafficked to the plasma membrane. We also report elsewhere that the N2a assay system is linear and nonsaturated. Furthermore the surface/cytoplasmic expression ratio is sensitive, as in neurons, to disruption of the PDZ interaction motif at the C-terminus of GAT1. We therefore believe that this assay system closely resembles the native GAT1 transporter, expressed in the GABAergic neurons that constitute the native environment of GAT1.

Whole footprint photobleach reveals lateral mobility

The question often arises whether FRAP actually detects lateral mobility or whether it detects fusion of vesicles, which are actively trafficking protein onto the membrane. To address this question, we perform “whole footprint” FRAP. Figure 1A displays pre-bleach, post-bleach, and recovery images of a whole footprint FRAP experiment. The post-bleach panel shows that > 90% of the footprint surface area is photobleached, and it includes a line profile across the bleached region. It is important to note that the ends of the line overlap non-photobleached regions. Figure 1B displays a kymograph, which represents the line profile, shown in Figure 1A, over time. The kymograph shows that recovery occurs from regions not photobleached, with fluorophore entering from the edges. This qualitative analysis indicates that FRAP largely reveals the lateral mobility of GAT1; however, it is possible that the speckles that appear in the image after ~ 60 s do represent some contribution from vesicle exocytosis (23). In separate experiments, we have visualized and tracked individual vesicles containing GAT1; these will be reported in a future study.

Fitting Data to FRAP Diffusion Model

Figure 1C displays GAT1 recovery in a FRAP experiment and two models for fitting to this recovery trace. The diffusion model in Figure 1C is for a circular bleach spot; it is derived by Axelrod *et al.* and modified by Sprague *et al.* (62-64). The model is as follows:

$$\frac{\partial f}{\partial t} = D_f \nabla^2 f$$

$$\tau_D = \frac{t_{\frac{1}{2}}}{\gamma} = \frac{\omega^2}{D_{eff}}$$

$$\sigma = 1 - A$$

$$F(t) = e^{-\frac{\tau_D}{2t}}\left[I_o\left(\frac{\tau_D}{2t}\right) + I_1\left(\frac{\tau_D}{2t}\right)\right] - \sigma$$

Based on the Axelrod-Sprague equation, γ is a constant that describes a circular Gaussian beam, τ_D is the recovery time constant, ω is the radius of the bleach spot, D_{eff} is the effective diffusion coefficient, A represents the recovery asymptote for GAT1-YFP8; therefore, σ is a correction factor that allows the diffusion model to converge to the GAT1-YFP8 recovery asymptote. Figure 1C shows that pure diffusion does not accurately describe the behavior of GAT1-YFP8 recovery. In particular, the model exhibits sharp recovery at early time points. Figure 1C also displays fitting of GAT1-YFP8 recovery to a double exponential decay, which models the experimental data precisely. The model is of the form: $F(t) = F_{bo} - ae^{-bt} - ce^{-dt}$, where F_{bo} is the initial value of fluorescence following photobleaching; a, b, c, and d are constants obtained through fitting. Because the double exponential fitting more accurately describes GAT1-YFP8 mobility, $t_{1/2}$ values are used in this study, rather than diffusion coefficients.

Comparing and Quantifying GAT1 mobility

To give context to GAT1 mobility, we compare its mobility to minimally mobile and maximally mobile proteins, represented respectively by soluble YFP and by YFP-syntaxin1A, a membrane protein and t-SNARE. Figures 2A and 2B display a montage of footprint photobleach performed on YFP, GAT1-YFP8 and YFP-syntaxin. (Footprint photobleach is chosen, because YFP is not a membrane protein and cannot be accurately analyzed with a perimeter photobleach; however, its mobility near the membrane can be obtained by focusing near the coverslip). Figure 2C displays the first 80 s of YFP, GAT1-YFP8, and YFP-Syntaxin recovery. Within the first seconds of detection, there is steep, unresolved recovery of YFP in which YFP recovers to 60% of its pre-bleach intensity; this limits the quantitative analysis of YFP mobile fraction. However, a qualitative observation of Figure 2C shows that the YFP recovery asymptote is greater than that of GAT1-YFP8, and by extrapolating the initial YFP photobleach to 20% (GAT1-YFP8 F_{bo}), we can infer that YFP has a higher mobile fraction than GAT1-YFP8. As shown in Figure 2B, and as previously reported, YFP-syntaxin clusters to form exocytosis docking sites at the membrane, so it should not be expected to have high membrane mobility (65). Figure 2C also displays the recovery of YFP-syntaxin from which a mobile fraction of 65% is calculated, resembling the GAT1-YFP8 mobile fraction of 60%.

Photobleach Regions

Variation in imaging settings such as laser intensity, bleach size/shape, and pixel dwell time can affect the results of quantitative photobleach experiments (66). To provide additional confirmation of FRAP results, GAT1 experiments are performed by photobleaching the cell footprint and perimeter and comparing the trends seen between these regions of interest. Figure 3A displays a footprint photobleach montage. The 5 s post-bleach panel shows that the region photobleached was a circle of area 8 μm^2. Figure 3B displays a montage representing perimeter photobleach, where the laser was focused on a plane midway through the cell, and a rectangular section including the cell membrane, 13 μm^2 was photobleached. It is important to note that perimeter photobleach recovery occurs in two dimensions, and the membrane fluorescence in the confocal slice is a line representation of this recovery. Figure 3C displays the quantitative results of footprint and perimeter photobleach experiments, giving mobile fractions of approximately 60% and 50%, respectively. These results suggest 40--50% of GAT1-YFP8 is immobilized. Since a significant fraction of surface GAT1 is immobile, we explore the possibility of GAT1 tethering to the cytoskeleton.

GAT1 interacts with cytoskeleton via actin but not via microtubules

We apply nocodazole for ~ 12 h to maximally disrupt microtubules (67). The first panel of Figure 4A displays microtubule distribution in an N2a cell labeled with TubulinTracker 488; the second panel includes nuclear labeling with Hoechst 33342. Figure 4B displays microtubule distribution following nocodazole treatment, indicating complete microtubule depolymerization. Figures 4C and 4D display the recovery traces following nocodazole treatment for footprint and perimeter photobleach, and for comparison, the recovery trace for an untreated sample. All traces show that nocodazole treatment has no significant affect on either the recovery time constant or the size of the mobile population.

Latrunculin B is used to disrupt actin filaments to determine whether GAT1 associates with actin. Figures 5A and 5B display cells with intact and disrupted actin filaments, respectively, as probed with rhodamine phalloidin labeling. Figure 5C displays the footprint photobleach trace for cells with and without intact actin filaments. Slight differences are observed between the untreated and the latrunculin B traces, which translates to a 20% increase in mobile fraction, as summarized in Figure 6A. Figure 5D displays the results of perimeter photobleach on cells with and without intact actin filaments. More pronounced differences in the untreated and latrunculin B traces translate to a 60% increase in the time constant for recovery and a 20% increase in the mobile fraction as reported in Figures 6A and 6B. Cytochalasin D, another actin disruptor, was used to confirm the actin depolymerization results. Figures 6A and 6B show that cytochalasin D treatment results in both an increased time constant and an increased mobile fraction compared to the untreated samples, resembling the latrunculin B results.

Disrupting PDZ binding increases GAT1 lateral mobility

Typically, actin binding occurs through an adaptor protein or by an interaction with a scaffolding protein such as a PDZ protein (60, 68-70). To determine whether PDZ binding links GAT1 to the actin cytoskeleton, we perform quantitative photobleaching on $GAT1_0$-GFP, a fluorescent GAT1 that cannot interact with PDZ proteins. In $GAT1_0$-GFP, added C-terminal residues (a linker followed by GFP) interrupt the endogenous PDZ-interaction domain of GAT1 (C-terminal sequence, -AYI-CO_2^-). As a result, homozygous $GAT1_0$-GFP knock-in mice show a 70% reduction in surface localization and synaptosomal GABA uptake (33). Figure 6C illustrates the difference between the fluorescent GABA transporters in this study: $GAT1_0$-GFP lacking all components to the PDZ-interacting domain versus GAT1-YFP8 having an added PDZ-interaction domain, downstream of the YFP moiety.

FRAP is performed on N2a cells transfected with $GAT1_0$-GFP. Figure 6D shows that $GAT1_0$-GFP is 30-40% more mobile on the membrane than GAT1-YFP8, indicating that the PDZ interaction domain contributes to GAT1 immobilization. Latrunculin B is added to probe the actin dependence of $GAT1_0$-GFP. Figure 6D also shows that depolymerizing actin does not significantly affect the mobile fraction. Since the PDZ-binding domain of $GAT1_0$-GFP is disrupted and shows no interaction with actin, we conclude that a GAT1 capable of interacting with PDZ proteins interacts with actin via its PDZ domain, either directly or indirectly.

Ezrin and Pals1 are expressed in N2a cells

FRAP results indicate that GAT1 interacts with the cytoskeleton through the PDZ-binding motif. Another membrane protein with this type of interaction is the Na^+/H^+ exchanger isoform 3 (NHE3), which is restrained to actin through interactions with the PDZ protein, sodium-hydrogen exchanger regulatory factor (NHERF) and the adaptor protein ezrin (71). To determine whether ezrin could link GAT1 to the cytoskeleton, we first performed real time quantitative reverse transcription polymerase chain reaction (RT-PCR), testing for expression of two genes: the PDZ protein known to interact with GAT1, Pals1 (72), and the linker molecule ezrin. Figure 7A shows that N2a cells express both ezrin and Pals1 at similar levels. mRNA expression is normalized to the β-actin control. γ-actin was also used as a control, with expression levels similar to β-actin.

FRET suggests a GAT1-ezrin interaction

Figures 7B-F display the results of FRET experiments that combine donor recovery after acceptor photobleach with channel unmixing. Figure 7B shows pre-bleach and post-bleach images of a representative cell expressing GAT1-YFP8 and ezrin-CFP. Following photodestruction of GAT1-YFP8 with a 514 nm argon laser, there is a 23% increase in ezrin-CFP fluorescence (Figure 7B). This increase is most prominently seen along the cell membrane. Figure 7E also displays this increase in CFP fluorescence, which indicates FRET between the two fluorophores. The FRET efficiency between GAT1-YFP8 and ezrin-CFP of 19% ± 2% is shown in Figure 7F. Table 1 displays a proximity between GAT1-YFP8 and ezrin-CFP of 64--68 Å. This is calculated, by applying the FRET efficiency (ε) and Förster distance (R_o) for an ECFP-EYFP FRET pair of 50 Å to the following equation: $r = R_o \sqrt[6]{\frac{1-\varepsilon}{\varepsilon}}$ (73).

Inactive ezrin forms C-terminal to N-terminal dimers in the cytosol (74, 75). Therefore, the previously studied FRET partners, ezrin-CFP/YFP-ezrin (74) were used as a positive control. As expected, Figure 7D shows that ezrin-CFP and YFP-ezrin are localized in the cytosol and exhibit the strongest interaction, with a distance of 63--67 Å between fluorophores (Table 1). The localization of ezrin oligomers to the cytosol versus GAT1 to the plasma membrane may explain the difference in time course between the GAT1-YFP8 and YFP-ezrin photobleach curves (Figure 7E). The cytosolic oligomer is expected to show less apparent photobleaching because of its mobility, as exemplified by cytosolic YFP in Figures 2A and 2C.

Actin disruption diminishes GAT1-ezrin interaction

Figures 7C and 7E show that GAT1-YFP8 photodestruction results in little or no increase in ezrin-CFP fluorescence when actin is disrupted. Latrunculin B exposure produces a FRET efficiency of 7% ± 5%, significantly less than the FRET value for both the untreated and ezrin-CFP/YFP-ezrin control samples (Figure 7F). This indicates that actin depolymerization greatly reduces the interaction between GAT1 and ezrin. Because 22% (5 of 23) GAT1-YFP8/ezrin-CFP + latrunculin B cells did not display detectable FRET, it is most appropriate to present an “at least” distance between GAT1 and ezrin following actin depolymerization (Table 1).

Discussion

This work establishes the role of lateral mobility in regulating GAT1 function by quantifying the mobility of GAT1 at the plasma membrane in an assay system resembling the native mouse neurons that express mGAT1. Previous studies on membrane proteins have also employed FRAP, the most appropriate quantitative method for measuring membrane protein mobility in conjunction with manipulations of PDZ interaction domains (76-78), although to our knowledge this is the first application of FRAP to a neurotransmitter transporter of the SLC6 family.

Our FRAP experiments show that ~ 50% of the membrane-localized GAT1 molecules are mobile. Of the ~ 50% that are immobile, a fraction associates with the actin cytoskeleton. This conclusion is based on a significant increase in the mobile fraction of GAT1 in two experiments: (1) in cells treated with pharmacological agents known to disrupt actin filaments, and (2) in cells expressing a form of fluorescently tagged GAT1 with a disrupted PDZ-interaction domain. Importantly, the magnitude of the increase in the mobile fraction of GAT1 is similar in both of these experiments. Moreover, the mobility of $GAT1_0$-GFP, which has a disrupted PDZ-interaction domain, could not be further increased by treating cells with an actin disruptor, further implicating this domain in the GAT1-actin interaction.

The fact that the PDZ domain of GAT1 plays an important role in tethering indicates a link between GAT1 and actin; most likely, this link is indirect and mediated by a PDZ protein and a linker protein. Ion channel binding to PDZ proteins provides a model for this interaction. PSD-95/SAP-90, a member of the membrane-associated guanylate kinase (MAGUK) family of PDZ proteins, serves as a scaffold for the NMDA receptor thereby clustering it on the postsynaptic membrane (79). This type of PDZ scaffolding also occurs through the action of two known PDZ-domain-containing proteins (Na^+/H^+ exchanger regulatory factor-1-2, NHERF1 and NHERF2) on the cystic fibrosis transmembrane conductance regulator (CFTR) (80). CFTR is linked to the actin cytoskeleton through interactions between the PDZ domains of the proteins NHERF-1 and NHERF-2, and the actin binding protein, ezrin (61, 76).

Recent biochemical investigations have established interactions between GAT1 and the PDZ protein, Pals1 (72) and between Pals1 and the actin adaptor, ezrin (81). We show via RT-PCR that Pals1 and ezrin are expressed in our cell system. Furthermore, GAT1 and ezrin participate in a latrunculin B-sensitive interaction. A direct link between GAT1 and ezrin is unlikely, because such direct linkage is typically stabilized via a series of positively charged residues in the juxta-membrane region (82, 83), a region neither found on the GAT1 N-terminal nor the GAT1 C-terminal domain. Altogether, this indicates that the mobility of GAT1 is restricted by the actin cytoskeleton joined by a PDZ protein (for which Pals1 is a strong candidate molecule in many neurons) and ezrin.

The cartoons in Figure 8 summarize these results. Figure 8A shows that an ezrin/PDZ complex can tether a membrane protein via the C-terminal PDZ interacting domain (AYI). Disrupting actin abolishes the tetramolecular GAT1-PDZ protein-ezrin-actin complex, either (Figure 8B1) by separating GAT1 from its PDZ protein or (Figure 8B2) by separating the ezrin-PDZ protein interaction, this frees GAT1 and results in higher membrane mobility. Finally, interrupting the endogenous C-terminal PDZ interacting domain of GAT1 with a linker and a GFP moiety, increases the membrane mobility of GAT1 (Figure 8C). It is possible that other members of the ezrin-radixin-moesin family of filamentous actin binding proteins may play a role in restricting GAT1 movements (70, 84).

The $t_{1/2}$ values for recovery of untreated GAT1-YFP8, are 3-10 times less than the $t_{1/2}$ measured previously for GAT1 trafficking to and from the plasma membrane (23), supporting the idea that our measurements are not appreciably distorted by cytoplasmic / surface trafficking. However, it is possible that the longest $t_{1/2}$ measured after actin disruption, ~ 1 min, does represent a component from cytoplasmic-surface interaction, which is further supported by kymographic analysis of whole-cell photobleach (Supplemental Figure 1). Furthermore, the increased $t_{1/2}$ following both latrunculin B and cytochalasin D treatment suggests that a GAT1 not bound to actin retains non-immobilizing interactions with certain molecule(s), which effectively increase its molecular weight. This conclusion is based on the $t_{1/2}$ relation to diffusion and subsequently to molecular mass (62-64).

Microtubules play a well-established role in protein trafficking to the plasma membrane. Studies on the glycine receptor and $GABA_A$ subunits suggest that microtubules may also affect receptor restriction to the plasma membrane via gephyrin scaffolding (60, 68, 84-86). Our results show that neither GAT1 immobilization nor its membrane diffusion depend on microtubules.

Physiological significance of GAT1 movements in the membrane

The GAT1 link to actin via ezrin may point to the role of this interaction in the pathophysiology and/or treatment of epilepsy. Although most studies on ezrin are focused on its role in epithelial structure, organization, and signaling, ezrin is also expressed in CNS neurons and is increased, at both the mRNA and protein levels, in certain epilepsies. Ezrin is upregulated in the hippocampus of patients with mesial temporal lobe epilepsy (87, 88). Likewise, in the lithium-pilocarpine treated rat model of , a temporal lobe epilepsy (TLE)(89), ezrin upregulation occurs within 48 hours of seizure induction (90). Epilepsies associated with malformations of cortical development such as focal cortical dysplasia (FCD_{IIb} and FCD_{IIa}) and gangliogliomas are also marked by neuronal ezrin accumulation (91). Although the role of ezrin upregulation in seizure progression has not been formally identified, recent evidence points to the role of ezrin as a downstream target in the phosphoinositide 3-kinase (PI3K) pathway (91, 92).

TLE also has strong ties to GABA transport; although TLE is marked by a loss of hippocampal neurons, GABAergic interneurons are preserved. In TLE there is a decrease in the number of GABA transporters (5, 6).

The identification of the interaction between GAT1, ezrin, and actin and the quantitative study by FRAP contributes to further understanding of how transporters are clustered, regulated and confined on the cell surface. Because GAT1 is an important drug target in the treatment of epilepsy, continued research into these protein interactions may lead to the discovery of additional therapeutics targeting GAT1 function (7, 93-95).

Materials and Methods

Molecular Biology

The $GAT1_0$-GFP construct has been described, and was previously termed mGAT1-GFP (33). In $GAT1_0$-GFP, added C-terminal residues (a linker followed by GFP) disrupt the endogenous PDZ-interaction domain of GAT1 (C-terminal sequence, -AYI-CO_2^-).

To generate the new fluorescent mutant, GAT1-YFP8, we added an intact PDZ-interaction motif at the C-terminus, following the YFP moiety. The wild-type mGAT1 open reading frame (ORF) was subcloned without its endogenous stop codon in to the *Hin*d III and *Eco*R I sites of the pcDNA3.1(+) expression vector (Invitrogen, Carlsbad, CA) multiple cloning site (MCS). The yellow fluorescent protein (YFP) (Clontech, Mountain View, CA) ORF into which we introduced the “monomeric” A206K mutation (96) was then subcloned downstream from, but in frame with the mGAT1 ORF at the *Not* I and *Xba* I sites of the pcDNA3.1(+) MCS. This resulted in a 12 amino acid spacer between the end of the mGAT1 sequence and the beginning of the fluorophore. We modified Geiser *et al*.’s method for the integration of PCR fragments without the use of restriction enzymes (97) to then add 8 codons worth of hGAT1 C-terminal sequence. These were amplified from a source plasmid using PfuTurbo C_x Hotstart polymerase with 5’ and 3’ extensions that corresponded to the 20--22 nucleotide regions that flanked the intended site of insertion such that the PCR product integrated in frame immediately after the fluorophore sequence when used as the primers in a subsequent QuikChange II XL mutagenesis PCR reaction (Stratagene, La Jolla, CA).

Ezrin-CFP and YFP-ezrin, gifts from Dr. Forte and Lixin Zhu, are previously described in Zhu *et al.* (74). YFP-syntaxin, a gift from Dr. W. Almers, is previously described in An *et al.* (41).

N2a Culture

Mouse neuro-2a (N2a) cells (ATCC, Manassas, VA) are grown at 37 °C in 95% air, 5% CO_2 in N2a culture medium containing the following: 44.5% DMEM, 44.5% OptiMEM, 10% fetal bovine serum, and 1% penicillin/streptomycin (10,000 I.U penicillin, 10,000 mg/ml streptomycin) (Invitrogen, Carlsbad, CA). Once cells are grown to confluence, cells are plated on glass bottom dishes at a density of 3×10^5 cells/dish. Prior to plating, 14 mm glass bottom dishes (#0, Mattek, Ashland, MA) are coated with 0.05% polyethylimine (PEI) (Sigma, St. Louis, MO) pH 8.4 in borate buffer. Transfection of a total of 1 µg DNA per plate is performed 16--24 hr later with Lipofectamine and Plus reagent (Invitrogen, Carlsbad, CA). The composition of the N2a imaging solution is as follows (mM): 128 NaCl, 2.4 KCl, 25 HEPES, 1.2 $MgCl_2$, 3.2 $CaCl_2$, 1.2 KH_2PO_4, and 10 D-glucose (98).

Nocodazole treatment

Cells are pretreated with 10 µM nocodazole in cell culture medium at 37 °C for 16--24 hr. This concentration and incubation time follow established protocols for maximally depolymerizing microtubules (67, 99, 100). Nocodazole (Sigma, St. Louis, MO) is dissolved in DMSO in a concentration of 5 mg/ml and stored at -20 °C. Nocodazole is added to N2a culture medium and cells are incubated for 16--24 hr. Prior to imaging, N2a culture medium is aspirated from cells, and cells are washed with imaging solution containing 10 µM nocodazole. Cells are allowed to equilibrate at room temperature for 30 min in the 10 µM nocodazole containing imaging solution.

Latrunculin B and Cytochalasin D treatment

Latrunculin B (Sigma-Aldrich, St. Louis, MO) is dissolved in DMSO and stored at -20 °C at a stock concentration of 2.5 mM. 5 µM latrunculin B is added to imaging medium and warmed to 37 °C. Cells are washed with warm imaging medium and the latrunculin B solution is added to cells. Cells are incubated for 1 hr in latrunculin B solution prior to imaging. Cytochalasin D (Sigma, St. Louis, MO) is dissolved in DMSO and stored at -20 °C at a stock concentration of 1 mg/ml. 1 µg/ml cytochalasin D is added to imaging medium and warmed to 37 °C. Cells are washed with warm imaging medium and the cytochalasin D solution is added to cells. Cells are incubated for 1 hr in cytochalasin D solution prior to imaging.

Microtubule and Nuclear labeling with TubulinTracker Green and Hoechst 33342

Microtubules are labeled according to the suppliers instructions using TubulinTracker Green reagent for live-cell tubulin labeling (Molecular Probes, Eugene, OR). Briefly, N2a nucleus is stained by addition of 10 µg Hoechst 33342; microtubules are stained with TubulinTracker in HBSS by incubating for 30 min at 37 ºC in a 5% CO_2 incubator. Cells are rinsed three-times with warm imaging solution.

Actin Labeling with Rhodamine Phalloidin

A 14 µM rhodamine-conjugated phalloidin (Cytoskeleton, Denver, CO) stock solution is prepared by dissolving in methanol and storing at -20 °C. A fresh 4% solution of paraformaldehyde (Fluka, St. Louis, MO) at pH 7.4 is prepared. Medium is aspirated from dishes and cells are rinsed twice with 1 X PBS. The 10 min, room temperature fixation and staining are performed by combining 4% paraformaldehyde, 0.1% Triton, and 2 units (5 µL) rhodamine phalloidin per dish. Following fixation, cells are washed twice with 1 X PBS.

Confocal Imaging

All FRAP experiments are performed in the Caltech Biological Imaging Center on an inverted Zeiss 510 Meta (Carl Zeiss, Thornwood, NY) using a 63 X Plan-Apochromat 1.4 NA oil immersion objective. The fluorescence is collected using a HFT KP 700/514 nm beam splitter and a 535 --590 nm bandpass filter. The detector gain is modified to allow for near-saturating conditions for a given region of interest (ROI). There is no change to gain settings for a given ROI. For footprint photobleach a circular ROI is chosen with an area of 9.4 ± 0.9 µm^2. For perimeter photobleach, a rectangular ROI is chosen with an area of 12.5 ± 1.2 µm^2. ROIs are photobleached at 25% laser transmission using the 514 nm laser line of a 40 mW argon laser. Photobleaching was optimized to obtain ~ 80% photodestruction within the ROI. This was performed by lasing each ROI 20 times at 25% laser transmission with a 1.60 µs pixel dwell time. Pre-bleach and recovery images are collected at 0.25% laser transmission at 5 s intervals. Lens zoom is set to 3 X. 12-bit images are collected at pixel resolution of 512 x 512. Pinhole diameter is set to 144 µm.

Dye labeled N2a cells are imaged on an inverted Zeiss 510 Meta at 12 bits and 512x512 pixel resolution. Stack slices were 0.10 µm. Hoechst 33342 nuclear labeled cells are imaged using a Plan-Apochromat 100x 1.4 NA oil immersion objective. Cells are excited using a two-photon pulsed laser tuned to 700 nm at 2.5% laser transmission. The fluorescence is collected using a HFT KP 700/488 beam splitter and FT 510 and BP 390--465 IR filters. A stack slice is 100 nm and the pinhole diameter is maximal (693 µm). TubulinTracker green labeled N2a cells are imaged using a 100x 1.4 NA oil immersion objective. Cells are excited with a 488 nm argon laser at 2.5% laser transmission. Fluorescence is collected with a HFT 488 beam splitter and NFT 490 and BP 500--550 IR filters. The stack slice is 100 nm and the pinhole diameter is 213 µm. Rhodamine phalloidin labeled N2a cells are imaged with a Plan-Neuofluar 63x 1.25 oil immersion objective. Cells were excited with a 543 nm helium neon laser at 7.75% laser transmission. The fluorescence is collected using a 488/543 beam splitter and NFT 545 and BP 565--615 filters. Zoom is 2X, a stack slice is 550 nm, and the pinhole is 121 µm.

FRET experiments are performed on a Nikon (Nikon Instruments, Melville, NY) C1 laser-scanning confocal microscope system equipped with spectral imaging capabilities and a Prior (Rockland, ME) remote-focus stage as described in Drenan *et al.* (101). Spectral FRET analysis is performed as described in Nashmi *et al.* (102). Data are reported as mean ± SEM.

FRAP Analysis

Raw data are processed using algorithms written in house (Matlab: MathWorks, Natick, MA) to obtain the ratio fluorescence = $\frac{f(t)-b(t)}{\left(f_{NB}(t)-b(t)\right)\times\left(f(t_o)-b(t_o)\right)}$. This expression is obtained by subtracting the background fluorescence, b(t), correcting for photobleaching that occurs during recovery scanning by obtaining the fluorescence in a region not bleached, f_{NB} (t), and normalizing to the pre bleach fluorescence intensity $f(t_o)$. Normalized traces are averaged; error bars are calculated as the standard error of the mean. Normalized data are fitted to a double exponential, 5 parameter regression in SigmaPlot (Systat Software Inc., San Jose, CA) of the form: $F(t)=F_{bo}-ae^{-bt}-ce^{-dt}$, where F_{bo} is the initial value of fluorescence following photobleaching, a, b, c, and d are constants obtained through fitting. The mobile fraction is determined by applying regression data to the following equation: $M_f=\frac{F_\infty-F_{bo}}{1-F_{bo}}$, where M_f is the mobile fraction and F_∞ is the asymptote of the recovery curve. Values for $t_{\frac{1}{2}}$ were determined by applying regression data to the following equations: $F_h = \frac{F_\infty + F_{bo}}{2}$, $t_{\frac{1}{2}} = t_h - t_{bo}$ where F_h is the value for fluorescence when half the recovery has occurred, t_h is the corresponding time for F_h, t_{bo} is the time, following photobleaching, when the first recovery image is obtained, and $t_{\frac{1}{2}}$ is the half time of equilibration (49).

Real time quantitative reverse transcription PCR

Total RNA is prepared using the RNeasy Plus Mini Kit (Qiagen, Valencia, CA). RNA concentrations are quantified using the ND-1000 UV-Vis Spectrophotometer (Nanodrop Technologies, Wilmington, DE). The primer and probe sets for Pals1, ezrin, β-actin, and γ-actin are designed by the Roche Universal Probe Library (UPL) Assay Design Center (Roche Applied Science, Indianapolis, IN). Primer sets were obtained from Integrated DNA Technologies (Coralville, IA). Table 1 displays the primer and probe sets used for RT-PCR analysis of each gene in N2a cells. One step RT-PCR is performed using the hydrolysis probe mix, 96-well plates, and the LightCycler 480 RNA Master system (Roche Applied Science) according to manufacturer instructions. Briefly, samples along with serially diluted mRNA (1:50, 1:100, 1:1000, 1:5000, 1:10000) are added to a plate, centrifuged 2 min at 1500 x g, and loaded into the instrument. The one step RT-PCR is performed as follows: 1 cycle reverse transcription at 61 ºC for 12 min; 1 cycle denaturation at 95 ºC for 30 s; 45 cycles amplification at 95 ºC for 10 s, 57 ºC for 30 s, and 72 ºC for 1 s; and 1 cycle cooling at 50 ºC for 10 s. Serial dilutions of mRNA provide the standard curves needed to quantify relative mRNA concentrations.

Statistical Analysis

Values are expressed as mean ± SEM. Unless otherwise noted. $p < 0.05$ is considered statistically significant.

Acknowledgements

This research is supported by grants from the NIH (DA-09121; DK-60623) and by an American Heart Association Postdoctoral Fellowship to Fraser Moss. We thank Elaine Bearer and Michael Quick for valuable discussions.

References

1. Guastella J, Nelson N, Nelson H, Czyzyk L, Keynan S, Miedel MC, Davidson N, Lester HA, Kanner BI. Cloning and expression of a rat brain GABA transporter. Science 1990;249(4974):1303-1306.
2. Minelli A, Brecha NC, Karschin C, DeBiasi S, Conti F. GAT-1, a high-affinity GABA plasma membrane transporter, is localized to neurons and astroglia in the cerebral cortex. J Neurosci 1995;15(11):7734-7746.
3. Morara S, Brecha NC, Marcotti W, Provini L, Rosina A. Neuronal and glial localization of the GABA transporter GAT-1 in the cerebellar cortex. Neuroreport 1996;7(18):2993-2996.
4. Radian R, Kanner BI. Stoichiometry of sodium- and chloride-coupled g-aminobutyric acid transport by synaptic plasma membrane vesicles isolated from rat brain. Biochemistry 1983;22(5):1236-1241.
5. Kavanaugh MP, Arriza JL, North RA, Amara SG. Electrogenic uptake of g-aminobutyric acid by a cloned transporter expressed in Xenopus oocytes. J Biol Chem 1992;267(31):22007-22009.
6. Mager S, Naeve J, Quick M, Labarca C, Davidson N, Lester HA. Steady states, charge movements, and rates for a cloned GABA transporter expressed in Xenopus oocytes. Neuron 1993;10(2):177-188.
7. Lester HA, Mager S, Quick MW, Corey JL. Permeation Properties of Neurotransmitter Transporters. Annual Review of Pharmacology and Toxicology 1994;34(1):219-249.
8. Chiu C-S, Jensen K, Sokolova I, Wang D, Li M, Deshpande P, Davidson N, Mody I, Quick MW, Quake SR, Lester HA. Number, Density, and Surface/Cytoplasmic Distribution of GABA Transporters at Presynaptic Structures of Knock-In Mice Carrying GABA Transporter Subtype 1-Green Fluorescent Protein Fusions. J Neurosci 2002;22(23):10251-10266.
9. Wang D, Quick MW. Trafficking of the Plasma Membrane g-Aminobutyric Acid Transporter GAT1. Size and rates of an acutely recycling pool. J Biol Chem 2005;280(19):18703-18709.
10. Triller A, Choquet D. Surface trafficking of receptors between synaptic and extrasynaptic membranes: and yet they do move! Trends in Neurosciences 2005;28(3):133-139.
11. Ashby MC, Maier SR, Nishimune A, Henley JM. Lateral Diffusion Drives Constitutive Exchange of AMPA Receptors at Dendritic Spines and Is Regulated by Spine Morphology. J Neurosci 2006;26(26):7046-7055.
12. Richards DA, de Paola V, Caroni P, Gahwiler BH, McKinney RA. AMPA-receptor activation regulates the diffusion of a membrane marker in parallel with dendritic spine motility in the mouse hippocampus. J Physiol (Lond) 2004;558(2):503-512.
13. Kirsch J, Betz H. The postsynaptic localization of the glycine receptor-associated

protein gephyrin is regulated by the cytoskeleton. J Neurosci 1995;15(6):4148-4156.

14. Sun F, Hug MJ, Lewarchik CM, Yun CHC, Bradbury NA, Frizzell RA. E3KARP Mediates the Association of Ezrin and Protein Kinase A with the Cystic Fibrosis Transmembrane Conductance Regulator in Airway Cells. J Biol Chem 2000;275(38):29539-29546.

15. Axelrod D, Koppel DE, Schlessinger J, Elson E, Webb WW. Mobility measurement by analysis of fluorescence photobleaching recovery kinetics. Biophys J 1976;16(9):1055-1069.

16. Sprague BL, Pego RL, Stavreva DA, McNally JG. Analysis of Binding Reactions by Fluorescence Recovery after Photobleaching. Biophys J 2004;86(6):3473-3495.

17. Sprague BL, McNally JG. FRAP analysis of binding: proper and fitting. Trends in Cell Biology 2005;15(2):84-91.

18. Lang T, Bruns D, Wenzel D, Riedel D, Holroyd P, Thiele C, Jahn R. SNAREs are concentrated in cholesterol-dependent clusters that define docking and fusion sites for exocytosis. Embo J 2001;20(9):2202-2213.

19. Weiss M. Challenges and Artifacts in Quantitative Photobleaching Experiments. Traffic 2004;5(9):662-671.

20. De Brabander MJ, Van de Velre RML, Aerts FEM, Borgers M, Janssen PAJ. The Effects of Methyl [5-(2-Thienylcarbonyl)-1H-benzimidazol-2-yl]carbamate, (R 17934; NSC 238159), a New Synthetic Antitumoral Drug Interfering with Microtubules, on Mammalian Cells Cultured in Vitro. Cancer Res 1976;36(3):905-916.

21. Chen L, Wang H, Vicini S, Olsen RW. The g-aminobutyric acid type A ($GABA_A$) receptor-associated protein (GABARAP) promotes $GABA_A$ receptor clustering and modulates the channel kinetics. PNAS 2000;97(21):11557-11562.

22. Jacob TC, Bogdanov YD, Magnus C, Saliba RS, Kittler JT, Haydon PG, Moss SJ. Gephyrin Regulates the Cell Surface Dynamics of Synaptic $GABA_A$ Receptors. J Neurosci 2005;25(45):10469-10478.

23. Bretscher A, Edwards K, Fehon RG. ERM proteins and merlin: integrators at the cell cortex. Nat Rev Mol Cell Biol 2002;3(8):586-599.

24. Yun CHC, Lamprecht G, Forster DV, Sidor A. NHE3 Kinase A Regulatory Protein E3KARP Binds the Epithelial Brush Border Na+/H+ Exchanger NHE3 and the Cytoskeletal Protein Ezrin. J Biol Chem 1998;273(40):25856-25863.

25. McHugh EM, Zhu W, Milgram S, Mager S. The GABA transporter GAT1 and the MAGUK protein Pals1: interaction, uptake modulation, and coexpression in the brain. Molecular and Cellular Neuroscience 2004;26(3):406-417.

26. Adams DS. Lab Math: A Handbook of Measurements, Calculations, and Other Quantitative Skills for Use at the Bench. Cold Spring Harbor Cold Spring Harbor Laboratory Press; 2003. p. 187-190.

27. Zhu L, Liu Y, Forte JG. Ezrin oligomers are the membrane-bound dormant form in gastric parietal cells. Am J Physiol Cell Physiol 2005;288(6):C1242-1254.

28. Gary R, Bretscher A. Ezrin self-association involves binding of an N-terminal domain to a normally masked C-terminal domain that includes the F-actin binding site. Mol Biol Cell 1995;6(8):1061-1075.

29. Bates IR, Hebert B, Luo Y, Liao J, Bachir AI, Kolin DL, Wiseman PW, Hanrahan JW. Membrane Lateral Diffusion and Capture of CFTR within Transient Confinement Zones. Biophys J 2006;91(3):1046-1058.

30. Cha B, Kenworthy A, Murtazina R, Donowitz M. The lateral mobility of NHE3 on the apical membrane of renal epithelial OK cells is limited by the PDZ domain proteins NHERF1/2, but is dependent on an intact actin cytoskeleton as determined by FRAP. J Cell Sci 2004;117(15):3353-3365.

31. Haggie PM, Stanton BA, Verkman AS. Increased Diffusional Mobility of CFTR at the Plasma Membrane after Deletion of Its C-terminal PDZ Binding Motif. J Biol Chem 2004;279(7):5494-5500.

32. Torres GE, Yao W-D, Mohn AR, Quan H, Kim K-M, Levey AI, Staudinger J, Caron MG. Functional Interaction between Monoamine Plasma Membrane Transporters and the Synaptic PDZ Domain-Containing Protein PICK1. Neuron 2001;30(1):121-134.

33. Lamprecht G, Seidler U. The emerging role of PDZ adapter proteins for regulation of intestinal ion transport. Am J Physiol Gastrointest Liver Physiol 2006;291(5):G766-777.

34. Cao X, Ding X, Guo Z, Zhou R, Wang F, Long F, Wu F, Bi F, Wang Q, Fan D, Forte JG, Teng M, Yao X. PALS1 Specifies the Localization of Ezrin to the Apical Membrane of Gastric Parietal Cells. J Biol Chem 2005;280(14):13584-13592.

35. Yonemura S, Hirao M, Doi Y, Takahashi N, Kondo T, Tsukita S, Tsukita S. Ezrin/Radixin/Moesin (ERM) Proteins Bind to a Positively Charged Amino Acid Cluster in the Juxta-Membrane Cytoplasmic Domain of CD44, CD43, and ICAM-2. J Cell Biol 1998;140(4):885-895.

36. Denker SP, Huang DC, Orlowski J, Furthmayr H, Barber DL. Direct Binding of the Na-H Exchanger NHE1 to ERM Proteins Regulates the Cortical Cytoskeleton and Cell Shape Independently of H+ Translocation. Molecular Cell 2000;6(6):1425-1436.

37. Kneussel M, Loebrich S. Trafficking and synaptic anchoring of ionotropic inhibitory

neurotransmitter receptors. Biology of the Cell 2007;099(6):297-309.

38. Kirsch J, Langosch D, Prior P, Littauer UZ, Schmitt B, Betz H. The 93-kDa glycine receptor-associated protein binds to tubulin. J Biol Chem 1991;266(33):22242-22245.

39. Kneussel M, Betz H. Receptors, gephyrin and gephyrin-associated proteins: novel insights into the assembly of inhibitory postsynaptic membrane specializations. J Physiol 2000;525(1):1-9.

40. Yang JW, Czech T, Felizardo M, Baumgartner C, Lubec G. Aberrant expression of cytoskeleton proteins in hippocampus from patients with mesial temporal lobe epilepsy. Amino Acids 2006;30(4):477-493.

41. Lee TS, Mane S, Eid T, Zhao H, Lin A, Guan Z, Kim JH, Schweitzer J, King-Stevens D, Weber P, Spencer SS, Spencer DD, de Lanerolle NC. Gene expression in temporal lobe epilepsy is consistent with increased release of glutamate by astrocytes. Mol Med 2007;13(1-2):1-13.

42. Andre V, Dube C, Francois J, Leroy C, Rigoulot M-A, Roch C, Namer IJ, Nehlig A. Pathogenesis and Pharmacology of Epilepsy in the Lithium-pilocarpine Model. Epilepsia 2007;48(s5):41-47.

43. Greene ND, Bamidele A, Choy M, de Castro SC, Wait R, Leung KY, Begum S, Gadian DG, Scott RC, Lythgoe MF. Proteome changes associated with hippocampal MRI abnormalities in the lithium pilocarpine-induced model of convulsive status epilepticus. PROTEOMICS 2007;7(8):1336-1344.

44. Majores M, Schick V, Engels G, Fassunke J, Elger C, Schramm J, Blümcke I, Becker A. Mutational and immunohistochemical analysis of ezrin-, radixin-, moesin (ERM) molecules in epilepsy-associated glioneuronal lesions. Acta Neuropathologica 2005;110(6):537-546.

45. Schick V, Majores M, Koch A, Elger CE, Schramm J, Urbach H, Becker AJ. Alterations of Phosphatidylinositol 3-Kinase Pathway Components in Epilepsy-associated Glioneuronal Lesions. Epilepsia 2007;48(s5):65-73.

46. Hoogland G, Spierenburg HA, van Veelen CW, van Rijen PC, van Huffelen AC, de Graan PN. Synaptosomal glutamate and GABA transport in patients with temporal lobe epilepsy. J Neurosci Res 2004;76(6):881-890.

47. Richerson GB, Wu Y. Role of the GABA transporter in epilepsy. Adv Exp Med Biol 2004;548:76-91.

48. Wu Y, Wang W, Richerson GB. Vigabatrin Induces Tonic Inhibition Via GABA Transporter Reversal Without Increasing Vesicular GABA Release. J Neurophysiol 2003;89(4):2021-2034.

49. Honmou O, Kocsis JD, Richerson GB. Gabapentin potentiates the conductance increase induced by nipecotic acid in CA1 pyramidal neurons in vitro. Epilepsy Research 1995;20(3):193-202.

50. Wu Y, Wang W, Richerson GB. GABA Transaminase Inhibition Induces Spontaneous and Enhances Depolarization-Evoked GABA Efflux via Reversal of the GABA Transporter. J Neurosci 2001;21(8):2630-2639.

51. Richerson GB, Wu Y. Role of the GABA Transporter in Epilepsy. In: Binder DK, Scharfman HE, editors. Advances in Experimental Medicine and Biology. New York: Kluwer Academic/Plenum Publishers; 2004. p. 76-91.

52. Zhang J, Campbell RE, Ting AY, Tsien RY. Creating new fluorescent probes for cell biology. Nat Rev Mol Cell Biol 2002;3(12):906-918.

53. Geiser M, Cebe R, Drewello D, Schmitz R. Integration of PCR fragments at any specific site within cloning vectors without the use of restriction enzymes and DNA ligase. Biotechniques 2001;31(1):88-90, 92.

54. An SJ, Almers W. Tracking SNARE Complex Formation in Live Endocrine Cells. Science 2004;306(5698):1042-1046.

55. Lu Y, Grady S, Marks MJ, Picciotto M, Changeux J-P, Collins AC. Pharmacological Characterization of Nicotinic Receptor-stimulated GABA Release From Mouse Brain Synaptosomes. J Pharmacol Exp Ther 1998;287(2):648-657.

56. Leach RN, Desai JC, Orchard CH. Effect of cytoskeleton disruptors on L-type Ca channel distribution in rat ventricular myocytes. Cell Calcium 2005;38(5):515-526.

57. Vasquez RJ, Howell B, Yvon AM, Wadsworth P, Cassimeris L. Nanomolar concentrations of nocodazole alter microtubule dynamic instability in vivo and in vitro. Mol Biol Cell 1997;8(6):973-985.

58. Drenan RM, Nashmi R, Imoukhuede PI, Just H, McKinney S, Lester HA. Subcellular Trafficking, Pentameric Assembly and Subunit Stoichiometry of Neuronal Nicotinic ACh Receptors Containing Fluorescently-Labeled a6 and b3 Subunits. Mol Pharmacol 2007:mol.107.039180.

59. Nashmi R, Dickinson ME, McKinney S, Jareb M, Labarca C, Fraser SE, Lester HA. Assembly of a4b2 Nicotinic Acetylcholine Receptors Assessed with Functional Fluorescently Labeled Subunits: Effects of Localization, Trafficking, and Nicotine-Induced Upregulation in Clonal Mammalian Cells and in Cultured Midbrain Neurons. J Neurosci 2003;23(37):11554-11567.

60. Rabut G, Ellenberg, Jan. Photobleaching Techniques to Study Mobility and Molecular Dyanmics of Proteins in Live Cells: FRAP, iFRAP, and FLIP. In: Robert D. Goldman DS, editor. Live Cell Imaging: A Lab Manual.

Cold Spring Harbor, New York: Cold Spring Harbor Laboratory Press; 2005. p. 101-126.

Figure Legends

Figure 1: Whole footprint photobleach reveals lateral mobility. A) Confocal images of GAT1-YFP8 localized at the cell footprint are shown before, and after photobleaching an area representing > 90% of the footprint surface area. Proportion bar,10 µm. B) The kymograph is obtained by performing line profile analysis of the photobleached region and plotting the line profile over time. The intensity ramp shows that photobleached regions are represented by the lower intensity colors, and increased fluorescence is represented by higher intensity colors. C) The diffusion model was simulated using the Axelrod-Sprague pure-diffusion model and data from GAT1-YFP8 footprint FRAP recovery. The GAT1-YFP8 recovery curve is not well fit by the Axelrod-Sprague pure-diffusion model. The GAT1-YFP8 footprint FRAP recovery curve does fit to a double exponential decay equation, $F(t) = F_{bo} - ae^{-bt} - ce^{-dt}$ with a, b, c, & d = 3.3, 0.30, 0.45, & 0.033, respectively.

Figure 2: Comparing GAT1 mobility. Footprint FRAP performed on (A) YFP, GAT1-YFP8 and (B) YFP-syntaxin. (C) Recovery curves show that YFP, which exhibits cytosolic localization, has a faster recovery than either of the membrane proteins. The initial YFP recovery is faster than the frequency of detection. The membrane proteins, GAT1-YFP8 and Syntaxin-YFP, recovered at nearly equivalent rates.

Figure 3: Photobleached regions. FRAP pre-bleach and post-bleach images of N2a cells expressing GAT1-YFP8. A) Photobleaching is confined to the cell footprint indicated by the red circle 8 μm^2. Scale bar, 3 µm. B) Photobleaching is confined to the cell perimeter, indicated by the red rectangle 13 μm^2. Scale bar, 4µm. C) GAT1-YFP8 footprint photobleach gave a recovery $t_{1/2}$ = 10 s and a mobile fraction of 60%. GAT1-YFP8 perimeter photobleach gave a recovery $t_{1/2}$=20 s and a mobile fraction of 50%.

Figure 4: GAT1 does not associate with microtubules. A/B) Microtubules are visible after treatment with TubulinTracker 488. The second panel sets display nuclear labeling with Hoechst 33342. B) Microtubules are disrupted by treatment with 10 µM nocodazole. Scale bars, 10 µm. C/D) Traces display GAT1-YFP8 fluorescence recovery in cells with and without intact microtubules. Cells are photobleached at the (C) footprint and at the cell (D) perimeter.

Figure 5: GAT1 associates with cytoskeleton through an interaction with actin. A/B) Actin is visible after N2a cells are treated with rhodamine-conjugated phalloidin. B) Actin filaments are disrupted by treatment with latrunculin B. Scale bars, 10 µm. Traces display GAT1-YFP8 fluorescence recovery in cells with and without an intact actin network. Fluorescence is photobleached at the cell (C) footprint and at the cell (D) perimeter.

Figure 6: Summary of GAT1 mobile fractions and recovery time constants. A) GAT1-YFP8 mobile fraction. Disrupting actin with 5 µM latrunculin B significantly increases the amount of freely diffusing GAT1 on the plasma membrane ($p < 0.001$, t-test). The addition of 1 µg/ml cytochalasin D, another actin depolymerizer, also significantly increases the mobile fraction when probed with footprint photobleach ($p < 0.001$, t-test). Depolymerizing microtubules with 10 µM nocodazole does not affect the mobile fraction of GAT1-YFP8. B) GAT1-YFP8 time constant. Disrupting actin with cytochalasin D or latrunculin B increases the time for recovery with perimeter photobleach ($p < 0.05$, Mann-Whitney). Cytochalasin D treatment also significantly increases the time constant for recovery with footprint photobleach ($p < 0.05$, Mann-Whitney). Microtubule disruption does not significantly affect the time constant. [GAT1-YFP8 footprint: n = 18, GAT1-YFP8 + nocodazole footprint: n = 8, GAT1-YFP8 + latrunculin B footprint: n = 12, GAT1-YFP8 + cytochalasin D footprint: n = 10. GAT1-YFP8 perimeter: n = 12, GAT1-YFP8 + nocodazole perimeter: n = 9, GAT1-YFP8 + latrunculin B perimeter: n = 12, GAT1-YFP8 + cytochalasin D perimeter: n = 10.] C) Schematics of GAT1-YFP8 and $GAT1_0$-GFP. $GAT1_0$-GFP is mostly found in vesicles near the plasma membrane (33); this faulty trafficking arises because the addition of linker and GFP moiety interrupts the PDZ binding motif. GAT1-YFP8 traffics properly due to the addition of 8 amino acids following the fluorescent protein, the final 3 amino acids being a consensus PDZ-binding motif, AYI-CO_2^-. D) $GAT1_0$-GFP has a higher mobile fraction than GAT1-YFP8 ($p < 0.05$, t-test). Disrupting actin does not significantly affect the mobile fraction of $GAT1_0$-GFP compared to $GAT1_0$-GFP mobility in cells with intact actin. [$GAT1_0$-GFP footprint: n = 9, $GAT1_0$-GFP + latrunculin B footprint: n = 9 $GAT1_0$-GFP perimeter: n = 12, $GAT1_0$-GFP + latrunculin B perimeter: n = 10].

Figure 7: Real-time quantitative reverse transcription polymerase chain reaction (RT-PCR) determines the expression of ezrin and Pals1 in N2a cells, and FRET reveals an interaction between ezrin and GAT1-YFP8. A) mRNA levels of β-actin, γ-actin, ezrin, and Pals1, normalized to β-actin expression. One-step RT-PCR shows that ezrin is expressed in N2a cells at levels similar to the PDZ protein Pals1. B/C/D/E/F) FRET results. When CFP and YFP fusion proteins are in close proximity (10-100

Å), 440 nm excitation of CFP (donor) results in nonradiative transfer of energy (FRET) to YFP (acceptor), resulting in an emission peak of 527 nm. Acceptor photobleaching reveals FRET by measuring incremental dequenching of CFP during photodestruction of YFP with a high intensity 514 nm laser line. Spectral imaging was performed on a confocal microscope at 5 nm resolution. B/C/D) Display pre-bleaching and post bleaching images of the respective CFP and YFP fused proteins. Scale bar 5 µm. E) GAT1-YFP8 and ezrin-CFP interact as represented by the 25% ± 3% increase in ezrin-CFP fluorescence with photodestruction of GAT1-YFP8. The disruption of actin through addition of 5 µm latrunculin B significantly abolished FRET between ezrin-CFP and GAT1-YFP8. As a positive control, FRET between YFP-ezrin and ezrin-CFP was performed, resulting in a 26% ± 3% increase in ezrin-CFP fluorescence with photodestruction of YFP-ezrin. F) The FRET efficiency for ezrin-CFP/GAT1-YFP8 was 19% ± 2%, for ezrin-CFP/GAT1-YFP8 + latrunculin B 7% ± 5%, and for ezrin-CFP/YFP-ezrin was 20% ± 2%. Values are represented as the mean of 23 replicates ± SEM. Significance was determined by Tukey's one way analysis of variance $p < 0.05$.

Figure 8: Schematic of GAT1 interaction with Pals1, ezrin, and actin. A) Schematic of GAT1-YFP8 interaction with actin via ezrin and Pals1. The additional PDZ domain following the YFP moiety restores the interaction between GAT1 and the PDZ protein. B) The addition of 5 µM latrunculin B disrupts actin, reduces the interaction between ezrin and GAT1 either by (B1) pulling away the GAT1-PDZ interaction or by (B2) reducing the interaction between ezrin and the PDZ protein. Altogether, this increases the mobility of GAT1 on the membrane. C) $GAT1_0$GFP, a GAT1 with a disrupted PDZ domain, is more mobile on the membrane, indicating that this domain may also stabilize the GAT1-ezrin-actin interaction.

Supplemental figure 1: Whole footprint photobleach of latrunculin B treated cells. A) Confocal images of GAT1-YFP8 localized at the cell footprint are shown before and after photobleaching an area of the cell representing > 90% footprint. Proportion bar,10 µm. B) A kymograph is obtained by performing line profile analysis of the photobleached region and plotting the line profile over time. The intensity ramp shows that photobleached regions are represented by the lower intensity colors, and increased fluorescence is represented by higher intensity colors.

Supplemental figure 2: Total internal reflection fluorescence images of N2a cells transfected with GAT1-YFP8 A) GAT1-YFP8 localizes on the cell membrane and in filopodia. Neither overnight treatment with (B) 10 µM nocodazole nor (C) 1 hr treatment with 5 µM latrunculin B affect cell attachment to the coverslip. C) Latrunculin B treatment does significantly reduce the number of filopodial contacts the coverslip.

Supplemental figure 3: Comparison of GAT1 mobile fractions. Perimeter photobleach indicates that disrupting actin filaments via latrunculin B treatment results in a significantly reduced recovery time constant for $GAT1_0$-GFP compared to GAT1-YFP8 ($p < 0.05$, Mann-Whitney). This result suggests that a GAT1 that can interact with PDZ proteins has a higher effective molecular weight than a GAT1 that cannot interact with PDZ proteins (recovery time constant proportional to the molecular weight of the species). [$GAT1_0$-GFP footprint: n = 9, $GAT1_0$-GFP + latrunculin B footprint: n = 9 GAT1-YFP footprint: n=18, $GAT1_0$-GFP perimeter: n = 12, $GAT1_0$-GFP + latrunculin B perimeter: n = 10, GAT1-YFP8 perimeter: n=12].

TABLES

Table 1. Distance between fluorophores obtained from FRET

FRET Pairs	r (Å)
GAT1-YFP8/Ezrin-CFP, n=25	66 ± 2
YFP-Ezrin/Ezrin-CFP, n=25	65 ± 2
GAT1-YFP8/Ezrin-CFP + Latrunculin B, n=18	> 72

*The “at least” estimate is presented because 5 out of 23 cells do not display FRET. Cells not exhibiting FRET would indicate fluorophore distances > 100 Å.

Table 2. Primers and UPL probes used in RT-PCR analysis of Pals1, ezrin, β-actin, and γ-actin expression in N2a cells. All primer/probe sets were designed using the Roche Universal Probe Library Assay Design Center.

Protein (Gene accession #)	Primer Sequences		UPL #
	Forward (5’→ 3’)	Reverse (5’→ 3’)	
Pals1 (NM_019579.1)	TGATTCCTAGTCAACAGATCAAGC	GTCAAAATGAGCTTTCACATGG	51
Ezrin (NM_009510.2)	AGCCGAATAGCCGAGGAC	GTCACCCGGACGTTGATT	21
β-Actin (NM_007393.1)	CTAAGGCCAACCGTGAAAAG	ACCAGAGGCATACAGGGACA	64
γ-Actin (NM_009609.2)	GAGCACGCTGTAGATGAGAAAG	GATCACTCAGTGGTGCTCACA	64

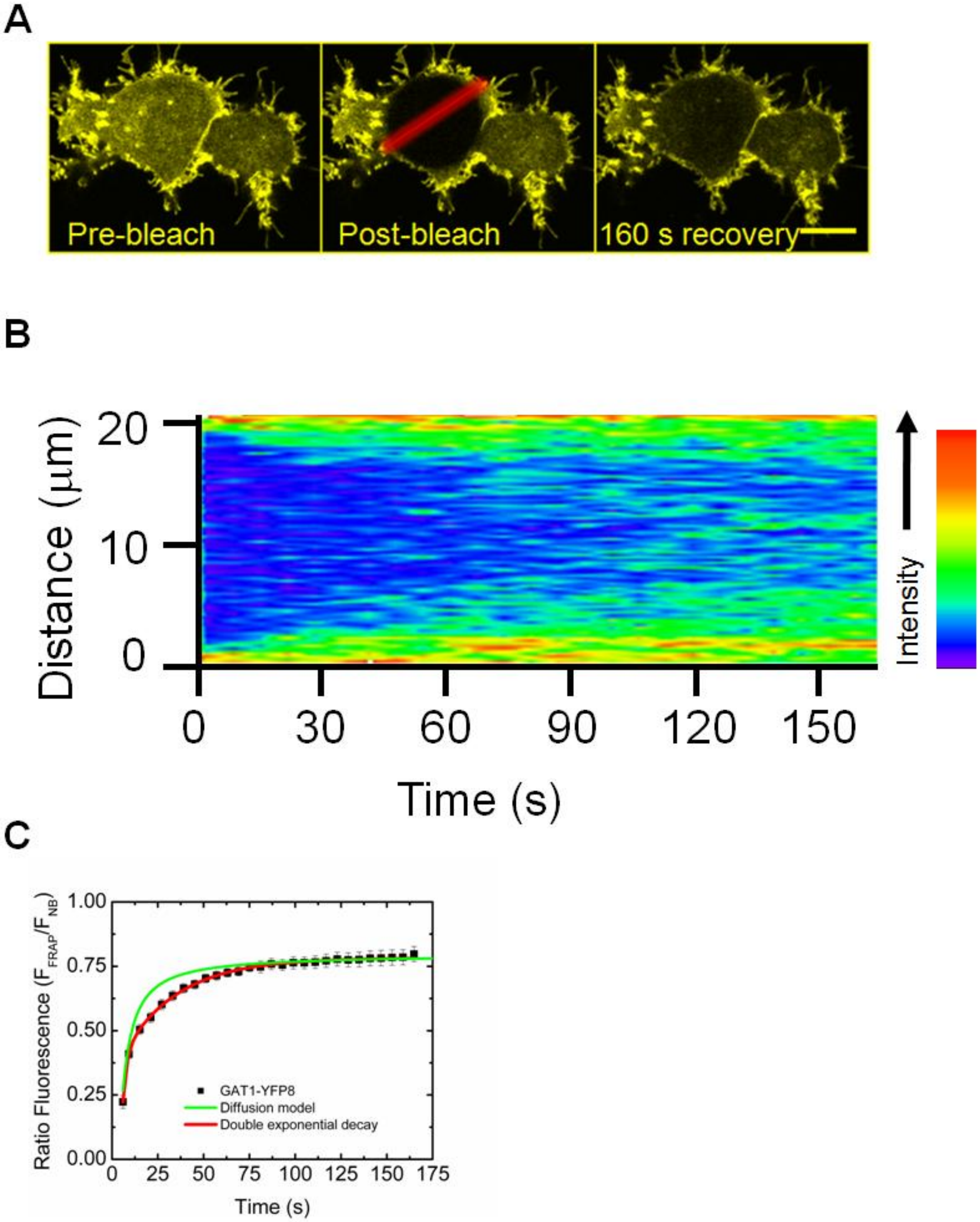
A
Pre-bleach
Post-bleach
160 s recovery
B
Distance (μm)
0
10
20
Time (s)
0
30
60
90
120
150
Intensity
C
Ratio Fluorescence (F_{FRAP}/F_{NB})
0.00
0.25
0.50
0.75
1.00
Time (s)
0
25
50
75
100
125
150
175
GAT1-YFP8
Diffusion model
Double exponential decay

Figure 1

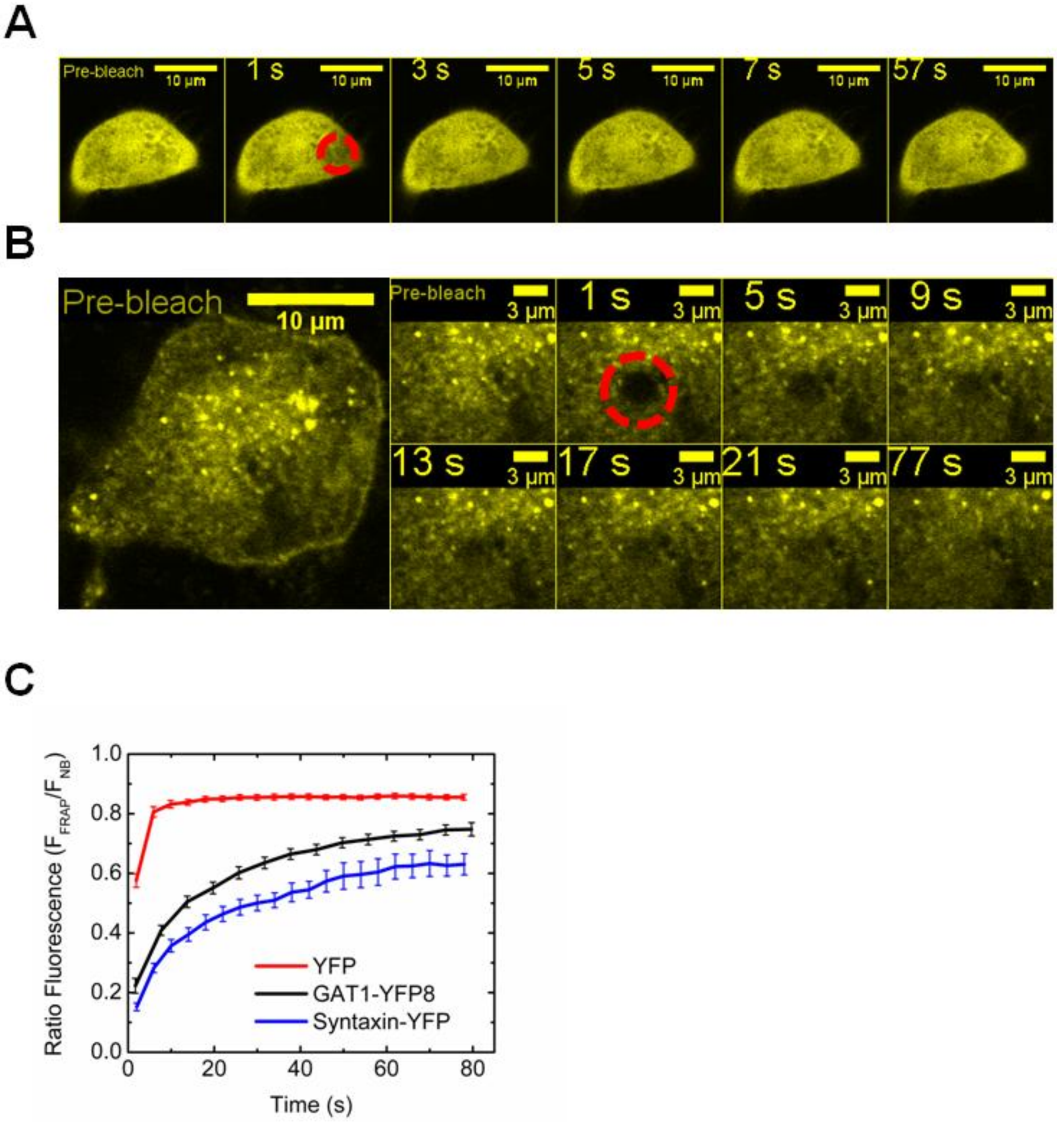
A
Pre-bleach
10 µm
1 s
3 s
5 s
7 s
57 s
B
Pre-bleach
10 µm
3 µm
1 s
5 s
9 s
13 s
17 s
21 s
77 s
C
Ratio Fluorescence (F_{FRAP}/F_{NB})
1.0
0.8
0.6
0.4
0.2
0.0
0
20
40
60
80
Time (s)
YFP
GAT1-YFP8
Syntaxin-YFP

Figure 2

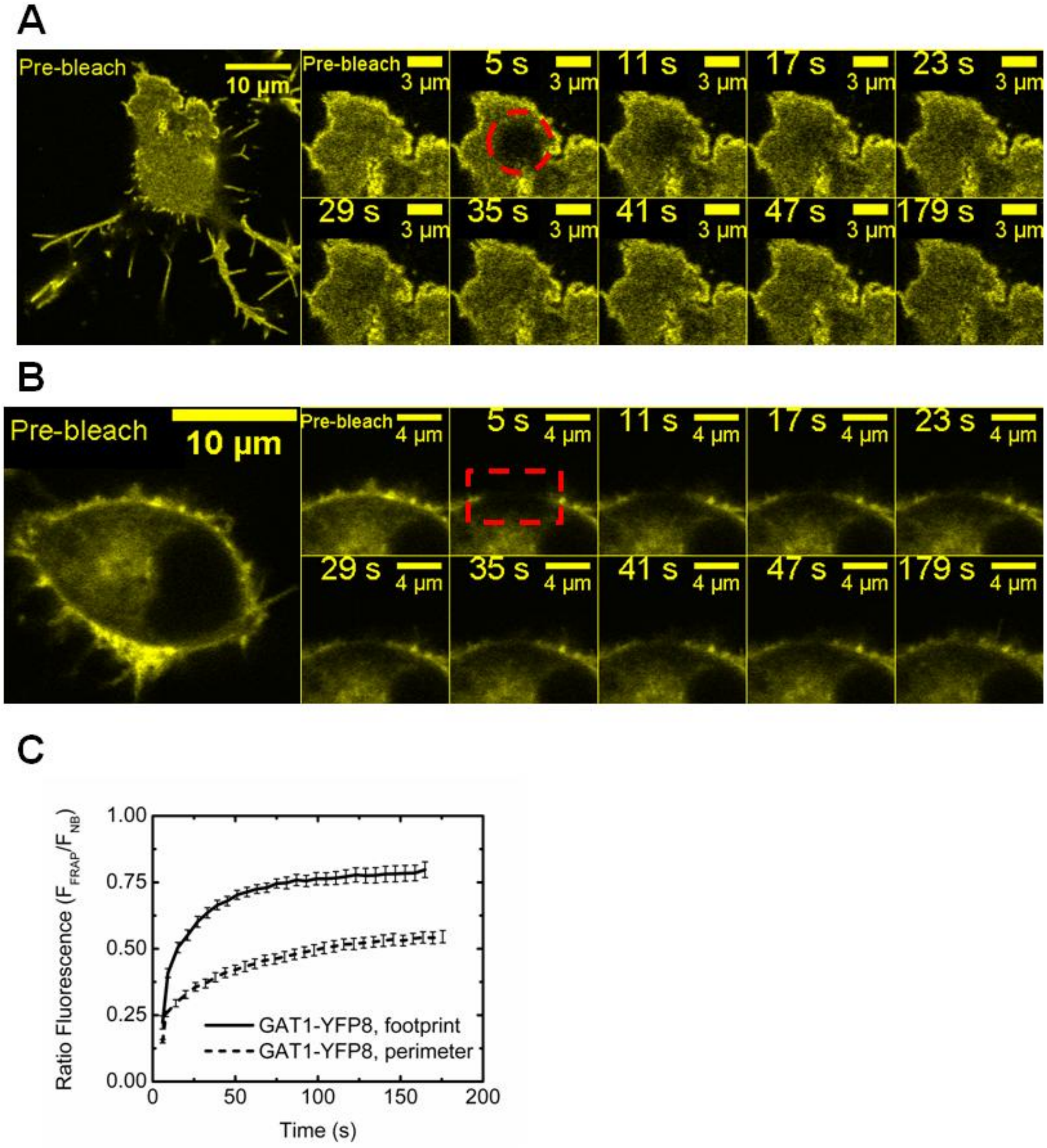
A
Pre-bleach
10 µm
Pre-bleach
3 µm
5 s
11 s
17 s
23 s
29 s
35 s
41 s
47 s
179 s
B
Pre-bleach
10 µm
Pre-bleach
4 µm
5 s
11 s
17 s
23 s
29 s
35 s
41 s
47 s
179 s
C
Ratio Fluorescence (F_{FRAP}/F_{NB})
1.00
0.75
0.50
0.25
0.00
0
50
100
150
200
Time (s)
GAT1-YFP8, footprint
GAT1-YFP8, perimeter

Figure 3

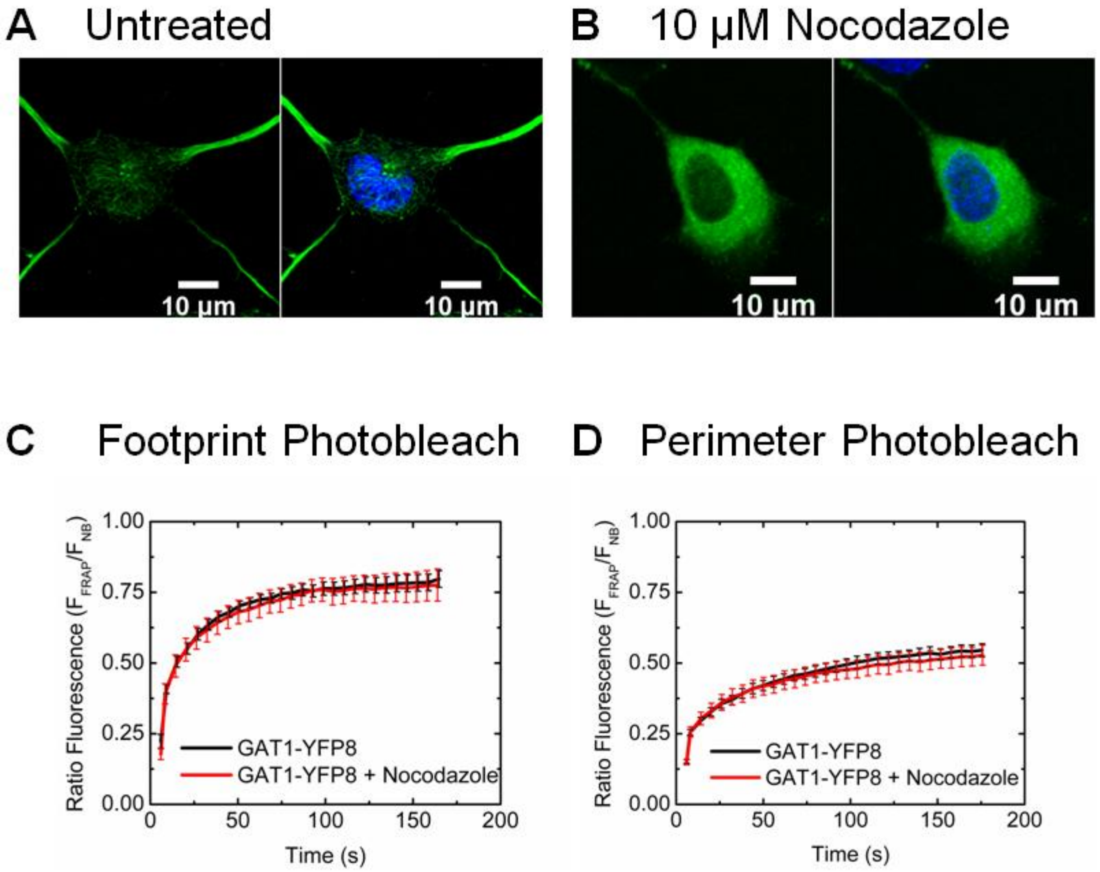
A
Untreated
B
10 µM Nocodazole
10 µm
10 µm
10 µm
10 µm
C
Footprint Photobleach
D
Perimeter Photobleach
Ratio Fluorescence (F_{FRAP}/F_{NB})
1.00
0.75
0.50
0.25
0.00
0
50
100
150
200
Time (s)
GAT1-YFP8
GAT1-YFP8 + Nocodazole
Ratio Fluorescence (F_{FRAP}/F_{NB})
1.00
0.75
0.50
0.25
0.00
0
50
100
150
200
Time (s)
GAT1-YFP8
GAT1-YFP8 + Nocodazole

Figure 4

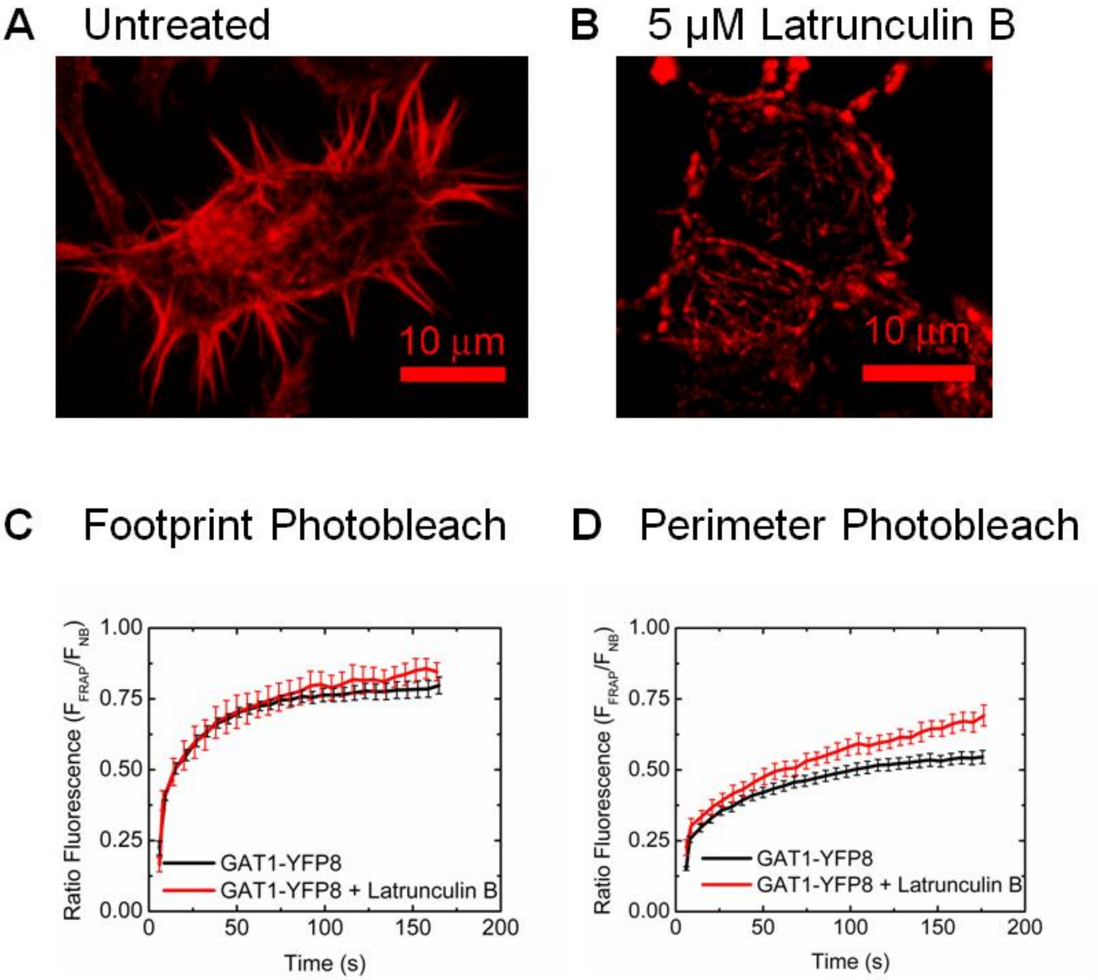
A
Untreated
10 µm
B
5 µM Latrunculin B
10 µm
C
Footprint Photobleach
D
Perimeter Photobleach
Ratio Fluorescence (F_{FRAP}/F_{NB})
1.00
0.75
0.50
0.25
0.00
0
50
100
150
200
Time (s)
GAT1-YFP8
GAT1-YFP8 + Latrunculin B

Figure 5

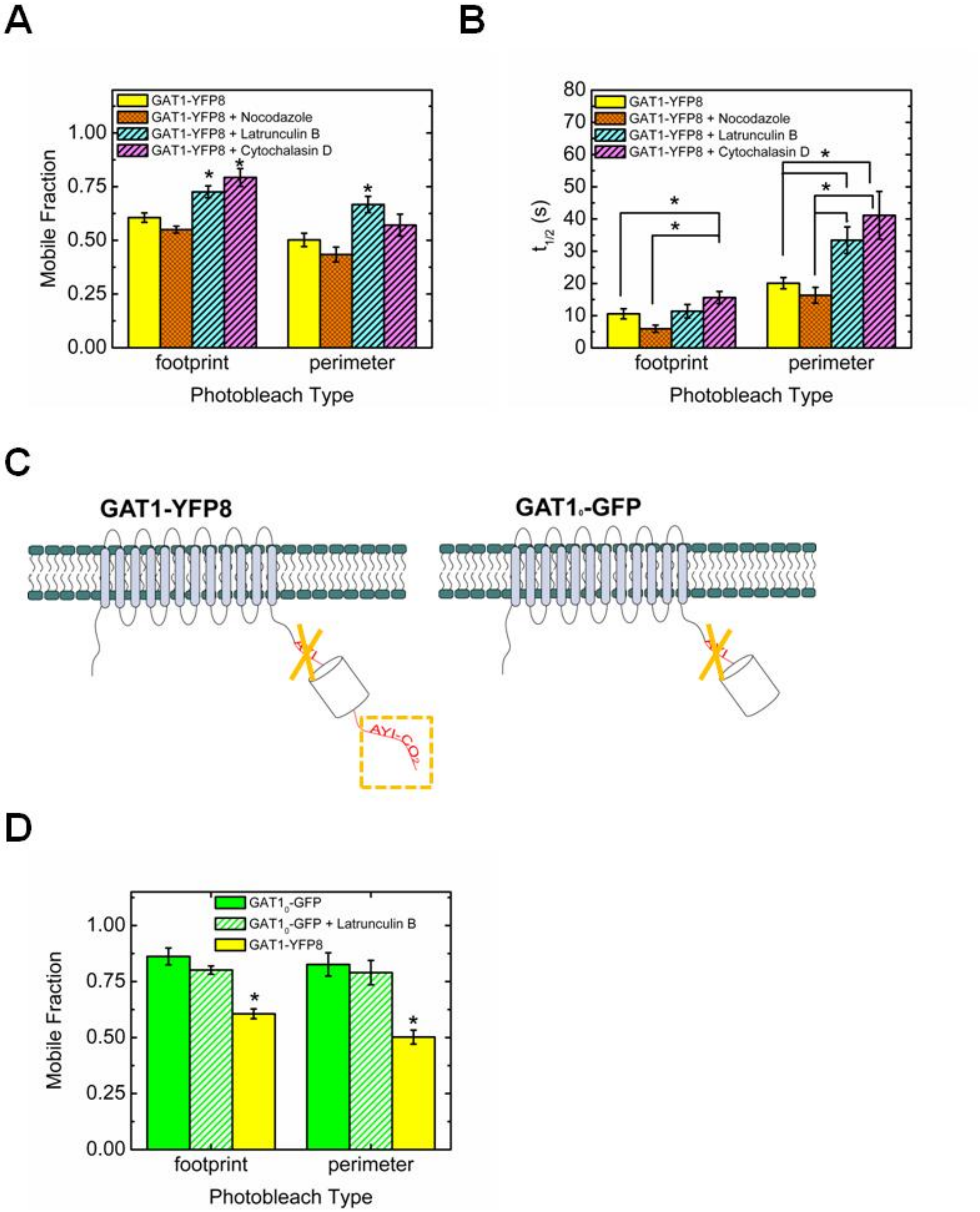
A
B
GAT1-YFP8
GAT1-YFP8 + Nocodazole
GAT1-YFP8 + Latrunculin B
GAT1-YFP8 + Cytochalasin D
Mobile Fraction
1.00
0.75
0.50
0.25
0.00
*
footprint
perimeter
Photobleach Type
$t_{1/2}$ (s)
80
70
60
50
40
30
20
10
0
C
GAT1-YFP8
GAT1₀-GFP
AYI
AYI-CO₂
D
GAT1₀-GFP
GAT1₀-GFP + Latrunculin B
GAT1-YFP8

Figure 6

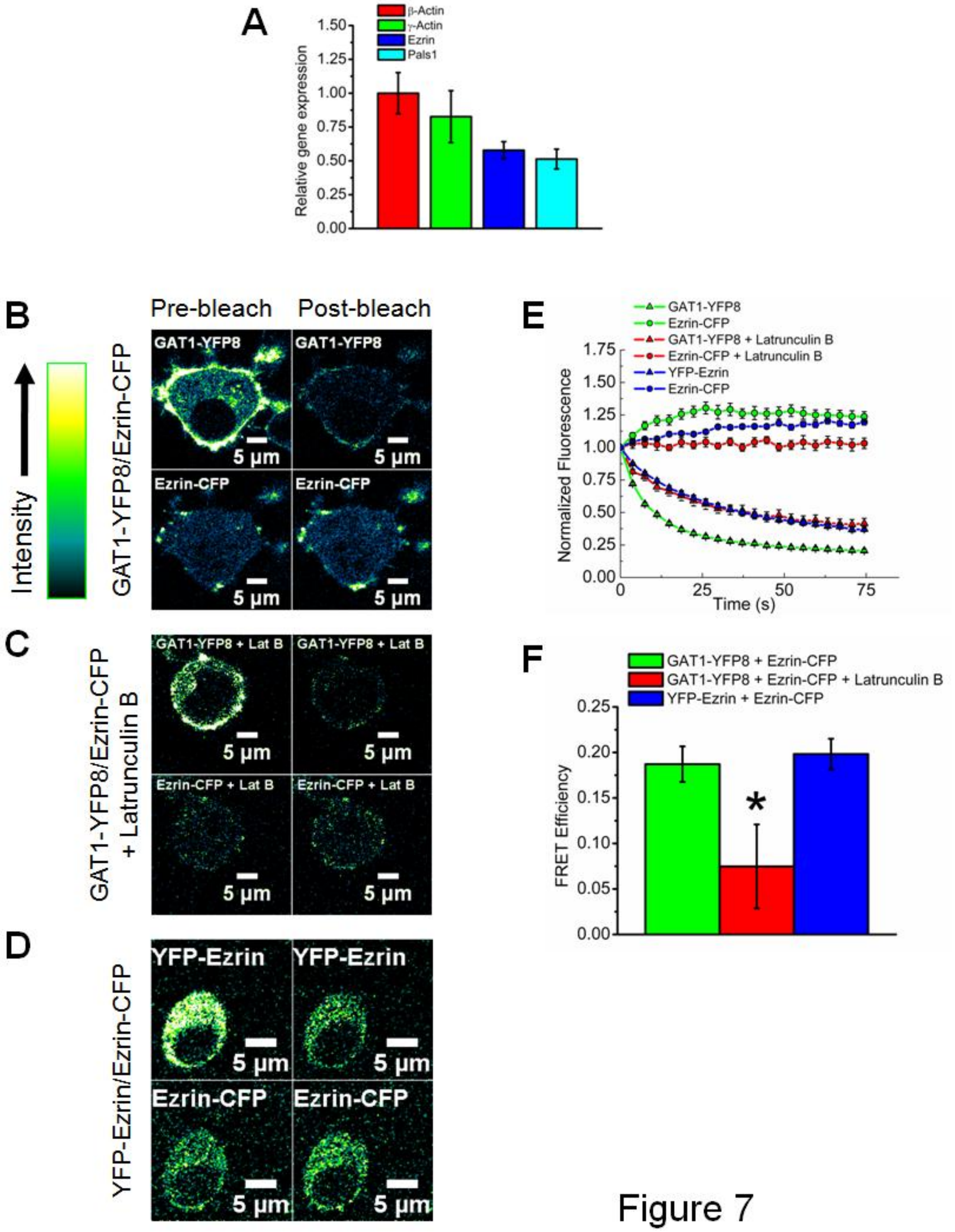
A
β-Actin
γ-Actin
Ezrin
Pals1
Relative gene expression
1.50
1.25
1.00
0.75
0.50
0.25
0.00
B
Pre-bleach
Post-bleach
Intensity
GAT1-YFP8/Ezrin-CFP
GAT1-YFP8
Ezrin-CFP
5 µm
C
GAT1-YFP8/Ezrin-CFP + Latrunculin B
GAT1-YFP8 + Lat B
Ezrin-CFP + Lat B
5 µm
D
YFP-Ezrin/Ezrin-CFP
YFP-Ezrin
Ezrin-CFP
5 µm
E
GAT1-YFP8
Ezrin-CFP
GAT1-YFP8 + Latrunculin B
Ezrin-CFP + Latrunculin B
YFP-Ezrin
Ezrin-CFP
Normalized Fluorescence
1.75
1.50
1.25
1.00
0.75
0.50
0.25
0.00
0
25
50
75
Time (s)
F
GAT1-YFP8 + Ezrin-CFP
GAT1-YFP8 + Ezrin-CFP + Latrunculin B
YFP-Ezrin + Ezrin-CFP
FRET Efficiency
0.25
0.20
0.15
0.10
0.05
0.00
*

Figure 7

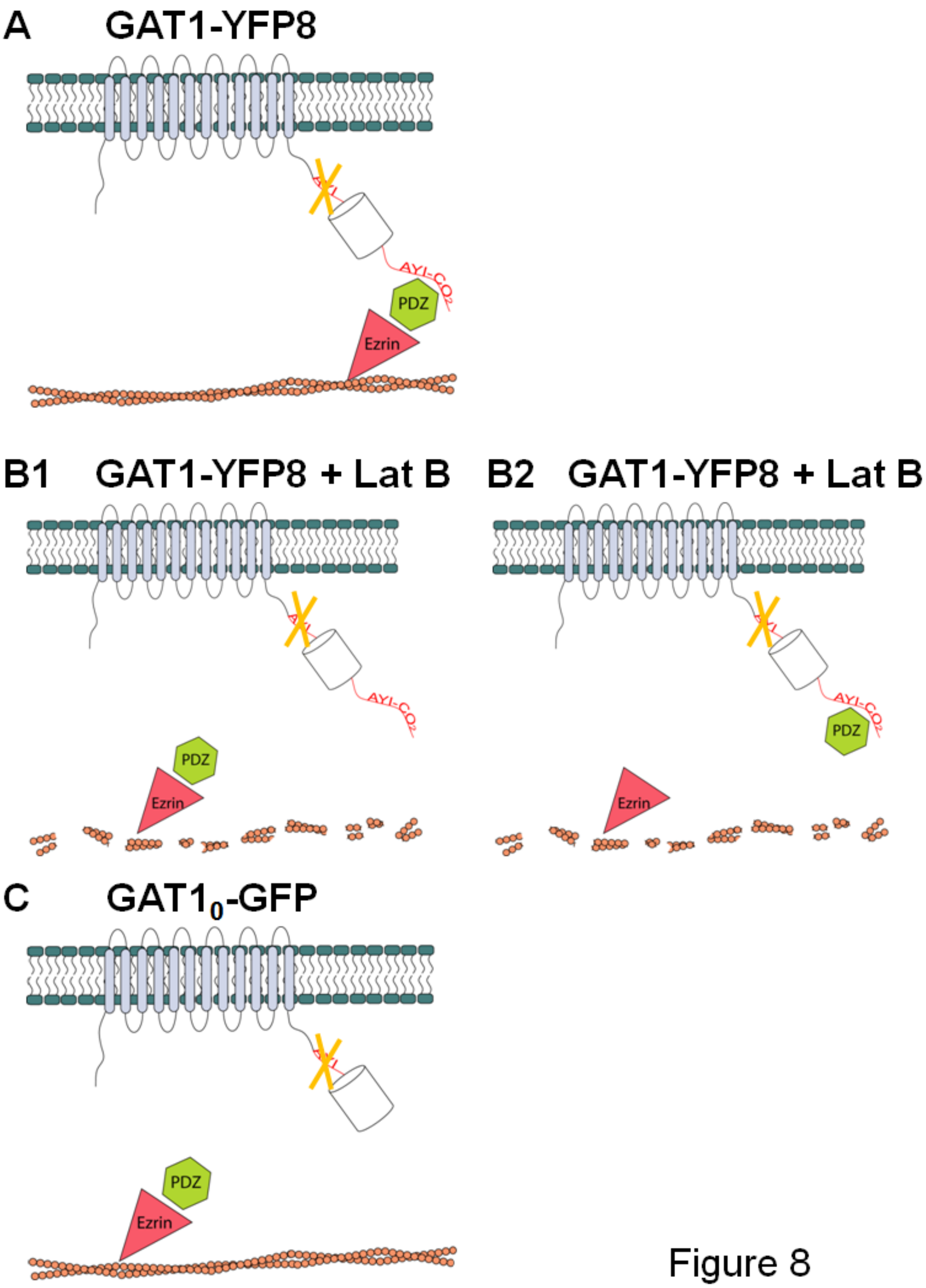
A
GAT1-YFP8
AYI
AYI-CO2
PDZ
Ezrin
B1
GAT1-YFP8 + Lat B
AYI
AYI-CO2
PDZ
Ezrin
B2
GAT1-YFP8 + Lat B
AYI
AYI-CO2
PDZ
Ezrin
C
GAT1$_0$-GFP
AYI
PDZ
Ezrin

Figure 8

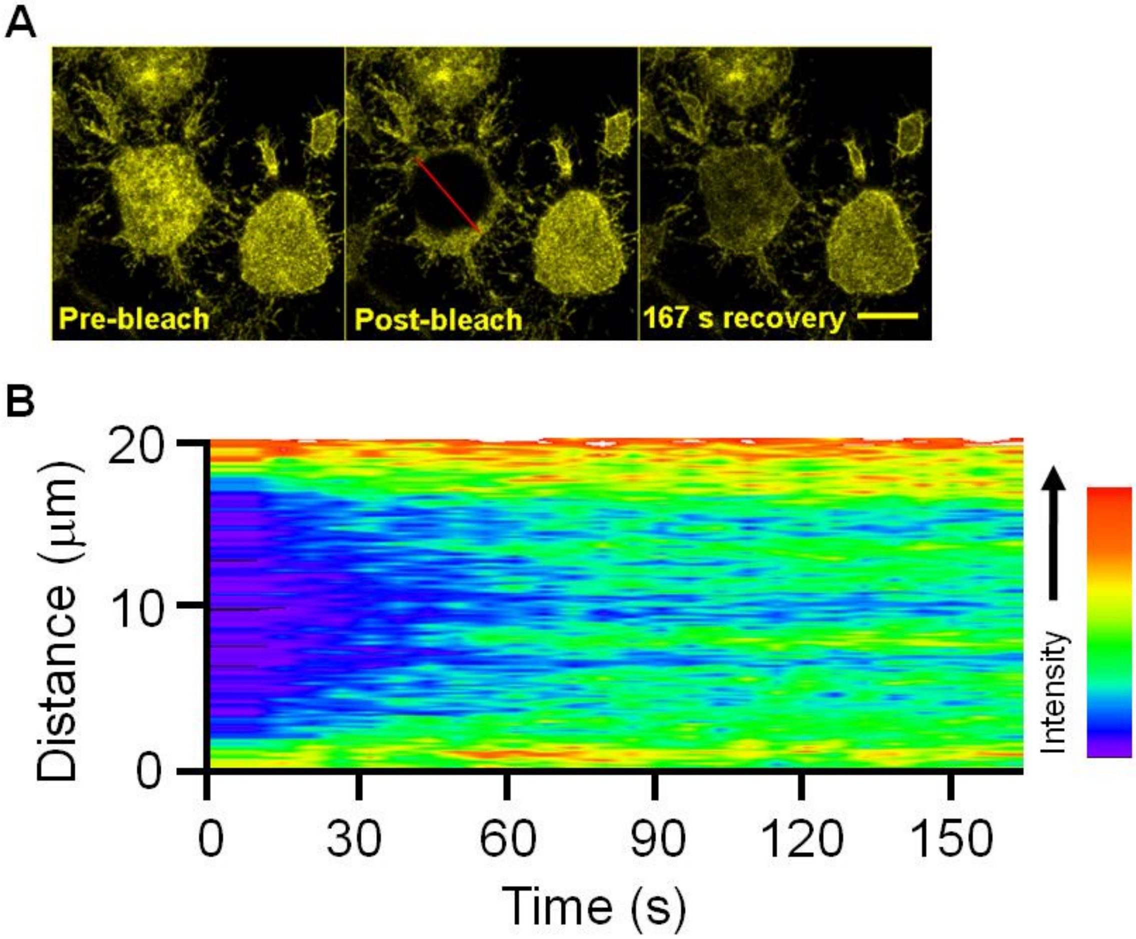

Supplemental figure 1

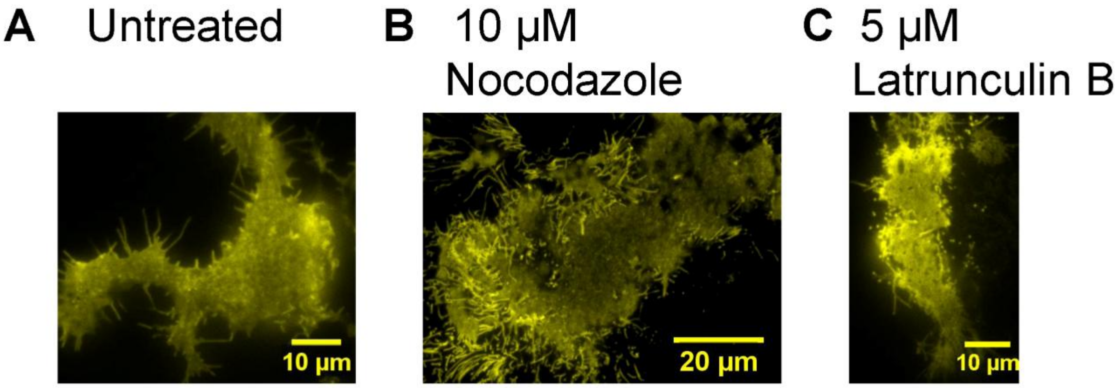

Supplemental figure 2

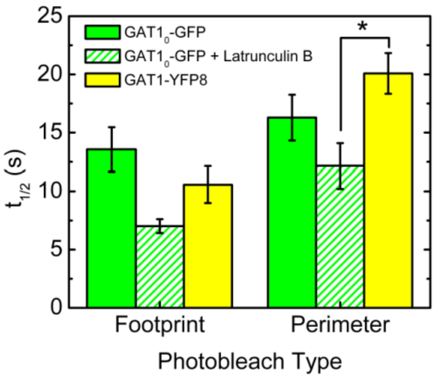

Supplemental figure 3

Chapter 3: Total internal reflection fluorescence microscopy and single molecule analysis reveal GAT1 vesicle kinematics and number of GAT1s per vesicle

Discoveries in the field of vesicle fusion provide direct ties to translational research. While the study of vesicle fusion classically has been applied to neurotransmitter- and neuropeptide-containing vesicles; there is evidence that secretory vesicles physiologically differ from vesicles trafficking membrane protein. For instance, GAT1 resides on a vesicle lacking neurotransmitter but containing some v-SNARE proteins. These differences in the vesicle composition suggest inherent differences in trafficking mechanisms, which can only be confirmed through further study of membrane protein trafficking. To this end, I apply total internal reflection fluorescence microscopy (TIRFM) to quantify the number of GAT1 molecules on vesicles and to observe the movement of vesicles containing fluorescently tagged GAT1 into the plasma membrane. I determine that these vesicles contain 3--7 molecules of GAT1 and uncover a population of GAT1 vesicles with ATP-dependent lateral displacement.

Introduction

GABA transporter subtype 1 (GAT1) transport of GABA into the presynaptic nerve terminal helps to maintain low extracellular GABA concentrations throughout the brain, prevent excessive tonic activation of synaptic and extrasynaptic receptors, and replenish the supply of presynaptic transmitter (1). Due to the important role GAT1 plays in modulating neuronal inhibition, many studies have focused on identifying regulators of GAT1 function. Some GAT1 regulators affect the dynamics the GAT1 vesicle, by controlling GAT1 internalization rates. For example, syntaxin 1A, a T-SNARE, can down-regulate GAT1 transport activity through interaction with the N-terminus of GAT1, and it can also increase the expression of GAT1 on the plasma membrane (2, 3). Protein kinase C (PKC) and tyrosine kinases can also increase GAT1 surface expression (4-7), with tyrosine kinases specifically decreasing GAT1 internalization rates. Additionally, when GAT1 contains a mutant PDZ domain, the transporter remains in the GAT1 vesicle, adjacent to the plasma membrane. This trafficking deficiency reduces GABA uptake by up to 70% (1, 8). Given that GAT1 trafficking plays an important role in GAT1-function, more study is needed into the vesicle that places GAT1 on the membrane.

The study of vesicle movement has been classically applied to neurotransmitter- and neuropeptide containing vesicles; however, there is evidence that synaptic vesicles differ from membrane protein trafficking vesicles, physiologically. For example, the GAT1 vesicle lacks neurotransmitter; the calcium sensor, synaptotagmin; and the synaptic vesicle marker, synaptophysin (9). Surface biotinylation has also shown that the GAT1 vesicle contains the V-SNARE, VAMP, along with rab11, rab3a, and syntaxin 1A (9). These differences in the vesicle composition suggest inherent differences in trafficking mechanisms, which can only be confirmed through further study of GAT1 trafficking.

Much of what is known about GAT1 trafficking has been established through studies on the glucose transporter, GLUT4. Between the two transporters there is similarity in second messenger signaling; PKC isoforms translocate both GLUT4 and GAT1 from vesicles onto the membrane (5, 10). However, all membrane protein vesicles may not respond to the same cues. There is at least one known difference between the trafficking of the non-neuronal GLUT4 and GAT1. GLUT4 vesicle fusion is upregulated by insulin (10), whereas there is no known correlating substrate that positively regulates GAT1 membrane distribution (11).

Our goal has been to exploit the nanometer resolution offered by total internal reflection fluorescence microscopy (TIRF) to visualize the GAT1 vesicle, quantify GAT1 vesicle kinematics, and quantify the number of GAT1 molecules on a GAT1 vesicle. Altogether, the data reveal an ATP dependent class of GAT1 vesicles, and mathematically establish the role of GAT1 vesicle fusion in modulating neuronal inhibition.

Materials and Methods

N2a Culture

Mouse neuroblastoma-2a (N2a) cells (ATCC, Manassas, VA) are grown at 37 °C in 95% air 5% CO_2 in N2a culture medium containing the following: 44.5% DMEM, 44.5% OptiMEM, 10% fetal bovine serum, and 1% penicillin/streptomycin (10,000 I.U penicillin, 10,000 mg/ml streptomycin) (Invitrogen, Carlsbad, CA). Once cells are grown to confluence, cells are plated on 14-mm pre-coated poly-D-lysine glass bottom dishes (#1.5, Mattek, Ashland, MA) at a density of 3×10^5 cells/dish. Transfection of a total of 1 µg DNA per plate is performed 16--24 hr later with Lipofectamine and Plus reagent (Invitrogen, Carlsbad, CA). The composition of the N2a imaging solution is as follows (mM): 128 NaCl, 2.4 KCl, 25 HEPES, 1.2 $MgCl_2$, 3.2 $CaCl_2$, 1.2 KH_2PO_4, and 10 D-glucose (12).

Dissociated culture

Cerebellum from embryonic (E18) pups is minced (~ 1 mm pieces) and added to sterile papain (pH 7.4). Digestion is performed for 20 minutes in a 35 ºC water bath. Cells are placed in 2 ml DNase (1 mg/ml) (Sigma, St. Louis, MO), washed in plating media, and titurated. 100 µL of cells are grown on polyethylimine-coated glass bottom dishes (400 cells per square mm). Cells are flooded with plating media approximately 3--4 hours after plating. After 2 days, 50% of the media is removed and is replaced with maintenance media. 50% of the maintenance media is refreshed every 4--6 days. 2 µL of Ara-C is added, if needed, within the first week of plating. Imaging is performed between 14--16 days post-plating. Plating medum includes 45 mL of the maintenance media and 5 mL of equine serum. Maintenance medium includes 500 mL neurobasal medium (Invitrogen, Carlsbad, CA) supplemented with 10 mL B27 (Invitrogen, Carlsbad, CA), and 1.25 mL glutamax (Invitrogen, Carlsbad, CA). The composition of the neuronal imaging solution is as follows (mM): 150 NaCl, 4 KCl, 10 HEPES, 2 $MgCl_2$, 2 $CaCl_2$, 10 D-glucose, and 2 L-ascorbic acid.

Total Internal Reflection Fluorescence (TIRF) Microscopy

Single fluorophore TIRF imaging is performed on an inverted IX71 (Olympus, Melville, NY) configured for TIR excitation as described in Drenan *et al.* (13). Briefly, IX71 imaging is carried out with an Olympus PlanApo 100X 1.45NA oil objective, samples are excited with a multi-line (458/488/515 nm) 40 mW argon laser (Melles Griot, Carlsbad, CA) and filtered with an XF104-2 (YFP) filter Cube (Omega Optical, Brattleboro, VT). Images are captured with a 16-bit-resolution Cascade 650 CCD (Roper Scientific, Tuscon, AZ) controlled by Slidebook 4.0 imaging software (Intelligent Imaging Innovations).

Addition of BamHI and HindIII restriction sites to EYFP via PCR

PCR is used to introduce the BamHI and HindIII restriction sites into the EYFPN1 sequence. The forward EYFP primer included a 7-nucleotide spacer followed by the BamHI restriction site, and a 5-nucleotide spacer, which placed the EYFPN1 in frame with the pQE32 start codon, and the first 7 codons of the EYFPN1 sequence (forward primer sequence: TCG ATC GGG ATC CGA TCG ATG GTG AGC AAG GGC GAG GAG). The reverse primer contained the final 9 codons of the EYFPN1 sequence, the HindIII restriction site, the SmaI restriction site, and an additional 2 nucleotides (reverse primer sequence: GAC CCG GGA AGC TTC TTT ACT TGT ACA GCT CGT CCA TGC CG). The primer melting points are greater than 78 ºC, as determined from the following equation: $T_m = 81.5 + 0.41(\%GC) - \frac{675}{N}$, where %GC corresponds to the percentage of nucleotides that are either G or C, and N corresponds to the total number of nucleotides contained in the primer. Polyacrylamide gel electrophoresis purified primers are obtained from Integrated DNA Technologies (Coralville, IA).

PCR is performed by combining 2 µL (100 µg) EYFPN1 vector, 1.25 µL (125 ng) forward primer, 1.25 µL (125 ng) reverse primer, 0.5 µL (10 mM) dNTPs, 40 µL nuclease free ddH2O, 5 µL Quikchange 10X reaction buffer, and 1 µL (2.5 U) PfuTurbo DNA polymerase (Stratagene, La Jolla, CA). The PCR reaction is performed under the conditions outlined in Table 1. Following PCR, the BamHI-EYFP-HindIII linear plasmid is separated by gel electrophoresis using a 1% agarose gel, removed with a razor, and purified using a Qiagen Gel Extraction Kit (Valencia, CA).

Table 2. PCR conditions

Segment	**Cycles**	**Temperature**	**Time**
1	1	95 ºC	2 minutes
2	30	95 ºC	30 seconds
		55 ºC	30 seconds
		68 ºC @ 2 kb/minute	1 minute, 37 seconds
3	1	68 ºC	7 minutes
4	1	4 ºC	∞

Subcloning and amplification of His6-YFP

The BamHI-EYFP-HindIII plasmid and pQE32 vector are sequentially digested, the pQE32 vector is dephosphorylated with shrimp alkaline phosphatase, and the vectors are ligated using T4 DNA ligase sites. Top ten cells are used for the transformation of the ligation product by electroporating 2 µL DNA, resuspending in 500 µL SOC media, incubating 1 hr on a 37 ºC shaker, and growing overnight on LB-Amp plates. Single colonies are added to 5 mL 2xyt+Amp and grown on 37 ºC shaker overnight. DNA is purified using the Qiagen Miniprep kit (Valencia, CA). XL1-blue cells are transformed by heat pulse with the miniprep product, incubated for 1 hr in a 37 ºC shaker, and grown overnight on LB-Amp plates. Single colonies are grown in 10 mL 2xyt overnight, 5 mL of which is then added to10mL 2xyt+amp and grown for 1 hr and diluted with 2xyt+amp to an 0.6 OD. Protein is amplified through addition of 1 mM IPTG. His-YFP is purified using Qiagen Ni-NTA spin columns (Valencia, CA) using solutions described in (14).

Quantifying His6-YFP concentration

His-YFP concentration is obtained by calibrating to a BSA standard via the BCA protein assay (Bio-rad, Hercules, CA), and multiplying this concentration value by the correction factor 0.764, reported from His_6-GFP amino acid analysis (15). His_6-YFP is stored at -20C as a 50% sucrose slurry. 10^{-11}, 10^{-12} M concentrations of His_6-YFP are incubated overnight at 4 ºC with 30 µL Qiagen Ni-NTA agarose beads (Valencia, CA).

Results

TIRF imaging of GAT1 plasma membrane distribution

Figure 1A displays the distribution of $GAT1_0$-GFP distribution in primary cultures from the cerebellum of homozygous neonatal $GAT1_0$-GFP knock-in mice with both widefield fluorescence and TIRF illumination. As previously reported, $GAT1_0$-GFP does not traffic properly due to the interruption of the endogenous PDZ-interaction domain by the fusion of the GFP molecule to the GAT1 C-terminus (1). Due to this deficiency, we moved to imaging GAT1-YFP8, a fluorescent GAT1 with WT trafficking, GABA uptake, and surface distribution. Figure 1B displays the distribution of GAT1-YFP8 on N2a cells. As a comparison, we imaged YFP-syntaxin which interacts with the GAT1 N-terminal domain, thereby down-regulating GABA transport. Figure 1C shows that YFP-syntaxin forms membrane clusters, this is consistent with previous reports that describe syntaxin membrane pools (13, 16). In contrast, Figure 1B shows that GAT1-YFP8 is distributed throughout the membrane and along filopodia, which are distinguished by arrows.

TIRF imaging of the GAT1 vesicle

Figure 2A displays the maximum lateral displacement of a GAT1-YFP8 vesicle. The average vesicle lateral displacement is 1.4 ± 0.1 µm when vesicles with zero displacement are discounted. Figure 2A also displays a zoomed view about the average vesicle displacement, showing that very few vesicles move distances greater than 4 µm. Figure 2B displays a histogram of the average vesicle velocity. Vesicles move between 0 and 1 µm/s, with an average vesicle velocity of 95 nm/s. Figure 2B displays a zoomed view of the vesicle velocity about the average.

Figures 3A and 4A display N2a cells transfected with GAT1-YFP8. Figure 3B represents the tracking of a vesicle that displays the type average vesicle displacement displayed in Figure 2A, moving a distance of 1.8 µm. The vesicle is present for 15 seconds and disappears after the sixth frame (acquisition 0.3 Hz). As displayed in Figure 2A, vesicles can exhibit long-range displacements (> 4 µm). Figure 4B displays a montage of a vesicle exhibiting this type of movement. The tracked vesicle has a displacement of 12 µm and traveling at a rate of 170 nm/s (acquisition 0.4 Hz). The vesicle travels a linear x-y path, which may indicate ATP-directed movement.

GAT1 vesicle movement depends on ATP

Cells are depleted of ATP to determine the role of energy in GAT1 vesicle movement. Figure 5A displays the results of a luciferase assay showing that cells reach maximal ATP depletion after 10 min. Figure 5B displays TIRF, widefield fluorescence, and brightfield images of a representative cell that has been depleted of ATP after a10-min treatment with 5 mM 2-deoxy-D-glucose and 5 μg/ml oligomycin. Following ATP depletion, vesicle visibility increases relative to an untreated N2a cell. Figure 4C displays the vesicle MSD plot for ATP depleted cells, untreated cells, and untreated cells displaying average displacement. Average vesicle displacement is defined as less than 2 standard deviations from the average vesicle displacement. Both the untreated cells and the ATP depleted cells display sigmoidal MSD. At short Δt, the untreated cells display directed movement. An inflection point occurs around a Δt of 20 s, at this point untreated cells display caged (constrained) vesicle movement. Untreated cells that give an average vesicle displacement exhibit caged movement at all Δt. Depleting ATP decreases the MSD for short Δt, but for Δt > 20 s, ATP depleted vesicles also exhibit caged movement.

Quantifying GAT1 number on vesicles

Single molecule imaging is employed to count the number of GAT1 molecules on vesicles that traffic GAT1 onto the membrane. Previous counting of $GAT1_0$-GFP on synapses applied His_6-GFP37 (1, 14, 15). We created His_6-YFP to count GAT1-YFP8 on vesicles as described in the Materials and Methods. Figure 5A displays single molecules of His_6-YFP tethered to Ni-NTA agarose beads. Presented in Figure 5B is the fluorescence intensity over time for a representative single molecule of His_6-YFP. This image shows that there is mild fluctuation in fluorescence intensity over time culminating with photobleach of the fluorophore. The step function photobleach seen in Figure 5B is representative of single molecule photobleach rather than ensemble photobleach, which would display exponentially decaying fluorescence intensity. Figure 5C displays the fluorescence intensity for single molecules of His_6-YFP represented as a histogram, with an average of 32 ± 1 arbitrary units.

Figure 6A illustrates the constraints to quantifying the number of GAT1 molecules per vesicle with TIRF. Figure 6A shows a poly-D-lysine substrate thickness of 12.5 nm (17) and a plasma membrane thickness of 4--7 nm (18, 19). The TIRF penetration depth represents the distance from the coverslip where the evanescent wave has decayed by 63%. It is defined as follows: $d = \frac{\lambda}{4\pi\sqrt{n_1^2 \sin^2\theta_c - n_2^2}}$ (20), where λ represents the wavelength (514 nm), n_1 represents the index of refraction for glass (1.51), θ_c represents the TIRF critical angle (~ 63^o), and n_2 represents the index of refraction within the cell (~ 1.38), giving a value of ~ 145 nm.

Since the single molecules of His_6-YFP are located at the coverslip, and the closest GAT1-YFP8 vesicle is located a distance of 16.5 nm from the coverslip, we correct for distance dependent His_6-YFP fluorescence decay using the following equation: $I = I_o e^{-\frac{z}{d}}$ (20). In this equation, I_o is the average single molecule fluorescence intensity at the coverslip (32 au) and d is the TIRF penetration depth (145 nm). Figure 7B divides the fluorescence intensity for GAT1-YFP8 vesicles by the His_6-YFP fluorescence intensity change over distance. Figure 7B shows that a vesicle at the plasma membrane appears to have 3 GAT1-YFP8 molecules per vesicle, while a vesicle 145 nm away appears to have fewer than 8 GAT1-YFP8 molecules per vesicle. Since dimerization is required for GAT1 endoplasmic reticulum export (21), a vesicle would contain 2--4 assembled dimers.

Discussion

We report GAT1 distribution on the membrane and characterize the vesicle that traffics GAT1 onto the membrane through fluorescence analysis of vesicle kinematics. We have also determined for the first time the number of transporter molecules on vesicles that traffic neurotransmitter transporters onto the membrane.

Despite the $GAT1_0$-GFP trafficking deficiency, we are able to view localization of the transporter on the membrane of primary cultures from neonatal mouse cerebellum. We were also able to view the distribution of a transporter with WT GABA uptake, which partitions correctly to the cell surface and intracellular compartments. GAT1-YFP8 membrane distribution is strikingly different from the distribution of YFP-Syntaxin, a T-SNARE that regulates GAT1 transport activity. The difference in surface localization indicates that only some transporter molecules are in close enough proximity to syntaxin pools to be subject to syntaxin regulation of GAT1 function. It is known that the phosphorylation of Munc18 by protein kinase C (PKC) causes the dissociation of the Munc18-syntaxin interaction, freeing syntaxin to associate with GAT1 (22). We have previously reported GAT1 tethering to actin, via a PDZ protein and ezrin. It would be notable to determine whether the signaling pathways that affect GAT1-syntaxin association also regulate GAT1 confinement.

A majority of our vesicles undergo displacements of 1.4 µm. This suggests a similarity between the GAT1 vesicle and the Na^+/K^+-ATPase vesicle, which also exhibits average displacements of ~ 1 µm (23). Additionally, > 80% of observed secretory vesicles in pollen tubes undergo displacements less than 1 µm (24) and 97% of chromaffin granules undergo average displacements of ~ 1 µm (25). The remaining 3% the chromaffin granules exhibit displacements > 10 µm (25).

Our results show that a small fraction of GAT1 vesicles have the ability to laterally traverse long distances near the plasma membrane. Long-range vesicles are governed by an ATP-dependent process. This conclusion is based on three observations: (i) When we consider the MSD of vesicles that move within two standard deviations of the average displacement, the MSD of these average vesicles is concave downward ($\propto t^{1/2}$), indicating caged (constrained) movement, which would not be directed by ATP (26, 27). (ii) When we include long-range vesicles in the MSD analysis, the trend is sigmoidal: displaying a concave upward MSD for short Δt, indicating directed movement ($\propto t^2$)(27), and displaying concave downward MSD for $\Delta t > 20$ s, indicating caged movement ($\propto t^{1/2}$) (26). (iii) The MSD for ATP treated cells indicates caged movement for $\Delta t > 20$ s ($\propto t^{1/2}$) (26, 27). Altogether, the long-range vesicles display ATP-dependent movement for $\Delta t < 20$ s, after which they display the same caged movement as average vesicles.

The fact that a majority of GAT1 vesicles display caged movement indicates a similarity between the GAT1 vesicle and other membrane protein containing vesicles. For example, both the GLUT4 vesicle and the TRPC vesicle display caged movement (28, 29). Constrained vesicle movement is also representative of the secretory, bovine chromaffin granule (30). However, the existence of a fraction of GAT1 vesicles that display ATP-directed, lateral movement reveals a sub-population of vesicles requiring further study. The rationale behind the long-range movement may include: ATP-dependent vesicle recruitment to exocytosis active zones (31), as exhibited by synaptic vesicles (32, 33) or recycling of vesicles from endosomal compartments (34).

It has been previously reported that a majority of GAT1 vesicles reside in a reserve pool (RP), which does not actively insert into the membrane (35). Wang *et al.* report that this pool comprises 70% of GAT1 vesicles. Although the GAT1 vesicle does not contain neurotransmitter (9), the approximate size of the reserve pool correlates well to the size of the synaptic vesicle reserve pool in the Drosophila neuromuscular junction (~ 70% of the available synaptic vesicles)(36). Since we do not observe vesicle fusion, it is possible that we are monitoring reserve pool vesicles. If the caged GAT1 vesicles are in fact reserve vesicles, it should be noted that their excitation by the evanescent wave signifies perimembrane residence; therefore, recruitment to the readily releasable pool would not require significant z-translocation.

Functional implications of GAT1 vesicle characterization.

Previous estimates of transporter on and off rates reported that 3--5 transporters are added to the membrane every second (35). Our estimate of transporter number per vesicle reveals a GAT1 vesicle fusion rate of 1 event per second. Since the complete time for one GAT1 transport cycle is ~ 100 ms, and the decay time constant of GABAergic postsynaptic currents is ~ 10 ms (37), GAT1 vesicle fusion does not have the ability to directly influence GABAergic synaptic transmission. However, the estimate of 1 vesicle per second suggests that the replenishment of GAT1 is a dynamic process that requires continuous recruitment of vesicle fusion machinery.

References

1. Chiu C-S, Jensen K, Sokolova I, Wang D, Li M, Deshpande P, Davidson N, Mody I, Quick MW, Quake SR, Lester HA. Number, Density, and Surface/Cytoplasmic Distribution of GABA Transporters at Presynaptic Structures of Knock-In Mice Carrying GABA Transporter Subtype 1-Green Fluorescent Protein Fusions. J Neurosci 2002;22(23):10251-10266.

2. Deken SL, Beckman ML, Boos L, Quick MW. Transport rates of GABA transporters: regulation by the N-terminal domain and syntaxin 1A. Nature Neuroscience 2000;3(10):998-1003.

3. Quick MW. The role of SNARE proteins in trafficking and function of neurotransmitter transporters. Handb Exp Pharmacol 2006(175):181-196.

4. Beckman ML, Bernstein EM, Quick MW. Multiple G Protein-Coupled Receptors Initiate Protein Kinase C Redistribution of GABA Transporters in Hippocampal Neurons. J Neurosci 1999;19(11):9RC-.

5. Quick MW, Corey JL, Davidson N, Lester HA. Second Messengers, Trafficking-Related Proteins, and Amino Acid Residues that Contribute to the Functional Regulation of the Rat Brain GABA Transporter GAT1. J Neurosci 1997;17(9):2967-2979.

6. Whitworth TL, Quick MW. Substrate-induced Regulation of gamma -Aminobutyric Acid Transporter Trafficking Requires Tyrosine Phosphorylation. J Biol Chem 2001;276(46):42932-42937.

7. Law RM, Stafford A, Quick MW. Functional Regulation of gamma -Aminobutyric Acid Transporters by Direct Tyrosine Phosphorylation. J Biol Chem 2000;275(31):23986-23991.

8. McHugh EM, Zhu W, Milgram S, Mager S. The GABA transporter GAT1 and the MAGUK protein Pals1: interaction, uptake modulation, and coexpression in the brain. Molecular and Cellular Neuroscience 2004;26(3):406-417.

9. Deken SL, Wang D, Quick MW. Plasma Membrane GABA Transporters Reside on Distinct Vesicles and Undergo Rapid Regulated Recycling. J Neurosci 2003;23(5):1563-1568.

10. Ishiki M, Klip A. Minireview: Recent Developments in the Regulation of Glucose Transporter-4 Traffic: New Signals, Locations, and Partners. Endocrinology 2005;146(12):5071-5078.

11. Bernstein EM, Quick MW. Regulation of gamma -Aminobutyric Acid (GABA) Transporters by Extracellular GABA. J Biol Chem 1999;274(2):889-895.

12. Lu Y, Grady S, Marks MJ, Picciotto M, Changeux J-P, Collins AC. Pharmacological Characterization of Nicotinic Receptor-stimulated GABA Release From Mouse Brain Synaptosomes. J Pharmacol Exp Ther 1998;287(2):648-657.

13. Drenan RM, Nashmi R, Imoukhuede P, Just H, McKinney S, Lester HA. Subcellular Trafficking, Pentameric Assembly, and Subunit Stoichiometry of Neuronal Nicotinic Acetylcholine Receptors Containing Fluorescently Labeled {alpha}6 and 3 Subunits. Mol Pharmacol 2008;73(1):27-41.

14. Unger M, Kartalov E, Chiu CS, Lester HA, Quake SR. Single-molecule fluorescence observed with mercury lamp illumination. Biotechniques 1999;27(5):1008-1014.

15. Chiu C-S, Kartalov E, Unger M, Quake S, Lester HA. Single-molecule measurements calibrate green fluorescent protein surface densities on transparent beads

for use with `knock-in' animals and other expression systems. Journal of Neuroscience Methods 2001;105(1):55-63.

16. Lang T, Bruns D, Wenzel D, Riedel D, Holroyd P, Thiele C, Jahn R. SNAREs are concentrated in cholesterol-dependent clusters that define docking and fusion sites for exocytosis. EMBO J 2001;20(9):2202-2213.

17. Braun D, Fromherz P. Fluorescence Interferometry of Neuronal Cell Adhesion on Microstructured Silicon. Physical Review Letters 1998;81(23):5241.

18. Lodish H, Berk A, Zipursky LS, Matsudaira P, Baltimore D, Darnell J. Molecular Cell Biology. Fourth ed. New York: W.H. Freeman; 1999.

19. Berg JM, Tymoczko JL, Stryer L. Biochemistry. fourth ed. New York: W. H. Freeman and Company; 2002.

20. Axelrod D, Davidson MW. Total Internal Reflection Fluorescence Microscopy Introduction and Theoretical Aspects. Olympus Microscopy Rescource Center: Olympus America, Inc.; 2008.

21. Korkhov VM, Farhan H, Freissmuth M, Sitte HH. Oligomerization of the {gamma}-Aminobutyric Acid Transporter-1 Is Driven by an Interplay of Polar and Hydrophobic Interactions in Transmembrane Helix II. J Biol Chem 2004;279(53):55728-55736.

22. Beckman ML, Bernstein EM, Quick MW. Protein Kinase C Regulates the Interaction between a GABA Transporter and Syntaxin 1A. J Neurosci 1998;18(16):6103-6112.

23. Bertorello AM, Komarova Y, Smith K, Leibiger IB, Efendiev R, Pedemonte CH, Borisy G, Sznajder JI. Analysis of Na+,K+-ATPase Motion and Incorporation into the

Plasma Membrane in Response to G Protein-coupled Receptor Signals in Living Cells. Mol Biol Cell 2003;14(3):1149-1157.

24. Wang X, Teng Y, Wang Q, Li X, Sheng X, Zheng M, Samaj J, Baluska F, Lin J. Imaging of Dynamic Secretory Vesicles in Living Pollen Tubes of Picea meyeri Using Evanescent Wave Microscopy. Plant Physiol 2006;141(4):1591-1603.

25. Oheim M, Stühmer W. Tracking chromaffin granules on their way through the actin cortex. European Biophysics Journal 2000;29(2):67-89.

26. Kolinski A, Skolnick J, Yaris R. On the short time dynamics of dense polymeric systems and the origin of the glass transition: A model system. The Journal of Chemical Physics 1986;84:1922.

27. Qian H, Sheetz MP, Elson EL. Single particle tracking. Analysis of diffusion and flow in two-dimensional systems. Biophys J 1991;60(4):910-921.

28. Li CH, Bai L, Li DD, Xia S, Xu T. Dynamic tracking and mobility analysis of single GLUT4 storage vesicle in live 3T3-L1 cells. Cell Res 2004;14(6):480-486.

29. Bezzerides VJ, Ramsey IS, Kotecha S, Greka A, Clapham DE. Rapid vesicular translocation and insertion of TRP channels. Nat Cell Biol 2004;6(8):709-720.

30. Steyer JA, Almers W. Tracking Single Secretory Granules in Live Chromaffin Cells by Evanescent-Field Fluorescence Microscopy. Biophys J 1999;76(4):2262-2271.

31. Lemke EA, Klingauf J. Single Synaptic Vesicle Tracking in Individual Hippocampal Boutons at Rest and during Synaptic Activity. J Neurosci 2005;25(47):11034-11044.

32. Ryan TA. Inhibitors of Myosin Light Chain Kinase Block Synaptic Vesicle Pool Mobilization during Action Potential Firing. J Neurosci 1999;19(4):1317-1323.

33. Jordan R, Lemke EA, Klingauf J. Visualization of Synaptic Vesicle Movement in Intact Synaptic Boutons Using Fluorescence Fluctuation Spectroscopy. Biophys J 2005;89(3):2091-2102.

34. Becker C, Sevilla L, Tomas E, Palacin M, Zorzano A, Fischer Y. The Endosomal Compartment Is an Insulin-Sensitive Recruitment Site for GLUT4 and GLUT1 Glucose Transporters in Cardiac Myocytes. Endocrinology 2001;142(12):5267-5276.

35. Wang D, Quick MW. Trafficking of the Plasma Membrane {gamma}-Aminobutyric Acid Transporter GAT1: SIZE AND RATES OF AN ACUTELY RECYCLING POOL. J Biol Chem 2005;280(19):18703-18709.

36. Kuromi H, Kidokoro Y. Exocytosis and Endocytosis of Synaptic Vesicles and Functional Roles of Vesicle Pools: Lessons from the Drosophila Neuromuscular Junction. Neuroscientist 2005;11(2):138-147.

37. Lester HA, Mager S, Quick MW, Corey JL. Permeation Properties of Neurotransmitter Transporters. Annual Review of Pharmacology and Toxicology 1994;34(1):219-249.

Figure Legends

Figure 1. TIRF imaging of fluorescent GAT1 distribution on neurons and N2a cells

A) Homozygous primary cultures from E18 GAT10-GFP knock-in mice display fluorescence on cell bodies, as previously reported by Chiu et al. Scale bar, 5 µm. Widefield fluorescence and TIRF images also show membrane localization. (B) GAT1-YFP8 transfected in N2a cells also shows complete labeling of the plasma membrane. (C) YFP-Synaxin, which can interact with the N-terminus of GAT1, displays clustered plasma membrane distribution. Scale bars, 10 µm.

Figure 2. GAT1-YFP8 vesicle kinematics

A) GAT1-YFP8 vesicle displacement histogram. The histogram shows the percentage of GAT1-YFP8 vesicles that display a maximal lateral displacement up to 12 µm. The average vesicle displacement is 1.4 ± 0.1 µm (± standard error of the mean). The histogram includes a magnified view about the average vesicle displacement. The histogram highlights the fact that only a few vesicles display the type of long-range movement. (B) GAT1-YFP8 vesicle velocity histogram. The histogram shows the percentage of GAT1-YFP8 vesicles that display a maximal lateral velocity greater than 0. The average vesicle velocity is 95 ± 3 nm/s.

Figure 3. Tracking of a GAT1-YFP8 vesicle exhibiting average displacement

A) TIRF image of an N2a cell transfected with GAT1-YFP8. Scale bar, 10 µm. The boxed region includes the vesicle that is tracked in (B). The vesicle moves a distance of 1.8 µm. The frame rate is 0.3 Hz and the proportion bars, 1 µm.

Figure 4. Tracking of a GAT1-YFP8 vesicle exhibiting long-range displacement

A) TIRF image of N2a cell expressing GAT1-YFP8. Scale bar, 10 µm. The boxed region includes the vesicle that is tracked in (B). (B) Long-range vesicle tracking. After frame 8, the vesicle goes out of the evanescent field and is not visible for 9 frames, during this time it continues its course, and is seen again in frame 18. This vesicle moves a distance of 12 µm. The frame rate is 0.4 Hz and the proportion bars, 1 µm.

Figure 5. ATP depletion

A) TIRF, brightfield, and widefield fluorescence images of a cell that has undergone ATP depletion. Vesicles can be seen in the TIRF image. Scale bars, 10 µm. (B) Luciferase assay confirming ATP depletion of cells treated with 5 mM 2-deoxy-D-glucose and 5 µg/ml oligomycin. N2a cells are maximally depleted of ATP after 10 minute incubation. (C) Mean square displacement of vesicles before and following ATP depletion display sigmoidal trends. The MSD results show that when long-range vesicle displacement (MSD > 2 standard deviations from the average) is included in the MSD calculation, there is an increase in MSD, corresponding to a vesicle dependence on ATP. When these long-range displacements are removed from the MSD calculation, there is no ATP dependence on displacement.

Figure 6. Quantifying the number of GAT1-YFP8 molecules/vesicle

A) Single molecules of His_6-YFP tethered to Ni-NTA agarose beads. Scale bar, 1 µm. (B) Representative fluorescence trace for a single molecule of His_6-YFP. The step function His_6-YFP photobleach trace is characteristic of single molecule photobleach. (C) Magnitude of single molecule photobleach as a percentage of observed single molecules. The average single molecule fluorescence is 32 ± 1 arbitrary units.

Figure 7. Distance dependence on # GAT1-YFP8 molecules per vesicle.

A) Schematic of vesicle distance from coverslip. The TIRF illumination field decays exponentially as the distance from the coverslip increases. His_6-YFP single molecule imaging occurs at the coverslip, and gives maximal fluorescence intensity values; however, the center of a vesicle containing the transporter can be at the closest, 41.5 nm from the coverslip. At this distance, the fluorescence intensity for a single molecule of His_6-YFP will be reduced by 25%. (B) Number of GAT1-YFP8 molecules/vesicle as a function of z distance from the coverslip. Using the exponential relation between distance and fluorescence intensity, the fluorescence from a vesicle is divided by the average magnitude of His_6-YFP fluorescence from 16.5--145 nm from the coverslip. This gives 3--8 molecules of GAT1-YFP8/vesicle. Because GAT1 exists as a dimer upon export from the endoplasmic reticulum, the number of GAT1-YFP8 dimers/vesicle is 2--4.

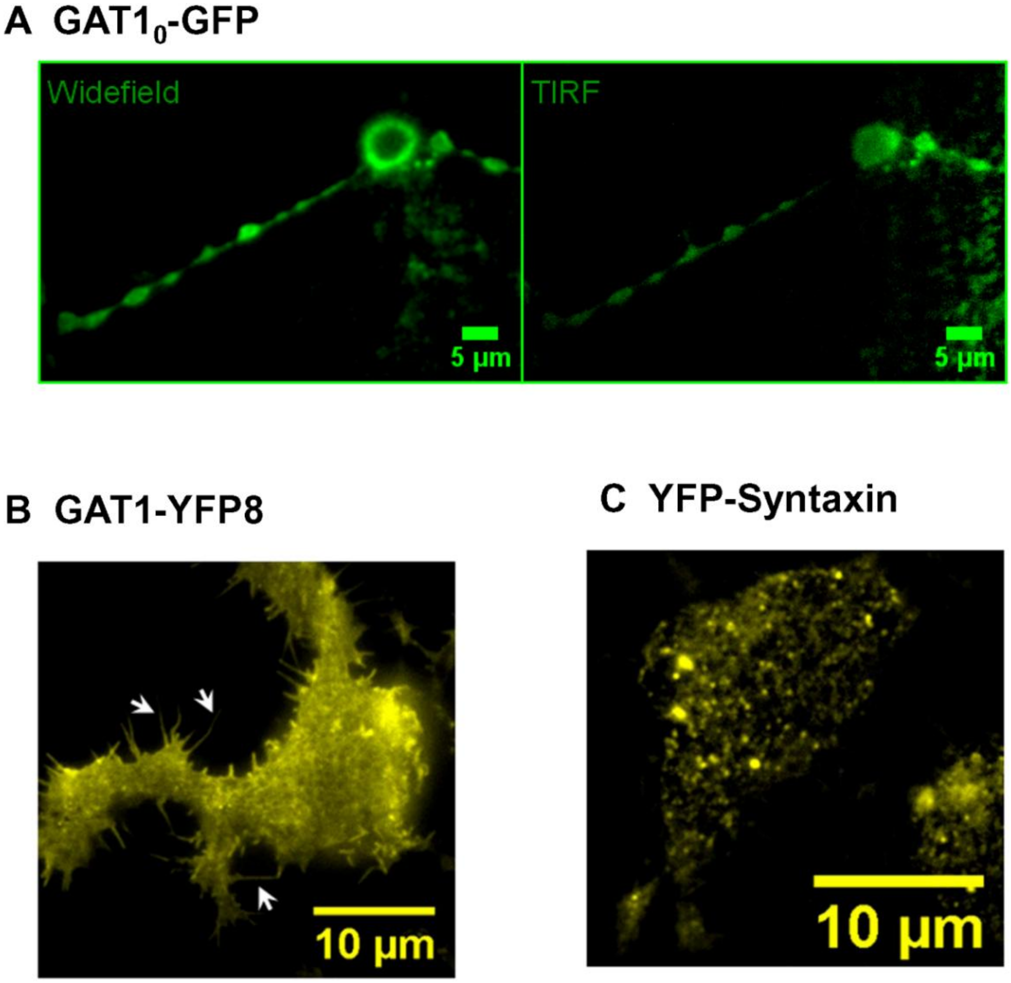

A GAT1_0-GFP

B GAT1-YFP8

C YFP-Syntaxin

Figure 1

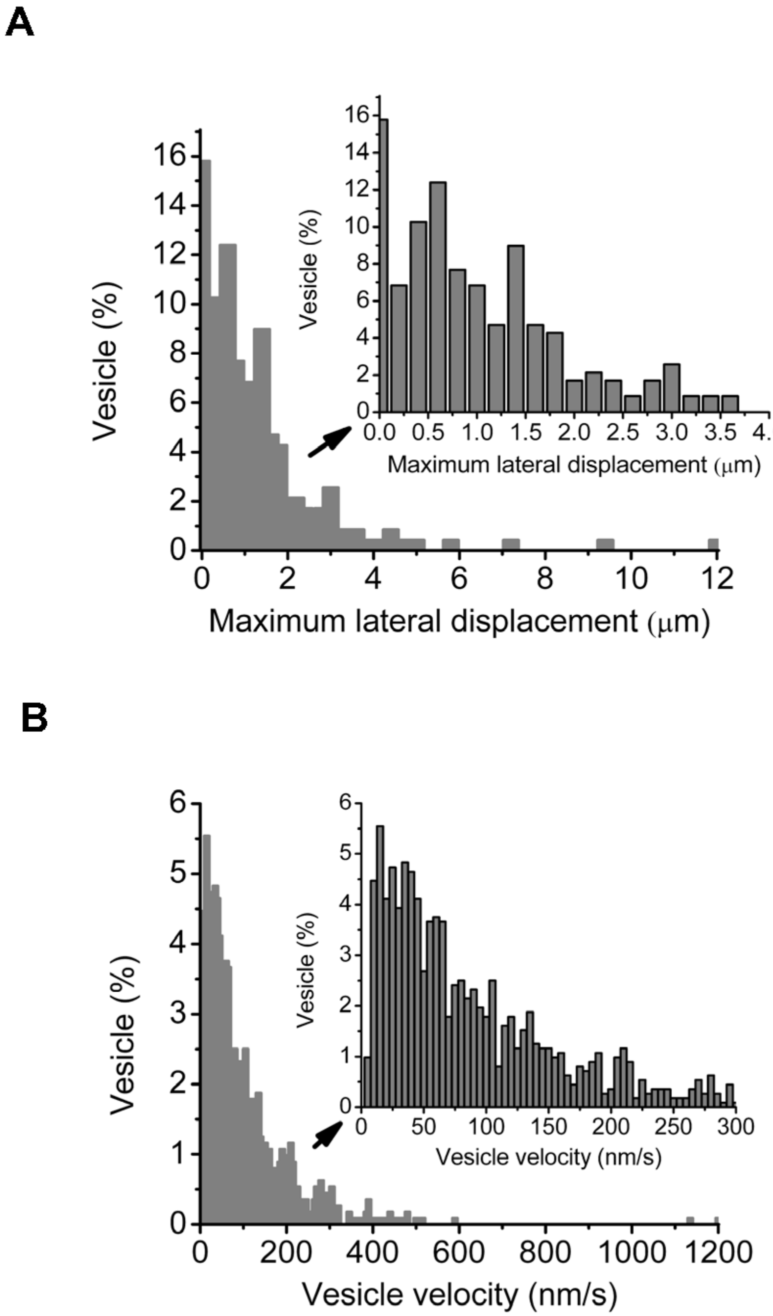
A
Vesicle (%)
0
2
4
6
8
10
12
14
16
0
2
4
6
8
10
12
Maximum lateral displacement (μm)
Vesicle (%)
0.0
0.5
1.0
1.5
2.0
2.5
3.0
3.5
4.0
Maximum lateral displacement (μm)
B
Vesicle (%)
0
1
2
3
4
5
6
0
200
400
600
800
1000
1200
Vesicle velocity (nm/s)
Vesicle (%)
0
50
100
150
200
250
300
Vesicle velocity (nm/s)

Figure 2

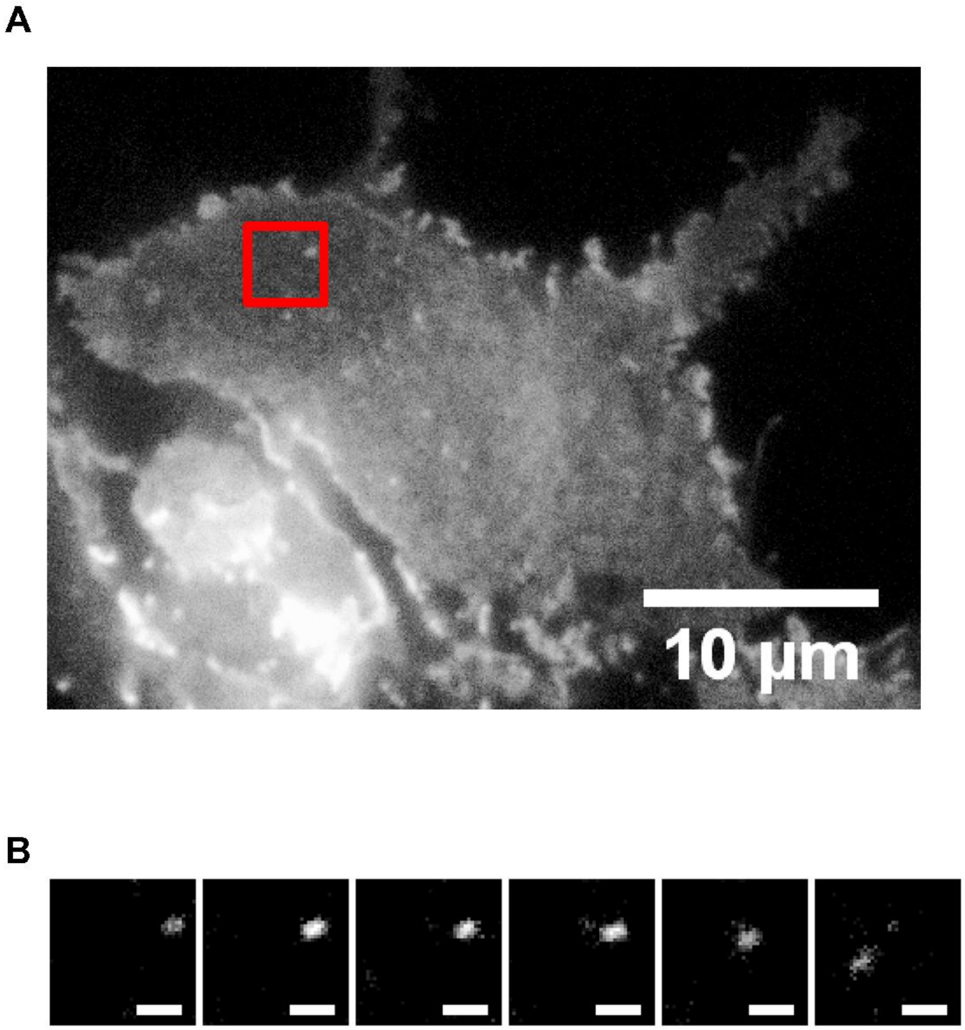

Figure 3

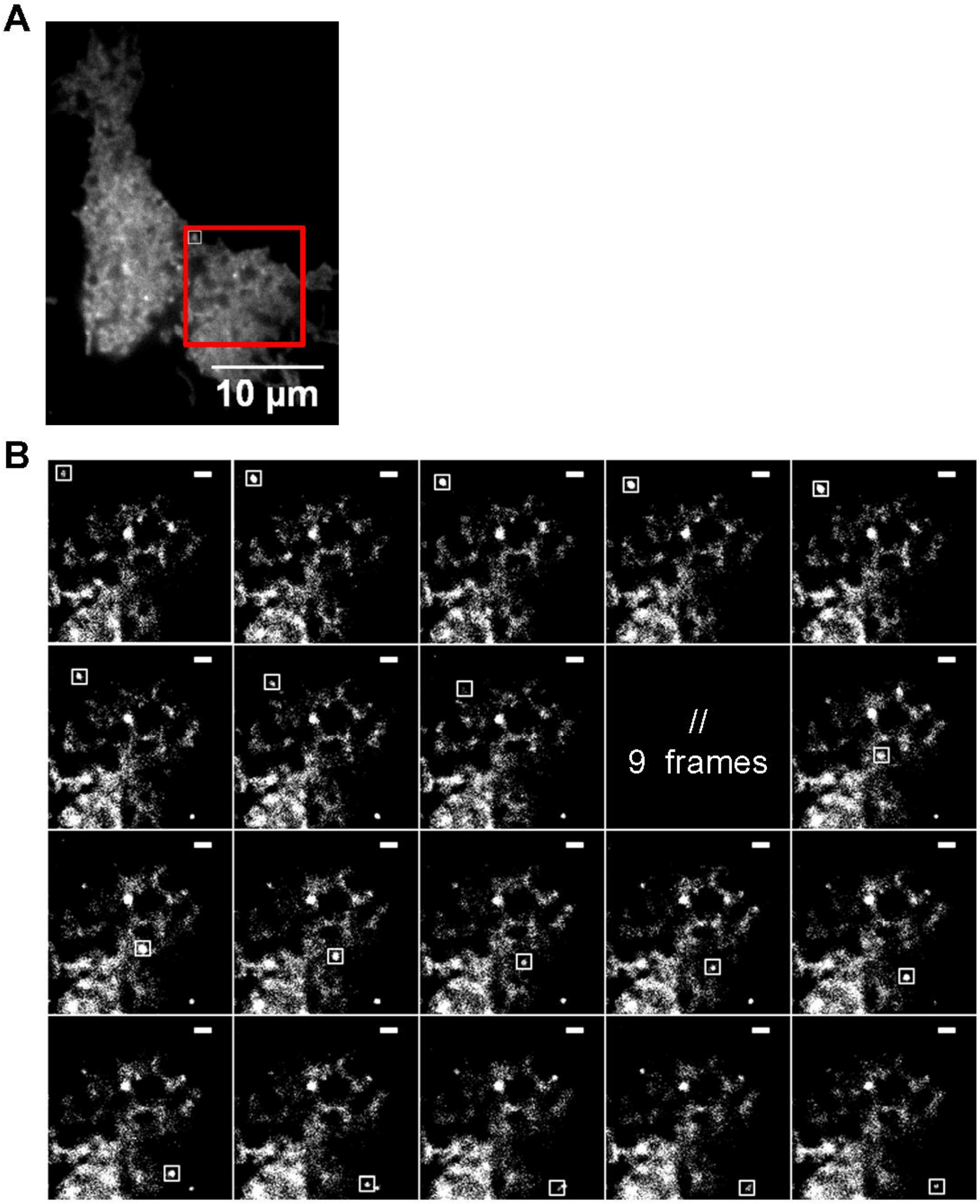

Figure 4

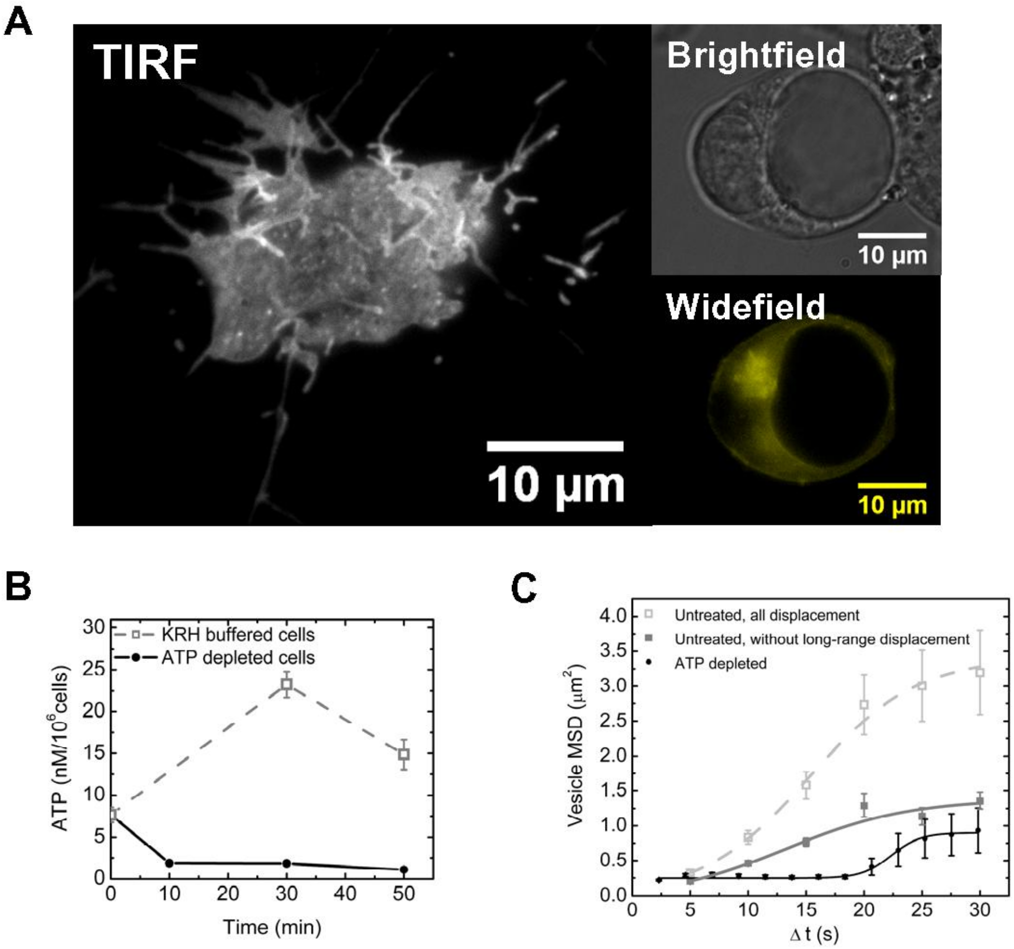
A
TIRF
10 µm
Brightfield
10 µm
Widefield
10 µm
B
KRH buffered cells
ATP depleted cells
ATP (nM/10^{6}cells)
0
5
10
15
20
25
30
Time (min)
0
10
20
30
40
50
C
Untreated, all displacement
Untreated, without long-range displacement
ATP depleted
Vesicle MSD (µm^2)
0.0
0.5
1.0
1.5
2.0
2.5
3.0
3.5
4.0
Δ t (s)
0
5
10
15
20
25
30

Figure 5

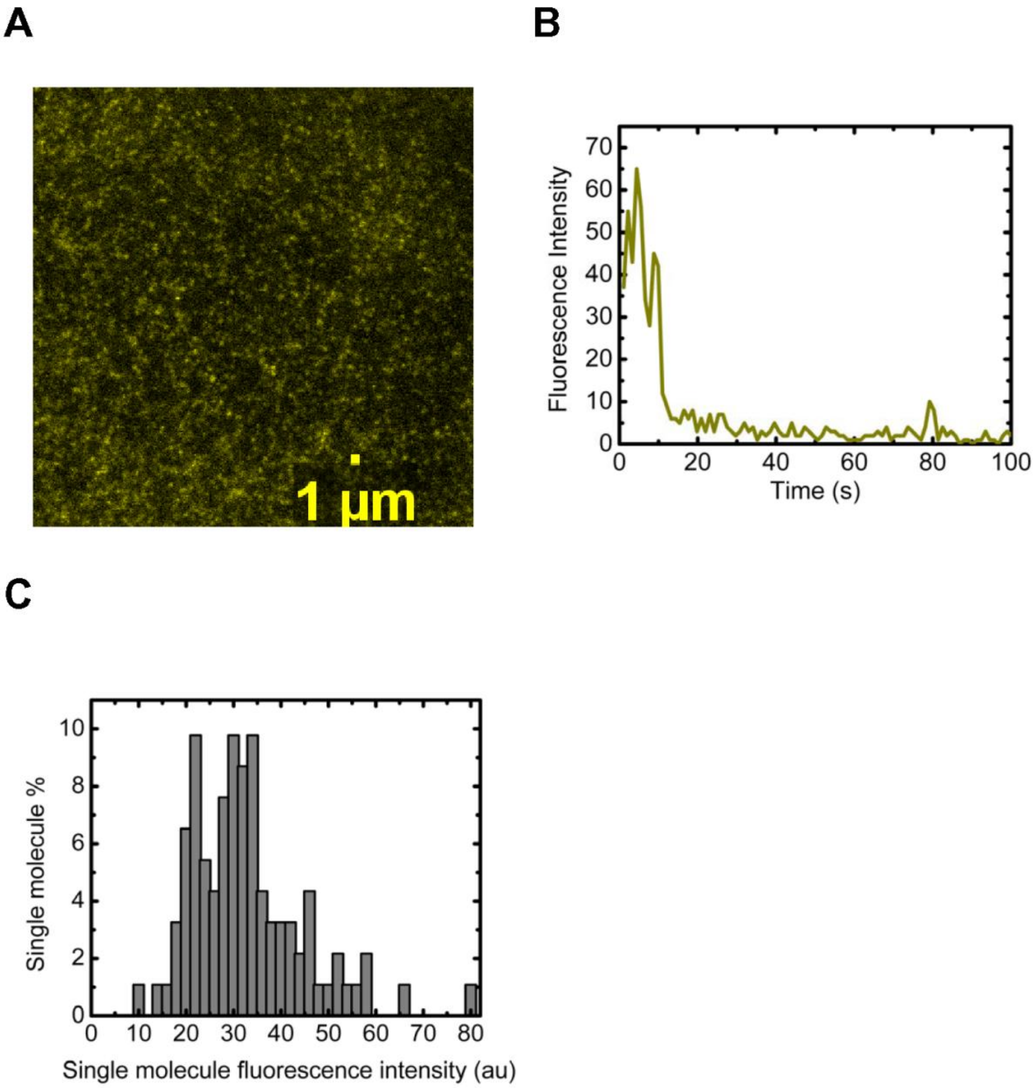
A
1 µm
B
Fluorescence Intensity
0
10
20
30
40
50
60
70
0
20
40
60
80
100
Time (s)
C
Single molecule %
0
2
4
6
8
10
0
10
20
30
40
50
60
70
80
Single molecule fluorescence intensity (au)

Figure 6

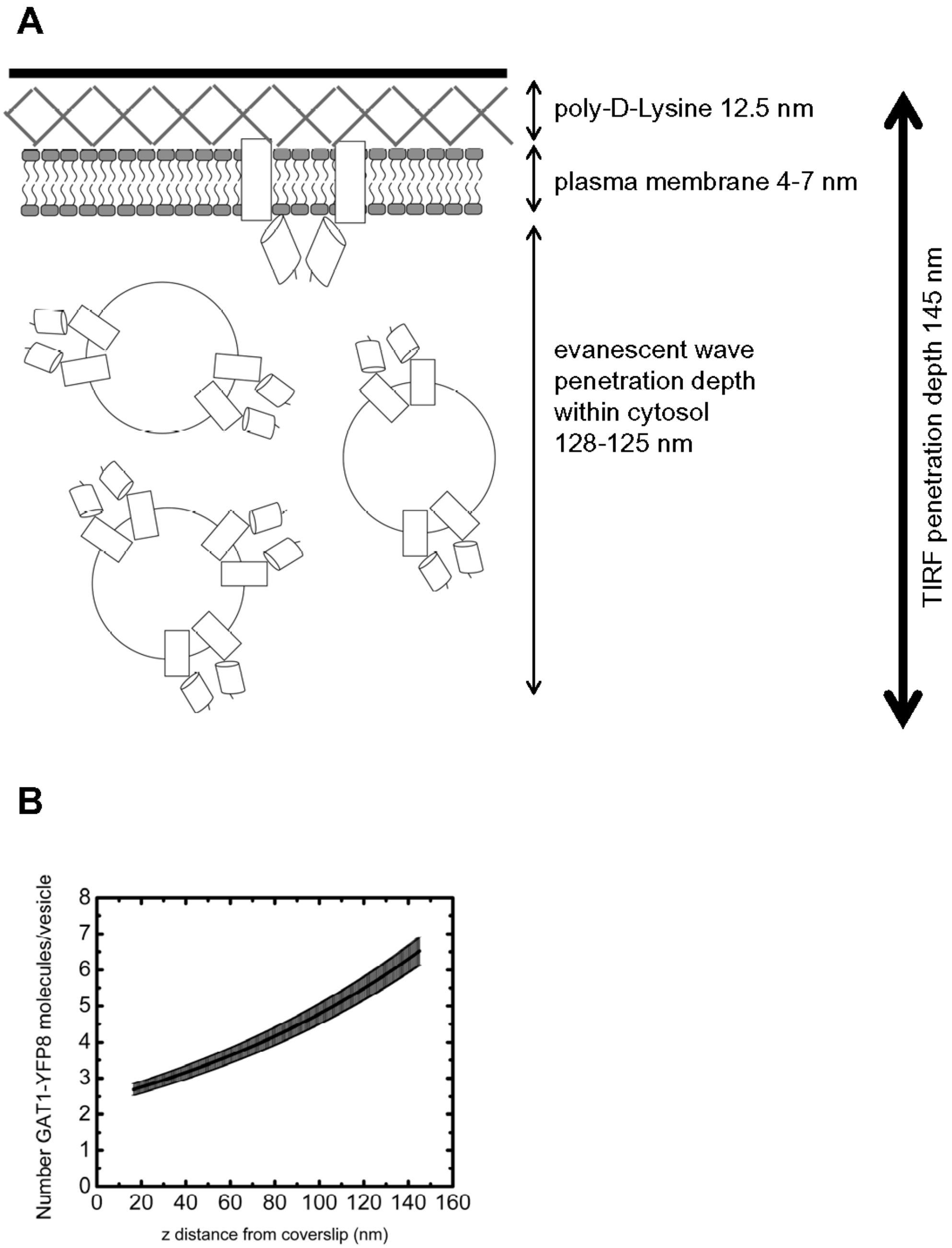
A
poly-D-Lysine 12.5 nm
plasma membrane 4-7 nm
evanescent wave penetration depth within cytosol 128-125 nm
TIRF penetration depth 145 nm
B
Number GAT1-YFP8 molecules/vesicle
z distance from coverslip (nm)
0
1
2
3
4
5
6
7
8
0
20
40
60
80
100
120
140
160

Figure 7

Chapter 4: Fluorescent mGAT1 constructs reveal motifs important for correct trafficking and dimerization

This chapter is modified from a manuscript being prepared for publication. We determine the trafficking, oligomerization, plasma membrane localization, and protein interactions of fluorescently labeled GAT1s. I determined the oligomerization states of the GABA transporters through fluorescence resonance energy transfer (FRET) studies, determined the plasma membrane localization through confocal microscopy, and contributed to the functional characterization of the transporter through GABA uptake experiments. Fraser Moss, Joanna Jankowsky, and Amber Southwell created the GAT1 fluorescent proteins, identified the appropriate cell line for the studies, established the transfection protocol, and performed functional characterization of GAT1 through kinetic studies of GABA uptake. Jia Hu performed the surface biotinylation experiments.

FLUORESCENT mGAT1 CONSTRUCTS REVEAL MOTIFS IMPORTANT FOR TRAFFICKING AND OLIGOMERIZATION

Fraser J. Moss[1], P. I. Imoukhuede[2], Jia Hu[3], Joanna L. Jankowsky[1], Michael W. Quick[3] and Henry A. Lester[1*]

Divisions of Biology[1] and Bioengineering [2], California Institute of Technology, Pasadena, California 91125, Department of Biological Sciences[3], University of Southern California, Los Angeles, California 90089

Running Title: Fluorescent mGAT1 Trafficking and Assembly

Address correspondence to: Henry A. Lester, Division of Biology, MC 156-29, California Institute of Technology, Pasadena, California 91125, USA. Tel. (626) 395-4946; Fax. (626) 564-8709; E-Mail: lester@caltech.edu

* To whom correspondence should be addressed.

Abstract

The protein-protein interactions, trafficking, and oligomerization of mGAT1, the mouse γ-aminobutyric acid (GABA) transporter, were studied using fourteen different fusions of mGAT1 with cyan, yellow, or green fluorescent protein (CFP, YFP, or GFP; collectively XFP). The constructs were expressed in neuroblastoma 2a cells, their function tested in a linear [^{3}H]GABA uptake assay, and their oligomerization probed with CFP-YFP Förster resonance energy transfer (FRET). XFP fused to the mGAT1 C-terminus (mGAT1XFP) significantly inhibited transporter function and trafficking despite the presence of a synthetic class II PDZ-interacting motif, -YKI. Replacing the terminal isoleucine with valine or adding the last 3 to 28 C-terminal residues of human GAT1 after the XFP restored wild-type function. Therefore a natural PDZ-interacting motif was minimally required for wild-type behavior. mGAT1XFP C-terminal fusions with wild-type function yielded up to 21% FRET efficiency, indicating efficient mGAT1 oligomerization. However, 45% FRET between one of these constructs and YFP-syntaxin 1A, which associates with the GAT1 N-terminus, indicated that the N- and C-terminals of mGAT1 oligomers are closer together in the cytosol than adjacent C-terminals. Adding the 45 hGAT1 C-terminal residues after mGAT1XFP resulted in little function, poor trafficking, and no detectable FRET. Similar properties were observed for an N-terminal XFP-mGAT1 fusion. These two constructs implicated the last ten residues of TM12 and the N-terminus in the mGAT1 oligomerization process. Inserting XFP between R565 and L566, resulted in 33% FRET but impaired function, which indicated the "RL" motif in the proximal C-terminus governs export from the endoplasmic reticulum but not transporter oligomerization.

Introduction

The γ-aminobutyric acid (GABA) transporter GAT1 is widely expressed in the mammalian brain. It is member of the solute carrier 6 (SLC6) gene family, which also includes transporters for dopamine (DAT), serotonin (SERT), norepinephrine (NET), and glycine (GlyT). This family is characterized by the co-transport of two Na^+ ions and one Cl^- ion to take up the neurotransmitter substrate against its thermodynamic gradient into the cell (125, 126).

GAT1 shapes the synaptic signaling events at inhibitory synapses by removing GABA within a few milliseconds of its release (127). Inhibition of GAT1 by pharmacological agents such as the antiepileptic tiagabine (128, 129), or its genetic knockout in mice, results in prolonged neurotransmitter lifetime in the synapse and concomitant increase in $GABA_A$ receptor-mediated tonic conductance, decreasing the excitability of the postsynaptic cell (3). Tiagabine is an effective therapy for epilepsy, but side effects include dizziness, asthenia, sedation, nonspecific nervousness ,and tremor (130, 131). The phenotype of GAT1 knockout mice reproduces many aspects of these side effects, indicating that they may arise directly from GAT1 inhibition.

In the healthy brain, density and surface/cytoplasm distribution of GAT1 transporters is tightly regulated. Previously, we quantified the mean number of GAT1 molecules in a presynaptic bouton to be 800--1300/μm^2, with 61--63% of these molecules expressed on the plasma membrane (8). This pool of transporters recycling to and from the plasma membrane plays a critical role in shaping neurotransmission and is both constitutively and functionally regulated (29, 132-138). Although SLC6 transporters are capable of transporting their substrate when expressed as monomers (139), oligomerization is a major factor in the release of newly synthesized transporter from the endoplasmic reticulum (140). The crystal structure of the leucine transporter $\mathrm{LeuT}_{\mathrm{Aa}}$ from the bacteria *Aquifex aeolicus*, (an orthologue of the mammalian SLC6 neurotransmitter transporters), crystallized as a dimer, with transmembrane domains (TM) 9 and 12 probably providing the interface for assembly (141). However, this structure likely represents only a low-order oligomerization state for these transporters, as evidence exists for the further oligomerization of transporter dimers (142, 143).

Even though oligomerization is absolutely required for release from the endoplasmic reticulum (ER), sequence elements in the cytoplasmic N- and C-termini exert additional control over trafficking. They can serve as substrates for cytosolic regulators such as kinases, or as motifs for interactions with other proteins, including PDZ (postsynaptic density 95/Discs large/zona occludens 1) domain-containing and soluble N-ethylmaleimide-sensitive fusion receptor (SNARE) proteins, which determine the insertion and withdrawal of transporter complexes from the cell surface (29, 134, 135, 137, 144, 145).

In this work, we describe a collection of mutated mGAT1 constructs with fusions to the cyan and yellow fluorescent proteins (CFP and YFP respectively, and XFP collectively). Some of these fluorescent mGAT1 molecules oligomerize, traffic, and function essentially as the wild-type mGAT1 in all respects. They have highlighted that a class II PDZ-interacting domain at the mGAT1 C-terminus is required for appropriate plasma membrane expression. Other fluorescent constructs with deficits in their trafficking and/or oligomerization have helped us to determine residues in the final transmembrane domain and in the cytoplasmic termini of GAT1 critical for efficient transporter trafficking and oligomerization. We also ascertained structural information about the cytoplasmic arrangement of these intracellular termini in mGAT1 oligomers. We find that the accurate comparison of mutated mGAT1 molecules to wild-type transporter required use of a non-saturated *in vitro* assay described herein. We propose this system as a model transient expression system for the characterization of all mutant neuronal transporters.

Experimental Procedures

Materials

pEYFP-C1 or pECFP-C1 vectors were purchased from Clontech (Mountain View, CA). The pcDNA3.1-YFP-syntaxin 1A construct was kindly provided by Wolfhard Almers (Vollum Institute, Oregon Health and Science University, Portland, OR). PfuTurbo C_x Hotstart polymerase and the Quickchange II XL site-directed mutagenesis kit was purchased from Stratagene (La Jolla, CA). The mouse neuroblastoma 2a (N2a; CCL-131) and the human embryonic kidney T/17 cell line (HEK 293T; CRL-11268) were obtained from ATCC (Manassas, VA). The pcDNA3.1(+) expression vector, Dulbecco's modified eagle media with 4 mM L-glutamine (DMEM), OptiMEM 1, fetal bovine serum (FBS), Lipofectamine and Plus reagents were purchased from Invitrogen (Carlsbad, CA). Penicillin/Streptomycin 100X and Sodium Pyruvate 100X solutions were purchased from Mediatech (Herndon, VA). 35-mm culture dishes with 14-mm glass bottoms of #0 thickness were procured from Mattek (Ashland, MA). Other tissue-culture plastic-ware was purchased from Greiner Bio-One (Monroe, CA). The bicinchoninic acid (BCA) protein assay, EZ-Link Sulfo-NHS-Biotin and immobilized monomeric avidin beads were obtained from Pierce (Rockford, IL). 4-Amino-*n*-[2,3-

^{3}H]butyric acid ([^{3}H]GABA; 87 Ci/mmol) and Amersham ECL Plus Western blotting detection reagents were obtained from GE Healthcare (Piscataway, NJ). Anti-GAT1 antibody AB1570W and goat anti-rabbit peroxidase conjugated secondary antibody were obtained from Chemicon International, Inc. (Temecula, CA). Anti-GFP rabbit antiserum 132002 was obtained from Synaptic Systems (Goettingen, Germany). Protease inhibitor cocktail tablets were obtained from Roche Diagnostics (Indianapolis, IN). Scinti-Safe 30% liquid scintillation cocktail was purchased from Fisher Scientific (Fair Lawn, NJ). Polyethyleneimine (PEI) 50% solution in H_2O, γ-amino-n-butyric acid (GABA) and all other reagents were purchased from SigmaAldrich (St. Louis, MO).

Molecular Biology

Wild-type mGAT1 and mGAT1GFP constructs have been described previously (8). To generate the fluorescent mutants mGAT1XFP* through mGAT1XFP45, the wild-type mGAT1 open reading frame (ORF) was subcloned without its endogenous stop codon in to the *Hin*d III and *Eco*R I sites of the pcDNA3.1(+) expression vector multiple cloning site (MCS). XFP ORFs were then subcloned downstream from, but in frame with the mGAT1 ORF at the *Not* I and *Xba* I sites of the pcDNA3.1(+) MCS. This resulted in a 12-amino-acid spacer between the end of the mGAT1 sequence and the beginning of the fluorophore. We modified Geiser *et al.'s* method for the integration of PCR fragments without the use of restriction enzymes (97) to add the final 3, 8, 20, 28, or 45 codons of the hGAT1 ORF. These were amplified from a source plasmid using PfuTurbo C_x Hotstart polymerase with 5' and 3' extensions corresponding to the 20--22 nucleotide regions that flanked the intended site of insertion, such that the PCR product integrated in frame immediately after the fluorophore sequence when used as the primers in a subsequent QuikChange II XL mutagenesis PCR reaction. For mGAT1XFP*, we simply added a GTC codon for valine after the fluorophore ORF. The same PCR insertion technique was applied to amplify and integrate YFP or CFP directly between residues R565 and L566 of mGAT1 to generate the mGAT1XFPCT constructs. Similarly, we used this approach to amplify the YFP or CFP ORFs with 15 additional codons from the downstream MCS of pEYFP-C1 or pECFP-C1 vectors, and fused the fragment directly onto the 5' end of the mGAT1 ORF in pcDNA3.1(+) to generate the XFP15mGAT1 N-terminally tagged constructs.

Cell culture and transfections

N2a cells were cultured at 37° C in 95% air / 5% CO_2 in media composed of 44.5% DMEM, 44.5% OptiMEM1, 5% FBS, 100 I.U/ml penicillin, and 100 μg/ml streptomycin. For all experiments, cells were plated onto either 12-well plates, 60-mm dishes or 35-mm culture dishes with 14-mm glass bottoms that we pre-coated with 0.05% PEI (pH 8.4 in borate buffer; 100 mM sodium borate, 100 mM boric acid). Transfections were performed using a modification of the manufacturer's Lipofectamine and Plus reagent protocol that resulted in non-saturated expression level of transporter (see Table 1). Cells were plated 16 h prior to transfection (Table 1, Step 1). The mass of cDNA in Table 1 is for the vector pcDNA3.1(+)mGAT1. To account for the difference in size between the wild-type mGAT plasmid and those of the fluorescent mGAT1 constructs or empty pcDNA3.1(+) vector, an equimolar equivalent of these cDNAs was used. The day of the transfection, cDNA was diluted in DMEM in one tube to which Plus reagent was subsequently added (Table 1, Step 2). In a second tube, Lipofectamine was diluted in DMEM (Table 1, Step 3). The tubes were briefly vortexed and incubated at room temperature for 15 min. The diluted Lipofectamine was subsequently added to the cDNA/Plus reagent dilution and vortexed (Step 4). The transfection mixes were incubated for a further 15 min at room temperature, while the pre-plated cells were washed once with DMEM to remove residual sera from the culture media and then placed in the appropriate volume of DMEM to perform the transfection (Table 1, Step 5). The cDNA/Plus/Lipofectamine mixes were then added to the cells (Table 1, Step 6), which were placed in the incubator for 16 h; then the transfection cocktail was replaced by complete N2a media. For experiments where cDNA quantity was the experimental variable, the amount transfected is stated in the relevant results section. However, cell density, amount of Lipofectamine and Plus reagents were kept constant for each size of culture dish/well; conditions remained within the manufacturer's recommended cDNA : transfectant ratio in any experiment. For GABA uptake experiments performed in HEK 293T cells, we plated 2 x 10^5 cells per well in 12-well plates pre-coated with PEI, 16 h before transfection. Otherwise, the transfection was performed as for N2a cells. HEK 293T cells were cultured at 37° C in 95% air/5% CO_2 in culture media composed of 88% DMEM, 10% FBS, 100 I.U/ml penicillin, 100 μg/ml streptomycin, and 1 mM sodium pyruvate.

GABA Uptake

Uptake assays were performed in 12-well plates 48 h after transfection as follows: Culture medium was aspirated and cells equilibrated for 10 min at room temperature in 1 ml Krebs-Ringer's (KRH) buffer containing (in mM): 130 NaCl, 1.3 KCl, 2.2 $CaCl_2$, 1.2 $MgSO_4$, 1.2 KH_2PO_4, 10 glucose, 10 HEPES, pH 7.4 (146). GABA uptake was initiated on aspiration of KRH buffer and addition of 500 μl 2.5, 5, 10, 30, or 80 μM

GABA and 25 nM [^{3}H]GABA in KRH at room temperature. Uptake was terminated by four rapid washes with KRH + GABA using the same total GABA concentration as used during the uptake step. Cells were lysed in 1 ml 2% SDS in phosphate-buffered saline (PBS). [^{3}H]GABA accumulation was assayed by liquid scintillation spectrometry. Specific uptake was normalized to the total protein in each well as determined using the BCA protein assay.

Surface biotinylation

48 h after transfection, N2a cells were incubated in Hank´s balanced salt solution (HBSS) containing 1 mg/ml biotin on ice for 30 min with gentle shaking. Excess biotin was removed by rapid washing twice in HBSS. Biotin was then quenched for 15 min on ice with 100 mM glycine dissolved in PBS/Ca^{2+}/Mg^{2+} (PBS plus 0.1 mM $CaCl_2$, and 0.2 mM $MgCl_2$). The cells were lysed with 500 µl radioimmunoprecipitation assay (RIPA) buffer (10 mM Tris-Cl, pH 7.4, 150 mM NaCl, 1 mM EDTA, 1% Triton X-100, 1% sodium deoxycholate, 0.1% SDS, supplemented with one protease inhibitor cocktail tablet per 10 ml) at 4 °C for 60 min, shaking vigorously. The cell lysates were centrifuged at 20,000 × g at 4 °C for 15 min to remove cell debris; 50 µl of cell lysate was saved for the quantification of total mGAT1 protein. The rest of the sample was mixed with 100 µl immobilized monomeric avidin beads and incubated on a rotating platform at 4 ºC overnight. The lysate was separated from the beads and kept for quantification of the intracellular mGAT1 fraction. The beads were then washed three times with ice-cold RIPA buffer and protein adsorbed by the beads (the plasma membrane bound fraction) was eluted with 100 µl SDS loading buffer (62.5 mM Tris-Cl, pH 6.8, 2% SDS, 100 mM β-mercaptoethanol) at room temperature for 30 min on a

rotating platform. Protein samples were quantified by standard Western blotting procedures using a 1:1000 dilution of AB1570W anti-GAT1 or a 1:5000 dilution of anti-GFP rabbit antiserum 132002 for the primary antibodies. Goat anti-rabbit peroxidase conjugated secondary antibody was applied at a 1:2000 dilution and blots were developed using the ECL Plus Western blotting detection reagent and an AlphaImager HP imaging system (Alpha Innotech, San Leandro, CA).

Förster Resonance Energy Transfer (FRET)

N2a cells were visualized at room temperature in KRH buffer, 48 h after transfection. A series of lambda stack X-Y images were collected from an inverted LSM 510 Meta laser scanning confocal microscope using an Achroplan IR 63X, 1.4 numerical aperture oil objective (Carl Zeiss, Thronwood, NY). Additional experiments were performed on an Eclipse C1si laser scanning confocal microscope using a 63X, 1.4 numerical aperture VC Plan Apo oil objective (Nikon Instruments Inc., Melville, NY). FRET was recorded using the donor recovery after acceptor photobleach (DRAP) technique, examining the dequenching of CFP during incremental photobleaching of YFP by the 514 nm argon laser line. Using reference spectra of YFP and CFP, lambda stacks were linearly unmixed and analyzed for FRET efficiency (147, 148). Using ImageJ (149), mean fluorescence intensities of CFP and YFP were determined by tracing the outer perimeter of the cell and subtracting background fluorescence, obtained from an area containing cells not expressing the construct. Fluorescence intensities of CFP and YFP at various time points after photobleaching were normalized to that at time 0 (100%). FRET efficiency (E) was calculated:

$$E = 1 - \left(\frac{I_{DA}}{I_D} \right) \qquad \text{(Equation 1)}$$

I_{DA} represents the normalized fluorescence intensity of CFP (100%) in the presence of non-bleached acceptor. I_D represents the normalized fluorescence intensity of CFP following 100% photobleach of the acceptor, YFP. The I_D value was extrapolated from a scatter plot of the percentage increase of CFP versus the percentage decrease of YFP for each cell (150). The distance between fluorophores (R) was calculated:

$$R = R_0 \left(E^{-1} - 1\right)^{1/6} \qquad \text{(Equation 2)}$$

R_0 is the Förster distance for the pair of fluorophores used in the experiment. The Förster distance depends on the overlap integral of the donor emission spectrum with the acceptor absorption spectrum and their mutual molecular orientation as expressed by:

$$R_0^{\ 6} = 8.8 \times 10^{23} \kappa^2 \eta^{-4} Q_0 J \qquad \text{(Equation 3)}$$

where κ^2 is the dipole orientation factor, η is the refractive index of the medium, Q_D is the fluorescence quantum yield of the donor in the absence of the acceptor, and J is the spectral overlap integral. For the purpose of this investigation $\eta^{-4} Q_D J$ can be assumed to be a constant of 2.41×10^{-14}. Resonance energy transfer equations were obtained from two sources (151, 152).

Results

A non-saturated [^{3}H]GABA uptake assay in heterologous cells

To evaluate the function of fluorescently modified mGAT1 constructs relative to wild-type, it was critical to establish an uptake assay in an appropriate heterologous expression system in which mGAT1 expression levels, the concentration of applied substrate, and the experimental time course were not saturating. We compared the function of the wild-type mGAT1 with mGAT1GFP, a construct known to have a major trafficking deficit *in vivo* (8), when expressed in two different mammalian cell lines. The N2a line is both neuronal and murine in origin and may possesses much of the necessary cellular machinery to process and traffic mGAT1 correctly; HEK 293T cells are a model mammalian line frequently used to assess the function of plasma membrane proteins. 0, 50, 100, 250, or 500 ng of wild-type mGAT1 plasmid or its equimolar equivalent of mGAT1GFP or pcDNA3.1(+) plasmid was transfected/well in 12- well plates. 20 min [^{3}H]GABA uptake experiments were performed in both low (2.5 μM) and high (80 μM) extracellular GABA concentrations ([GABA]$_O$). [^{3}H]GABA uptake in N2a cells transfected with wild-type mGAT1 remained in the linear range for transfections up to 100 ng cDNA/well in both 2.5 μM and 80 μM [GABA]$_O$ (Figures 1A and 1B). For transfections of $\geq$ 250 ng cDNA/well, the uptake began to saturate. Importantly, [^{3}H]GABA uptake by N2a cells transfected with the mGAT1GFP construct was reduced (28--65%) for all cDNA transfection amounts in both 2.5 μM and 80 μM [GABA]$_O$, reproducing the functional deficit reported for synaptosome preparations from mGAT1GFP knock-in mice (8). This was not the case for HEK 293T cells. [^{3}H]GABA uptake was almost completely saturated in 2.5 μM [GABA]$_O$ in cells transfected with as little as 100 ng cDNA/well of wild-type mGAT1 plasmid (V_{100ng} = 83.5 ± 1.9 fmol/μg/min; V_{max} = 86.9 ± 2.4 fmol/μg/min; Fig. 1C). Furthermore, maximum [^{3}H]GABA uptake for mGAT1GFP was not significantly different (V_{max} = 93.5 ± 17.9 fmol/μg/min) from wild-type mGAT1 for all transfections performed

(Figure 1C). This indicated that plasma membrane surface expression of mGAT1, when expressed at the levels we tested in HEK 293T cells, was not dependent on the same mechanisms that exist in its native environment. Therefore, we decided a) that N2a cells are the more suitable cell type in which to perform our experiments and b) that we should transfect 100 ng/well of wild-type mGAT1 plasmid or its equimolar equivalent of fluorescent mGAT1 plasmid to assess transporter function at non-saturated expression levels. In addition, we established that for these transfection conditions [^{3}H]GABA uptake remained linear for up to 60 min in both 2.5 μM or 80 μM $[\text{GABA}]_O$ as linear regression analysis of the 3, 10, 20, and 60 min data points revealed $r^2 = 0.997$ and 0.989 respectively (Figure 1D and 1E).

Functional characterization of fluorescent mGAT1 constructs

We generated fourteen fluorescent mGAT1 constructs to study trafficking and dimerization of the GAT1 transporter. Our previously characterized construct mGAT1GFP (8) served as the template for the majority of our new designs. For all constructs described in this study, we exchanged the GFP fluorophore for CFP or YFP to facilitate the study of protein-protein interactions by FRET.

One series of modified constructs was designed to relieve the trafficking deficit that occurs because the GFP fusion blocks access to the free carboxylate group of the isoleucine in the mGAT1 ^{596}AYI^{598} PDZ class II interacting C-terminal residues in mGAT1GFP (137). In a serendipitous quirk of the cloning of the mGAT1GFP into the expression vector, the construct’s C-terminal residues are -YKI (Supplemental figure 1). In a broad definition, this sequence represents a consensus PDZ class II interacting motif (X-ϕ-X-ϕ, where ϕ designates a hydrophobic residue and X any amino acid (153, 154)).

However, mining the Ensembl databases using Biomart (http://www.ebi.ac.uk/biomart) and applying the GO:0005886 “plasma membrane” cellular component filter did not yield any membrane proteins that possess this exact sequence at their C-termini. Therefore we defined the terminal residue P(0) more narrowly. We chose to perform a single conservative amino acid substitution, changing the terminal isoleucine residue present in mGAT1GFP to a valine in mGAT1XFP* (Supplemental figure 1). The resulting C-terminal sequence, -YKV, reconstituted a functional PDZ class II interacting motif present in Ephrin B receptors, a species known to rely on interactions with PDZ domain containing proteins for clustering and shown experimentally to interact with the PDZ proteins, syntenin, the Fas-associated phosphatase, FAP-1, protein interacting with C kinase 1, PICK1, and the glutamate receptor interacting protein, GRIP (155-157). Also, PICK1’s PDZ domain shows a preference for class II binding motifs with valine at P(0) over those terminating with isoleucine or leucine (158).

In another series of constructs, mGAT1XFP3, mGAT1XFP8, mGAT1XFP20, mGAT1XFP28, and mGAT1XFP45, had the most C-terminal 3, 8, 20, 28, or 45 residues of hGAT1 appended after the mGAT1XFP fusion (Supplemental figure 1). The differences in nucleotide sequence between the hGAT1 and mGAT1 C-termini were a useful source of positive identification when we analyzed the clones during construction. We expected that these constructs would allow us to determine a) how much extra native C-terminal sequence was required to generate wild-type-like mGAT1XFP behavior and b) whether additional regulatory signals resided in the C-terminal. Furthermore, comparison of mGAT1XFP3-45 and mGAT1XFP* function might also highlight any sequence specificity for the PDZ interactions that occur at the mGAT1 C-terminal.

In the third construct strategy, we interrupted the mGAT1 C-terminus with the XFP moiety shortly after the end of TM12 between residues R565 and L566 (Supplemental figure 1). Our fourth and final pair of constructs were N-terminal XFP15mGAT1 fusions, the number between the fluorophore and the transporter indicating the length of the linker fusing the two protein species together (Supplemental figure 1).

We applied the non-saturating parameters described above to transfect all 14 fluorescently tagged mGAT1 constructs into N2a cells. We studied both their distribution by laser scanning confocal fluorescence microscopy (Figure 2A), and we compared their function to non-fluorescent wild-type mGAT1 in 20-minute [^{3}H]GABA uptake assays (Figure 2B). mGAT1GFP is visible throughout the cytoplasm of N2a cells, but also appears to be expressed in the plasma membrane region. However, as expected from our earlier work in the assay optimization and previously published studies (8), [^{3}H]GABA uptake by the mGAT1GFP construct was significantly reduced (24 ± 0.03%) compared to wild-type. These data support our previous findings in synaptic boutons from mGAT1GFP knock-in mice, that mGAT1GFP is primarily an intercellular species; concentrating within few hundred nm of the plasma membrane, only a small fraction of the transporter pool actually appearing on the cell surface (8).

The constructs mGAT1XFP*, mGAT1XFP3, mGAT1XFP8, mGAT1XFP20, and mGAT1XFP28 localized primarily in the plasma membrane when expressed at non-saturating levels in N2a cells (Figure 2A). We confirmed that this was genuine surface-membrane expression in three separate assays. 1) For all five constructs, [^{3}H]GABA uptake from transfected N2a cells was not significantly different from wild-type mGAT1

(Figure 2B). 2) Surface biotinylation experiments determined that the percentage of the total expressed mGAT1XFP*, mGAT1XFP3, mGAT1XFP8, mGAT1XFP20, or mGAT1XFP28 protein that inserted into the plasma membrane was not significantly different from wild-type mGAT1 (Figure 2C). 3) Concentration dependence of [^{3}H]GABA uptake for mGAT1XFP*, mGAT1XFP8, mGAT1YFP3 and mGAT1YFP20 was identical to wild-type mGAT1 (Figure 2D). Each panel of Figure 2D presents the concentration dependence data for two fluorescent constructs vs. wild-type mGAT1 transfections performed on the same day. Within each set of experiments the K_m and V_{max} for the fluorescently tagged transporters were not significantly different from those of wild-type mGAT1. Collectively, these data indicated that reconstituting a naturally occurring PDZ class II interacting motif at the C-terminal of an mGAT1XFP fusion protein was both necessary and sufficient to confer wild-type like plasma membrane expression when expressed in N2a cells, whether the motif's sequence was the native mGAT1 -AYI sequence or the alternative Ephrin B receptor-like -YKV residues. Furthermore, in the N2a cell assay that we employed, residues P(-3) to P(-27) of the GAT1 C-terminus contain little additional information that influences transporter trafficking to the plasma membrane or its normal function.

In contrast to the wild-type behavior of mGAT1XFP* and 3-28, it was clear that mGAT1XFP45 was located primarily inside the cell (Figure 2A) and this was reflected in its markedly impaired [^{3}H]GABA uptake compared to wild-type mGAT1 (22 ± 0.03%; Figure 2B) and very small fraction of the total mGAT1XFP45 protein that partitioned into the plasma membrane (2.8 ± 0.6% compared to 44 ± 4.5% for wild-type; Figure 2C). It should be noted that mGAT1XFP45 was particularly challenging to process during surface biotinylation experiments because the majority of the protein sample aggregated in the well of the acrylamide gels and did not separate under electrophoresis. We are certain that this experimental difficulty amplified the actual shift in ratio from membrane to intracellular partitioned mGAT1XFP expression. Nonetheless, these three lines of evidence combined indicated that there was a marked biochemical difference between mGAT1XFP45 protein and the other fluorescent constructs, so that mGAT1XFP45 remained intracellular and also aggregated in detergent concentrations that readily solubilized other mGAT1XFP fusions. Furthermore, this difference apparently arose because mGAT1XFP45 possesses two copies of the GAT1 P(-28) to P(-44) C-terminal amino acids, which presumably dominated any trafficking rescue conferred by the presence of the C-terminal -AYI PDZ class II interacting motif.

Although constructed with an entirely different approach, mGAT1CFPCT and mGAT1YFPCT, like mGAT1XFP45, were primarily expressed intracellularly (Figure 2A) and exhibited reduced [^{3}H]GABA uptake compared to wild-type mGAT1 (35 ± 2% and 23 ± 2% respectively; Figure 2B). C-terminal residues P(0) through P(-32) remained intact in mGAT1XFPCT and therefore so too did any potential PDZ interaction. Consequently, it appeared that inserting the XFP moiety between R565 and L566 impeded appropriate trafficking of mGAT1XFPCT upstream from interaction with PDZ domain containing proteins.

The N-terminally-labeled XFP15mGAT1 fusions were also primarily retained within the cell (Figure 2A), and displayed significantly reduced [^{3}H]GABA uptake compared to wild type mGAT1 (CFP15mGAT1 35 ± 2% and YFP15mGAT1 28 ± 6%; Figure 2B). This extended our previous experience with an N-terminally-labeled

GFPmGAT1 fusion that had only eight amino acids in its linker between the fluorophore and the mGAT1 (8). Apparently lengthening the linker by an additional seven amino acids did not rescue the N-terminal interaction necessary for insertion of GAT1 into the plasma membrane.

mGAT1XFP constructs reveal important interactions for dimerization and trafficking

We applied the DRAP technique to measure FRET between the CFP and YFP moieties of paired mGAT1XFP constructs when expressed in N2a cells under the same non-saturating transfection conditions described for all previous experiments. We first investigated oligomerization between mGAT1XFP* and mGAT1XFP8 pairs, constructs that function like wild-type mGAT1 in uptake and surface biotinylation experiments (Figures 3A and 3B). To quantify FRET between the mGAT1 oligomers, we constructed a scatterplot of the photobleach-induced changes in CFP and YFP fluorescence of each cell during the entire bleaching time and fitted a regression line to the data (Figure 3C). The *y*-intercepts for the regression lines for the mGAT1CFP*/mGAT1YFP* and the mGAT1CFP8/mGAT1YFP8 transfection pairs were 1.10 ± 0.01 and 1.26 ± 0.01, respectively (Figure 3C). When inserted into equation 1, these translated to FRET efficiencies of 21% for mGAT1CFP*/mGAT1YFP* and 9% for mGAT1CFP8/mGAT1YFP8. We inserted these FRET efficiencies into Equation 2 (assuming R_0 = 49.2 Å for the CFP-YFP pair and $\kappa^2 = 0.67$ (159)) to determine that the fluorophores in mGAT1CFP8/mGAT1YFP8 and mGAT1CFP*/mGAT1YFP* pairs are separated by 72 Å and 61 Å, respectively. Given that mGAT1XFP* and mGAT1XFP8 are essentially identical with the exception of 8 amino acids after the fluorophore, we were initially surprised that these two construct sets yielded such a difference in measured FRET efficiency. One possibility for mGAT1XFP* having increased FRET compared to mGAT1XFP8 is that oligomer assembly is more efficient in this construct. Previous investigations from our laboratory performed with the α4-YFP and β2-CFP labeled nicotinic acetylcholine receptor subunits have demonstrated that marked differences in FRET efficiencies can result from improved receptor assembly (150). However, [^{3}H]GABA uptake and biotinylation assays had already demonstrated that mGAT1XFP* and mGAT1XFP8 insert into the plasma membrane with equal efficiency; and we know from the work of other laboratories that this process is dependent on the efficient assembly of the mGAT1 subunits (139, 144). Therefore the difference in FRET efficiency most likely occurs because the fluorophores are closer together or the dipoles are orientated slightly differently to one another to yield an increased FRET efficiency for mGAT1XFP* compared to mGAT1XFP8.

In addition to studying the fluorescent constructs that behaved like wild-type in functional assays, we were also interested to learn what FRET could reveal about the assembly and trafficking (or lack thereof) of the constructs which showed impaired function. We found no measurable FRET between mGAT1CFP45/mGAT1YFP45 co-expressed in N2a cells (Figure 4A), indicating that the intracellular retention of this protein highlighted by our previous functional and biochemical experiments occurred in large part because the assembly of mGAT1XFP45 oligomers was severely impaired. Furthermore, oligomerization of mGAT1YFP45 could not be rescued by co-expression with the wild-type-like mGAT1CFP8 (Figure 4B), which displayed the same strong plasma membrane localization as if it were expressed alone (Figure 4C). These results were confirmed by [^{3}H]GABA uptake assay. Assays were performed on N2a cells cotransfected with 50 ng mGAT1CFP8 plasmid plus an additional 0, 12.5, 25, or 50 ng of mGAT1CFP8, mGAT1YFP8, or mGAT1YFP45. Figure 4D shows that under these non-saturating transfection conditions, increasing the quantity of mGAT1CFP8 or mGAT1YFP8 co-expressed with 50 ng of mGAT1CFP8 augmented [^{3}H]GABA uptake, such that upon the eventual transfection of 100 ng total of mGAT1XFP8 uptake was greater than twice that for 50 ng mGAT1XFP8. However, co-expression of up to 50 ng of mGAT1XFP45 was unable to significantly improve the [^{3}H]GABA uptake from 50 ng mGAT1CFP8 alone (Figure 4D). Surprisingly, the presence of increasing levels of mGAT1XFP45 did not decrease the function of mGAT1CFP8; i.e., mGAT1XFP45 did not exert a dominant-negative effect on the trafficking of mGAT1CFP8. That mGAT1XFP45 did not sequester normally functioning mGAT1 molecules indicated that possessing two copies per transporter protein of the P(-28) through P(-44) C-terminal residues resulted in an autoinhibition of mGAT1XFP45 oligomerization.

The mGAT1XFPCT constructs had also shown impaired function in [^{3}H]GABA uptake assays (Figure 2A). However, these constructs produced a robust FRET signal upon co-expression of mGAT1CFPCT with mGAT1YFPCT (Figure 4E). When mGAT1YFPCT photobleach was plotted against mGAT1CFPCT photorecovery, the regression line intercepted the *y*-axis at 1.50 ± 0.01, implying a FRET efficiency of 33% (Figure 4F). This suggested that mGAT1XFPCT constructs could oligomerize but had their trafficking to the membrane inhibited by locating the fluorophore between residues R565 and L566.

[^{3}H]GABA uptake experiments had determined that the N-terminally-labeled XFP15mGAT1 constructs were poorly expressed on the plasma membrane (Figure 2A).

We asked whether placing the XFP only 15 residues from the N-terminus of mGAT1 had disturbed a protein-protein interaction crucial for normal plasma membrane expression. A well-studied interaction of the GAT1 N-terminus occurs with syntaxin1A (160-162), which acts as a positive regulator of GAT1 surface expression. Treatment of neurons in hippocampal culture with botulinum neurotoxin 1C, which cleaves syntaxin 1A, causes a reduction in surface-expressed mGAT1 and a corresponding increase in the cytosolic transporter (161). We co-expressed a YFP-syntaxin 1A fusion protein with both mGAT1CFP8 and CFP15mGAT1 in N2a cells and measured good FRET efficiencies between the co-expressed proteins in both transfections (Figures 5A and 5B, respectively). The *y*-axis intercept of the regression lines for mGAT1CFP8/YFP-syntaxin 1A and CFP15mGAT1/YFP-syntaxin 1A were 1.78 ± 0.002 and 1.41 ± 0.006 respectively (Figure 5C), implying FRET efficiencies of 44% and 29% (Equation 1). Assuming the canonical $R_0 = 49.2$ Å and $\kappa^2 = 0.67$ for CFP (159), these efficiencies imply that the distance between the fluorophores is 51.2 Å and 58.0 Å for mGAT1CFP8/YFP-syntaxin 1A and CFP15mGAT1/YFP-syntaxin 1A, respectively (Equation 2). This indicates that the mGAT1 N- and C-termini could reside as close as 7 Å from one another. Whether this represents an intra- or inter-molecular convergence of termini in an mGAT1 oligomer cannot be determined from these data. That YFP-syntaxin 1A yielded a lower FRET efficiency with the N-terminal CFP15mGAT1 fusion than the C-terminal mGAT1CFP8 indicated that, although the syntaxin 1A binding site is located closer to the fluorophore in CFP15mGAT1, there must be a deficiency in the association of the two molecules. However, a FRET efficiency of 29% indicated that the N-terminal CFP fusion nonetheless allowed a substantial physical interaction between mGAT1 and syntaxin 1A. We suspected that rather than directly interfering with syntaxin 1A-mGAT1 binding, the XFP15mGAT1 fusions were oligomerization deficient which reduced the availability of mGAT1 transporter complexes to couple with syntaxin 1A. CFP15mGAT1 and YFP15mGAT1 showed no detectable FRET when co-expressed (Figure 5D), indicating that these constructs indeed likely fail to oligomerize and consequently reduce the amount of transporter oligomers available to interact with syntaxin 1A in the exocyst.

Discussion

A linear assay system for mGAT1 in N2a cells

Various cell lines and transient transfection techniques have been applied to investigate the oligomerization and trafficking of SLC6 transporters (8, 132, 135, 143-145, 163-168). However, over-expression of neurotransmitter transporters *in vitro* may often fail to recapitulate the behavior of the protein in its native *in vivo* environment. The data presented in this study, as well as our laboratory's previously reported findings, have shown that when mGAT1GFP is transiently expressed in the widely used HEK 293T cell line, its [^{3}H]GABA uptake appears normal despite its significant trafficking deficits *in vivo* (8). Several possible mechanisms could prevent mGAT1GFP from recapitulating its neuronal cell behavior when expressed in HEK 293T cells. The first is overexpression caused by the presence of the simian virus 40 (SV40) large T-antigen in HEK 293T cells, which allows for episomal replication of transfected plasmids such as pcDNA3.1(+) used here that contain the SV40 origin of replication. Consistent with this hypothesis, we find that [^{3}H]GABA uptake becomes saturated in HEK 293T cells transfected with as little as 50--100 ng of mGAT1 plasmid, whereas transfection of 500 ng of mGAT1 plasmid into

N2a cells (which lack the SV40 T antigen) remained unsaturated. We suspect overexpression of mGAT1 in HEK 293T cells could saturate the cellular trafficking machinery so that it is no longer able to dynamically regulate transporter number at the cell surface. Under these conditions, mutants like mGAT1GFP are mistargeted to the membrane when they should be retained within the cell.

A second explanation for the difference in trafficking between HEK 293T cells and mouse neurons is that HEK 293T cells do not express the necessary collection of associating proteins to regulate GAT1 trafficking appropriately. For example, PICK1 is expressed in N2a cells, but is hardly detectable in HEK 293 cells (168). However, because HEK 293T cells appear to process and traffic mGAT1GFP like wild-type mGAT1, it suggests that this cell type does not utilize PDZ interactions to deliver GAT1 to the plasma membrane. Rather HEK 293T cells may use a distinct pathway for this process. In fact, hNET mutants with truncated C-termini function like wild-type transporter in HEK 293 cells (from which HEK 293T is derived), although in many other cell lines truncation mutants exhibited reduced substrate uptake (169).

HEK 293T cells were invaluable for pioneering heterologous expression studies of excitability proteins (170) and still serve well when one desires sheer quantity rather than faithful processing, assembly, sorting, regulation, and targeting. However, our studies required a system that more closely resembled the native environment in which mGAT1 normally expressed. We developed a heterologous transfection protocol and uptake assay in the N2a cell line that was non-saturating with respect to protein expression level, substrate concentration, and time course. We chose to work with the N2a cell line because its background closely matched that of the mGAT1 protein that we were studying; mouse and neuronal. We therefore expected that it would express the appropriate complement of accessory proteins for assessing mGAT1 assembly and trafficking. While we cannot claim perfect fidelity, the lack of saturation provides confidence that changes in expression, oligomerization, and trafficking are readily detected under these assay conditions.

Trafficking domains in the mGAT1 C-terminus

We used the above N2a expression system to express fluorescently tagged mGAT1 transporter mutants and identify regions critical for mGAT1 assembly and trafficking. We show that constructs mGAT1XFP*, mGAT1XFP3, mGAT1XFP8, mGAT1XFP20, and mGAT1XFP28 all function without significant difference from wild-type mGAT1; the additional C-terminal residues after the fluorophore in this series rescued deficits observed in the original mGAT1GFP construct. These data demonstrate that the terminal residues of mGAT1 must form a PDZ class II interacting domain for appropriate plasma membrane expression, whether the primary sequence of that motif is the native -AYI from GAT1 or another type II motif from a different receptor (-YKV). Nevertheless, the rules for recognition of the class II PDZ-interacting motif extend further than the consensus X-ϕ-X-ϕ pattern. The identity and combination of the hydrophobic residues at P(0) and P(-2) is critical (154, 171). The terminal -YKI sequence of mGAT1GFP is not present at the C-terminus of any known membrane protein and clearly is not utilized by PDZ-domain-containing proteins in N2a cells or *in vivo* (8). Besides the terminal -AYI sequence, there are apparently no other motifs that influence trafficking between the P(-3) and P(-28) positions in the GAT1 C-terminus. These findings corroborate previous studies of truncation mutations in neuronal SLC6 transporter trafficking (144, 145).

One potential caveat to the apparent equivalence of -YKV and -AYI terminal residues in our constructs is the significant difference in FRET efficiency between mGATCFP*/mGAT1YFP* and mGAT1CFP8/mGAT1YFP8. However, we show that the [^{3}H]GABA uptake and surface biotinylation were similar between the two constructs and comparable to wild-type mGAT1, suggesting that the differing FRET efficiencies were not attributable to variations in either construct design's ability to form functional oligomers. Rather, we believe the variation in FRET efficiencies resulted from different distances between the CFP and YFP molecules or altered relative orientations of the chromophore dipoles in the mGAT1XFP* vs. the mGAT1XFP8 transporter oligomers. These two constructs differ only in their most C-terminal residues: mGAT1XFP* terminates with the residues –ELYKV, while mGAT1XFP8 terminates -KEAYI. Though both motifs represent class II PDZ interacting domains, these two particular sequences are almost unique in nature to the Ephrin B receptors and the GAT1 transporter respectively (157, 172). It is conceivable that by changing the primary sequence of mGAT1's PDZ interacting motif we have changed the identity of the interacting proteins with which GAT1 now associates. The -AYI motif of GAT1 can interact with the PDZ domain containing protein PALS1 (137), with similar data showing the interaction of Ephrin B receptors and Syntenin, FAP-1, GRIP, and PICK1 (155-157). These potential interacting partners range in size from 627 amino acids to 2485 amino acids. If substitution of the PDZ interaction motif altered mGAT1's preferred interacting partner, the size of the interacting protein will no doubt influence the arrangement of the adjacent fluorophores on the C-terminal of mGAT1XFP* and mGAT1XFP8 oligomers.

Our studies also confirmed the presence of a important trafficking motif in the mGAT1 C-terminus recently identified by Farhan et al. (163). Our mGAT1XFPCT constructs disrupted an "RL" motif by placing the fluorophore directly between residues R565 and L566. This construct readily formed oligomers but exhibited poor trafficking to the plasma membrane. Farhan *et al.* showed this motif to be responsible for binding the COPII coat protein Sec24D, which mediates export of assembled transporters from the ER. Our data thus support Farhan *et al.*'s findings that the “RL” motif in the proximal C-terminus controls ER export in a manner that is dominant over the presence of a class II PDZ-interacting motif at the distal C-terminus.

Structural implications of the FRET data for mGAT1 oligomers

Our FRET experiments with the YFP-CFP pairs of our various constructs provided structural insight into the relationship between the N- and C-termini of the mGAT1 dimer. The greatest FRET efficiency that we measured for mGAT1 oligomers in this study was 33% for the mGAT1XFPCT CFP-YFP pair. According to Equation 2, the calculated distance between the two fluorophores was 55 Å. However, this calculation was based on the canonical Förster distance (R_0) for a CFP-YFP combination of 49.2 Å which assumes that the relative dipole orientation factor κ^2 is 0.67 for rapid random orientation (159). The CFP and YFP molecules consist of β-cans 24 Å in diameter and 42 Å in length (173) at the center of which is the fluorescent chromophore. The major dipole moment of the fluorophore is oriented approximately 60° from the long axis the β-can (174). In reality, κ^2 can range from 0.01 to 4. Our measured FRET efficiency therefore implies that the chromophores are separated by a minimum of 27.5 Å and a maximum of 74.6 Å. Comparison of the mGAT1XFPCT sequence with the structure of LeuT$_{Aa}$ (141) fuses the fluorophores in mGAT1XFPCT only two amino acids after the terminal α-helical residue of TM12. The ends of TM12 are only 15 Å apart in the LeuT$_{Aa}$ crystal structure dimer. The dimensions of XFP limit the smallest measurable distance for side-by- side chromophores in an oligomerized membrane protein to 24 Å (173). Therefore, the separation range we measured for the chromophores in mGAT1XFPCT oligomers corroborates the close proximity of the cytoplsmic ends of TM12 inferred for the SLC6 transporters from the LeuT$_{Aa}$ crystal structure (141).

Although less informative than the C-terminal XFP fusions, our N-terminal XFPmGAT1 yielded insight into the structural requirements for mGAT1 dimerization. In our attempts to build a fluorescent mGAT1 with the XFP on the N-terminus, we extended the linker by another seven amino acids, to 15 residues, compared to an 8-residue linker in a previously published construct (8). Another laboratory has made N-terminal XFP-GAT fusions with a longer, 27-amino acid linker that functions identically to wild-type GAT1 (139). In contrast, our FRET experiments with the shorter 15-amino acid linker show that transporter oligomerization is inhibited by the N-terminal fluorophore, although the monomers appeared to retain the ability to associate with syntaxin 1A. It would therefore appear that the trafficking deficit in our N-terminal constructs must be caused by steric hindrance of an interaction that is important for its oligomerization, rather than for its export to the plasma membrane.

Finally, our FRET experiments predict the distance separating the N- and C-termini of adjacent mGAT1 molecules in an oligomer. It has been previously reported that the distance between the adjacent N- and C-termini in a hSERT oligomer is less than the distance between pairs of N-termini or C-termini (143). FRET data from our fluorescent mGAT1 constructs agrees with this finding, although via a different experimental approach. We calculated the distances from measured FRET efficiencies for the separation of the fluorophores in mGAT1CFP8/YFP-syntaxin 1A that the N- and C-termini are separated by approximately 51 Å. FRET efficiencies for mGAT1CFP*/mGAT1YFP* or mGAT1CFP8/mGAT1YFP8 complexes indicate that the C-termini to C-termini distance is between 61--72 Å.

A role for the final 10 residues of TM12 in oligomerization

The crystal structure of the bacterial orthologue of mGAT1, LeuT_{Aa}, suggested that TM9 and TM12 could be the major interfaces for the dimerization of SLC6 transporters. It further showed that the last 10 residues of TM12 extend beyond the transmembrane region into the cytosol as α-helices that are separated by only 8.3 Å at their closest point (141). Prior to the crystallization of LeuT_{Aa}, at least four regions---including leucine repeats in TM2 (175), a glycophorin A-like motif in TM6 (176), and symmetrical interfaces (142) on TM4 and the TM11-12 region (143) --- had been suggested to support SLC6 transporter oligomerization. The LeuT_{Aa} structure has now placed some of these postulated contact sites in question, implying they may instead be important for quaternary structure of transporter monomers rather than for oligomer assembly (140). Further support for the importance of the TM12 region comes from the ability of a TM11-12 hSERT partial transporter to homodimerize when expressed alone and to strongly inhibit surface trafficking of full-length hSERT when the two are co-expressed. Our current data suggests that a critical region of interaction is located in the last 10 amino acids of TM12. The non-functional mGAT1XFP45 constructs were particularly informative. FRET experiments show that mGAT1XFP45 does not associate with other mGAT1XFP45 molecules or with mGAT1XFP8. In addition, functional experiments determined that normal expression of the wild-type-like mGAT1CFP8 was not adversely affected by co-expression of increasing quantities of mGAT1YFP45. Most reported transporter mutants with trafficking and assembly deficits exert a dominant negative effect upon the expression of the wild-type protein (139, 143-145, 163, 177). That mGAT1XFP45 did not follow this rule suggested that it was inhibiting its own assembly via an intra-molecular interaction. To understand why mGAT1XFP45 did not co-assemble with other GAT1 monomers, we compared its primary sequence with the construct mGAT1XFP28 that behaves essentially as wild-type mGAT1 in our functional assay. The difference between the two constructs is the presence of the extra P(-28) to P(-44) hGAT1 C-terminal sequence after the fluorophore in mGAT1XFP45. We hypothesize that auto-inhibition of oligomerization occurs in the nascent mGAT1XFP45 protein when the second copy of the α-helical P(-34) through P(-44) C-terminal region from hGAT1 located after the XFP moiety is able to associate with the mGAT1 TM12 within the same polypeptide. Considering that mGAT1XFPCT, in which the fluorophore bisects residues P(-32) and P(-33) (R565 and L566), dimerized but did not traffic, we do not expect that the residues C-terminal to P(-34) are involved in dimerization.

Conclusion

We have described a stringent technique to assay the function of neuronal SLC6 transporters *in vitro* and determined that regions in both the N-terminus and TM12 are critical for GAT1 oligomerization. The interface for GAT1 oligomerization almost certainly requires association of the final 10 residues of TM12 from each monomer. We have also highlighted two motifs that control GAT1 trafficking to the plasma membrane that are present in the C-termini and determined information about the arrangement N- and C-termini of mGAT1 oligomers in the cytosol.

References

1. Chen N-H, Reith MA, Quick M. Synaptic uptake and beyond: the sodium- and chloride-dependent neurotransmitter transporter family SLC6. Pflügers Archiv European Journal of Physiology 2004;447(5):519-531.

2. Giros B, Jaber M, Jones SR, Wightman RM, Caron MG. Hyperlocomotion and indifference to cocaine and amphetamine in mice lacking the dopamine transporter. Nature 1996;379(6566):606-612.

3. Chiu CS, Brickley S, Jensen K, Southwell A, McKinney S, Cull-Candy S, Mody I, Lester HA. GABA transporter deficiency causes tremor, ataxia, nervousness, and increased GABA-induced tonic conductance in cerebellum. J Neurosci 2005;25(12):3234-3245.

4. Alberts B, Bray D, Hopkin K, Johnson A, Lewis J, Raff M, Roberts K, Walter P. Essential cell biology. second ed. New York: Garland Science; 2004.

5. Hoogland G, Spierenburg HA, van Veelen CW, van Rijen PC, van Huffelen AC, de Graan PN. Synaptosomal glutamate and GABA transport in patients with temporal lobe epilepsy. J Neurosci Res 2004;76(6):881-890.

6. Richerson GB, Wu Y. Role of the GABA transporter in epilepsy. Adv Exp Med Biol 2004;548:76-91.

7. Wu Y, Wang W, Richerson GB. GABA Transaminase Inhibition Induces Spontaneous and Enhances Depolarization-Evoked GABA Efflux via Reversal of the GABA Transporter. J Neurosci 2001;21(8):2630-2639.

8. Chiu CS, Jensen K, Sokolova I, Wang D, Li M, Deshpande P, Davidson N, Mody I, Quick MW, Quake SR, Lester HA. Number, density, and surface/cytoplasmic distribution of GABA transporters at presynaptic structures of knock-in mice carrying

GABA transporter subtype 1-green fluorescent protein fusions. J Neurosci 2002;22(23):10251-10266.

9. Cohen-Kfir E, Lee W, Eskandari S, Nelson N. Zinc inhibition of {gamma}-aminobutyric acid transporter 4 (GAT4) reveals a link between excitatory and inhibitory neurotransmission. Proceedings of the National Academy of Sciences 2005;102(17):6154-6159.

10. Ana Gadea AML-C. Glial transporters for glutamate, glycine, and GABA: II. GABA transporters. Journal of Neuroscience Research 2001;63(6):461-468.

11. Schousboe A, Sarup A, Larsson OM, White HS. GABA transporters as drug targets for modulation of GABAergic activity. Biochemical Pharmacology 2004;68(8):1557-1563.

12. Liu QR, Lopez-Corcuera, B., Mandiyan, S., Nelson, H., Nelson, N. Molecular Characterization of Four Pharmacologically Distinct alpha-aminobutyric acid transporters in mouse brain. The Journal of Biological Chemistry 1993;268(3):2106-2112.

13. Matskevitch I, Wagner CA, Stegen C, Broer S, Noll B, Risler T, Kwon HM, Handler JS, Waldegger S, Busch AE, Lang F. Functional Characterization of the Betaine/gamma -Aminobutyric Acid Transporter BGT-1 Expressed in Xenopus Oocytes. J Biol Chem 1999;274(24):16709-16716.

14. Kempson SA, Montrose MH. Osmotic regulation of renal betaine transport: transcription and beyond. Pflügers Archiv European Journal of Physiology 2004;449(3):227-234.

15. Guastella J, Brecha N, Welgmann C, Lester HA, Davidson N. Cloning, expression, and localization of a rat brain high-affinity glycine transporter. Proceedings

of the National Academy of Sciences of the United States of America 1992;89:7189-7193.

16. Bennnett ER, Kanner, B.I. The Membrane Topology of GAT-1, a (Na+ + Cl-)-coupled gamma-Aminobutyric Acid Transporter from Rat Brain. The Journal of Biological Chemistry 1997;272(2):1203-1210.

17. Korkhov VM, Farhan H, Freissmuth M, Sitte HH. Oligomerization of the {gamma}-Aminobutyric Acid Transporter-1 Is Driven by an Interplay of Polar and Hydrophobic Interactions in Transmembrane Helix II. J Biol Chem 2004;279(53):55728-55736.

18. Hastrup H, Karlin, A., Javitch, J.A. Symmetrical dimer of hte human dopamine transporter revealed by cross-linking Cys-306 at the extracellular end of the sixth transmembrane segmetn. Proccedings of the National Academy of Acience USA 2001;98:10055-10060.

19. Schmid JA, Scholze, P., Kudlacek, O., Freissmuth, M., Singer, E.A., Sitte, H.H. Oligomerization of the Human Serotonin Transporter and fo the Rat GABA Transporter 1 Visualized by Fluorescence Resonance Energy Transfer Microscopy in Living Cells. The Journal of Biological Chemistry 2001;276(6):3805-3810.

20. Yamashita A, Singh SK, Kawate T, Jin Y, Gouaux E. Crystal structure of a bacterial homologue of Na+/Cl--dependent neurotransmitter transporters. Nature 2005;437(7056):215-223.

21. Farhan H, Reiterer V, Korkhov VM, Schmid JA, Freissmuth M, Sitte HH. Concentrative Export from the Endoplasmic Reticulum of the {gamma}-Aminobutyric Acid Transporter 1 Requires Binding to SEC24D. J Biol Chem 2007;282(10):7679-7689.

22. Farhan H, Korkhov VM, Paulitschke V, Dorostkar MM, Scholze P, Kudlacek O, Freissmuth M, Sitte HH. Two Discontinuous Segments in the Carboxyl Terminus Are Required for Membrane Targeting of the Rat {gamma}-Aminobutyric Acid Transporter-1 (GAT1). J Biol Chem 2004;279(27):28553-28563.

23. Wang D, Quick MW. Trafficking of the Plasma Membrane g-Aminobutyric Acid Transporter GAT1. Size and rates of an acutely recycling pool. J Biol Chem 2005;280(19):18703-18709.

24. Deken SL, Wang D, Quick MW. Plasma Membrane GABA Transporters Reside on Distinct Vesicles and Undergo Rapid Regulated Recycling. J Neurosci 2003;23(5):1563-1568.

25. Lodish H, Berk A, Zipursky LS, Matsudaira P, Baltimore D, Darnell J. Molecular Cell Biology. Fourth ed. New York: W.H. Freeman; 1999.

26. Beckman ML, Bernstein EM, Quick MW. Protein Kinase C Regulates the Interaction between a GABA Transporter and Syntaxin 1A. J Neurosci 1998;18(16):6103-6112.

27. Beckman ML, Bernstein EM, Quick MW. Multiple G Protein-Coupled Receptors Initiate Protein Kinase C Redistribution of GABA Transporters in Hippocampal Neurons. J Neurosci 1999;19(11):9RC-.

28. Quick MW, Corey JL, Davidson N, Lester HA. Second Messengers, Trafficking-Related Proteins, and Amino Acid Residues that Contribute to the Functional Regulation of the Rat Brain GABA Transporter GAT1. J Neurosci 1997;17(9):2967-2979.

29. Quick MW. The role of SNARE proteins in trafficking and function of neurotransmitter transporters. Handb Exp Pharmacol 2006(175):181-196.

30. Deken SL, Beckman ML, Boos L, Quick MW. Transport rates of GABA transporters: regulation by the N-terminal domain and syntaxin 1A. Nature Neuroscience 2000;3(10):998-1003.

31. Law RM, Stafford A, Quick MW. Functional Regulation of gamma - Aminobutyric Acid Transporters by Direct Tyrosine Phosphorylation. J Biol Chem 2000;275(31):23986-23991.

32. Whitworth TL, Quick MW. Substrate-induced Regulation of gamma - Aminobutyric Acid Transporter Trafficking Requires Tyrosine Phosphorylation. J Biol Chem 2001;276(46):42932-42937.

33. Chiu C-S, Jensen K, Sokolova I, Wang D, Li M, Deshpande P, Davidson N, Mody I, Quick MW, Quake SR, Lester HA. Number, Density, and Surface/Cytoplasmic Distribution of GABA Transporters at Presynaptic Structures of Knock-In Mice Carrying GABA Transporter Subtype 1-Green Fluorescent Protein Fusions. J Neurosci 2002;22(23):10251-10266.

34. Purves D, Augustine GJ, Fitzpatrick D, Katz LC, LaMantia A-S, McNamara JO, Williams SM. Neuroscience. 2nd ed. Sunderland: Sinauer Associates; 2001. p. 681.

35. White HS, Watson WP, Hansen SL, Slough S, Perregaard J, Sarup A, Bolvig T, Petersen G, Larsson OM, Clausen RP, Frolund B, Falch E, Krogsgaard-Larsen P, Schousboe A. First Demonstration of a Functional Role for Central Nervous System Betaine/{gamma}-Aminobutyric Acid Transporter (mGAT2) Based on Synergistic Anticonvulsant Action among Inhibitors of mGAT1 and mGAT2. J Pharmacol Exp Ther 2005;312(2):866-874.

36. Clausen RP, Moltzen EK, Perregaard J, Lenz SM, Sanchez C, Falch E, Frolund B, Bolvig T, Sarup A, Larsson OM, Schousboe A, Krogsgaard-Larsen P. Selective inhibitors of GABA uptake: synthesis and molecular pharmacology of 4-N-methylamino-4,5,6,7-tetrahydrobenzo[d]isoxazol-3-ol analogues. Bioorganic & Medicinal Chemistry 2005;13(3):895-908.

37. Michael DJ, Ritzel RA, Haataja L, Chow RH. Pancreatic {beta}-Cells Secrete Insulin in Fast- and Slow-Release Forms. Diabetes 2006;55(3):600-607.

38. Lynch BA, Lambeng N, Nocka K, Kensel-Hammes P, Bajjalieh SM, Matagne A, Fuks B. The synaptic vesicle protein SV2A is the binding site for the antiepileptic drug levetiracetam. PNAS 2004;101(26):9861-9866.

39. Toomre D, Steyer JA, Keller P, Almers W, Simons K. Fusion of Constitutive Membrane Traffic with the Cell Surface Observed by Evanescent Wave Microscopy. J Cell Biol 2000;149(1):33-40.

40. Liu T, Tucker WC, Bhalla A, Chapman ER, Weisshaar JC. SNARE-Driven, 25-Millisecond Vesicle Fusion In Vitro. Biophys J 2005;89(4):2458-2472.

41. An SJ, Almers W. Tracking SNARE Complex Formation in Live Endocrine Cells. Science 2004;306(5698):1042-1046.

42. Halliday D, Resnick, R., Krane, K.S. . Physics. Fourth ed. New York: John Wiley & Sons, Inc.; 1992.

43. Axelrod D. Total Internal Reflection Fluorescence Microscopy in Cell Biology. Methods in Enzymology 2003;361:1-33.

44. Dickinson ME, Bearman G, Tilie S, Lansford R, Fraser SE. Multi-spectral imaging and linear unmixing add a whole new dimension to laser scanning fluorescence microscopy. Biotechniques 2001;31(6):1272, 1274-1276, 1278.

45. Nashmi R, Dickinson ME, McKinney S, Jareb M, Labarca C, Fraser SE, Lester HA. Assembly of a4b2 nicotinic acetylcholine receptors assessed with functional fluorescently labeled subunits: effects of localization, trafficking, and nicotine-induced upregulation in clonal mammalian cells and in cultured midbrain neurons. J Neurosci 2003;23(37):11554-11567.

46. Triller A, Choquet D. Surface trafficking of receptors between synaptic and extrasynaptic membranes: and yet they do move! Trends in Neurosciences 2005;28(3):133-139.

47. Wells KS, Sandison, D.R., Strickler, J., Webb, W.W. Quantitative Fluorescence Imaging with Laser Scanning Confocal Microscopy. In: Pawley JB, editor. Handbook of Biological Confocal Microscopy. New York and London: Plenum Press; 1990. p. 27-39.

48. Axelrod D, Koppel, D.E., Schlessinger, J., Elson, E., Webb, W.W. . Mobility measurement by analysis of fluorescence photobleaching recovery kinetics. Biophysical Journal 1976;16:1055-1069.

49. Rabut G, Ellenberg, Jan. Photobleaching Techniques to Study Mobility and Molecular Dyanmics of Proteins in Live Cells: FRAP, iFRAP, and FLIP. In: Robert D. Goldman DS, editor. Live Cell Imaging: A Lab Manual. Cold Spring Harbor, New York: Cold Spring Harbor Laboratory Press; 2005. p. 101-126.

50. Wey CL, Cone, R.A., Edidin, M.A. Lateral Diffusion of Rhodopsin in Photoreceptor Cells Measured by Fluorescence Photobleaching and Recovery. Biophysical Journal 1981;33:225-232.

51. Guastella J, Nelson N, Nelson H, Czyzyk L, Keynan S, Miedel MC, Davidson N, Lester HA, Kanner BI. Cloning and expression of a rat brain GABA transporter. Science 1990;249(4974):1303-1306.

52. Minelli A, Brecha NC, Karschin C, DeBiasi S, Conti F. GAT-1, a high-affinity GABA plasma membrane transporter, is localized to neurons and astroglia in the cerebral cortex. J Neurosci 1995;15(11):7734-7746.

53. Morara S, Brecha NC, Marcotti W, Provini L, Rosina A. Neuronal and glial localization of the GABA transporter GAT-1 in the cerebellar cortex. Neuroreport 1996;7(18):2993-2996.

54. Radian R, Kanner BI. Stoichiometry of sodium- and chloride-coupled g-aminobutyric acid transport by synaptic plasma membrane vesicles isolated from rat brain. Biochemistry 1983;22(5):1236-1241.

55. Kavanaugh MP, Arriza JL, North RA, Amara SG. Electrogenic uptake of g-aminobutyric acid by a cloned transporter expressed in Xenopus oocytes. J Biol Chem 1992;267(31):22007-22009.

56. Mager S, Naeve J, Quick M, Labarca C, Davidson N, Lester HA. Steady states, charge movements, and rates for a cloned GABA transporter expressed in Xenopus oocytes. Neuron 1993;10(2):177-188.

57. Lester HA, Mager S, Quick MW, Corey JL. Permeation Properties of Neurotransmitter Transporters. Annual Review of Pharmacology and Toxicology 1994;34(1):219-249.

58. Ashby MC, Maier SR, Nishimune A, Henley JM. Lateral Diffusion Drives Constitutive Exchange of AMPA Receptors at Dendritic Spines and Is Regulated by Spine Morphology. J Neurosci 2006;26(26):7046-7055.

59. Richards DA, de Paola V, Caroni P, Gahwiler BH, McKinney RA. AMPA-receptor activation regulates the diffusion of a membrane marker in parallel with dendritic spine motility in the mouse hippocampus. J Physiol (Lond) 2004;558(2):503-512.

60. Kirsch J, Betz H. The postsynaptic localization of the glycine receptor-associated protein gephyrin is regulated by the cytoskeleton. J Neurosci 1995;15(6):4148-4156.

61. Sun F, Hug MJ, Lewarchik CM, Yun CHC, Bradbury NA, Frizzell RA. E3KARP Mediates the Association of Ezrin and Protein Kinase A with the Cystic Fibrosis Transmembrane Conductance Regulator in Airway Cells. J Biol Chem 2000;275(38):29539-29546.

62. Axelrod D, Koppel DE, Schlessinger J, Elson E, Webb WW. Mobility measurement by analysis of fluorescence photobleaching recovery kinetics. Biophys J 1976;16(9):1055-1069.

63. Sprague BL, Pego RL, Stavreva DA, McNally JG. Analysis of Binding Reactions by Fluorescence Recovery after Photobleaching. Biophys J 2004;86(6):3473-3495.

64. Sprague BL, McNally JG. FRAP analysis of binding: proper and fitting. Trends in Cell Biology 2005;15(2):84-91.

65. Lang T, Bruns D, Wenzel D, Riedel D, Holroyd P, Thiele C, Jahn R. SNAREs are concentrated in cholesterol-dependent clusters that define docking and fusion sites for exocytosis. EMBO J 2001;20(9):2202-2213.

66. Weiss M. Challenges and Artifacts in Quantitative Photobleaching Experiments. Traffic 2004;5(9):662-671.

67. De Brabander MJ, Van de Velre RML, Aerts FEM, Borgers M, Janssen PAJ. The Effects of Methyl [5-(2-Thienylcarbonyl)-1H-benzimidazol-2-yl]carbamate, (R 17934; NSC 238159), a New Synthetic Antitumoral Drug Interfering with Microtubules, on Mammalian Cells Cultured in Vitro. Cancer Res 1976;36(3):905-916.

68. Chen L, Wang H, Vicini S, Olsen RW. The g-aminobutyric acid type A ($GABA_A$) receptor-associated protein (GABARAP) promotes $GABA_A$ receptor clustering and modulates the channel kinetics. PNAS 2000;97(21):11557-11562.

69. Jacob TC, Bogdanov YD, Magnus C, Saliba RS, Kittler JT, Haydon PG, Moss SJ. Gephyrin Regulates the Cell Surface Dynamics of Synaptic $GABA_A$ Receptors. J Neurosci 2005;25(45):10469-10478.

70. Bretscher A, Edwards K, Fehon RG. ERM proteins and merlin: integrators at the cell cortex. Nat Rev Mol Cell Biol 2002;3(8):586-599.

71. Yun CHC, Lamprecht G, Forster DV, Sidor A. NHE3 Kinase A Regulatory Protein E3KARP Binds the Epithelial Brush Border Na+/H+ Exchanger NHE3 and the Cytoskeletal Protein Ezrin. J Biol Chem 1998;273(40):25856-25863.

72. McHugh EM, Zhu W, Milgram S, Mager S. The GABA transporter GAT1 and the MAGUK protein Pals1: interaction, uptake modulation, and coexpression in the brain. Molecular and Cellular Neuroscience 2004;26(3):406-417.

73. Adams DS. Lab Math: A Handbook of Measurements, Calculations, and Other Quantitative Skills for Use at the Bench. Cold Spring Harbor Cold Spring Harbor Laboratory Press; 2003. p. 187-190.

74. Zhu L, Liu Y, Forte JG. Ezrin oligomers are the membrane-bound dormant form in gastric parietal cells. Am J Physiol Cell Physiol 2005;288(6):C1242-1254.

75. Gary R, Bretscher A. Ezrin self-association involves binding of an N-terminal domain to a normally masked C-terminal domain that includes the F-actin binding site. Mol Biol Cell 1995;6(8):1061-1075.

76. Bates IR, Hebert B, Luo Y, Liao J, Bachir AI, Kolin DL, Wiseman PW, Hanrahan JW. Membrane Lateral Diffusion and Capture of CFTR within Transient Confinement Zones. Biophys J 2006;91(3):1046-1058.

77. Cha B, Kenworthy A, Murtazina R, Donowitz M. The lateral mobility of NHE3 on the apical membrane of renal epithelial OK cells is limited by the PDZ domain proteins NHERF1/2, but is dependent on an intact actin cytoskeleton as determined by FRAP. J Cell Sci 2004;117(15):3353-3365.

78. Haggie PM, Stanton BA, Verkman AS. Increased Diffusional Mobility of CFTR at the Plasma Membrane after Deletion of Its C-terminal PDZ Binding Motif. J Biol Chem 2004;279(7):5494-5500.

79. Torres GE, Yao W-D, Mohn AR, Quan H, Kim K-M, Levey AI, Staudinger J, Caron MG. Functional Interaction between Monoamine Plasma Membrane Transporters and the Synaptic PDZ Domain-Containing Protein PICK1. Neuron 2001;30(1):121-134.

80. Lamprecht G, Seidler U. The emerging role of PDZ adapter proteins for regulation of intestinal ion transport. Am J Physiol Gastrointest Liver Physiol 2006;291(5):G766-777.

81. Cao X, Ding X, Guo Z, Zhou R, Wang F, Long F, Wu F, Bi F, Wang Q, Fan D, Forte JG, Teng M, Yao X. PALS1 Specifies the Localization of Ezrin to the Apical Membrane of Gastric Parietal Cells. J Biol Chem 2005;280(14):13584-13592.

82. Yonemura S, Hirao M, Doi Y, Takahashi N, Kondo T, Tsukita S, Tsukita S. Ezrin/Radixin/Moesin (ERM) Proteins Bind to a Positively Charged Amino Acid Cluster in the Juxta-Membrane Cytoplasmic Domain of CD44, CD43, and ICAM-2. J Cell Biol 1998;140(4):885-895.

83. Denker SP, Huang DC, Orlowski J, Furthmayr H, Barber DL. Direct Binding of the Na-H Exchanger NHE1 to ERM Proteins Regulates the Cortical Cytoskeleton and Cell Shape Independently of H+ Translocation. Molecular Cell 2000;6(6):1425-1436.

84. Kneussel M, Loebrich S. Trafficking and synaptic anchoring of ionotropic inhibitory neurotransmitter receptors. Biology of the Cell 2007;099(6):297-309.

85. Kirsch J, Langosch D, Prior P, Littauer UZ, Schmitt B, Betz H. The 93-kDa glycine receptor-associated protein binds to tubulin. J Biol Chem 1991;266(33):22242-22245.

86. Kneussel M, Betz H. Receptors, gephyrin and gephyrin-associated proteins: novel insights into the assembly of inhibitory postsynaptic membrane specializations. J Physiol 2000;525(1):1-9.

87. Yang JW, Czech T, Felizardo M, Baumgartner C, Lubec G. Aberrant expression of cytoskeleton proteins in hippocampus from patients with mesial temporal lobe epilepsy. Amino Acids 2006;30(4):477-493.

88. Lee TS, Mane S, Eid T, Zhao H, Lin A, Guan Z, Kim JH, Schweitzer J, King-Stevens D, Weber P, Spencer SS, Spencer DD, de Lanerolle NC. Gene expression in temporal lobe epilepsy is consistent with increased release of glutamate by astrocytes. Mol Med 2007;13(1-2):1-13.

89. Andre V, Dube C, Francois J, Leroy C, Rigoulot M-A, Roch C, Namer IJ, Nehlig A. Pathogenesis and Pharmacology of Epilepsy in the Lithium-pilocarpine Model. Epilepsia 2007;48(s5):41-47.

90. Greene ND, Bamidele A, Choy M, de Castro SC, Wait R, Leung KY, Begum S, Gadian DG, Scott RC, Lythgoe MF. Proteome changes associated with hippocampal MRI abnormalities in the lithium pilocarpine-induced model of convulsive status epilepticus. PROTEOMICS 2007;7(8):1336-1344.

91. Majores M, Schick V, Engels G, Fassunke J, Elger C, Schramm J, Blümcke I, Becker A. Mutational and immunohistochemical analysis of ezrin-, radixin-, moesin (ERM) molecules in epilepsy-associated glioneuronal lesions. Acta Neuropathologica 2005;110(6):537-546.

92. Schick V, Majores M, Koch A, Elger CE, Schramm J, Urbach H, Becker AJ. Alterations of Phosphatidylinositol 3-Kinase Pathway Components in Epilepsy-associated Glioneuronal Lesions. Epilepsia 2007;48(s5):65-73.

93. Wu Y, Wang W, Richerson GB. Vigabatrin Induces Tonic Inhibition Via GABA Transporter Reversal Without Increasing Vesicular GABA Release. J Neurophysiol 2003;89(4):2021-2034.

94. Honmou O, Kocsis JD, Richerson GB. Gabapentin potentiates the conductance increase induced by nipecotic acid in CA1 pyramidal neurons in vitro. Epilepsy Research 1995;20(3):193-202.

95. Richerson GB, Wu Y. Role of the GABA Transporter in Epilepsy. In: Binder DK, Scharfman HE, editors. Advances in Experimental Medicine and Biology. New York: Kluwer Academic/Plenum Publishers; 2004. p. 76-91.

96. Zhang J, Campbell RE, Ting AY, Tsien RY. Creating new fluorescent probes for cell biology. Nat Rev Mol Cell Biol 2002;3(12):906-918.

97. Geiser M, Cebe R, Drewello D, Schmitz R. Integration of PCR fragments at any specific site within cloning vectors without the use of restriction enzymes and DNA ligase. Biotechniques 2001;31(1):88-90, 92.

98. Lu Y, Grady S, Marks MJ, Picciotto M, Changeux J-P, Collins AC. Pharmacological Characterization of Nicotinic Receptor-stimulated GABA Release From Mouse Brain Synaptosomes. J Pharmacol Exp Ther 1998;287(2):648-657.

99. Leach RN, Desai JC, Orchard CH. Effect of cytoskeleton disruptors on L-type Ca channel distribution in rat ventricular myocytes. Cell Calcium 2005;38(5):515-526.

100. Vasquez RJ, Howell B, Yvon AM, Wadsworth P, Cassimeris L. Nanomolar concentrations of nocodazole alter microtubule dynamic instability in vivo and in vitro. Mol Biol Cell 1997;8(6):973-985.

101. Drenan RM, Nashmi R, Imoukhuede PI, Just H, McKinney S, Lester HA. Subcellular Trafficking, Pentameric Assembly and Subunit Stoichiometry of Neuronal Nicotinic ACh Receptors Containing Fluorescently-Labeled a6 and b3 Subunits. Mol Pharmacol 2007:mol.107.039180.

102. Nashmi R, Dickinson ME, McKinney S, Jareb M, Labarca C, Fraser SE, Lester HA. Assembly of a4b2 Nicotinic Acetylcholine Receptors Assessed with Functional Fluorescently Labeled Subunits: Effects of Localization, Trafficking, and Nicotine-Induced Upregulation in Clonal Mammalian Cells and in Cultured Midbrain Neurons. J Neurosci 2003;23(37):11554-11567.

103. Ishiki M, Klip A. Minireview: Recent Developments in the Regulation of Glucose Transporter-4 Traffic: New Signals, Locations, and Partners. Endocrinology 2005;146(12):5071-5078.

104. Bernstein EM, Quick MW. Regulation of gamma -Aminobutyric Acid (GABA) Transporters by Extracellular GABA. J Biol Chem 1999;274(2):889-895.

105. Drenan RM, Nashmi R, Imoukhuede P, Just H, McKinney S, Lester HA. Subcellular Trafficking, Pentameric Assembly, and Subunit Stoichiometry of Neuronal Nicotinic Acetylcholine Receptors Containing Fluorescently Labeled {alpha}6 and 3 Subunits. Mol Pharmacol 2008;73(1):27-41.

106. Unger M, Kartalov E, Chiu CS, Lester HA, Quake SR. Single-molecule fluorescence observed with mercury lamp illumination. Biotechniques 1999;27(5):1008-1014.

107. Chiu C-S, Kartalov E, Unger M, Quake S, Lester HA. Single-molecule measurements calibrate green fluorescent protein surface densities on transparent beads

for use with `knock-in' animals and other expression systems. Journal of Neuroscience Methods 2001;105(1):55-63.

108. Braun D, Fromherz P. Fluorescence Interferometry of Neuronal Cell Adhesion on Microstructured Silicon. Physical Review Letters 1998;81(23):5241.

109. Berg JM, Tymoczko JL, Stryer L. Biochemistry. fourth ed. New York: W. H. Freeman and Company; 2002.

110. Axelrod D, Davidson MW. Total Internal Reflection Fluorescence Microscopy Introduction and Theoretical Aspects. Olympus Microscopy Rescource Center: Olympus America, Inc.; 2008.

111. Bertorello AM, Komarova Y, Smith K, Leibiger IB, Efendiev R, Pedemonte CH, Borisy G, Sznajder JI. Analysis of Na+,K+-ATPase Motion and Incorporation into the Plasma Membrane in Response to G Protein-coupled Receptor Signals in Living Cells. Mol Biol Cell 2003;14(3):1149-1157.

112. Wang X, Teng Y, Wang Q, Li X, Sheng X, Zheng M, Samaj J, Baluska F, Lin J. Imaging of Dynamic Secretory Vesicles in Living Pollen Tubes of Picea meyeri Using Evanescent Wave Microscopy. Plant Physiol 2006;141(4):1591-1603.

113. Oheim M, Stühmer W. Tracking chromaffin granules on their way through the actin cortex. European Biophysics Journal 2000;29(2):67-89.

114. Kolinski A, Skolnick J, Yaris R. On the short time dynamics of dense polymeric systems and the origin of the glass transition: A model system. The Journal of Chemical Physics 1986;84:1922.

115. Qian H, Sheetz MP, Elson EL. Single particle tracking. Analysis of diffusion and flow in two-dimensional systems. Biophys J 1991;60(4):910-921.

116. Li CH, Bai L, Li DD, Xia S, Xu T. Dynamic tracking and mobility analysis of single GLUT4 storage vesicle in live 3T3-L1 cells. Cell Res 2004;14(6):480-486.

117. Bezzerides VJ, Ramsey IS, Kotecha S, Greka A, Clapham DE. Rapid vesicular translocation and insertion of TRP channels. Nat Cell Biol 2004;6(8):709-720.

118. Steyer JA, Almers W. Tracking Single Secretory Granules in Live Chromaffin Cells by Evanescent-Field Fluorescence Microscopy. Biophys J 1999;76(4):2262-2271.

119. Lemke EA, Klingauf J. Single Synaptic Vesicle Tracking in Individual Hippocampal Boutons at Rest and during Synaptic Activity. J Neurosci 2005;25(47):11034-11044.

120. Ryan TA. Inhibitors of Myosin Light Chain Kinase Block Synaptic Vesicle Pool Mobilization during Action Potential Firing. J Neurosci 1999;19(4):1317-1323.

121. Jordan R, Lemke EA, Klingauf J. Visualization of Synaptic Vesicle Movement in Intact Synaptic Boutons Using Fluorescence Fluctuation Spectroscopy. Biophys J 2005;89(3):2091-2102.

122. Becker C, Sevilla L, Tomas E, Palacin M, Zorzano A, Fischer Y. The Endosomal Compartment Is an Insulin-Sensitive Recruitment Site for GLUT4 and GLUT1 Glucose Transporters in Cardiac Myocytes. Endocrinology 2001;142(12):5267-5276.

123. Wang D, Quick MW. Trafficking of the Plasma Membrane {gamma}-Aminobutyric Acid Transporter GAT1: SIZE AND RATES OF AN ACUTELY RECYCLING POOL. J Biol Chem 2005;280(19):18703-18709.

124. Kuromi H, Kidokoro Y. Exocytosis and Endocytosis of Synaptic Vesicles and Functional Roles of Vesicle Pools: Lessons from the Drosophila Neuromuscular Junction. Neuroscientist 2005;11(2):138-147.

125. Kavanaugh MP, Arriza JL, North RA, Amara SG. Electrogenic uptake of gamma-aminobutyric acid by a cloned transporter expressed in Xenopus oocytes. J Biol Chem 1992;267(31):22007-22009.

126. Mager S, Naeve J, Quick M, Labarca C, Davidson N, Lester HA. Steady states, charge movements, and rates for a cloned GABA transporter expressed in Xenopus oocytes. Neuron 1993;10(2):177-188.

127. Lester HA, Cao Y, Mager S. Listening to neurotransmitter transporters. Neuron 1996;17(5):807-810.

128. Braestrup C, Nielsen EB, Sonnewald U, Knutsen LJ, Andersen KE, Jansen JA, Frederiksen K, Andersen PH, Mortensen A, Suzdak PD. (R)-N-[4,4-bis(3-methyl-2-thienyl)but-3-en-1-yl]nipecotic acid binds with high affinity to the brain gamma-aminobutyric acid uptake carrier. J Neurochem 1990;54(2):639-647.

129. Hog S, Greenwood JR, Madsen KB, Larsson OM, Frolund B, Schousboe A, Krogsgaard-Larsen P, Clausen RP. Structure-activity relationships of selective GABA uptake inhibitors. Curr Top Med Chem 2006;6(17):1861-1882.

130. Adkins JC, Noble S. Tiagabine. A review of its pharmacodynamic and pharmacokinetic properties and therapeutic potential in the management of epilepsy. Drugs 1998;55(3):437-460.

131. Kalviainen R. Long-term safety of tiagabine. Epilepsia 2001;42 Suppl 3:46-48.

132. Whitworth TL, Quick MW. Substrate-induced regulation of gamma-aminobutyric acid transporter trafficking requires tyrosine phosphorylation. J Biol Chem 2001;276(46):42932-42937.

133. Zahniser NR, Doolen S. Chronic and acute regulation of Na+/Cl- -dependent neurotransmitter transporters: drugs, substrates, presynaptic receptors, and signaling systems. Pharmacol Ther 2001;92(1):21-55.

134. Loder MK, Melikian HE. The dopamine transporter constitutively internalizes and recycles in a protein kinase C-regulated manner in stably transfected PC12 cell lines. J Biol Chem 2003;278(24):22168-22174.

135. Holton KL, Loder MK, Melikian HE. Nonclassical, distinct endocytic signals dictate constitutive and PKC-regulated neurotransmitter transporter internalization. Nat Neurosci 2005;8(7):881-888.

136. Wang D, Quick MW. Trafficking of the plasma membrane gamma-aminobutyric acid transporter GAT1. Size and rates of an acutely recycling pool. J Biol Chem 2005;280(19):18703-18709.

137. McHugh EM, Zhu W, Milgram S, Mager S. The GABA transporter GAT1 and the MAGUK protein Pals1: interaction, uptake modulation, and coexpression in the brain. Mol Cell Neurosci 2004;26(3):406-417.

138. Deken SL, Wang D, Quick MW. Plasma membrane GABA transporters reside on distinct vesicles and undergo rapid regulated recycling. J Neurosci 2003;23(5):1563-1568.

139. Scholze P, Freissmuth M, Sitte HH. Mutations within an intramembrane leucine heptad repeat disrupt oligomer formation of the rat GABA transporter 1. J Biol Chem 2002;277(46):43682-43690.

140. Farhan H, Freissmuth M, Sitte HH. Oligomerization of neurotransmitter transporters: a ticket from the endoplasmic reticulum to the plasma membrane. Handb Exp Pharmacol 2006(175):233-249.

141. Yamashita A, Singh SK, Kawate T, Jin Y, Gouaux E. Crystal structure of a bacterial homologue of Na+/Cl--dependent neurotransmitter transporters. Nature 2005;437(7056):215-223.

142. Hastrup H, Sen N, Javitch JA. The human dopamine transporter forms a tetramer in the plasma membrane: cross-linking of a cysteine in the fourth transmembrane segment is sensitive to cocaine analogs. J Biol Chem 2003;278(46):45045-45048.

143. Just H, Sitte HH, Schmid JA, Freissmuth M, Kudlacek O. Identification of an additional interaction domain in transmembrane domains 11 and 12 that supports oligomer formation in the human serotonin transporter. J Biol Chem 2004;279(8):6650-6657.

144. Farhan H, Korkhov VM, Paulitschke V, Dorostkar MM, Scholze P, Kudlacek O, Freissmuth M, Sitte HH. Two discontinuous segments in the carboxyl terminus are required for membrane targeting of the rat gamma-aminobutyric acid transporter-1 (GAT1). J Biol Chem 2004;279(27):28553-28563.

145. Torres GE, Carneiro A, Seamans K, Fiorentini C, Sweeney A, Yao WD, Caron MG. Oligomerization and trafficking of the human dopamine transporter. Mutational analysis identifies critical domains important for the functional expression of the transporter. J Biol Chem 2003;278(4):2731-2739.

146. Ramamoorthy S, Giovanetti E, Qian Y, Blakely RD. Phosphorylation and regulation of antidepressant-sensitive serotonin transporters. J Biol Chem 1998;273(4):2458-2466.

147. Dickinson ME, Bearman G, Tille S, Lansford R, Fraser SE. Multi-spectral imaging and linear unmixing add a whole new dimension to laser scanning fluorescence microscopy. Biotechniques 2001;31(6):1272, 1274-1276, 1278.

148. Lansford R, Bearman G, Fraser SE. Resolution of multiple green fluorescent protein color variants and dyes using two-photon microscopy and imaging spectroscopy. J Biomed Opt 2001;6(3):311-318.

149. Abramoff MD, Magelhaes PJ, Ram SJ. Image Processing with ImageJ. Biophotonics International 2004;11(7):36-42.

150. Nashmi R, Dickinson ME, McKinney S, Jareb M, Labarca C, Fraser SE, Lester HA. Assembly of alpha4beta2 nicotinic acetylcholine receptors assessed with functional fluorescently labeled subunits: effects of localization, trafficking, and nicotine-induced upregulation in clonal mammalian cells and in cultured midbrain neurons. J Neurosci 2003;23(37):11554-11567.

151. Lakowicz JR. Principles of fluorescence spectroscopy. 3rd ed. New York: Springer; 2006.

152. Meer BWvd, Coker G, Chen SYS. Resonance energy transfer : theory and data. New York: VCH; 1994.

153. Hung AY, Sheng M. PDZ domains: structural modules for protein complex assembly. J Biol Chem 2002;277(8):5699-5702.

154. Sheng M, Sala C. PDZ domains and the organization of supramolecular complexes. Annu Rev Neurosci 2001;24:1-29.

155. Lin D, Gish GD, Songyang Z, Pawson T. The carboxyl terminus of B class ephrins constitutes a PDZ domain binding motif. J Biol Chem 1999;274(6):3726-3733.

156. Bruckner K, Pablo Labrador J, Scheiffele P, Herb A, Seeburg PH, Klein R. EphrinB ligands recruit GRIP family PDZ adaptor proteins into raft membrane microdomains. Neuron 1999;22(3):511-524.

157. Torres R, Firestein BL, Dong H, Staudinger J, Olson EN, Huganir RL, Bredt DS, Gale NW, Yancopoulos GD. PDZ proteins bind, cluster, and synaptically colocalize with Eph receptors and their ephrin ligands. Neuron 1998;21(6):1453-1463.

158. Madsen KL, Beuming T, Niv MY, Chang CW, Dev KK, Weinstein H, Gether U. Molecular determinants for the complex binding specificity of the PDZ domain in PICK1. J Biol Chem 2005;280(21):20539-20548.

159. Patterson GH, Piston DW, Barisas BG. Forster distances between green fluorescent protein pairs. Anal Biochem 2000;284(2):438-440.

160. Beckman ML, Bernstein EM, Quick MW. Multiple G protein-coupled receptors initiate protein kinase C redistribution of GABA transporters in hippocampal neurons. J Neurosci 1999;19(11):RC9.

161. Horton N, Quick MW. Syntaxin 1A up-regulates GABA transporter expression by subcellular redistribution. Mol Membr Biol 2001;18(1):39-44.

162. Fan HP, Fan FJ, Bao L, Pei G. SNAP-25/syntaxin 1A complex functionally modulates neurotransmitter gamma-aminobutyric acid reuptake. J Biol Chem 2006;281(38):28174-28184.

163. Farhan H, Reiterer V, Korkhov VM, Schmid JA, Freissmuth M, Sitte HH. Concentrative Export from the Endoplasmic Reticulum of the {gamma}-Aminobutyric Acid Transporter 1 Requires Binding to SEC24D. J Biol Chem 2007;282(10):7679-7689.

164. Korkhov VM, Farhan H, Freissmuth M, Sitte HH. Oligomerization of the {gamma}-aminobutyric acid transporter-1 is driven by an interplay of polar and hydrophobic interactions in transmembrane helix II. J Biol Chem 2004;279(53):55728-55736.

165. Mazei-Robison MS, Blakely RD. Expression studies of naturally occurring human dopamine transporter variants identifies a novel state of transporter inactivation associated with Val382Ala. Neuropharmacology 2005;49(6):737-749.

166. Melikian HE, Buckley KM. Membrane trafficking regulates the activity of the human dopamine transporter. J Neurosci 1999;19(18):7699-7710.

167. Schmid JA, Scholze P, Kudlacek O, Freissmuth M, Singer EA, Sitte HH. Oligomerization of the human serotonin transporter and of the rat GABA transporter 1 visualized by fluorescence resonance energy transfer microscopy in living cells. J Biol Chem 2001;276(6):3805-3810.

168. Bjerggaard C, Fog JU, Hastrup H, Madsen K, Loland CJ, Javitch JA, Gether U. Surface targeting of the dopamine transporter involves discrete epitopes in the distal C terminus but does not require canonical PDZ domain interactions. J Neurosci 2004;24(31):7024-7036.

169. Bauman PA, Blakely RD. Determinants within the C-terminus of the human norepinephrine transporter dictate transporter trafficking, stability, and activity. Arch Biochem Biophys 2002;404(1):80-91.

170. Lester HA. Heterologous expression of excitability proteins: route to more specific drugs? Science 1988;241(4869):1057-1063.

171. Harris BZ, Lim WA. Mechanism and role of PDZ domains in signaling complex assembly. J Cell Sci 2001;114(Pt 18):3219-3231.

172. Guastella J, Nelson N, Nelson H, Czyzyk L, Keynan S, Miedel MC, Davidson N, Lester HA, Kanner BI. Cloning and expression of a rat brain GABA transporter. Science 1990;249(4974):1303-1306.

173. Ormo M, Cubitt AB, Kallio K, Gross LA, Tsien RY, Remington SJ. Crystal structure of the Aequorea victoria green fluorescent protein. Science 1996;273(5280):1392-1395.

174. Inoue S, Shimomura O, Goda M, Shribak M, Tran PT. Fluorescence polarization of green fluorescence protein. Proc Natl Acad Sci U S A 2002;99(7):4272-4277.

175. Scholze P, Norregaard L, Singer EA, Freissmuth M, Gether U, Sitte HH. The role of zinc ions in reverse transport mediated by monoamine transporters. J Biol Chem 2002;277(24):21505-21513.

176. Hastrup H, Karlin A, Javitch JA. Symmetrical dimer of the human dopamine transporter revealed by cross-linking Cys-306 at the extracellular end of the sixth transmembrane segment. Proc Natl Acad Sci U S A 2001;98(18):10055-10060.

177. Hahn MK, Robertson D, Blakely RD. A mutation in the human norepinephrine transporter gene (SLC6A2) associated with orthostatic intolerance disrupts surface expression of mutant and wild-type transporters. J Neurosci 2003;23(11):4470-4478.

Footnotes

This research is supported by grants from the NIH (DA-09121; DA-10509) and by an American Heart Association Postdoctoral Fellowship to Fraser Moss. We thank Jo Ann Trinkle and Amber Southwell for technical assistance and Dr. Raad Nashmi for his comments on the manuscript.

Figure Legends

Figure 1. Establishing a non-saturated [^{3}H]GABA uptake assay in an appropriate cell type. 50, 100, 250, or 500 ng of wild-type mGAT1 plasmid or an equimolar equivalent of mGAT1GFP and pcDNA3.1(+) plasmids were transfected/well. 20-min uptakes were performed on transfected N2a cells in 2.5 μM (A) or 80 μM (B) $[\text{GABA}]_O$. (C) The same transfections were performed in HEK 293T cells, and 20- min uptakes were performed in 2.5 μM extracellular $[\text{GABA}]_O$. Each point represents the mean of 6 transfections ± S.E.M. Time course experiments were performed in 2.5 μM (D) or 80 μM (E) $[\text{GABA}]_O$ on N2a cells transfected with 100 ng/well wild-type mGAT1 plasmid or an equimolar equivalent of the pcDNA3.1(+) plasmid. Each data point represents the mean of 6 transfections ± S.E.M.

Figure 2. Functional characterization of fluorescent mGAT1 constructs. (A) Representative fluorescence microscopy images of live cells expressing each of the fluorescent constructs 48 h after transfection using the non-saturating parameters described in the experimental procedures. Scale bar = 10 μm. Beside the image of each construct's expression in N2a cells, a cartoon schematic describes the location of the fluorophore in the mGAT1 protein sequence. A key to the color code used in these cartoons is located at the top of the panel. (B) 20-min [^{3}H]GABA uptake from N2a cells transfected with 100 ng/well of mGAT1 wild-type plasmid or an equimolar equivalent of the fluorescently tagged mGAT1 plasmids or blank pcDNA3.1(+) vector. Results represent the mean ± S. E. M of between 6 and 18 transfections for each construct. * denotes significant difference compared to wild-type, $P \leq 0.05$ (one-way analysis of variance (ANOVA) with Tukey's post hoc test). (C) Surface biotinylation experiments

comparing the plasma membrane partitioning of mGAT1XFP constructs that had displayed wild-type like [^{3}H]GABA uptake and one which presented an uptake deficit. Representative bands of the biotinylated mGAT1 surface fractions are displayed above the graph. Bands were arranged in the image to correspond to the appropriate column in the graph. Results represent the mean ± S. E. M of between 5 and 8 transfections for each construct. * denotes significant difference compared to wild-type, $P \leq 0.05$ (one-way ANOVA with Tukey's post hoc test). (D) We examined the concentration dependence relationship of six selected clones whose uptake was closest to wild-type in panel B. Panels from left to right present three experiments in which the constructs were tested in pairs vs. wild-type mGAT1 (100 ng cDNA transfected per 12-well-plate well). The non-specific uptake was determined from wells transfected with empty pcDNA3.1(+) vector, and subtracted from the test samples, but is displayed for reference in each plot. No significant difference was found between any of the fluorescent clones and wild-type mGAT1 for all concentrations as determined by one-way ANOVA with Tukey's post hoc test, $P \leq 0.05$. Data represents the mean uptake for each concentration ± S. E. M for between 6 and 9 transfections.

Figure 3. Förster resonance energy transfer between wild-type like fluorescent mGAT1 proteins. Plots of acceptor photobleach and donor photorecovery for mGAT1CFP*/mGAT1YFP* (A; n=10) or mGAT1CFP8/mGAT1YFP8 (B; n=7) co-expressed in N2a cells. (C) A scatter plot of CFP photorecovery versus YFP photobleach for the FRET pairs in panels A and B. FRET efficiency for each transfection was calculated by extrapolating to the *y*-axis intercept, the value for which was entered into Equation 1.

Figure 4. Oligomerization state of mGAT1XFP constructs with functional deficits. Plots of acceptor photobleach and donor photorecovery for mGAT1CFP45/mGAT1YFP45 (A; n = 12) and mGAT1CFP8/mGAT1YFP45 co-transfections in N2a cells (B; n = 12). (C) Representative image of N2a cells co-expressing mGAT1CFP8 and mGAT1YFP45. Scale bar = 10 μM. (D) $[^3H]$GABA uptake assay from N2a cells in 12-well plates expressing 50 ng of mGAT1CFP8 together with increasing co-transfection amounts of mGAT1CFP8, mGAT1YFP8, or mGAT1YFP45. Results for 12.5, 25, 50 ng mGAT1YFP8 and mGAT1YFP45 transfected alone are included for reference. Each data point is the mean ± the S.E.M of at least 6 separate transfections. Significant differences for the mGAT1YFP8/mGAT1CFP8 co-transfections or the mGAT1CFP8/mGAT1CFP8 co-transfections compared to 50 ng mGAT1CFP8 alone are denoted by * and #, respectively, $P \leq 0.05$ (One-way ANOVA with Tukey's post hoc test). (E) Mean acceptor photobleach and donor photorecovery for mGAT1CFPCT/mGAT1YFPCT transfected N2a cells (n = 5). (F) A scatter plot of mean mGAT1CFPCT photorecovery versus mGAT1YFPCT photobleach.

Figure 5. Association of fluorescent mGAT1 constructs with syntaxin 1A. Plots of mean acceptor photobleach and donor photorecovery for mGAT1CFP8/YFP-synatxin 1A (A; n = 5) and CFP15mGAT1/ YFP-synatxin 1A co-transfections in N2a cells (B; n = 8). (C) A scatter plot of CFP photorecovery versus YFP photobleach for the FRET pairs in panels A and B. (D) Mean acceptor photobleach and donor photorecovery for the CFP15mGAT1/YFP15mGAT1 co-transfection in N2a cells (n = 5).

Table

Table 1. Cell density, transfection reagent and cDNA quantities required for non-saturated transient mGAT1 expression in N2a cells

Dish/plate	Area (cm^2)	Cells per well	cDNA (ng)	PLUS reagent (µl)	Final Diluted Volume in Serum Free DMEM (µl)	Lipofectamine Reagent (µl)	Volume Media on Cells (DMEM)	Final Transfection Volume (ml)
Protocol Steps		1	2	3	2 & 3	4	5	6
96 well	0.50	1.75×10^4	12.5	1	10	0.5	0.05	0.07
48 well	0.95	3.50×10^4	25	2	17.5	0.75	0.1	0.125
24 well	1.9	7.00×10^4	50	4	25	1	0.2	0.25
12 well	3.8	1.37×10^5	100	5	50	2	0.4	0.50
6 well /35 mm	9.6	3.50×10^5	250	6	100	4	0.8	1.0
60 mm	28.3	1.03×10^6	750	8	250	12	2	2.5
100 mm	78.6	2.86×10^6	2000	20	750	30	5	6.5

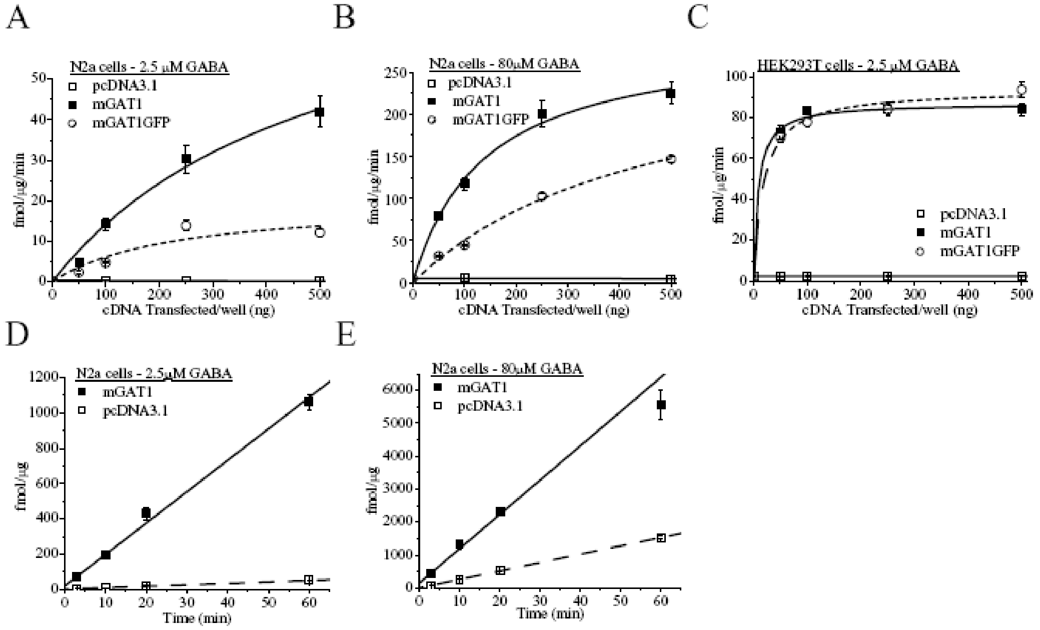
A
N2a cells - 2.5 μM GABA
pcDNA3.1
mGAT1
mGAT1GFP
fmol/μg/min
cDNA Transfected/well (ng)
0
10
20
30
40
50
100
200
300
400
500
B
N2a cells - 80μM GABA
pcDNA3.1
mGAT1
mGAT1GFP
fmol/μg/min
cDNA Transfected/well (ng)
0
50
100
150
200
250
300
400
500
C
HEK293T cells - 2.5 μM GABA
pcDNA3.1
mGAT1
mGAT1GFP
fmol/μg/min
cDNA Transfected/well (ng)
0
20
40
60
80
100
200
300
400
500
D
N2a cells - 2.5μM GABA
mGAT1
pcDNA3.1
fmol/μg
Time (min)
0
200
400
600
800
1000
1200
10
20
30
40
50
60
E
N2a cells - 80μM GABA
mGAT1
pcDNA3.1
fmol/μg
Time (min)
0
1000
2000
3000
4000
5000
6000
10
20
30
40
50
60

Figure 1

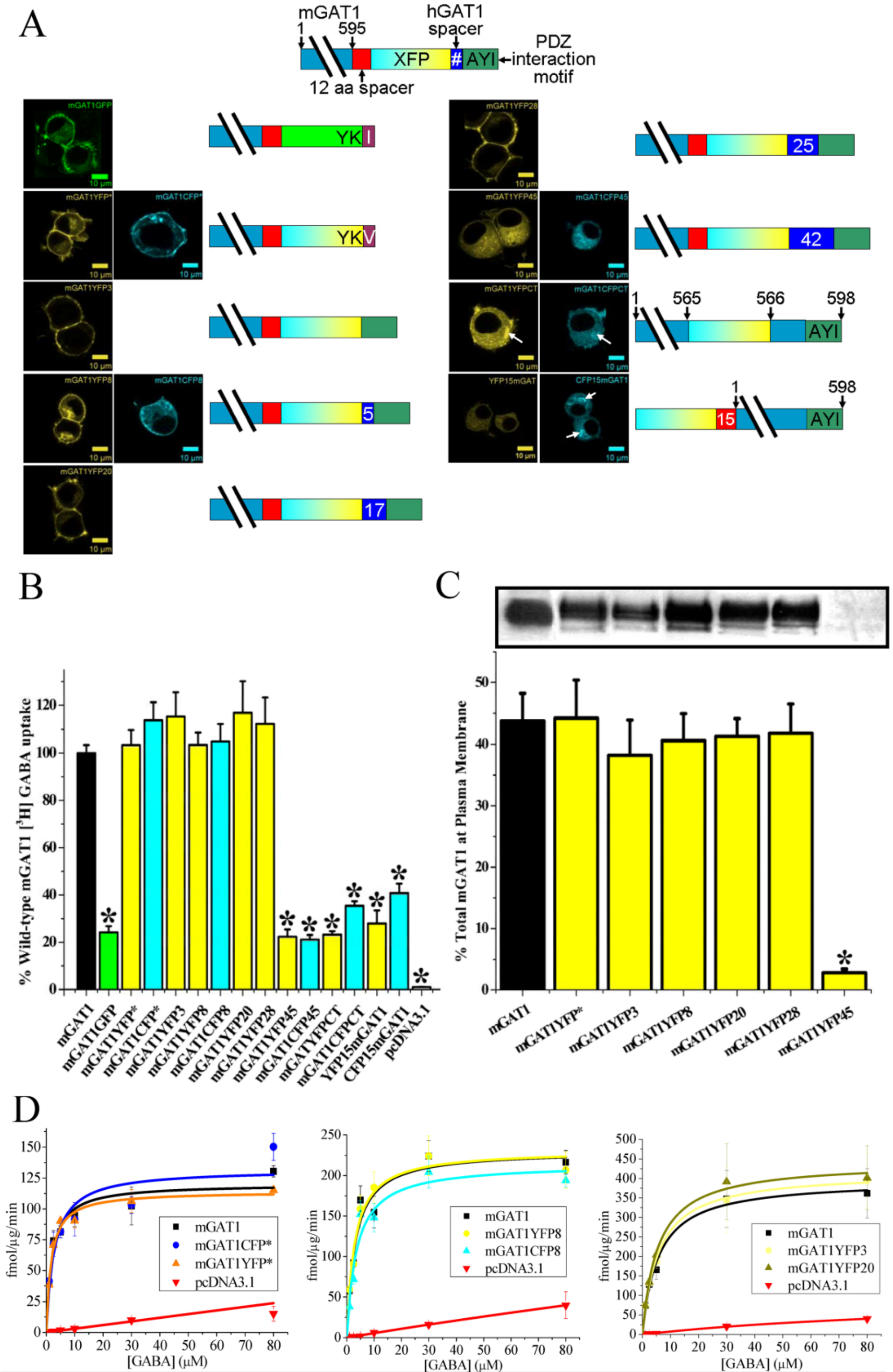

Construct	K_m (µM)	V_{max} (fmol/µg/min)
mGAT1	2.04 ± 0.28	130.85 ± 4.12
mGAT1YFP*	1.64 ± 0.21	125.44 ± 3.32
mGAT1CFP*	2.51 ± 0.60	138.55 ± 8.01

Construct	K_m (µM)	V_{max} (fmol/µg/min)
mGAT1	3.03 ± 0.77	231.03 ± 14.88
mGAT1YFP8	2.87 ± 0.56	231.41 ± 11.15
mGAT1CFP8	3.60 ± 0.96	214.73 ± 15.10

Construct	K_m (µM)	V_{max} (fmol/µg/min)
mGAT1	5.71 ± 0.81	396.23 ± 15.49
mGAT1YFP3	5.73 ± 0.42	417.55 ± 8.48
mGAT1YFP20	5.54 ± 0.55	442.97 ± 12.00

Figure 2

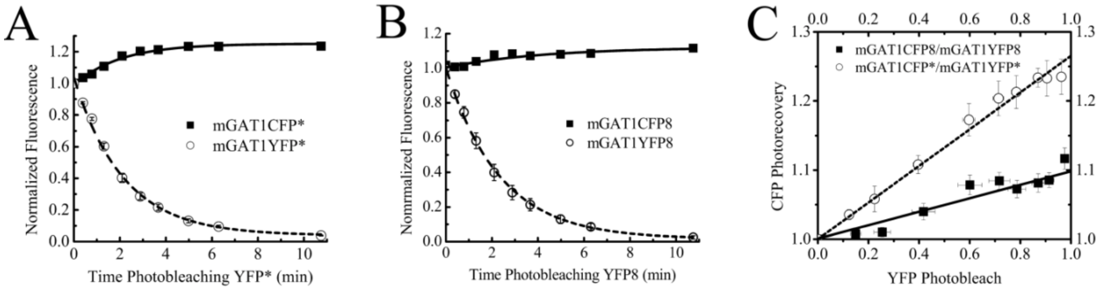
A
1.2
1.0
0.8
0.6
0.4
0.2
0.0
Normalized Fluorescence
0
2
4
6
8
10
Time Photobleaching YFP* (min)
mGAT1CFP*
mGAT1YFP*
B
1.2
1.0
0.8
0.6
0.4
0.2
0.0
Nonrmalized Fluorescence
0
2
4
6
8
10
Time Photobleaching YFP8 (min)
mGAT1CFP8
mGAT1YFP8
C
0.0
0.2
0.4
0.6
0.8
1.0
1.3
1.2
1.1
1.0
CFP Photorecovery
mGAT1CFP8/mGAT1YFP8
mGAT1CFP*/mGAT1YFP*
YFP Photobleach
CFP Photorecovery

Figure 3

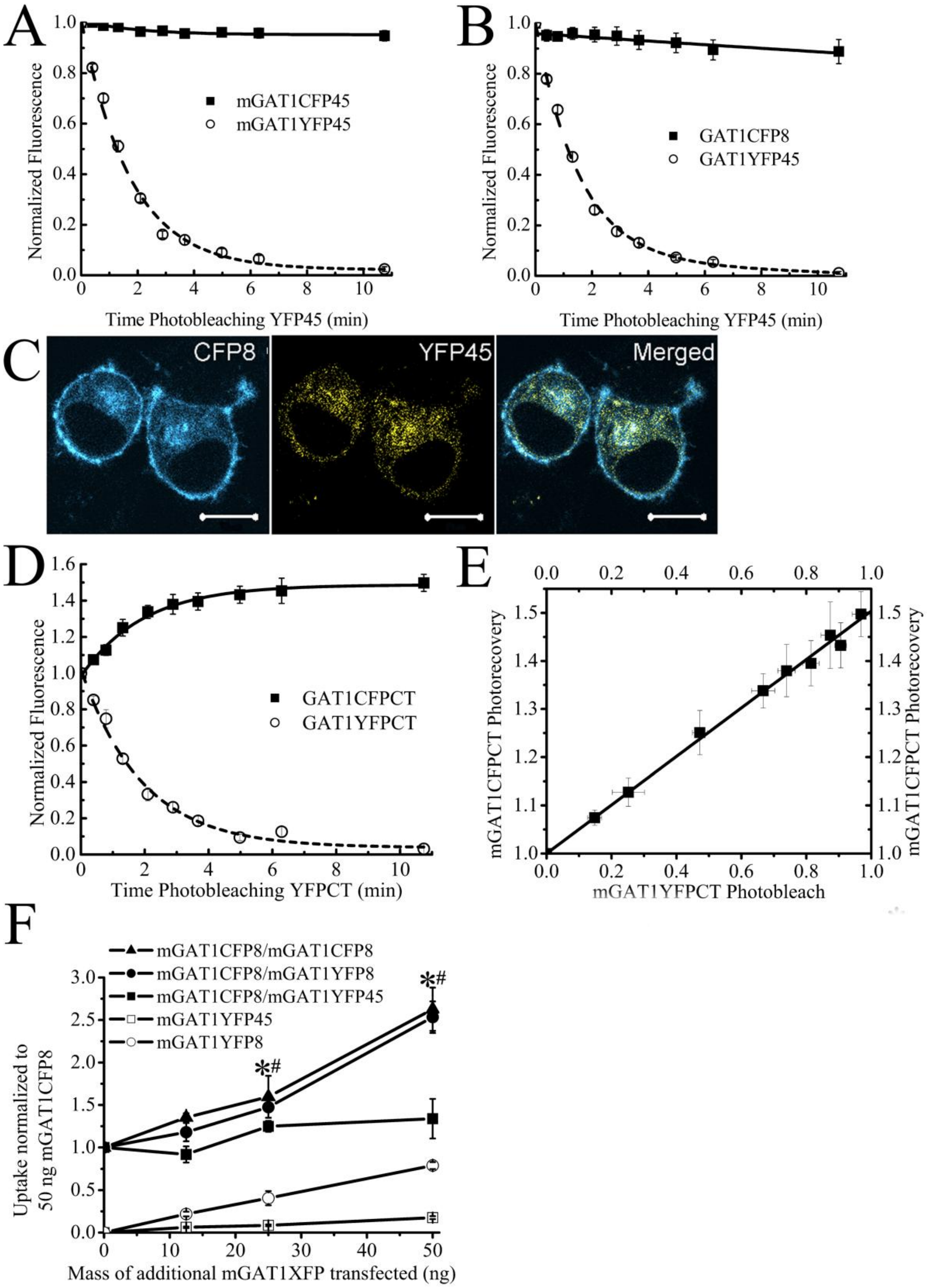
A
Normalized Fluorescence
mGAT1CFP45
mGAT1YFP45
Time Photobleaching YFP45 (min)
B
Normalized Fluorescence
GAT1CFP8
GAT1YFP45
Time Photobleaching YFP45 (min)
C
CFP8
YFP45
Merged
D
Normalized Fluorescence
GAT1CFPCT
GAT1YFPCT
Time Photobleaching YFPCT (min)
E
mGAT1CFPCT Photorecovery
mGAT1YFPCT Photobleach
F
mGAT1CFP8/mGAT1CFP8
mGAT1CFP8/mGAT1YFP8
mGAT1CFP8/mGAT1YFP45
mGAT1YFP45
mGAT1YFP8
Uptake normalized to 50 ng mGAT1CFP8
Mass of additional mGAT1XFP transfected (ng)
*#
*#

Figure 4

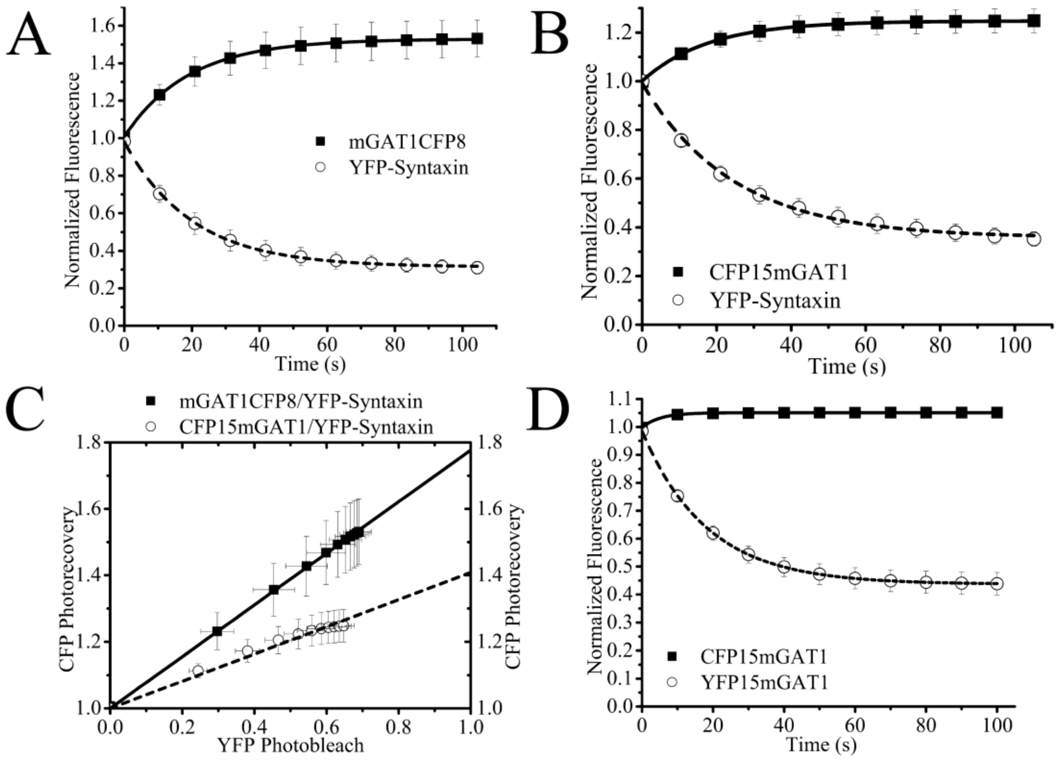
A
Normalized Fluorescence
Time (s)
mGAT1CFP8
YFP-Syntaxin
B
Normalized Fluorescence
Time (s)
CFP15mGAT1
YFP-Syntaxin
C
mGAT1CFP8/YFP-Syntaxin
CFP15mGAT1/YFP-Syntaxin
CFP Photorecovery
YFP Photobleach
D
Normalized Fluorescence
Time (s)
CFP15mGAT1
YFP15mGAT1

Figure 5

Appendix I: GABA transporters: Structure, oligomerization, trafficking, and pharmacology determine neuronal excitability

This appendix reviews the structure, oligomerization, trafficking and pharmacology of GABA transporter. I describe the physiological and pathological roles of the GABA transporters, physiological consequences of GABA transporter malfunction, and neurotransmitter reuptake mechanisms. Fraser Moss and Herwig Just describe the following: class, subtypes, structure, function, and regulation of GABA transporters.

GABA Transporters: Structure, Oligomerization, Trafficking, and Pharmacology Determine Neuronal Excitability.

Fraser J. Moss[1], P. I. Imoukhuede [1,2], Herwig Just[1] and Henry A. Lester[1]

Division of Biology[1] and Bioengineering Program[2], California Institute of Technology, Pasadena, California 91125, USA

Keywords: GABA, Transporter, Structure, Trafficking, Oligomerization, PDZ-interacting motif, Antiepileptic

Acknowledgements: Preparation of this review was supported by a grant from the N. I. H. (DA-09121), an American Heart Association fellowship for F. J. M. and from a Schrödinger fellowship (J2486) from the Austrian Science Fund (F. W. F.) for H. J.

Synopsis

γ-aminobutyric acid (GABA) is the principal inhibitory neurotransmitter in the vertebrate central nervous system. Activation of ionotropic and metabotropic GABA receptors by GABA reduces the excitability of the cell, inhibiting neuronal firing. Plasma membrane GABA transporters maintain the extracellular GABA concentration in the vicinity of the synapse and consequently control the activity of the GABA receptors. Synaptic transporters play an important role in terminating neurotransmission while extrasynaptic transporters control GABAergic tone. Here we review how the structure, assembly, trafficking, and pharmacology of the four known GABA transporter isoforms modulates extracellular [GABA] and determines neuronal excitability.

Physiological Roles of the GABA transporters

The canonical role of GABA transporters (GATs) is to remove GABA from the synapse following phasic neurotransmitter release, terminating GABAergic neurotransmission. GABAergic transmission is usually inhibitory, because $GABA_A$ and $GABA_B$ receptors activate Cl^- and K^+ channels, respectively (although some young neurons have a high intracellular Cl^- concentration, producing a depolarized Cl^- equilibrium potential and therefore leading to excitatory GABAergic postsynaptic events). Additionally, GATs perpetually maintain the ambient extracellular concentration ($[GABA]_o$) at a non-zero concentration which dictates the amplitude of tonic GABAergic currents via activation of extrasynaptic GABA receptors. Even after synaptic activity, $[GABA]_o$ is much less than the intracellular GABA concentration ($[GABA]_i$) in the presynaptic boutons and surrounding glia. To move the neurotransmitter against this concentration gradient, an electrogenic process co-transports GABA with Na^+ and Cl^- down the combined electrochemical gradient of the co-transported ions. GATs are therefore attractive targets in the treatment of epilepsy because inhibiting GABA uptake, through either pharmacological or genetic intervention, prolongs neurotransmitter lifetime and increases ambient $[GABA]_o$ to decrease excitability. Importantly, GATs are equally able to transport substrate in either the forward (into the cell) or reverse (out of the cell) direction. Reverse GABA transport is a physiological process that occurs under depolarizing conditions. Consequently, inhibitory interneuron activation can stimulate both quantal GABA release from synaptic vesicles and nonvesicular GABA release via reverse GABA transport. During periods of high-frequency stimulation, synaptic vesicle stores may become depleted but the transporter-mediated GABA release continues. Furthermore, surrounding astroglia can become depolarized and release GABA through reverse transport. Therefore, during a seizure, reverse transport could have an important neuroprotective function.

This chapter serves as a brief introduction to the several GAT isoforms expressed in the brain and how their differential tissue distribution, their structure, and their physiological and pharmacological modulation can control neuronal excitability.

Classification and Differential CNS Expression of GABA Transporters

The GATs are part of the neurotransmitter sodium symporter (NSS) transporter family which includes transporters for the neurotransmitters dopamine, serotonin (5HT), norepinephrine, and glycine. The NSS transporters are also known as the solute carrier 6 (SLC6) family of membrane proteins. Our laboratory helped to clone the first SLC6 transporter, rat GAT-1 (SLC6A1); 21 human SLC6 transporter genes were subsequently identified, including three other GABA transporters: GAT-2 (SLC6A13), GAT-3 (SLC6A11), and the betaine/GABA transporter, BGT-1 (SLC6A12). GAT-2, GAT-3, and BGT-1 respectively show 51%, 50%, and 48% amino acid identity with GAT-1, conservation occurring primarily in their predicted transmembrane spanning regions (Figure 1). The “GAT” nomenclature of the GABA transporters is not the same across species (Table 1). The SLC6 gene nomenclature offers a standardized taxonomy but because this thesis focuses on human epilepsy, we prefer to use the more descriptive human/rat classification of the transporter proteins.

Differential CNS Distribution of GAT Isoforms

Expression of GAT-1 and GAT-3 is restricted to the brain, whereas BGT-1 and GAT-2 are found in peripheral tissues and in the CNS. GAT-1 is the predominant GABA transporter in the CNS and is localized primarily on axons and presynaptic boutons of GABAergic inhibitory neurons, but is also expressed in astrocytes.

Our laboratory generated knock-in mice expressing GAT-1 transporters fused to green fluorescent protein (GFP). These mice allow direct visualization and quantification of GAT-1 expression *in situ*, strongly complementing earlier immunohistochemical and radiolabeling studies. The cerebellar pinceaux exhibit impressively high GAT-1 density, containing almost 8 million GAT-1 molecules per pinceau. The Bergman glia in the molecular layer and the axons and boutons of Golgi cells in the glomeruli of the granule cell layer account for the more diffuse GAT-1-GFP expression elsewhere in the cerebellum. In the hippocampus, GAT-1 is localized to the axons and synaptic boutons of basket and chandelier cells in strata oriens and pyramidale. A bouton in stratum oriens expresses 79% of the GAT-1 volume density observed in a cerebellar pinceau. The relative fluorescence intensity of GAT-1-GFP in the neuropil of hippocampal pyramidal and dentate gyrus cell layers is approximately 50% of that seen in cerebellar pinceaux but no clear axon or bouton labeling is observed due to high fluorescence in surrounding astrocytes. In human hippocampus, the termini of GAT-1-expressing axon terminals cluster with high density around the dentate gyrus granule cell somata. GAT-1 expresses at low levels in the cerebellar white matter, striatum, and most thalamic nuclei, the latter tissue restricting GAT-1 expression to the astrocytes. Higher expression occurs in the GABAergic thalamic reticular nucleus. In neocortex, GAT-1 immunostaining is associated exclusively with punctate structures resembling axon terminals around the perikarya, and especially in cartridges surrounding the proximal portions of the apical dendrites of pyramidal cells. Cartridges are comprised at least in part by the terminals of cortical chandelier and basket cells.

Weak GAT-2 expression is detected in neurons and astrocytes in the cerebral cortex, cerebellum, brainstem, and hippocampus. The greatest GAT-2 expression occurs in the leptomeninges, ependyma and choroid plexus. Similarly to GAT-1 and GAT-3, distal astrocytic processes express GAT-2. However, GAT-2 is uniquely expressed in astrocytic cell bodies and proximal processes. Neuronal GAT-2 expression occurs in axon terminals, mainly in deep layers of rat cerebral cortex, but in areas distant from the synaptic cleft. Weak GAT-2 expression is also detected in the cytoplasm of dendrites from rat cortical neurons. It is unclear if these transporters are ever present at the dendrite surface. Thus, the subcellular distribution of GAT-2 suggests that its primary function is modulating the ambient $[GABA]_o$ rather than terminating GABAergic neurotransmission.

The physiological role of GAT-3 is probably similar to GAT-2, as it is exclusively expressed in distal astrocytic processes. GAT-3 is present in the hindbrain, midbrain, olfactory bulb, subfornical organ, hypothalamus, thalamus, and brainstem. Within the basal ganglia, GAT-3 expression is high in globus pallidus, subthalamic nucleus, and substantia nigra but low in the caudate nucleus and putamen. In the neocortex, punctate GAT-3 labeling of distal astrocytic processes forms a continuous sheet around the somata of both pyramidal and nonpyramidal neurons in all layers.

BGT-1 was first identified in kidney, where it accumulates the osmolyte betaine in the hypertonic environment of the renal medulla. Nonetheless, it is also expressed in the CNS, although its distribution does not closely correlate with GABAergic pathways, despite having a higher substrate affinity for GABA than betaine. Astrocytic cultures from rat brain express BGT-1; while monkey BGT-1 expression has been reported in the somata and dendrites of excitatory pyramidal neurons in cerebral cortex and in the CA fields of the hippocampus.

Temporal lobe epilepsy (TLE) has strong ties to GABA transport; although GABAergic interneurons are preserved in sclerotic hippocampal tissue from TLE patients, there is a marked reduction in the typical punctate GAT-1 immunoreactivity around the cell bodies of pyramidal cells in the CA regions and granule cells of the dentate gyrus. This indicates reduced GABAergic innervation of these cell types, predisposing them to hyperexcitability. Furthermore, TLE is also characterized by a decrease in glutamate-induced GABA transport reversal; since seizures are marked by elevated glutamate concentrations, reduced GAT-1 reversal in these conditions would lessen the contribution of reverse GABA transport on seizure inhibition. These regional increases in excitability may be further compounded by general increases in extrasynaptic GAT-3, which could lead to excess GABA removal, thus reducing GABAergic tone and promoting hyperexcitablity.

Structure, Function and Regulation of GABA Transporters

Structure --- insights from recent crystal structure

When GAT-1 was first cloned in 1990, its primary sequence predicted that the transporter possessed 12 transmembrane (TM) spanning segments topologically oriented in the plasma membrane with the carboxy (C-) and amino (N-) termini residing in the cytoplasm. Functional characterization determined that GABA transport was dependent on the co-transport of two Na^+ ions and one Cl^-. In 2005, Eric Gouaux's laboratory reported the crystal structure of a functional leucine transporter, $LeuT_{Aa}$, a homologue of the mammalian NSS transporters (20--25% sequence identity) isolated from the bacteria *Aquifex aeolicus*. The LeuT$_{Aa}$ crystal structure provides a model on which all future structure/function research on NSS transporters can be based. Importantly, features were revealed that could not have been predicted from fifteen years of previous experimental data. TMs 1--5 and TMs 6--10 form a structural repeat arranged around a pseudo-two-fold axis in the plane of the membrane (Figures 2A and 2B). TM1 and TM6 run antiparallel to each other at the core of the protomer and the center of their helices unwind in the middle of the plasma membrane (Figure 2A). The exposed main-chain carbonyl oxygen and nitrogen atoms afford hydrogen bonding partners that form most of the contacts with the bound substrate (Figure 2C). The unwinding of TM1 and TM6 further stabilizes the substrate. The negative α-helical dipole moments of TM1a and TM6a are placed adjacent to the amino group of the leucine and the positive moment of TM1b is located next to its carboxy group. The two Na^+ ions co-transported with substrate stabilize the unwound helices at the transporter core for high-affinity substrate binding. Na1 makes direct contact with the carboxyl group of the substrate (Figures 2C and 3A) which, at limiting substrate concentrations could determine the apparent Na^+ affinity of substrate transport. Residues from TM3, TM7, and TM8 form the remainder of the dehydrated substrate/Na^+ binding core. The selectivity for Na^+ as the co-transporting ion arises simply because the pockets are too small to accommodate larger cations like K^+ (Figures 3A and 3B). LeuT$_{Aa}$ does not require Cl^- co-transport to function, but a Cl^- ion functions as the trigger of the conformational changes that allow substrate to permeate to the cytoplasm in mammalian NSS transporters. The Cl^- is proposed to bind within 5Å of Na1; the proximity allows the Cl^- to strongly couple with

Na1 and stabilize the substrate binding site. Cl^- is coordinated by the residues that align with GAT-1 Tyr86, Ser295, Asn327, and Ser331 (Figure 3C). One laboratory also reports the involvement of Gln291. Asn327 is conserved in almost all known NSS members. Ser331 is conserved in all mammalian Cl^--dependent NSS. Replacing Ser331 or Asn327 (or their aligning residues) in GAT-1, GAT-3, SERT, or DAT (the dopamine transporter), with a carboxylic residue makes substrate transport independent of Cl^-. Reciprocal mutations in the Cl^--independent $LeuT_{Aa}$ make leucine transport Cl^--dependent. Thus all NSS transporters require a negative charge (from co-transported Cl^- or an acidic side chain) to be supplied in this pocket during substrate transport.

In the general “alternating access transport” scheme, a transporter has a cavity that is alternately available for substrate/ion permeation from the extracellular or intracellular side of the membrane; and substrate and co-transported ions must all be bound together before translocation across the membrane occurs. Access to the cavity is controlled by intracellular and extracellular “gates” which open and close with conformational changes in the transporter. The $LeuT_{Aa}$ structure captures the protein in an intermediate substrate occluded state, in which both these gates are closed. The closed extracellular gate is formed by a water-mediated salt bridge between Arg30 and Asp404 and beneath that, the large hydrophobic side chains on Tyr108 and Phe253. The occluded structure and sulphydryl accessibility studies on mammalian NSS suggest that the extracellular gate opens via movements in TMs 1, 3, 6, and 10 moving Arg30 and Asp404 apart, coupled to a major rearrangement of extracellular loop 4 (ECL4) whose V-shaped tip forms a lid that dips into the extracellular cavity when the gate is closed. The closed cytoplasmic gate is more complicated, comprising 20 Å of packed protein between the substrate and the cytoplasmic face of the protein. Part of this is formed by the backbones of TM1a, TM6b, and TM8 below the substrate binding site, an Arg5-Asp369 charge pair, an Arg5-Ser267 H-bond, and an Arg5-Tyr268 cation-π interaction at the cytoplasmic face. Trp8 inserts between the backbones of TM1 and TM6b and anchors the N-terminus including Arg5. These residues are conserved throughout the NSS family, and mutation of the aligning amino acids in mammalian NSS transporters impairs transport.

Experiments on SERT have begun to define the pathway through which the substrate diffuses from the transporter core to the cytoplasm. When cysteine residues are substituted at positions that correspond to $\mathrm{LeuT_{Aa}}$ residues Gly190, Ile191, Phe194, Ile197, Ala198 and Thr201 in the cytoplasmic half of TM5, the cysteines become extremely reactive to sulphydryl reagents in the presence of 5HT. This indicates that these residues, which are buried in the $\mathrm{LeuT_{Aa}}$ occluded structure, become available in a substrate-bound state. They are protected from MTSEA reaction in the presence of cocaine, which traps the SERT in the extracellular-facing conformation.

Trafficking --- modulating transporter number at the plasma membrane

The number of GABA transporters at the plasma membrane shapes neurotransmission and controls excitability. Quantifying the fluorescence intensity in presynaptic boutons and axons in the cerebellum and hippocampus of GAT-1GFP knock-in mice determined that the membrane density of GAT-1 molecules ranges from 800--1300 per μm^2. Of this value, 61--63% of these molecules are inserted in the plasma membrane, and the reminder are just below the membrane in cytoplasmic vesicles (see below). However, the interplay of constitutive and functional regulatory elements controls the density of transporter at the cell surface at any given point in time.

Constitutive transporter trafficking

Several laboratories, including ourselves, have measured Förster resonance energy transfer (FRET) between transporters fused with the cyan and yellow fluorescent proteins (CFP and YFP respectively) to demonstrate the constitutive oligomerization of transporter protomers. Although single transporter protomers are transport competent, mutations that prevent oligomerization eliminate FRET; and the fluorescently tagged transporter proteins are retained in intracellular compartments. LeuT_{Aa} crystallized as a dimer, with TM9 and TM12 probably providing the assembly interface. However, this structure likely represents only a low-order oligomerization state for these transporters, as evidence exists for the further oligomerization of transporter dimers. FRET between YFP tagged Sec24D, a fluorescently tagged component of the COPII vesicle coat, and a CFP tagged GAT-1 demonstrates that after oligomerization, export from the endoplasmic reticulum (ER) occurs via COPII coated vesicles. Sec24D interacts with a conserved motif (R/L-I/L consensus sequence) in the C-terminal of all NSS transporters. Transporters lacking this proximal C-terminal motif are retained in the ER and exert a dominant negative effect when co-expressed with wild-type protein. Additionally, the ER retention of oligomerization deficient mutants in which the Sec24D interaction is preserved demonstrates that COPII vesicle coat interaction is necessary but not sufficient for ER export.

GAT-1 transporters are delivered to the plasma membrane on a population of vesicles ~ 50 nm in diameter that are distinct from neurotransmitter-containing vesicles. This probably allows regulated transporter expression independent of neurotransmitter release. These vesicles insert their cargo into the plasma membrane under control of the exocyst.

The three most C-terminal residues of GAT-1 conform to a consensus sequence for a type II PDZ-interacting motif (Figure 1, PDZ = **P**ostsynaptic density 95/**D**iscs large/**Z**ona occludens 1). This sequence mediates transporter interaction with the exocyst by association with PDZ-domain-containing proteins and stabilizes the transporter in this location once inserted. Importantly, NSS transporters are primarily located intracellularly unless they interact with a PDZ-domain containing protein at their distal C-terminus. For example, a truncated GAT-1 lacking the PDZ-interacting epitope exhibits impaired plasma membrane expression *in vitro*. Similarly, GAT-1GFP knock-in mice, which express the same amount of total GAT-1 protein as wild type mice, exhibit a three-fold decrease in cell surface expressed transporter, because the GFP masks the endogenous PDZ-interacting epitope (-AYI). Yet the GAT-1GFP mice do not phenocopy GAT-1 knockout mice, which have a constant 25--32 Hz tremor in their limbs and tail and display ataxia and anxiety. Thus, there appears to remain a default exocyst-independent pathway through which sufficient GAT1-GFP can be delivered to the cell surface to maintain wild-type-equivalent GABAergic tone.

Live-cell imaging of GAT-1 molecules suggests that plasma membrane GAT-1 is tethered to the actin cytoskeleton via a multi-component protein assembly in which the PDZ-interaction forms an important link. Through fluorescence recovery after photobleaching (FRAP), we recently established that GAT-1 exhibits 30% greater lateral mobility in the plasma membrane when the PDZ-interacting domain is disrupted. Therefore, interaction with PDZ proteins mediates transporter anchoring in the membrane. A candidate PDZ-domain containing scaffold protein that mediates these properties is the membrane associated guanylate kinase (MAGUK) PALS1 (protein associated with LIN-7, subtype 1). The PALS1/GAT-1 interaction is dependent on the C-terminal –AYI residues and its co-expression with GAT-1 promotes increased transporter surface expression, presumably by stabilizing the residence of membrane - inserted GAT-1. Neuronal expression of PALS1 and GAT-1 does not perfectly overlap, and it follows that both molecules almost certainly interact with other partners in some cell types and in some subcellular compartments. The interaction of GAT-1 with PDZ-domain containing MAGUKs may play a cell-specific and compartment-specific role in regulating transporter availability, location, and stability.

GAT-2, GAT-3, and BGT-1 possess PDZ-type-I-like interacting motifs at their C-termini (Figure 1). GAT-2 and BGT-1 interact with PDZ proteins, including $G_{\alpha i}$-interacting protein COOH terminus (GIPC) and LIN-7, respectively, to stabilize their presence in the plasma membrane. Deletion of these motifs results in redistribution of transporter to intracellular regions but does not perturb the sorting of GAT-2 or BGT-1 to the appropriate cellular compartments. GAT-2 and BGT-1 sort to the basolateral surface when expressed in Madin-Darby canine kidney II (MDCK) cells, a well-established expression system to study polarized sorting of proteins into cellular compartments. The seven amino acids immediately proximal to the PDZ-interacting motifs in GAT-2 and BGT-1 comprise a motif unique to these particular transporters that dictates their delivery to the basolateral surface of MDCK cells (Figure 1). In general, basolateral sorting in epithelial cells corresponds to somatodendric sorting in neurons, while apical sorting, which is observed for GAT-1 and GAT-3, corresponds to axonal (and consequently presynaptic) sorting, although not all proteins fit this paradigm. Truncation of the entire GAT-1 C-terminus does not perturb its apical sorting, but removing the three C-terminal residues from GAT-3 is sufficient to result in mixed apical and basolateral sorting. The -THF terminal amino acids of GAT-3 resemble but do not rigidly conform to a Type-I PDZ interacting motif (X-S/T-X-V/L) and reportedly bind the PDZ-domain protein CAP70. For GAT-3 at least, the PDZ-interaction may therefore play an important role in both axonal sorting in neurons and stabilizing its expression in the plasma membrane.

Constitutive endocytosis of NSS transporters from the plasma membrane is controlled in large part by the non-polar residues within the non-classical endocytic motifs present in their proximal C-termini (consensus sequence L(X)ERLAY(X)IT, Figure 1). Regulated endocytosis and exocytosis occur through pathways distinct from the constitutive processes.

Regulated transporter trafficking

One third of the total cellular GAT-1 resides in a pool acutely recycling between the plasma membrane and cytoplasm. In the basal state, 33% of this pool resides in the plasma membrane. However, protein kinase and phosphatase activity serves to modulate the transporter cytoplasmic/plasma membrane distribution equilibrium through multiple and distinct pathways. The motif in the proximal C-terminus responsible for constitutive internalization is also implicated in protein kinase C (PKC)-induced transporter endocytosis. PKC-mediated endocytosis is absolutely dependent on the L(X)ERL portion of the L(X)ERLAY(X)IT region and is located immediately downstream from a conserved putative serine/threonine phosphoacceptor residue. Stimulation of PKC promotes a relative decrease in surface transporter levels, attenuating transporter recycling and redistributing transporter to the endosomal compartments. Stimulating tyrosine kinase activity has the opposite effect: When high neuronal activity elicits large amounts of quantal GABA release, the cell may benefit from redistributing transporters from the intracellular pool to the plasma membrane in a rapid homeostatic response to maintain the local [GABA] close to equilibrium $[\text{GABA}]_o$. As substrate permeates the transporter, conformational changes present tyrosines at the cytoplasmic ends of TM2 or TM7 for modification. The phosphorylated side-chains signal for reduced transporter internalization, resulting in substrate- induced transporter up-regulation. Analogously, direct inhibition of tyrosine kinases results in rapid attenuation of uptake by GAT-1. NSS transporters therefore exist in mutually exclusive PKC or tyrosine kinase phosphorylated states, and the relative abundance of each of these states dictates the proportion of the recycling transporter pool that is present at the plasma membrane. Nonetheless, direct transporter phosphorylation is often insufficient to drive redistribution. PKC mediated regulation is still reported even after removal of all consensus phosphorylation sites in the transporter. Protein phosphatases (PP) also regulate transporter function; in general, PP1 and PP2A inhibition down-regulates transporter activity. Elevated $[\text{Ca}^{2+}]_i$ is also reported to decrease GAT-mediated uptake via calmodulin- and calpain-sensitive pathways.

The SNARE complex protein syntaxin 1A is present in the distinct vesicle population that delivers GAT-1 to the cell surface; its co-expression with GAT-1 results in increased transporter numbers on the plasma membrane. A paradoxical feature of this interaction is that syntaxin 1A also serves as negative regulator of the transporter’s intrinsic properties. Syntaxin 1A binds to three negatively charged aspartates in the GAT-1 N-terminus (Figure 1), but a cluster of four arginines in GAT-1 IL4 competes with syntaxin 1A at this binding site. Syntaxin 1A interaction with GAT-1 N-terminus releases IL4, which inhibits GABA transport. However, chronic exposure to substrate relieves this inhibition by causing dissociation of syntaxin 1A from the transporter, freeing the N-terminus to sequester IL4. The GAT-1/syntaxin 1A interaction probably forms only part of a multimeric protein complex that modulates transporter function. PKC-mediated phosphorylation of syntaxin 1A binding partners (e.g., Munc 18) inhibits their interaction with the SNARE proteins and promotes the syntaxin 1A- mediated effects on GAT-1, while SNAP-25, another SNARE protein, both potentiates syntaxin 1A-mediated inhibition of substrate transport and promotes GAT-1 surface expression. GAT-2 and GAT-3 are not modulated by syntaxin 1A, and FRET indicates that no direct interaction occurs between syntaxin 1A and these transporters, presumably because their N-termini lack the necessary triplet of aspartate residues present in the N-terminus of GAT-1 and other NSS family members (Figure 1).

Pharmacology --- Modulation of the GABA Transporter by Antiepileptics

GATs are an attractive target in anticonvulsive therapy, because their inhibition leads to activity-dependent prolongation of GABA signals in otherwise hypo-GABAergic synapses. Although many GABA transporter inhibitors possess antiepileptic properties in animal models, tiagabine is the only FDA-approved second-generation antiepileptic drug that selectively inhibits a GABA transporter, GAT-1. Tiagabine-mediated GAT-1 inhibition enhances GABAergic inhibition by prolonging phasic GABA currents. The drug also blocks reverse transport, so it potentially has pro-convulsive properties. Cognitive side-effects of tiagabine are minimal in comparison to first-generation antiepileptics such as valproate, which cause general psychomotor slowing. Nonetheless, the major side-effect of tiagabine is tremor, which can be accompanied by ataxia, dizziness, asthenia, sedation, and nonspecific nervousness. Genetic knock-out of GAT-1 produces mice with increased GABA$_A$-receptor-mediated tonic conductance in both cerebellar granule and Purkinje cells, and a slower decay of spontaneous inhibitory postsynaptic currents in cerebellar granule cells. This points to increased extracellular [GABA]$_o$ due to the lack of GAT-1-mediated clearance. Importantly, these mice also partially phenocopy several of the clinical side effects of tiagabine, particularly tremor, indicating the side-effects are inherent to a clinical strategy that specifically targets GAT-1 rather than to non-selective actions on other targets.

Gabapentin and vigabatrin, other antiepileptics in clinical use, do not act directly on GATs, but still influence their function. They indirectly enhance reverse GABA transport during high-frequency stimulation, which could be neuroprotective during seizure.

Although primarily localized on astrocytes and in extrasynaptic regions, BGT-1 is emerging as an attractive antiepileptic target. EF1502 is an equipotent, non-competitive GAT-1/BGT-1 inhibitor. It has a broad-spectrum anticonvulsant profile in animal models of generalized and partial epilepsy, exhibits a superior tolerability profile in comparison to tiagabine, and displays a synergistic rather than additive anticonvulsant interaction when co-administered with tiagabine. The efficacy of EF1502 is likely explained by its inhibition of extrasynaptic BGT-1, increasing GABA-induced tonic conductance. Similarly, co-administration of NO711 (a selective GAT-1 inhibitor) and SNAP-5114 (a GAT-2/-3 inhibitor) in rat neocortex increased GABAergic tone, but application of either drug alone was insufficient to effect tonic currents. Administration of non-GAT-1 transporter inhibitors alone show enhanced efficacy in the generalized epilepsy models, but reduced efficacy on partial seizures when compared to tiagabine. To date there is no known compound that specifically targets BGT-1, GAT-2, or GAT-3. The development of anticonvulsants that specifically target each GAT isoform is therefore of great importance. Administration of these compounds alone or in combination could form the basis of new treatment paradigms for controlling CNS GABAergic disorders in a regional or cell-type specific manner. The recent advances in our understanding of how the NSS transporters' molecular structure relates to their function might allow the design of new compounds that specifically modulate either forward or reverse substrate transport modes, leading to exceptionally refined treatment of complex neurological disorders.

Further readings

Chiu CS, Brickley S, Jensen K, Southwell A, McKinney S, Cull-Candy S, Mody I, Lester HA (2005) GABA transporter deficiency causes tremor, ataxia, nervousness, and increased GABA-induced tonic conductance in cerebellum. *J Neurosci* **25**,3234-3245.

Chiu CS, Jensen K, Sokolova I, Wang D, Li M, Deshpande P, Davidson N, Mody I, Quick MW, Quake SR, Lester HA (2002) Number, density, and surface/cytoplasmic distribution of GABA transporters at presynaptic structures of knock-in mice carrying GABA transporter subtype 1-green fluorescent protein fusions. *J Neurosci* **22**,10251-10266.

Conti F, Zuccarello LV, Barbaresi P, Minelli A, Brecha NC, Melone M (1999) Neuronal, glial, and epithelial localization of γ-aminobutyric acid transporter 2, a high-affinity γ-aminobutyric acid plasma membrane transporter, in the cerebral cortex and neighboring structures. *J Comp Neurol* **409**,482-494.

Farhan H, Freissmuth M, Sitte HH (2006) Oligomerization of neurotransmitter transporters: a ticket from the endoplasmic reticulum to the plasma membrane. *Handb Exp Pharmacol*,233-249.

Forrest LR, Tavoulari S, Zhang YW, Rudnick G, Honig B (2007) Identification of a chloride ion binding site in Na+/Cl -dependent transporters. *Proc Natl Acad Sci U S A* **104**,12761-12766.

Guastella J, Nelson N, Nelson H, Czyzyk L, Keynan S, Miedel MC, Davidson N, Lester HA, Kanner BI (1990) Cloning and expression of a rat brain GABA transporter. *Science* **249**,1303-1306.

Hoogland G, Spierenburg HA, van Veelen CW, van Rijen PC, van Huffelen AC, de Graan PN (2004) Synaptosomal glutamate and GABA transport in patients with temporal lobe epilepsy. *J Neurosci Res* **76**,881-890.

Jensen K, Chiu CS, Sokolova I, Lester HA, Mody I (2003) GABA transporter-1 (GAT1)-deficient mice: differential tonic activation of $GABA_A$ versus $GABA_B$ receptors in the hippocampus. *J Neurophysiol* **90**,2690-2701.

Kanner BI (2006) Structure and Function of Sodium-coupled GABA and Glutamate Transporters. *J Membr Biol* **213**,89-100.

Muth TR, Caplan MJ (2003) Transport protein trafficking in polarized cells. *Annu Rev Cell Dev Biol* **19**,333-366.

Quick MW (2006) The role of SNARE proteins in trafficking and function of neurotransmitter transporters. *Handb Exp Pharmacol*,181-196.

Rudnick G (2006) Structure/function relationships in serotonin transporter: new insights from the structure of a bacterial transporter. *Handb Exp Pharmacol*,59-73.

Yamashita A, Singh SK, Kawate T, Jin Y, Gouaux E (2005) Crystal structure of a bacterial homologue of Na^+/Cl^--dependent neurotransmitter transporters. *Nature* **437**,215-223.

Zomot E, Bendahan A, Quick M, Zhao Y, Javitch JA, Kanner BI (2007) Mechanism of chloride interaction with neurotransmitter:sodium symporters. *Nature*, advance online publication 19 August 2007 | doi:10.1038/nature06133.

Figure Legends

Figure 1: Alignment, secondary structure, and regulatory elements in GABA transporters

A sequence alignment of the four known GABA transporter isoforms with the $LeuT_{Aa}$ bacterial leucine transporter to highlight regions of sequence similarity (presumably leading to structural similarity). Identical residues are highlighted in orange. Transmembrane helices are labeled above the sequences; helices in green (TM 1--5) have pseudo-two-fold symmetry with helices in blue (TM 6--10). TM11 and TM12 which are not part of this symmetry are colored purple and magenta, respectively. Helical regions in intracellular loops (IL) and extracellular loops (EL) are identified by boxed slashes above the sequences. The red and blue triangles below the sequences highlight residues involved in coordinating ions Na1 and Na2, respectively, and those residues whose side-chains interact with the Na^+ ions are shown as green letters. Residues that coordinate the Cl^- ion are marked by green triangles below the alignment. The filled black circles specify the residues involved in binding the leucine substrate in $LeuT_{Aa}$, and residues whose side chains interact with the leucine are shaded yellow. The red and black diamonds indicate the charged pairs at the extracellular and cytoplasmic entrances, respectively. The residues that form the $LeuT_{Aa}$ dimer interface in TM9 and TM12 are shown as underlined brown letters. N-terminal residues involved in syntaxin 1A binding are shown as bold red letters, while IL4 arginines, their interaction partners in the absence of syntaxin 1A, are shown as bold blue letters. The C-terminal sequence implicated in constitutive and PKC-regulated endocytosis is boxed. The R/K-I/L COPII interacting residues are highlighted in red. Distal C-terminal sequences that mediate somatodendritic (basolateral) sorting are highlighted in dark blue. PDZ-interacting motifs are colored cyan.

Figure 2: Topology, folded structure, and substrate binding site in the LeuT$_{Aa}$ bacterial homologue of the mammalian GABA transporters

Panel A shows the membrane topology of the SLC6 transporters as exemplified by LeuT$_{Aa}$. Leucine substrate is shown coordinated in the center of the unwound regions of TM1 and TM6; the two Na$^+$ ions are shown as purple circles. IL = intracellular loop; EL = extracellular loop. Green arrows highlight region of β-sheet structure; the α-helical TM domains are labeled 1--12 and colored according to their pseudo-two-fold symmetrical arrangement in the membrane, which is displayed in panel (B). The black ellipse in panel B marks the rotation axis for this symmetry. Panel C depicts the hydrogen bonds and ionic interactions that coordinate the substrate (leucine) and the Na$^+$ ion in the transporter binding site which makes direct contact with the leucine. Ion spheres are 25% actual size in order to display all the interactions. Image was generated from the 2A65 PDB LeuT$_{Aa}$ crystal structure using PyMOL v0.99 (DeLano Scientfic, San Francisco, CA).

Figure 3: Residues that coordinate the binding of the co-transported Na$^+$ and Cl$^-$ ions in NSS transporters

A) Na1 in LeuT$_{Aa}$ coordinated by residues from TM1a, TM1b, TM6a, and TM7, together with the bound leucine, are shown. The location of Na2 is shown in the background. B)

TM1a and TM8 residues from $\mathrm{LeuT_{Aa}}$ that coordinate Na2 are shown, with the location of Na1 and leucine in the background. C) Residues from TM2, TM6a and TM7 that coordinate $\mathrm{Cl^-}$ in the GAT-1 transporter. Residue numbering is for GAT-1 in this panel. Underlined residues are almost completely conserved in all NSS transporters. In all panels ion spheres are 25% actual size in order to display all the interactions. We include the interaction between Gln291 and the $\mathrm{Cl^-}$ ion reported by Zomot *et al.*, which is not present in the homology models of Forrest *et al.* (see Further Reading). Panels A and B were generated using PyMOL v0.99 from the 2A65 PDB $\mathrm{LeuT_{Aa}}$ crystal structure. Panel C was generated using PyMOL v0.99 from a homology model of GAT-1 based on $\mathrm{LeuT_{Aa.}}$ kindly provided to the authors for the purpose of this review by Dr. L.R. Forrest and Dr. B. Honig (Howard Hughes Medical Institute, Center for Computational Biology and Bioinformatics, and Department of Biochemistry and Molecular Biophysics, Columbia University, NY).

Table 1 Cross-species nomenclature of cloned GABA transporters with official gene symbols

Species	***Nomenclature***			
Human/Rat	GAT-1	BGT-1	GAT-2	GAT-3
Mouse	GAT1	GAT2	GAT3	GAT4
Gene name	SLC6A1	SLC6A12	SLC6A13	SLC6A11

Suggested Cross-References

George Richerson
GABA transporters: Regulation of tonic inhibition

Arne Schousboe
Glial modulation of excitability via glutamate and GABA transporters

Figure 1

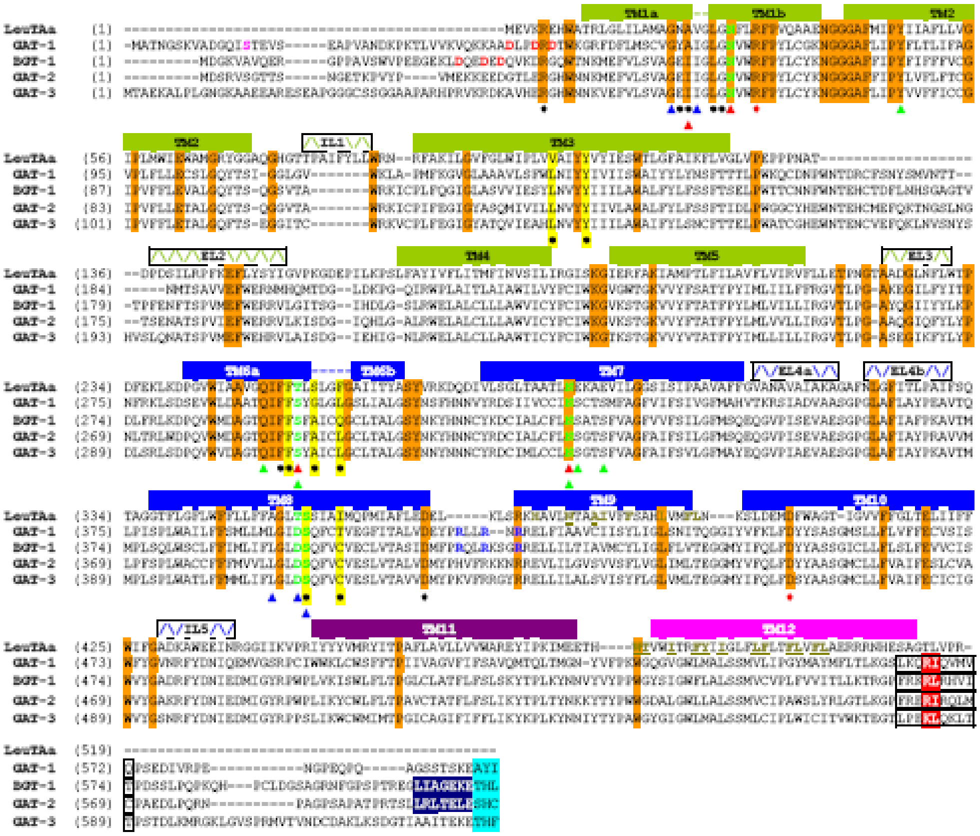
TM1a
TM1b
TM2
IL1
TM3
EL2
TM4
TM5
EL3
TM6a
TM6b
TM7
EL4a
EL4b
TM8
TM9
TM10
IL5
TM11
TM12
LeuTAa
GAT-1
BGT-1
GAT-2
GAT-3

Figure 2

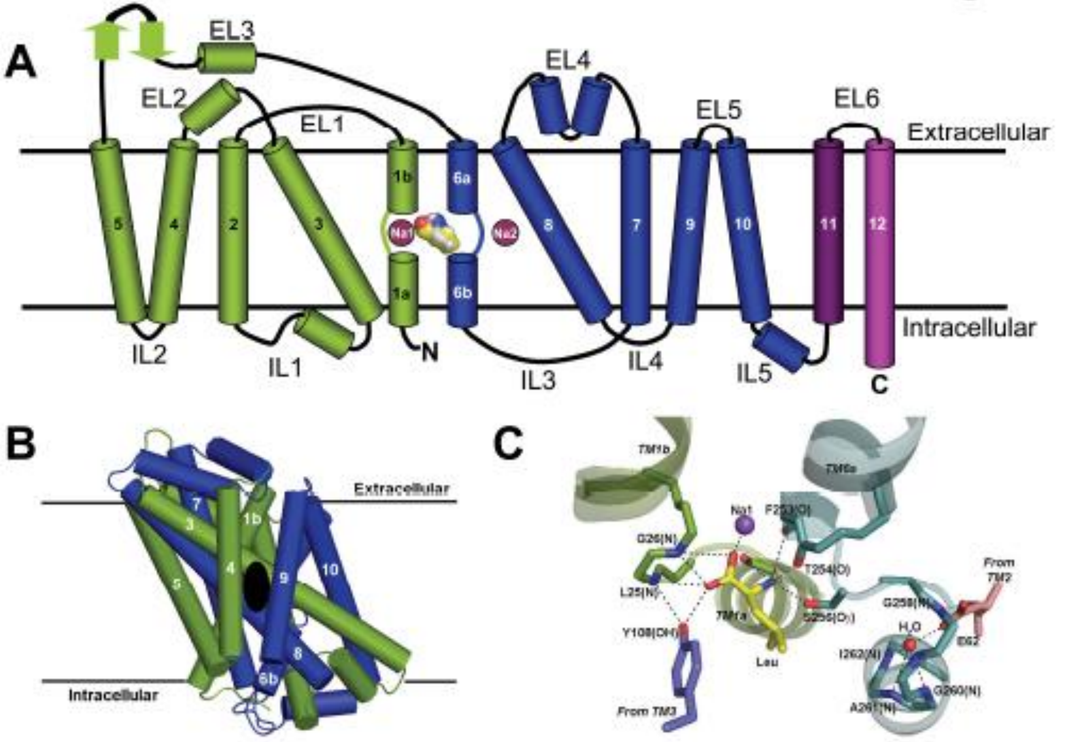
A
EL3
EL2
EL1
EL4
EL5
EL6
Extracellular
5
4
2
3
1b
Na1
1a
6a
Na2
6b
8
7
9
10
11
12
Intracellular
IL2
IL1
N
IL3
IL4
IL5
C
B
Extracellular
7
3
1b
4
9
10
5
8
6b
Intracellular
C
TM1b
TM6a
Na1
F253(O)
G26(N)
T254(O)
L25(N)
TM1a
S256(Oγ)
From TM2
G258(N)
H2O
E62
Y108(OH)
Leu
I262(N)
G260(N)
A261(N)
From TM3

Figure 3

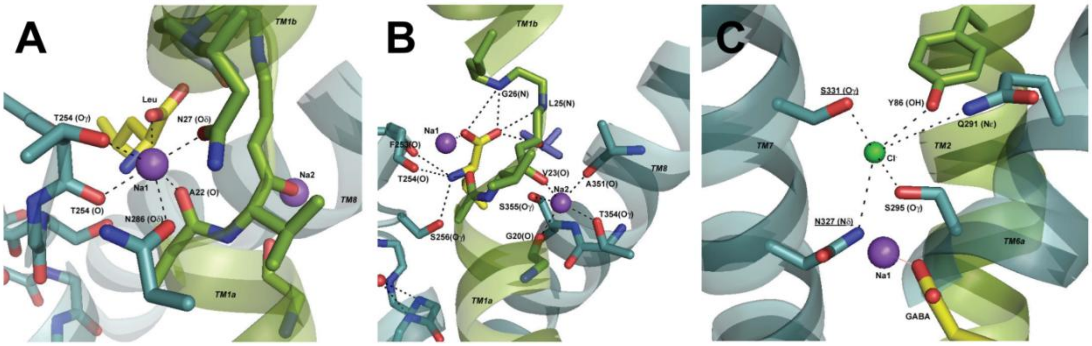
A
TM1b
Leu
T254 (Oγ)
N27 (Oδ)
Na1
Na2
A22 (O)
TM8
T254 (O)
N286 (Oδ)
TM1a
B
TM1b
G26(N)
L25(N)
Na1
F253(O)
T254(O)
V23(O)
TM8
A351(O)
Na2
S355(Oγ)
T354(Oγ)
G20(O)
S256(Oγ)
TM1a
C
S331 (Oγ)
Y86 (OH)
Q291 (Nε)
TM7
Cl-
TM2
S295 (Oγ)
N327 (Nδ)
TM6a
Na1
GABA

Appendix II: Biophysical properties of neuronal nicotinic acetylcholine receptors

This appendix describes the trafficking, assembly, and stoichiometry of fluorescently labeled α6 and β3 subunits of the neuronal nicotinic acetylcholine receptor. I performed the TIRF studies along with the rhodamine phalloidin fluorescence characterization.

0026-895X/08/7301-27–41$20.00
MOLECULAR PHARMACOLOGY
Copyright © 2008 The American Society for Pharmacology and Experimental Therapeutics
Mol Pharmacol 73:27–41, 2008

Vol. 73, No. 1
39180/3287915
Printed in U.S.A.

Subcellular Trafficking, Pentameric Assembly, and Subunit Stoichiometry of Neuronal Nicotinic Acetylcholine Receptors Containing Fluorescently Labeled α6 and β3 Subunits[S]

Ryan M. Drenan, Raad Nashmi, Princess Imoukhuede, Herwig Just, Sheri McKinney, and Henry A. Lester

Division of Biology, California Institute of Technology, Pasadena, California

Received July 2, 2007; accepted October 11, 2007

ABSTRACT

Neuronal nicotinic acetylcholine (ACh) receptors are ligand-gated, cation-selective ion channels. Nicotinic receptors containing α4, α6, β2, and β3 subunits are expressed in midbrain dopaminergic neurons, and they are implicated in the response to smoked nicotine. Here, we have studied the cell biological and biophysical properties of receptors containing α6 and β3 subunits by using fluorescent proteins fused within the M3-M4 intracellular loop. Receptors containing fluorescently tagged β3 subunits were fully functional compared with receptors with untagged β3 subunits. We find that β3- and α6-containing receptors are highly expressed in neurons and that they colocalize with coexpressed, fluorescent α4 and β2 subunits in neuronal soma and dendrites. Förster resonance energy transfer (FRET) reveals efficient, specific assembly of β3 and α6 into nicotinic receptor pentamers of various subunit compositions. Using FRET, we demonstrate directly that only a single β3 subunit is incorporated into nicotinic acetylcholine receptors (nAChRs) containing this subunit, whereas multiple subunit stoichiometries exist for α4- and α6-containing receptors. Finally, we demonstrate that nicotinic ACh receptors are localized in distinct microdomains at or near the plasma membrane using total internal reflection fluorescence (TIRF) microscopy. We suggest that neurons contain large, intracellular pools of assembled, functional nicotinic receptors, which may provide them with the ability to rapidly up-regulate nicotinic responses to endogenous ligands such as ACh, or to exogenous agents such as nicotine. Furthermore, this report is the first to directly measure nAChR subunit stoichiometry using FRET and plasma membrane localization of α6- and β3-containing receptors using TIRF.

α6 nicotinic ACh receptor subunits are expressed in several catecholaminergic nuclei in the central nervous system, including retinal ganglion cells (Gotti et al., 2005b), locus coeruleus (Léna et al., 1999), and dopaminergic neurons located in the substantia nigra and ventral tegmental area (Whiteaker et al., 2000; Zoli et al., 2002; Champtiaux et al., 2003). Ligand-binding studies using the α6-specific probe α-conotoxin MII suggest that many α6* (* indicates that other subunits may be present in the receptor) receptors are located on presynaptic terminals in the superior colliculus and striatum (Whiteaker et al., 2000). Indeed, this binding activity disappears in the brains of α6 knockout mice (Champtiaux et al., 2002). This strikingly specific expression pattern could indicate a unique function for α6* receptors, and α6* receptors are candidate drug targets for diseases or disorders such as Parkinson's disease or nicotine addiction (Quik and McIntosh, 2006).

Functional, voltage-clamped α6-dependent responses are elusive in heterologous expression systems such as *Xenopus laevis* oocytes (Kuryatov et al., 2000; Broadbent et al., 2006), but native α6* receptors are readily studied using synaptosome preparations from brain tissue (Whiteaker et al., 2000;

ABBREVIATIONS: HEK, human embryonic kidney; nAChR, nicotinic acetylcholine receptor; ACh, acetylcholine; YFP, yellow fluorescent protein; CFP, cyan fluorescent protein; FRET, Förster resonance energy transfer; TIRF, total internal reflection fluorescence; PCR, polymerase chain reaction; DMEM, Dulbecco's modified Eagle's medium; WT, wild-type; XFP, yellow or cyan fluorescent protein; NA, numerical aperture; *E*, FRET efficiency; GluCl, glutamate-gated chloride; HS, high sensitivity; LS, low sensitivity.

This work was supported by the Plum Foundation; National Institutes of Health (NIH) Grants DA017279, DA019375, DA009121, and NS11756; and by Philip Morris International/USA. R.N. was supported by fellowships from the Elizabeth Ross Foundation, University of California Office of the President Tobacco Related Disease Research Program (UCOP TRDRP) Grant 10FT-0174, and the National Alliance for Research on Schizophrenia and Depression. H.J. was supported by the Austrian Science Fund (Fonds zur Förderung der wissenschaftlichen Forschung; Erwin Schrödinger Fellowship J2486). R.M.D. was supported by a fellowship from UCOP TRDRP (15FT-0030) and an NIH National Research Service Award (DA021492).

Article, publication date, and citation information can be found at http://molpharm.aspetjournals.org.

doi:10.1124/mol.107.039180.

[S] The online version of this article (available at http://molpharm.aspetjournals.org) contains supplemental material.

Grady et al., 2002; Champtiaux et al., 2003; Gotti et al., 2005a). Indeed, α-conotoxin MII-sensitive receptors are pharmacologically and stoichiometrically distinct from α-conotoxin MII-resistant receptors in mediating [^{3}H]dopamine release from striatal synaptosomes (Grady et al., 2002; Salminen et al., 2007). Recent studies using α4 and β3 knockout mice demonstrate the existence of functional α6β2, α6β2β3, α6α4β2, and α6α4β2β3 receptors (Salminen et al., 2007). It is noteworthy that native α6α4β2β3 receptors have the highest affinity (EC_{50} = 0.23 ± 0.08 μM) for nicotine of any nicotinic receptor reported to date. Because nicotine is likely to be present at concentrations ≤0.5 μM in the cerebrospinal fluid of smokers (Rowell, 2002), only those receptors with the highest affinity for nicotine, including some α4* and α6* receptors, are likely to be important in nicotine addiction. Although previous studies offer major conceptual advances in our understanding of α6* receptors in the brain, there is a lack of information regarding the subcellular localization and biophysical properties of α6 subunits.

β3 subunits are expressed in most of the same locations as α6, including midbrain dopaminergic neurons projecting to the striatum (Zoli et al., 2002). β3 knockout mice demonstrate that β3 subunits are important for the biogenesis of α6* receptors in the brain (Cui et al., 2003; Gotti et al., 2005a). This is corroborated by studies in *X. laevis* oocytes and tissue culture cells (Kuryatov et al., 2000). β3 also increases α6-specific binding activity in HEK293 cells (Tumkosit et al., 2006). Uncertainty exists, however, because others have reported that β3 incorporation into nAChRs acts as a dominant negative (Boorman et al., 2003; Broadbent et al., 2006), suppressing ACh-evoked responses by an incompletely understood gating mechanism. This effect occurred apparently without significantly altering the surface expression of nAChRs. What is clear is that β3 acts more like a muscle β subunit than a "typical" neuronal β subunit; it does not participate in forming the α:non-α interface that comprises the neuronal ligand binding site, and other β subunits, either β2 or β4, must be present to form functional nicotinic receptors (Broadbent et al., 2006). This presents a problem both for basic and therapeutic-oriented research on β3* receptors, because there are no pharmacological ligands that can visually or functionally isolate β3-specific actions in cell culture systems or intact brain tissue. Given the precise localization and unique functional properties of β3* receptors, potential for therapeutic intervention that would be afforded by β3-specific probes, and involvement in nicotine addiction (Bierut et al., 2007), it is important to develop and exploit tools to study β3.

We have sought to compare characteristics of α6 and β3 with the better understood α4 and β2 subunits. We previously generated fluorescently labeled α4 and β2 subunits, and we used these subunits to study assembly, trafficking, and nicotine-dependent up-regulation of α4β2 receptors (Nashmi et al., 2003). We have now fluorescently labeled α6 and β3 subunits by inserting a yellow fluorescent protein (YFP) or cyan fluorescent protein (CFP) in the M3-M4 intracellular loop. With this approach, one can optically monitor functional nicotinic ACh receptors containing these subunits in live cells and in real time. We measured 1) functional responses using two-electrode voltage-clamp and patch-clamp electrophysiology, 2) subcellular distribution and colocalization in neurons using confocal microscopy and spectral imaging, 3) receptor assembly and subunit stoichiometry using Förster resonance energy transfer (FRET), and 4) plasma membrane localization and distribution patterns using total internal reflection fluorescence (TIRF) microscopy.

Materials and Methods

Reagents. Unless otherwise noted, all chemicals were from Sigma-Aldrich (St. Louis, MO). DNA oligonucleotides for PCR and site-directed mutagenesis were synthesized by Integrated DNA Technologies, Inc. (Coralville, IA). Restriction enzymes for molecular biology were purchased from Roche Diagnostics (Indianapolis, IN) or New England Biolabs (Ipswich, MA). Glass-bottomed dishes (35 mm) coated with L-polylysine were purchased from MatTek (Ashland, MA).

Cell Culture and Transfection. N2a cells (American Type Culture Collection, Manassas, VA) were maintained in Dulbecco's modified Eagle's medium (high glucose with 4 mM L-glutamine; Invitrogen, Carlsbad, CA)/Opti-MEM (Invitrogen) mixed at a ratio of 1:1 and supplemented with 10% fetal bovine serum (Invitrogen), penicillin (Mediatech, Herndon, VA), and streptomycin (Invitrogen). N2a cells were transfected in DMEM without serum or antibiotics. Transfection was carried out using Lipofectamine/PLUS (Invitrogen) according to the manufacturer's instructions and with the following modifications. For a 35-mm dish, 1 to 2 μg of total plasmid DNA was mixed with 100 μl of DMEM and 6 μl of PLUS reagent. DMEM/DNA was combined with a mixture of 100 μl of DMEM and 4 μl of Lipofectamine reagent. Rat hippocampal neurons were dissociated and plated on glass-bottomed imaging dishes as described previously (Slimko et al., 2002). For primary neuron transfection, Lipofectamine 2000 (Invitrogen) was used in conjunction with Nupherin (BIOMOL Research Laboratories, Plymouth Meeting, PA) as described below. In brief, in total 1 μg of DNA was incubated with 20 μg of Nupherin in 400 μl of Neurobasal medium without phenol red (Invitrogen), whereas 10 μl of Lipofectamine 2000 was mixed in 400 μl of Neurobasal medium (Invitrogen). After 15 min, the two solutions were combined and incubated for 45 min. Neuronal cultures in 35-mm glass-bottomed culture dishes were incubated in the resulting 800-μl mixture for 120 min, followed by removal of transfection media and refeeding of the original, pretransfection culture media.

Plasmids and Molecular Biology. Mouse α4 and β2 nAChR cDNAs in pCI-neo, both untagged and modified with YFP or CFP fluorescent tags, have been described previously (Nashmi et al., 2003). Mouse α3 and β3 nAChR cDNAs in pCDNA3.1 were a generous gift of Jerry Stitzel (Institute for Behavioral Genetics, University of Colorado, Boulder, CO). A full-length mouse α6 I.M.A.G.E. cDNA (ID no. 4501558) was obtained from Open Biosystems (Huntsville, AL). A modified α6 cDNA was constructed that 1) lacked the 5′ and 3′ untranslated regions and 2) contained a Kozak sequence (GCC ACC) before the ATG start codon to facilitate efficient translation initiation. Rat β4 cloned into pAMV was provided by Cesar Labarca (California Institute of Technology, Pasadena, CA). pEYFP-N1 and pECFP-N1 (Clontech, Mountain View, CA) were used to construct fluorescent nAChR cDNAs. mGAT1 labeled with CFP was provided by Fraser Moss (California Institute of Technology). YFP-Syntaxin was provided by Wolfhard Almers (Vollum Institute, Oregon Health and Science University, Portland, OR). CFP-tau was provided by George Bloom (University of Virginia, Charlottesville, VA). A QuikChange (Stratagene, La Jolla, CA) kit was used to construct β3 (WT or XFP-modified) cDNAs containing a V13′S point mutation.

To design fluorescently labeled α6 and β3 subunits, we chose to insert the XFP moiety in the M3-M4 loop each subunit. We have previously found that this region is appropriate for insertion in nAChR α4 and β2 subunits (Nashmi et al., 2003), the nAChR γ subunit (data not shown), and GluCl α and β subunits (Slimko et al., 2002). Similar to our previous studies, we inserted the XFP moiety in the M3-M4 loop at positions that avoided the conserved amphipathic

α-helix and putative cell sorting motifs and phosphorylation sites (Fig. 1, A and B). To construct nAChRs with XFP inserted into the M3-M4 loop, a two-step PCR protocol was used. First, YFP or CFP was amplified with PCR using oligonucleotides (sequences available upon request) designed to engineer 5′ and 3′ overhangs of 15 base pairs that were identical to the site where XFP was to be inserted, in frame, into the nAChR M3-M4 loop. A Gly-Ala-Gly flexible linker was engineered between the nAChR sequence and the sequence for YFP/CFP at both the 5′ and 3′ ends. In the second PCR step, 100 ng of the first PCR reaction was used as a primer pair in a modified QuikChange reaction using *Pfu* Ultra II (Stratagene, Cedar Creek, TX) polymerase and the appropriate nAChR cDNA as a template. All DNA constructs were confirmed with sequencing and, in some cases, restriction mapping.

cRNA for injection and expression in *X. laevis* oocytes was prepared using a T7 or SP6 in vitro transcription kit (mMessage mMachine; Ambion, Foster City, CA) according to the manufacturer's instructions. RNA yield was quantified with absorbance at 260 nm. RNA quality was assessed by observing absorbance profiles across a range of wavelengths between 220 and 320 nm. Spectrophotometric analysis was performed using a ND-1000 spectrophotometer (NanoDrop, Wilmington, DE).

Confocal Microscopy. N2a cells were plated on 35-mm glass-bottomed dishes, transfected with nAChR cDNAs, and they were imaged live 24–48 h after transfection. *X. laevis* oocytes were imaged 3 days after RNA injection. Oocytes were placed in an imaging chamber and allowed to settle for 20 min before imaging. To eliminate autofluorescence, growth medium was replaced with an extracellular solution containing the following components: 150 mM NaCl, 4 mM KCl, 2 mM $CaCl_2$, 2 mM $MgCl_2$, 10 mM HEPES, and 10 mM D-glucose, pH 7.4. Cells were imaged with a Nikon (Nikon Instruments, Melville, NY) C1 laser-scanning confocal microscope system equipped with spectral imaging capabilities and a Prior (Rockland, ME) remote-focus device. For oocytes, a Nikon Plan Apo 20 × 0.75 numerical aperture (NA) air objective was used, whereas a Nikon Plan Apo 60 × 1.40 NA oil objective was used for mammalian tissue culture cells. Pinhole diameter was 30–60 μm, and cells were imaged at 12-bit intensity resolution over 512 × 512 pixels at a pixel dwell time of 4 to 6 μs. CFP was excited using a 439.5-nm modulated diode laser, and YFP was excited with an argon laser at 514.5-nm. In most cases, imaging was carried out using the Nikon C1si DEES grating and spectral detector with 32 parallel photomultiplier tubes. This allowed us to collect spectral images (λ stacks). In such images, each pixel of the X-Y image contains a list of emission intensity values across a range of wavelengths. We collected light between 450 and 600 nm at a bandwidth of 5 nm. The 515-nm channel was intentionally blocked while we used the 514.5-nm laser for YFP bleaching. Because the emission profile of YFP and CFP significantly overlap, we used the Nikon EZC1 linear unmixing algorithm to reconstruct YFP and CFP images. Experimental spectral images with both YFP- and CFP-labeled nAChR subunits were unmixed using reference spectra from images with only YFP- or CFP-labeled nAChR subunits. For each pixel of a spectral image, intensity of YFP and CFP was determined from fluorescence intensity values at the peak emission wavelength derived from the reference spectra.

Spectral FRET Analysis. To examine FRET between various nAChR subunits, the acceptor photobleaching method (Nashmi et al., 2003) was used with a modified fluorescence recovery after photobleaching macro built into the Nikon EZC1 imaging software. In this method, FRET was detected by recording CFP dequenching during incremental photodestruction of YFP. A spectral image was acquired once before YFP bleaching and at six time points every 10 s during YFP bleaching at 514.5 nm. Laser power during bleaching varied from cell to cell, but was between 25 and 50%. One bleach scan per cycle was used. This bleaching protocol was optimized to achieve 70 to 80% photodestruction of YFP while still enabling us to record incremental increases in CFP emission at each time point. In the confocal microscope, nAChRs labeled with XFP usually exhibit a uniform, intracellular distribution, regardless of the subunit being examined. This is consistent with our previous observations (Nashmi et al., 2003). To measure FRET, spectral images were unmixed into their CFP and YFP components as described above. We found little or no difference in FRET for various cellular structures or organelles in N2a cells, and we measured CFP and YFP mean intensity throughout the entire cell by selecting the cell perimeter as the boundary of a region of interest in Nikon's EZC1 software. CFP and

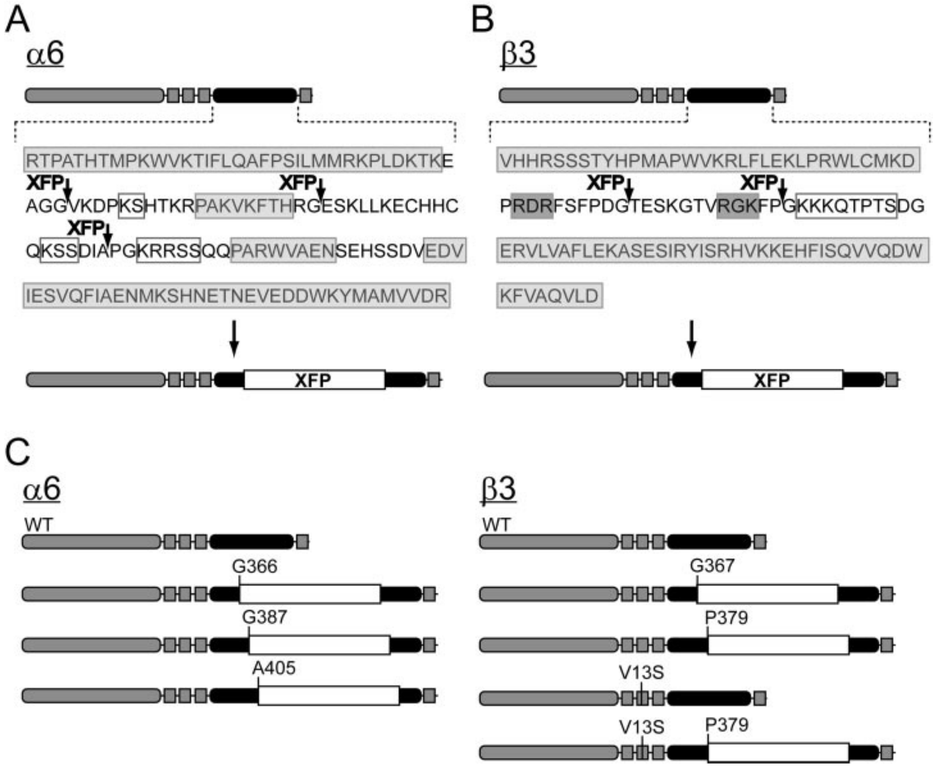

Fig. 1. $\alpha6$ and $\beta3$ nicotinic ACh receptor constructs used in this study. A, XFP insertion points in the $\alpha6$ M3-M4 intracellular loop. The M3-M4 loop primary sequence of the mouse $\alpha6$ nAChR subunit was analyzed for sequences predicted to be involved in forming α-helices (light gray boxes), phosphorylation sites (white boxes), or intracellular trafficking motifs (dark gray boxes); these were specifically avoided. Arrows adjacent to XFP indicate insertion points. The inserted XFP (YFP or CFP) protein was modified 1) to have a flexible Gly-Ala-Gly linker flanking the XFP coding sequence and 2) to lack its STOP codon. B, XFP insertion points in $\beta3$ M3-M4 intracellular loop. Mouse $\beta3$-XFP fusion proteins were designed similarly to $\alpha6$, as indicated in A. C, $\alpha6$ and $\beta3$ nAChR constructs used in this study. In addition to WT, three $\alpha6$-XFP and two $\beta3$-XFP fusions were constructed. A V13′S mutation on the WT and XFP background was introduced into $\beta3$ for characterization in *X. laevis* oocytes.

YFP components were saved in Excel format, and fluorescence intensities were normalized to the prebleach time point (100%). FRET efficiency (E) was calculated as $E = 1 - (I_{\mathrm{DA}}/I_{\mathrm{D}})$, where I_{DA} represents the normalized fluorescence intensity of CFP (100%) in the presence of both donor (CFP) and acceptor (YFP), and I_{D} represents the normalized fluorescence intensity of CFP in the presence of donor only (complete photodestruction of YFP). The I_{D} value was extrapolated from a scatter plot of the fractional increase of CFP versus the fractional decrease of YFP. The E values were averaged from several cells per condition (see Table 1 for n values). Data are reported as mean ± S.E.M.

TIRF Microscopy. N2a cells cultured in glass-bottomed, polyethylenimine-coated imaging dishes were transfected with cDNA mixtures as described above. Cells, superfused with the same imaging solution used for confocal microscopy, were imaged 18 to 24 h after transfection to minimize overexpression artifacts. TIRF images were obtained with an inverted microscope (Olympus IX71; Olympus America, Inc., Center Valley, PA) equipped with a 488-nm air-cooled argon laser (P/N IMA101040ALS; Melles Griot, Carlsbad, CA). Laser output was controlled with a UNIBLITZ shutter system and drive unit (P/N VMM-D1; Vincent Associates, Rochester, NY) equipped with a Mitutoyo (Mitutoyo America, City of Industry, CA) micrometer to control TIRF evanescent field illumination. TIRF imaging was carried out with an Olympus PlanApo 100 × 1.45 NA oil objective, and images were captured with a 16-bit resolution Photometrics Cascade charge-coupled device camera (Photometrics, Tucson, AZ) controlled by SlideBook 4.0 imaging software (Intelligent Imaging Innovations, Santa Monica, CA).

Two-Electrode Voltage-Clamp Electrophysiology. Stage V to VI *X. laevis* oocytes were isolated as described previously (Quick and Lester, 1994). Stock RNAs were diluted into diethyl pyrocarbonate-treated water and injected 1 day after isolation. RNA was injected in a final volume of 50 nl per oocyte using a digital microdispenser (Drummond Scientific, Broomall, PA). After injection, oocytes were incubated in ND-96 solution (96 mM NaCl, 2 mM KCl, 1 mM $CaCl_2$, 1 mM $MgCl_2$, and 5 mM HEPES/NaOH, pH 7.6) supplemented with 50 μg/ml gentamicin and 2.5 mM sodium pyruvate. After 1 to 4 days for nAChR expression, oocytes were used for recording or confocal microscopy.

TABLE 1

FRET efficiency calculations for nicotinic ACh receptors with various subunit compositions

Unless noted otherwise, all experiments with α6 and β3 subunits were performed with $\alpha 6^{\mathrm{A405}}$ and $\beta 3^{\mathrm{P379}}$. Data are reported as mean FRET E ± S.E.M. n refers to the number of independently analyzed cells.

Subunit Composition	FRET E	n
	%	
α4C/β2Y	29 ± 2	10
α4/β2C/β3Y	22 ± 2	9
α4C/β2/β3Y	20 ± 2	8
β3Y/GAT1C	−3 ± 3	9
$\alpha 4/\beta 2C/\beta 3Y^{\mathrm{G367}}$	22 ± 1	7
α6Y/β2C	36 ± 2	12
α6Y/GAT1C	1 ± 4	9
$\alpha 6Y^{\mathrm{G387}}/\beta 2C$	38 ± 2	7
$\alpha 6Y^{\mathrm{G366}}/\beta 2C$	29 ± 2	11
α6Y/β2C/β3	32 ± 2	13
α6Y/β2/β3C	25 ± 3	8
α6/β2Y/β3C	36 ± 2	14
α4Y/α4C/β2	22 ± 2	10
α4/β2Y/β2C	16 ± 2	9
α6Y/α6C/β2	28 ± 2	22
α4/β2/β3Y/β3C	3 ± 1	10
α4Y/α4C/β2/β3	14 ± 1	10
α6Y/α6C/β2/β3	21 ± 1	10
α6Y/α4C/β2	22 ± 1	21
α6Y/α4C/β2/β3	21 ± 2	11
β3Y/GluCl βC	6 ± 4	5
α6Y/GluCl βC	14 ± 2	5

Y refers to YFP, and C refers to CFP.

Agonist-activated nicotinic receptor responses were measured by two-electrode voltage-clamp recording using a GeneClamp 500 (Molecular Devices, Sunnyvale, CA) voltage clamp. Electrodes were constructed from Kwik-Fil borosilicate glass capillary tubes (1B150F-4; WPI, Sarasota, FL) using a programmable microelectrode puller (P-87; Sutter Instrument Company, Novato, CA). The electrodes had tip resistances of 0.8 to 2.0 MΩ after filling with 3 M KCl. During recording, oocytes were superfused with Ca^{2+}-free ND-96 via bath-application and laminar-flow microperfusion using a computer-controlled application and washout system (SF-77B; Warner Instruments, Hamden, CT) (Drenan et al., 2005). The holding potential was −50 mV, and ACh was diluted in Ca^{2+}-free ND-96 and applied to the oocyte for 2 to 10 s followed by rapid washout. Data were sampled at 200 Hz and low-pass filtered at 10 Hz using the GeneClamp 500 internal low-pass filter. Membrane currents from voltage-clamped oocytes were digitized (Digidata 1200 acquisition system; Molecular Devices) and stored on a PC running pCLAMP 9.2 software (Molecular Devices). Concentration-response curves were constructed by recording nicotinic responses to a range of agonist concentrations (six to nine doses) and for a minimum of six oocytes. EC_{50} and Hill coefficient values were obtained by fitting the concentration-response data to the Hill equation. All data are reported as mean ± S.E.M.

Whole-Cell Patch-Clamp Electrophysiology. N2a cells expressing YFP-labeled nicotinic receptors were visualized with an inverted microscope (Olympus IMT-2, DPlan 10 × 0.25 NA and MPlan 60 × 0.70 NA) under fluorescence illumination (mercury lamp). Patch electrodes (3–6 MΩ) were filled with pipette solutions containing 88 mM KH_2PO_4, 4.5 mM $MgCl_2$, 0.9 mM EGTA, 9 mM HEPES, 0.4 mM $CaCl_2$, 14 mM creatine phosphate (Tris salt), 4 mM Mg-ATP, and 0.3 mM GTP (Tris salt), pH 7.4 with KOH. The extracellular solution was 150 mM NaCl, 4 mM KCl, 2 mM $CaCl_2$, 2 mM $MgCl_2$, 10 mM HEPES, and 10 mM D-glucose, pH 7.4. Standard whole-cell recordings were made using an Axopatch 1-D amplifier (Molecular Devices), low-pass filtered at 2 to 5 kHz, and digitized online at 20 kHz (pClamp 9.2; Molecular Devices). Series resistance was compensated 80%, and the membrane potential was held at −70 mV. Recorded potentials were corrected for junction potential.

ACh was delivered using a two-barrel glass θ-shaped tube (outer diameter ~200 μm; pulled from 1.5-mm-diameter θ-shaped borosilicate tubing) connected to a piezoelectric translator (LSS-3100, Burleigh Instruments, Fishers, NY) as described previously (Nashmi et al., 2003). ACh was applied for 500 ms (triggered by pCLAMP 9.2), and solution exchange rates measured from open tip junction potential changes during application with 10% extracellular solution were typically ~300 μs (10–90% peak time). Data are reported as mean ± S.E.M. for the peak current response to 1 μM ACh, and statistical significance was determined using a Wilcoxon signed rank test.

Results

Design and Construction of α6 and β3 XFP Fusions. Based on previous work (Slimko et al., 2002; Nashmi et al., 2003), we chose to insert XFP fusions in the M3-M4 loop of mouse α6 and β3 nAChR subunits. Like all members of the Cys-loop family, α6 and β3 have predicted α-helices at the N- and C-terminal ends of their M3-M4 loop (Fig. 1, A and B) that may be important in ion permeation (Miyazawa et al., 1999). In addition to avoiding these regions, we also avoided potential phosphorylation sites and trafficking motifs (Fig. 1, A and B). Our XFP fusion cassette also consisted of a Gly-Ala-Gly flexible linker flanking the XFP open reading frame on both the N- and C-terminal side. We built three independent XFP fusions for α6 and two XFP fusions for β3 (Fig. 1C). These were designated according to the residue immediately N-terminal to the beginning of the Gly-Ala-Gly linker (e.g.,

$\alpha6$-YFP$^{\mathrm{G366}}$ denotes that the GAG-YFP-GAG cassette was inserted between G366 and V367). Unless otherwise noted, all experiments were conducted with $\alpha6$-XFP$^{\mathrm{A405}}$ and $\beta3$-XFP$^{\mathrm{P379}}$.

Functional Expression of $\alpha6$ and $\beta3$ Subunits. Despite exhaustive attempts to functionally reconstitute $\alpha6^*$ nAChRs in *X. laevis* oocytes and mammalian tissue culture cells, we recorded no robust, reproducible responses from cells expressing $\alpha6$, either with untagged subunits or the fluorescent subunits (Supplemental Data; Table 1). $\beta3$-YFP, however, was well expressed on the plasma membrane of *X. laevis* oocytes when coexpressed with $\alpha3$ and $\beta4$ subunits to support functional expression (Fig. 2A). As a control for oocyte autofluorescence, we imaged oocytes expressing untagged $\beta3$ subunits (Fig. 2A). No fluorescence was detected in this case, indicating that our $\beta3$-YFP signal was specific.

$\beta3$ subunits do not drastically alter the EC_{50} for ACh or nicotine when incorporated into nAChRs (Boorman et al., 2003), but they do profoundly alter single-channel kinetics (Boorman et al., 2003). Channel burst duration was significantly shortened for nAChRs containing $\beta3$ versus those without it (Boorman et al., 2003), suggesting that $\beta3$ reduces the probability of channel opening, P_{open}. Consistent with this, macroscopic voltage-clamped responses from oocytes and mammalian cells expressing $\beta3^*$ receptors were significantly smaller than for non-$\beta3^*$ receptors (Broadbent et al., 2006). To assess the functionality of our $\beta3$-YFP construct, we compared the ability of untagged and YFP-labeled $\beta3$ subunits to attenuate nicotinic responses. $\beta3$ must be coexpressed with other α and β subunits, so we chose to use $\alpha3\beta4$ receptors for this purpose. We did so because $\beta3$ has been well characterized with this receptor combination (Boorman et al., 2003; Broadbent et al., 2006). When WT, untagged $\beta3$ was coexpressed with $\alpha3\beta4$ receptors, we found a significant attenuation of the peak response to 200 μM ACh (Fig. 2B), consistent with previous findings (Broadbent et al., 2006). When $\beta3$-YFP was tested in this assay, it was also able to attenuate the maximal response in a manner identical to untagged $\beta3$ (Fig. 2B). It is possible that, although $\beta3$-WT attenuates responses via a gating mechanism on the plasma membrane, YFP-labeled $\beta3$ might do so via a different mechanism such as sequestering $\alpha3$ or $\beta4$ subunits inside the cell. To further test the functionality of YFP-labeled $\beta3$, we took advantage of the fact that a gain-of-function TM2 mutation in $\beta3$ is able to reverse the attenuation of peak responses seen for $\beta3$-WT (Broadbent et al., 2006). We reasoned that if the YFP label in the M3-M4 loop is not disturbing the function of $\beta3$, we should detect the same gain-of-function response for unlabeled and YFP-labeled $\beta3$ when they are engineered to express a mutation of this sort. When a Val13′ to Ser mutation (V13S) was introduced into unlabeled $\beta3$, we observed not only a reversal of this attenuation behavior, but a significant increase in the peak response to 200 μM ACh with $\alpha3\beta4$ receptors (Fig. 2C). When $\beta3$-YFP$^{\mathrm{V13S}}$ was tested in this assay, we observed an identical behavior. Taken together, these data suggest that $\beta3$-YFP is fully functional and incorporates into nAChRs in *X. laevis* oocytes.

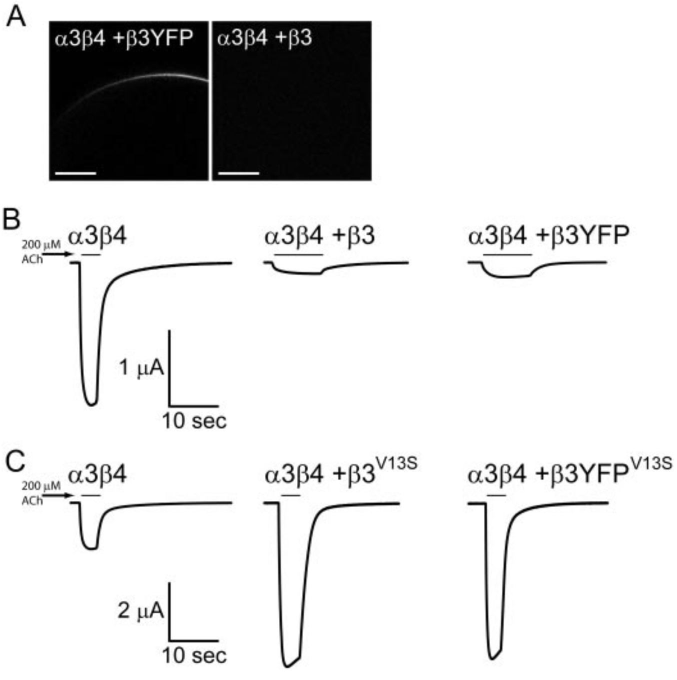

Fig. 2. Fluorescently labeled $\beta3$ subunits are functional and expressed on the cell surface in *X. laevis* oocytes. A, *X. laevis* oocytes were injected with cRNA encoding WT (control) or YFP-labeled $\beta3$ (15 ng) along with $\alpha3$ (2 ng) and $\beta4$ (3 ng). The oocyte surface was imaged with direct fluorescence confocal microscopy. True YFP signal was acquired by linear unmixing of the background fluorescence spectra (untagged $\beta3$ with $\alpha3\beta4$) and a YFP reference spectrum. Scale bar, 54 μm. B, fluorescently labeled $\beta3$ subunits are indistinguishable from WT subunits in their ability to attenuate nicotinic receptor responses. A representative voltage-clamped response from *X. laevis* oocytes expressing $\alpha3\beta4$, $\alpha3\beta4\beta3$, or $\alpha3\beta4\beta3$-YFP is shown. Agonist (ACh; 200 μM) was applied and removed as indicated by the bar. C, reversal of $\beta3$-mediated suppression of nicotinic responses is identical in untagged and YFP-labeled hypersensitive $\beta3$. Representative voltage-clamped responses from oocytes expressing $\alpha3\beta4$, $\alpha3\beta4\beta3^{\mathrm{V13S}}$, or $\alpha3\beta4\beta3$-YFP$^{\mathrm{V13S}}$ are shown. Agonist application is identical to B.

To further characterize our $\beta3$-YFP construct, we constructed concentration-response curves for $\alpha3\beta4$ receptors containing either $\beta3$ WT or $\beta3$-YFP. Consistent with previous reports (Boorman et al., 2000), we measured an EC_{50} for ACh of 230 ± 22 μM for $\alpha3\beta4\beta3$ receptors, which is slightly higher than for $\alpha3\beta4$ (165 ± 9 μM) (Fig. 3A). When $\beta3$-YFP was substituted for WT $\beta3$, the EC_{50} was shifted slightly, but acceptably, to 109 ± 8 μM (Fig. 3A). We also noticed that the addition of $\beta3$ to $\alpha3\beta4$ receptors increased the Hill coefficient from 1.5 ± 0.1 to 2.0 ± 0.3, and this effect was retained when $\beta3$-YFP was coexpressed with $\alpha3\beta4$ receptors. Likewise, we also constructed concentration-response relationship curves for oocytes expressing $\beta3^{\mathrm{V13S}}$ and $\beta3$-YFP$^{\mathrm{V13S}}$. Compared with the EC_{50} for $\alpha3\beta4\beta3$ (230 ± 22 μM), we measured an EC_{50} for $\alpha3\beta4\beta3^{\mathrm{V13S}}$ of 28 ± 3 μM (Fig. 3B). This is consistent with others who have reported an approximate 6-fold reduction in EC_{50} for the inclusion of $\beta3$ with a similar hypersensitive mutation, Val9'Ser (Boorman et al., 2000). We reasoned that if $\beta3$-YFP retained the WT function of $\beta3$, then there should be a similar gain-of-function phenotype when it is coexpressed with $\alpha3\beta4$. We measured an EC_{50} for $\alpha3\beta4\beta3$-YFP$^{\mathrm{V13S}}$ of 34 ± 3 μM (Fig. 3B), confirming that this construct behaves identically to $\beta3$-WT. Collectively, our work in *X. laevis* oocytes with YFP-labeled $\beta3$ subunits suggests that insertion of YFP into the M3-M4 loop does not significantly alter the assembly, subcellular trafficking, or function of this subunit.

Subcellular Localization and Trafficking of $\alpha6$ and $\beta3$ Subunits. To probe the subcellular localization and trafficking of $\alpha6^*$ and $\beta3^*$ receptors, we chose a mouse neuroblastoma cell line, N2a, to transiently express our fluorescent nicotinic receptor subunits. We prefer these cells over, for example, HEK293 cells, because they 1) are of mouse origin, the same species as our fluorescent constructs; 2) are of neuronal origin, suggesting that they will be a permissive environment for correct expression, subcellular localization, and assembly of our ectopic nAChR subunits; and 3) express only moderate quantities of transfected membrane protein. To study the subcellular localization of $\beta3^*$ receptors, we coexpressed β3-YFP with the previously described fluorescently labeled $\alpha4$ and $\beta2$ subunits (Nashmi et al., 2003). $\beta3$ is able to assemble and function when coexpressed with $\alpha4\beta2$ receptors (Broadbent et al., 2006). When coexpressed with fluorescent $\alpha4$ or $\beta2$ receptors, β3-YFP was localized primarily in the endoplasmic reticulum of live N2a cells (Fig. 4A, i and B, i). We used CFP-labeled $\alpha4$ (Fig. 4B, ii) or $\beta2$ (Fig. 4, A and C, ii) subunits along with a confocal microscope with spectral imaging capabilities to unambiguously assign YFP and CFP signals to each pixel for the spectral images of the cells. In these experiments, YFP was assigned green, CFP was assigned red, and yellow indicated pixels where β3-YFP was colocalized with either β2-CFP (Fig. 4A, iii) or α4-CFP (Fig. 4B, iii). We noted that β3-YFP was completely colocalized with either $\alpha4$ or $\beta2$ in this experiment, suggesting that these subunits are assembled in the same pentameric receptors. To further define the extent of this colocalization, we plotted the β3-YFP and α4-CFP or β2-CFP pixel intensity across a two-dimensional region of interest transecting the cell (Fig. 4, A and B, iv). We noted that the YFP and CFP intensity profiles strongly resembled each other, suggesting that these subunits were indeed colocalized and coassembled in intracellular compartments of the cell. With respect to $\alpha4\beta2^*$ receptors, this localization pattern is not an artifact of overexpression, because this is the same pattern we observed previously (Nashmi et al., 2003). This is also the expression pattern of endogenous, YFP-labeled $\alpha4^*$ receptors in α4-YFP knockin mice (Nashmi et al., 2007). This indicates that 1) a large pool of intracellular receptors exists in neurons, and 2) YFP tag does not interfere with the delivery of receptors to the plasma membrane. Thus, the localization pattern we observe here for $\beta3$ subunits is the expected result if it is assembling with $\alpha4\beta2$ receptors.

We expressed α6-YFP along with β2-CFP in N2a cells, and we analyzed its localization pattern as described above for $\beta3$. We also found that $\alpha6$ was localized in intracellular compartments in the cell (Fig. 4C, i), and that it was completely colocalized with $\beta2$ subunits (Fig. 4C, ii–iv). Although

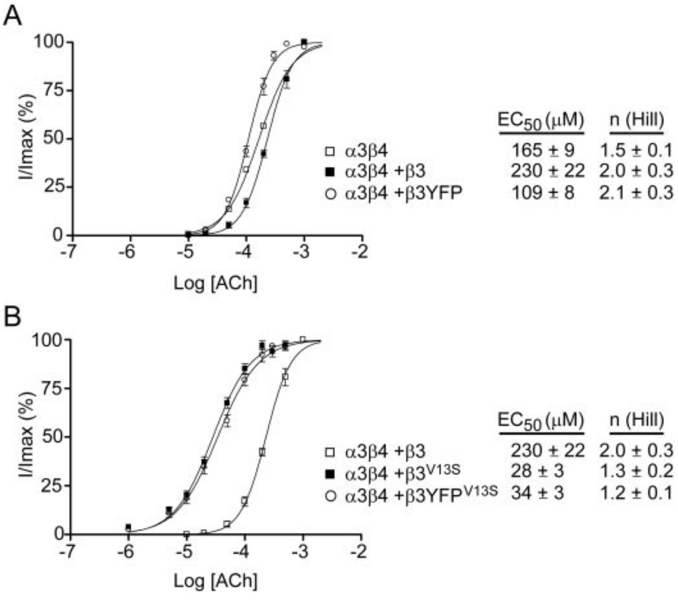

Fig. 3. $\beta3$ nAChR subunit function is not affected by XFP insertion in M3-M4 loop. A, concentration-response relations for WT and fluorescently labeled $\beta3$-containing receptors are similar. *X. laevis* oocytes expressing the indicated receptor subunits were voltage-clamped during agonist application and washout. Peak responses to the indicated ACh concentration (molar) were normalized and the data were fitted to the Hill equation. B, concentration-response relation for $\beta3$ subunits with a hypersensitive mutation is not affected by the presence of YFP in the M3-M4 loop. *X. laevis* oocytes were assayed and data were analyzed as described in A. $\alpha3\beta4$ data from A are shown for comparison. Error bars are ± S.E.M., and $n = 6$ for each condition.

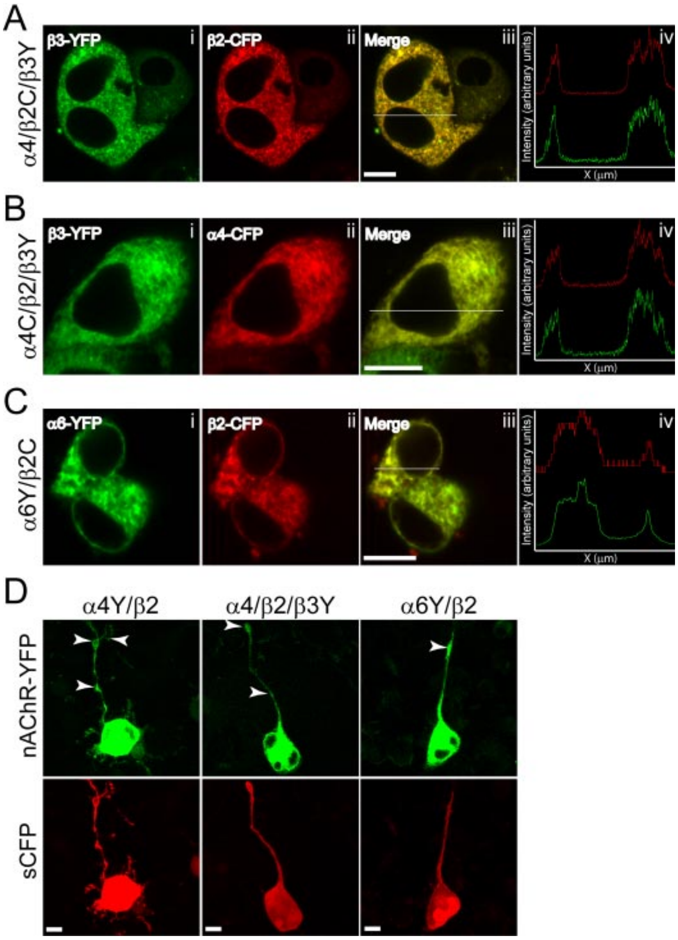

Fig. 4. β3-YFP and α6-YFP expression in neuronal cells. A, $\beta3$ and $\beta2$ nAChR subunits are localized similarly in N2a cells. N2a cells expressing $\alpha4\beta$2-CFPβ3-YFP receptors were imaged live with spectral confocal microscopy. Spectral images were acquired and specific β3-YFP and β2-CFP signals were extracted with linear unmixing. Green (β3-YFP; i) and red (β2-CFP; ii) pseudocolor was assigned, and yellow (Merge; iii) indicates colocalized proteins. Pixel intensities for the YFP and CFP channel were plotted (iv) along a line (iii) transecting the imaged cell. B, $\beta3$ and $\alpha4$ nAChR subunits are localized similarly in N2a cells. N2a cells expressing α4-CFP$\beta2\beta$3-YFP receptors were imaged live as described in A. C, $\alpha6$ and $\beta2$ nAChR subunits are localized similarly in N2a cells. N2a cells expressing α6-YFPβ2-CFP were imaged live as described in A and B. D, α4-YFP, β3-YFP, and α6-YFP are localized intracellularly and in processes in differentiated neurons. N2a cells were differentiated for 2 days (see *Materials and Methods* for details) to induce neurite outgrowth, followed by transfection with the indicated nAChR cDNA combinations plus soluble CFP to mark cellular morphology. One day after transfection, cells were imaged live as described in A to C. Scale bar, 10 μm.

this is the first fluorescence imaging reported for $\alpha6^*$ receptors, there is other evidence to corroborate our findings. Studies with [^{3}H]epibatidine demonstrate that a significant portion of $\alpha6\beta2$ and $\alpha6\beta2\beta3$ receptors are intracellular (~50 and ~20%, respectively), although some are delivered to the surface (Kuryatov et al., 2000; Tumkosit et al., 2006).

To further investigate the subcellular localization and trafficking of $\alpha6$ and $\beta3$ subunits, we imaged live, differentiated N2a cells and primary neurons. N2a cells can be induced to differentiate and undergo neurite outgrowth if serum is withdrawn and an activator of protein kinase A, dibutyryl-cAMP, is added (Fowler et al., 2001). In our previous work, $\alpha4\beta2$ receptors were localized to dendrites, but not axons, when expressed in primary midbrain neurons (Nashmi et al., 2003). We were interested in whether our fluorescent nicotinic receptor subunits were localized to N2a cell processes in a manner analogous to dendrites in primary neurons. Furthermore, we wanted to address the question of whether $\beta3$ is localized with other subunits at distal sites such as dendrites. This is an unsolved question, as there is no high-affinity probe (pharmacological or immunological) that can reliably and unambiguously isolate $\beta3^*$ receptors. N2a cells were plated on glass-bottomed dishes, and they were then differentiated for 2 days (see *Materials and Methods*) followed by transfection with various combinations of YFP-labeled and unlabeled nAChR subunits. Cells were also cotransfected with an expression plasmid for soluble CFP to mark total cell morphology. We found that $\alpha4\beta2$ receptors were indeed localized to neuronal processes in differentiated N2a cells (Fig. 4D, arrow), along with abundant expression in the cell soma. When $\beta3$-YFP was coexpressed with $\alpha4\beta2$, we observed a very similar pattern. We found that $\beta3$ was present even at the most distant elements of neuronal processes (Fig. 4D, arrow). Because this pattern is identical to that of $\alpha4\beta2$ in differentiated N2a cells, we conclude that $\beta3$ is likely assembling with $\alpha4\beta2$ receptors and that the YFP label in the M3-M4 loop is not disrupting the normal cellular trafficking of $\alpha4\beta2\beta3$ pentamers. To further characterize the localization of $\beta3^*$ receptors, we coexpressed $\beta3$-YFP with $\alpha4\beta2$ receptors in primary rat hippocampal neurons (Nashmi et al., 2003). To minimize overexpression artifacts, cells were imaged live only 18 to 24 h after transfection. We found that $\beta3^*$ receptors were localized very similarly to $\alpha4\beta2$ receptors in our previous studies with primary neurons; we noted uniform localization in the soma, suggestive of endoplasmic reticulum, and dendritic localization (Fig. 5A, arrow) and an absence of localization in axons. A high-magnification micrograph demonstrates the dendritic localization of these putative $\alpha4\beta2\beta3$ receptors (Fig. 5A, right). In cells coexpressing $\alpha4/\beta2/\beta3$Y with soluble CFP [to mark total cell morphology, similar to Nashmi et al. (2003)], $\beta3$ subunits did not traffic to a subregion of the cell interior likely to be axons (data not shown). To more directly determine whether $\beta3^*$ receptors could be localized to axons in these neurons, we coexpressed $\alpha4\beta2\beta3$Y receptors with a CFP-labeled axonal marker, tau. The tau-CFP decorated axons in hippocampal neurons, with proximal (relative to the cell body) portions of the axon being labeled more strongly than distal portions (Fig. 5B). In all cells examined, we noted the presence of YFP-labeled $\beta3$ subunits in these proximal axons but not distal axons (Fig. 5B, arrow). These data in differentiated N2a cells and primary neurons suggest that $\beta3$ assembles efficiently with $\alpha4\beta2$ receptors, and it is thus cotrafficked and targeted to distal sites in neurons.

Because $\alpha6$-YFP* receptors do not function in our hands, we wanted to determine whether this is due to a subtle trafficking defect that could prevent the correct delivery of $\alpha6$-YFP to the plasma membrane. Although we could readily detect $\alpha6$ fluorescence in the cell body of undifferentiated N2a cells, we wanted to further probe the cellular trafficking of $\alpha6^*$ receptors by expressing them in differentiated N2a cells that contain processes. To evaluate the subcellular localization of $\alpha6^*$ receptors, we expressed $\alpha6$-YFP with $\beta2$ in differentiated N2a cells. To our surprise, we found that $\alpha6\beta2$ receptors were trafficked to neuronal processes in a manner analogous to $\alpha4\beta2$ and $\alpha4\beta2\beta3$ receptors (Fig. 4D, arrow). To further address this question, we expressed $\alpha6$-YFP$\beta2$ receptors in rat hippocampal neurons as described for $\alpha4\beta2\beta3$-YFP. We observed a localization pattern for $\alpha6$-YFP that was very similar to $\alpha4\beta2\beta3$-YFP. These receptors were well expressed in the cell soma, but they were readily detectable in dendrites as well (Fig. 5A, arrow). In experiments with coexpressed soluble CFP and $\alpha6$-YFP$\beta2$ receptors, $\alpha6$ subunits were not detected in putative axons (data not shown). In tau-CFP/$\alpha6$-YFP$\beta2$ coexpression experiments, $\alpha6$ subunits (similar to $\alpha4\beta2$ but not $\alpha4\beta2\beta3$ receptors) were not detected in tau-labeled axons (Fig. 5B, arrow). These data indicate that, although $\alpha6^*$ receptors produce little or no agonist-induced conductance in mammalian tissue culture cells, they are expressed well and trafficked similarly compared with $\alpha4\beta2$ and $\beta3^*$ receptors.

FRET Revealed Assembly of $\alpha6$ and $\beta3$ Subunits into nAChR Pentamers. The fact that $\alpha4/\beta2/\beta3$ and $\alpha6/\beta2$ subunits are colocalized in the cell body and cotargeted to processes and dendrites in neurons suggests that they are assembled into pentameric receptors. The question of receptor assembly is often answered by simply measuring agonist-induced conductance increases in cells expressing a subunit combination of interest, or by applying a selective agonist or inhibitor to a pure receptor population of known pharmacological properties. This approach is not applicable, however, for $\alpha6^*$ and $\beta3^*$ receptors. $\alpha6^*$ receptors do not function well in heterologous expression systems, so it is not straightforward to determine the extent to which free $\alpha6$ subunits

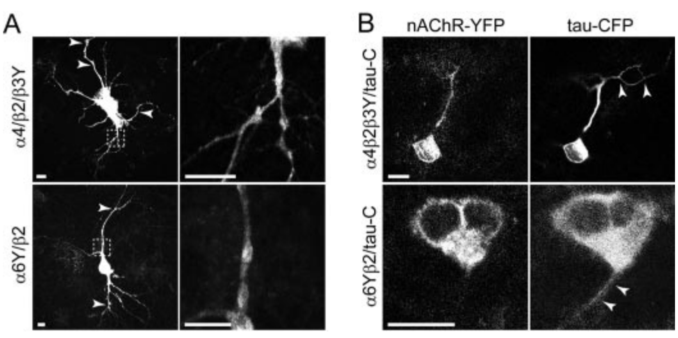

Fig. 5. Localization of $\beta3^*$ and $\alpha6^*$ receptors in primary neurons. A, $\beta3$-YFP and $\alpha6$-YFP are localized in the cell soma and in dendrites in primary hippocampal neurons. E18 rat hippocampal neurons were plated and cultured for 14 days followed by transfection with the indicated nAChR cDNAs. One day after transfection, cells were imaged live. Right, higher magnification image of the boxed area in the left panel. B, $\beta3^*$ and $\alpha6^*$ receptors are absent from axons. Neurons were transfected with the indicated nAChR cDNAs along with CFP-tau, followed by live confocal imaging as described in A. Scale bar, 10 μm.

assemble into pentameric receptors. Similarly for $\beta3$, although it is functional in oocytes (Fig. 2), there are no pharmacological probes that can be applied to $\beta3^*$ receptors to study their assembly or subunit composition. Others have indirectly measured receptor assembly of nicotinic subunits by using biochemical techniques such as immunoprecipitation (Zoli et al., 2002; Champtiaux et al., 2003) and centrifugation (Kuryatov et al., 2000) or by forcing subunits to assemble by using molecular concatamers (Tapia et al., 2007). To directly determine whether two nicotinic receptor subunits interact and, possibly, assemble to form pentameric receptors, we have used FRET coupled with our CFP- and YFP-tagged receptors. In the context of our nicotinic receptor subunits labeled with YFP or CFP in the M3-M4 loop, only subunits that interact will undergo FRET, because FRET occurs only when donors and acceptors are within 100 Å. Furthermore, we previously demonstrated that the efficiency of FRET directly correlates with the number of functional, plasma membrane-localized pentameric receptors (Nashmi et al., 2003). To measure FRET between subunits, we used the acceptor photobleaching method (Nashmi et al., 2003). In this method, we measure CFP dequenching during incremental photodestruction of YFP. CFP was excited at 439 nm, whereas YFP was bleached at 514 nm (Fig. 6A). Because the emission spectra for CFP and YFP overlap significantly, we imaged using a confocal microscope with spectral imaging capabilities along with a linear unmixing algorithm (described under *Materials and Methods*).

Fluorescent $\alpha4$ and $\beta2$ subunits are functional and undergo robust FRET in mammalian cells (Nashmi et al., 2003), so we used these subunits in our acceptor photobleaching assay with XFP-tagged $\beta3$ and $\alpha6$. We expressed $\beta3$-YFP with untagged $\alpha4$ and $\beta2$-CFP in N2a cells, followed by live cell FRET imaging. We recorded the whole-cell fluorescence intensity for $\beta3$-YFP and $\beta2$-CFP before and after photobleaching of YFP with the 514-nm laser, and we expressed with pseudocolor intensity scaling (Fig. 6B). In this experiment, $\beta2$-CFP was clearly dequenched after $\beta3$-YFP photodestruction (Fig. 6B), indicating that the two subunits had been undergoing FRET. In a similar experiment, we recorded multiple spectral images at several time points during YFP photodestruction. This revealed a corresponding increase in CFP intensity (Fig. 6C). A reciprocal experiment was also done, where $\beta3$-YFP was coexpressed with $\alpha4$-CFP and untagged $\beta2$. We recorded a similar dequenching for $\alpha4$-CFP after YFP photobleaching (Fig. 6, D and E), indicating FRET between these subunits as well. Both for $\beta2/\beta3$ and $\alpha4/\beta3$ FRET, we found no difference between FRET inside the cell versus FRET at the cell periphery at or near the plasma membrane. These results directly demonstrate that $\beta3$ is able to assemble with $\alpha4\beta2$ receptors in neuronal cells. This assembly likely occurs in the endoplasmic reticulum, which is consistent with previous findings (Nashmi et al., 2003).

There are many different putative $\alpha6^*$ receptor subtypes in brain, including $\alpha6\beta2$, $\alpha6\beta2\beta3$, $\alpha6\alpha4\beta2$, and $\alpha6\alpha4\beta2\beta3$ (Salminen et al., 2007). To begin to study $\alpha6^*$ receptor assembly, we measured FRET between $\alpha6$-YFP and $\beta2$-CFP. In response to YFP bleaching, we recorded a robust dequenching of $\beta2$-CFP throughout the cell, indicating FRET between these subunits (Fig. 6, F and G). The pattern of localization and FRET pattern was identical to $\alpha4\beta2\beta3$ receptors.

To further quantify FRET between $\alpha4/\beta2$ subunits and

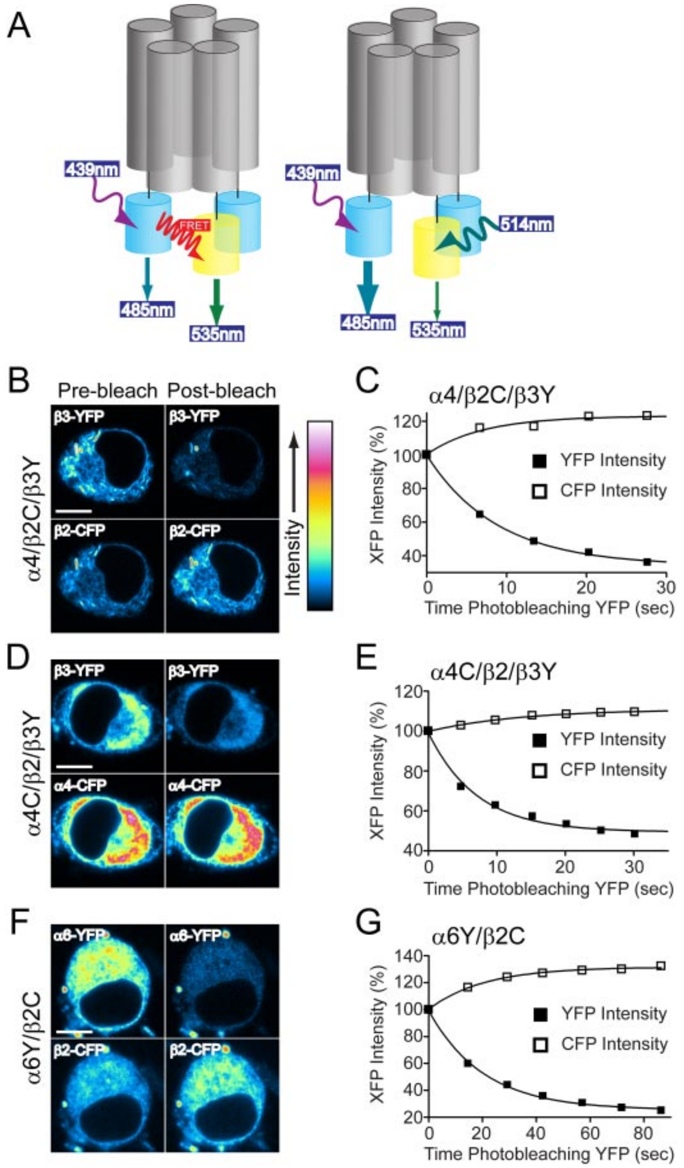

Fig. 6. FRET reveals assembly of $\beta3$ and $\alpha6$ nAChR subunits with $\alpha4$ and $\beta2$. A, Nicotinic receptor FRET schematic diagram. Gray cylinders indicate nAChR subunits, whereas cyan or yellow cylinders attached to nAChR subunits indicate CFP or YFP, respectively. FRET between nAChR subunits used the acceptor photobleaching method. When subunits are assembled, 439-nm excitation of CFP (donor) results in some emission of CFP at 485 nm, and some nonradiative transfer of energy (FRET) to YFP (acceptor) and resulting in emission at 535 nm. Acceptor photobleaching reveals FRET by measuring incremental dequenching of CFP during photodestruction of YFP with high-power 514-nm excitation. B, $\beta3$ assembles with $\beta2$ in the presence of $\alpha4$. N2a cells expressing $\alpha4\beta2$-CFP$\beta3$-YFP receptors were imaged live for FRET. The 439-nm laser line was coupled to a confocal microscope equipped with spectral imaging capabilities; this instrument generated spectral images before and after photodestruction of YFP using the 514-nm laser. Specific CFP and YFP signals were generated with linear unmixing as described under *Materials and Methods*. YFP and CFP intensity throughout the cell before and after YFP photodestruction is shown using intensity scaling. C, plot of $\beta3$-YFP and $\beta2$-CFP intensity during incremental photodestruction of $\beta3$-YFP. Normalized data from a representative cell were fitted to an exponential decay. D, $\beta3$ assembles with $\alpha4$ in the presence of $\beta2$. N2a cells expressing $\alpha4$-CFP$\beta2\beta3$-YFP were imaged live for FRET as described in B. E, plot of $\beta3$-YFP and $\alpha4$-CFP intensity during incremental photodestruction of $\beta3$-YFP, similar to C. F, $\alpha6$ assembles with $\beta2$. N2a cells expressing $\alpha6$-YFP$\beta2$-CFP were imaged live for FRET as described in B. G, plot of $\alpha6$-YFP and $\beta2$-CFP intensity during incremental photodestruction of $\alpha6$-YFP, similar to C. Scale bar, 10 μm.

β3 or α6, we measured FRET *E* values for various receptor subtypes. α4-CFPβ2-YFP, α4β2-CFPβ3-YFP, and α4-CFPβ2β3-YFP receptors were expressed in N2a cells followed by acceptor photobleaching FRET (Fig. 7A). We acquired spectral images with 439-nm laser excitation before and during incremental photobleaching of YFP-labeled subunits, followed by extraction of true CFP and YFP image data using linear unmixing (see *Materials and Methods*). A scatterplot of CFP intensity in response to YFP photobleaching reveals FRET between the subunits in question (Fig. 7B) when the slope of the linear regression line is >0. This slope was used to calculate FRET efficiency values, which were expressed as bar graphs (Fig. 7C) or listed (Table 1). As shown qualitatively in Fig. 6, significant FRET occurred in all nAChR pentamer conditions. We noted a higher FRET *E* for α4C/β2Y than for β3Y with either β2C or α4C (Y, YFP; C, CFP). To assess the specificity of this measurement, we also measured FRET between β3 and a non-nAChR, CFP-labeled protein, mGAT1. GAT1 is also a multipass transmembrane protein with a CFP-tag at its C terminus, which faces the cytoplasm. This protein is mainly localized to the endoplasmic reticulum (data not shown). These two points are important, because it was critical for a specificity probe to have 1) the same membrane topology as our labeled nicotinic receptors, with respect to the attached fluorophore; and 2) the same subcellular localization such that they are capable of interacting with each other. In N2a cells expressing β3-YFP and mGAT1-CFP, we could not detect any FRET between these proteins (Table 1; Fig. 7C). In an even more rigorous test, we assessed FRET between β3-YFP and another Cys-loop receptor labeled in the M3-M4 loop, the CFP-labeled GluCl β subunit (Slimko et al., 2002; Nashmi et al., 2003). FRET between β3 and the GluCl β subunit was significantly smaller (FRET $E = 6 \pm 4\%$) than for α4 or β2 nAChR subunits (Table 1; Fig. 7C). Thus, our FRET results between β3 and other labeled nAChR subunits cannot be explained by random collision or interaction with unassembled subunits. Finally, we were interested in whether subtle changes in the location of the fluorophore within the β3 M3-M4 loop could influence its ability to undergo FRET with another subunit. FRET *E* decreases strongly with the distance between fluorophores. We reasoned that changes in the insertion point of YFP in β3, while holding the position of CFP in β2 constant, might alter FRET between these two subunits. To address this, we compared the FRET *E* between β2-CFP and two different β3-YFP constructs, β3-YFP$^{\mathrm{P379}}$ and β3-YFP$^{\mathrm{G367}}$, which have different insertion points for YFP within the M3-M4 loop. To our surprise, there was no change in the FRET *E* for these two subunits (Table 1; Fig. 7D).

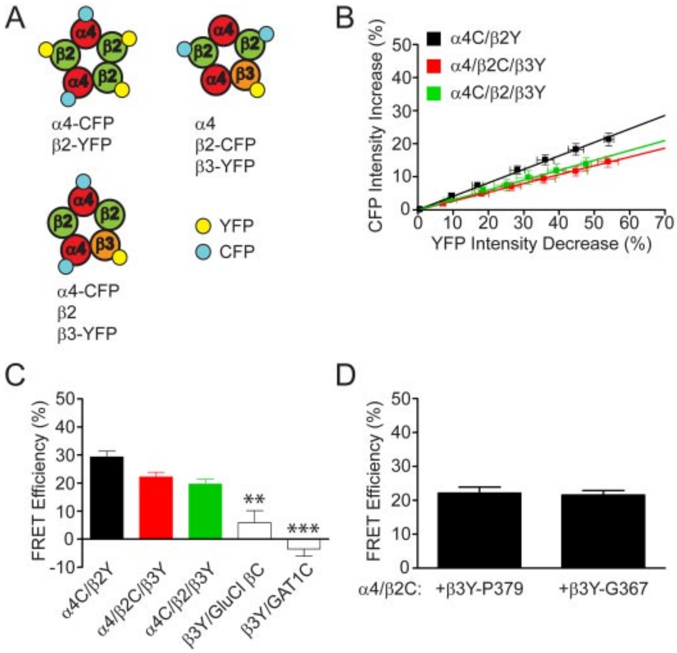

Fig. 7. β3 specifically assembles with α4β2 nAChRs. A, fluorescently labeled nicotinic receptor pentamers assayed for FRET in this experiment. N2a cells expressing the indicated receptor pentamers were assayed live for FRET using the acceptor photobleaching method. B, linear plots of donor (CFP) dequenching versus acceptor (YFP) photodestruction for nAChRs with the indicated fluorescent subunits. FRET efficiency was calculated by extrapolating linear regression plots to 100% YFP photodestruction as described under *Materials and Methods*. C, specific FRET signal detected between β3 and α4 or β2. The FRET efficiency for the given donor-acceptor pair was calculated from the linear plot shown in B as described under *Materials and Methods*. FRET between β3-YFP and mGAT1-CFP or GluCl β-CFP was measured as a specificity control. D, FRET efficiency for β3-YFP does not depend on the insertion site in the M3-M4 loop. Two β3-YFP constructs, β3-YFP$^{\mathrm{P379}}$ and β3-YFP$^{\mathrm{G367}}$, were compared for their ability to assemble with α4β2-CFP as measured by FRET. FRET efficiency was calculated as described in C. Error bars are ± S.E.M., and $n = 5$ to 15 cells for each condition. ***, $p < 0.001$; **, $p < 0.01$.

We quantitatively measured FRET between α6 and α4/β2 subunits as well. We expressed either α6Yβ2C or α6Yα4Cβ2 in N2a cells to measure FRET (Fig. 8A). The latter receptor was studied because recent work indicates that nAChR receptors containing both α6 and α4 1) exist and are functional in mouse brain tissue (Salminen et al., 2007), and 2) are both necessary to form the nAChR subtype with the highest affinity for nicotine yet reported in a functional assay (Salminen et al., 2007). Acceptor photobleaching FRET experiments reveal robust CFP dequenching in response to YFP photobleach for both of these receptor subtypes, indicating FRET (Fig. 8B). Similar to β3-YFP* receptors, we measured FRET *E* values for these two subtypes, and we found a FRET *E* of $36.0 \pm 2.4\%$ for α6Yβ2C and $21.9 \pm 1.1\%$ for α6Yα4Cβ2 (Table 1; Fig. 8C). We also assessed the specificity of our FRET measurements for α6 by measuring FRET between α6-YFP and mGAT1-CFP as described above for Fig. 7. Similar to β3 and mGAT1, we could record no significant FRET between α6 and mGAT1 (Table 1; Fig. 8C). FRET experiments between α6 and the GluCl β subunit, the most rigorous test conducted, yielded a small FRET signal (FRET $E = 14 \pm 2\%$) (Table 1; Fig. 8C). Because these subunits presumably do not form functional channels, there may be a small distortion of our α6 FRET signals that is due to partially assembled receptors. Because this signal is significantly smaller than for all other α6 combinations, FRET between subunits in pentameric receptors remains the most plausible explanation for the energy transfer we observe for α6. Finally, we studied FRET between β2-CFP and three α6-YFP constructs (α6-YFP$^{\mathrm{A405}}$, α6-YFP$^{\mathrm{G387}}$, and α6-YFP$^{\mathrm{G366}}$) that differed only in their insertion point for YFP within the M3-M4 loop. Again, we were surprised to find no significant difference in FRET *E* between these three α6 constructs (Table 1; Fig. 8D).

Several results described above gave us confidence that our XFP-labeled β3 and α6 constructs were performing as expected. After confirming that these subunits assemble and traffic normally when expressed independently of each other, we used these constructs together to study α6β2β3 nAChRs. This receptor represents a modest population of the total striatal nAChR pool, and it contributes to nicotine-stimulated dopamine release (Salminen et al., 2007). α6β2β3 receptors, where one subunit is untagged and the remaining subunits are either YFP- or CFP-tagged (α6Yβ2Cβ3, α6Yβ2β3C, and α6β2Yβ3C), were expressed in N2a cells (Fig. 9A). We measured robust donor dequenching for all receptor subtypes (Fig. 9B), which was confirmed with FRET *E* measurements (Table 1; Fig. 9C). Thus, aside from α6 functional measurements, we conclude that XFP-labeled α6 and β3 subunits exhibit normal subcellular trafficking and assembly compared with our well characterized fluorescent α4 and β2 subunits.

α6 and β3 Subunit Stoichiometry Probed with FRET. Having established that fluorescently labeled α6 and β3 are functional (β3 only), have a reasonable subcellular localization pattern, and assemble into nicotinic receptor pentamers with other subunits, we used these tools to probe an important question facing the nicotinic receptor field: subunit stoichiometry. A variety of creative approaches have been taken to understand subunit stoichiometry, including immunoprecipitation (Zoli et al., 2002; Champtiaux et al., 2003), density gradient centrifugation (Kuryatov et al., 2000), molecular concatamers/linked subunits (Tapia et al., 2007), reporter mutations (Boorman et al., 2000), and mouse genetic approaches (Gotti et al., 2005a; Salminen et al., 2007). We now use FRET to address the problem of subunit stoichiometry because FRET occurs only when subunits are directly interacting, and often assembled, with one another.

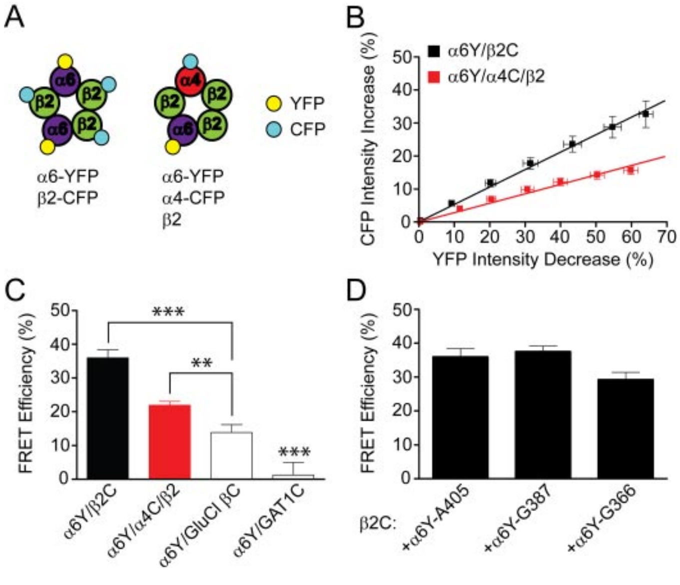

Fig. 8. α6 specifically assembles with α4 and β2 nAChR subunits. A, fluorescently labeled nicotinic receptor pentamers assayed for FRET in this experiment. N2a cells expressing the indicated receptor pentamers were assayed live for FRET using the acceptor photobleaching method. B, linear plots of donor (CFP) dequenching versus acceptor (YFP) photodestruction for nAChRs with the indicated fluorescent subunits. FRET efficiency was calculated by extrapolating linear regression plots to 100% YFP photodestruction as described under *Materials and Methods*. C, specific FRET signal detected between α6 and α4 or β2. The FRET efficiency for the given donor-acceptor pair was calculated from the linear plot shown in B as described under *Materials and Methods*. FRET between α6-YFP and mGAT1-CFP or GluCl β-CFP was measured as a specificity control. D, FRET efficiency for α6-YFP does not depend on the insertion site in the M3-M4 loop. Three α6-YFP constructs, α6-YFP^{A405}, α6-YFP^{G387}, and α6-YFP^{G366}, were compared for their ability to assemble with β2-CFP as measured by FRET. FRET efficiency was calculated as described in C. Error bars are ± S.E.M., and $n = 5$ to 15 cells for each condition. ***, $p < 0.001$; **, $p < 0.01$.

We have previously shown that FRET efficiency correlates directly with functional receptor pentamers (Nashmi et al., 2003). To examine the number of α6 and β3 subunits in a nicotinic receptor pentamer, we first used FRET to examine the stoichiometry of a well studied receptor, namely, α4β2 receptors. It is widely accepted that α4 and β2 subunits assemble to form both high-sensitivity (HS) and low-sensitivity (LS) receptors. Cells often produce a mixture of these two receptors (Buisson and Bertrand, 2001; Nashmi et al., 2003), although they can be induced to express a pure population of one or the other (Nelson et al., 2003; Briggs et al., 2006). The subunit stoichiometry of HS receptors is postulated to be $(\alpha4)_2(\beta2)_3$, whereas the LS receptors is thought to be $(\alpha4)_3(\beta2)_2$ (Nelson et al., 2003). Regardless of the fraction of HS and LS receptors, we took advantage of the fact that all α4β2 receptors presumably contain two or more α4 and two or more β2 subunits. We reasoned that when cells express α4-YFP and α4-CFP along with β2 (Fig. 10A), a fraction of the receptors will contain both YFP- and CFP-labeled α4 subunits, and they will therefore be detectable by FRET. Confirming this hypothesis, we did detect modest dequenching of α4-CFP upon incremental α4-YFP photobleaching (Fig. 10B). FRET *E* for α4Yα4Cβ2 receptors was 22.2 ± 2.3% (Table 1; Fig. 10C). We also conducted a similar experiment with β2, and we found a modest FRET signal (FRET *E* = 16.3 ± 1.7%) between β2-YFP and β2-CFP within the same pentamer (Table 1; Fig. 10, B and C). We next used this assay to determine whether α6* and β3* receptors have one or more than one α6 or β3 subunit per pentamer. N2a cells expressing either α6Yα6Cβ2 or α4β2β3Yβ3C receptors were

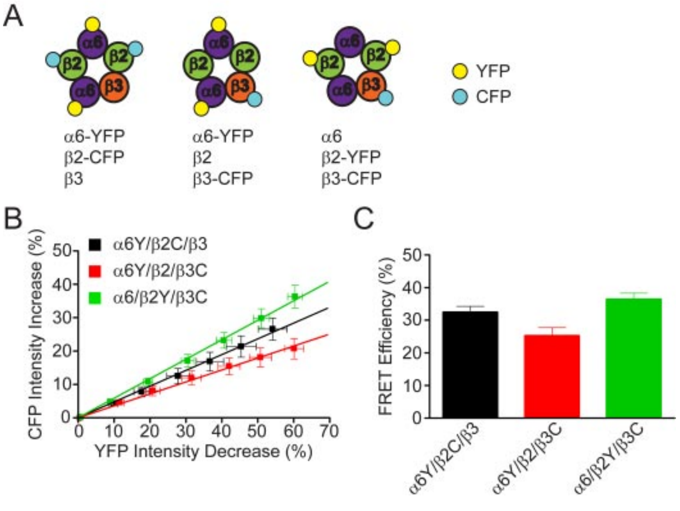

Fig. 9. FRET reveals assembly of α6β2β3 nAChRs. A, fluorescently labeled nicotinic receptor pentamers assayed for FRET in this experiment. N2a cells expressing the indicated receptor pentamers were assayed live for FRET using the acceptor photobleaching method. B, linear plots of donor (CFP) dequenching versus acceptor (YFP) photodestruction for nAChRs with the indicated fluorescent subunits. FRET efficiency was calculated by extrapolating linear regression plots to 100% YFP photodestruction as described under *Materials and Methods*. C, specific FRET signal detected between α6-YFP and β2-CFP with β3 present, α6-YFP and β3-CFP with β2 present, and β2-YFP and β3-CFP with α6 present. The FRET efficiency for the given donor-acceptor pair was calculated from the linear plot shown in B as described under *Materials and Methods*. Error bars are ± S.E.M., and $n = 10$ to 15 cells for each condition.

analyzed for FRET (Fig. 10A). We measured a strong FRET signal between α6-YFP and α6-CFP in donor dequenching (Fig. 10B), corresponding to a robust FRET *E* of 27.8 ± 1.7% (Table 1; Fig. 10C). Thus, these data are the first to directly demonstrate that α6* receptors are capable of containing at least two α6 subunits, similar to other α subunits such as α3 and α4. In contrast to α6, β3 is thought to be an "ancillary subunit", only able to incorporate into nAChRs with other α and β subunits (Groot-Kormelink et al., 1998). We could detect little or no FRET between β3-YFP and β3-CFP (FRET *E* = 2.6 ± 1.3%) (Table 1; Fig. 10, B and C). This was a specific result, because β3-YFP and β3-CFP were able to FRET with other subunits (Figs. 7 and 9), thus ruling out the notion that one of these subunits is not able to undergo FRET. These data are the first to directly demonstrate that receptors containing β3 subunits are only able to incorporate a single copy of this subunit. We interpret this to mean that β3 incorporates into the "accessory" position in a nAChR pentamer (Tumkosit et al., 2006), and it likely does not contribute to either of the two α:non-α interfaces that form the ligand-binding sites.

After confirming via FRET that β3 incorporates into nAChRs at a frequency of one subunit per pentamer, we used β3 coexpression to further probe the subunit stoichiometry of α4* and α6* receptors. We coexpressed β3-WT with α4-YFP, α4-CFP, and β2 such that β3 was in excess. In this experiment, β3 is incorporated into α4-XFPβ2 receptors and will displace either an α4 or β2 subunit. There was a significant decline in FRET for cells expressing α4Yα4Cβ2β3 receptors versus those expressing α4Yα4Cβ2 (Table 1; Fig. 10, D and G). We interpret this result to mean that β3 incorporation has fixed the subunit stoichiometry of FRET-competent receptors to $(\alpha4Y)_1(\alpha4C)_1(\beta2)_2(\beta3)_1$ versus the following mixture of FRET-competent receptors without β3: $(\alpha4Y)_2(\alpha4C)_1(\beta2)_2$, $(\alpha4Y)_1(\alpha4C)_2(\beta2)_2$ and $(\alpha4Y)_1(\alpha4C)_1(\beta2)_3$. A reduction in FRET for two XFP-labeled α4 subunits (YFP and CFP) versus three is reasonable and expected based on the work of others (Corry et al., 2005), and on our calculations that predict the relative FRET efficiencies in pentamers with XFP-labeled subunits (data not shown). Thus, β3 incorporation into nAChR pentamers likely displaces one subunit, and

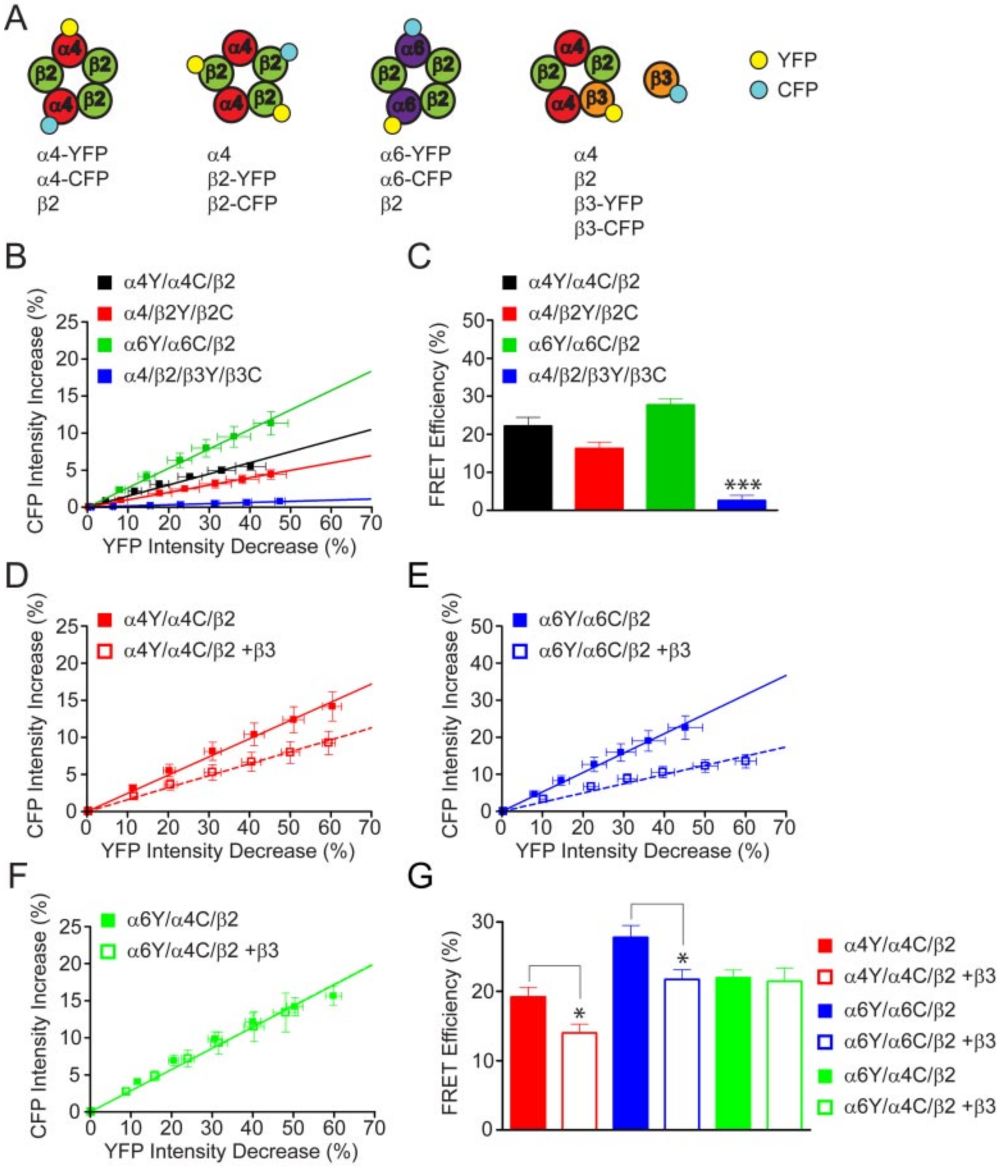

Fig. 10. β3 and α6 subunit stoichiometry studied by FRET. A, fluorescently labeled nicotinic receptor pentamers assayed for FRET in this experiment. N2a cells expressing the indicated receptor pentamers were assayed live for FRET using the acceptor photobleaching method. B, linear plots of donor (CFP) dequenching versus acceptor (YFP) photodestruction for nAChRs with the indicated fluorescent subunits. FRET efficiency was calculated by extrapolating linear regression plots to 100% YFP photodestruction as described under *Materials and Methods.* C, α6-containing receptors have multiple α6 subunits whereas β3-containing receptors have only one β3 subunit. The FRET efficiency for the given donor-acceptor pair was calculated from the linear plot shown in B as described under *Materials and Methods.* D to F, linear plots of donor (CFP) dequenching versus acceptor (YFP) photodestruction for nAChRs with the indicated fluorescent subunits. FRET efficiency was calculated by extrapolating linear regression plots to 100% YFP photodestruction as described under *Materials and Methods.* G, β3 coexpression with α4β2 or α6β2 receptors reduces FRET between YFP- and CFP-labeled α subunits. FRET *E* value for a given subunit combination was calculated from the linear plot in D, E, or F. Error bars are ± S.E.M., and *n* = 10 to 15 cells for each condition. ***, $p < 0.001$; *, $p < 0.05$.

results in a decrease in $\alpha4$ to $\alpha4$ FRET for pentamers with a mixed subunit stoichiometry.

To determine whether $\alpha6^*$ receptors have a fixed or a mixed subunit stoichiometry, we coexpressed $\beta3$ in excess with $\alpha6$-YFP, $\alpha6$-CFP, and $\beta2$. If $\alpha6^*$ receptors only incorporate two $\alpha6$ subunits, we expect to observe little or no change in FRET between $\alpha6$-YFP and $\alpha6$-CFP because $\beta3$ will only displace one unlabeled $\beta2$ subunit. However, if $\alpha6^*$ receptors exist as a mixture of $(\alpha6)_2(\beta2)_3$ and $(\alpha6)_3(\beta2)_2$ subtypes similar to $\alpha4^*$ receptors, we expect to observe a similar decline in FRET when $\beta3$ is present to induce only the $(\alpha6)_2(\beta2)_2\beta3$ stoichiometry. The latter was the case. We noted a significant decline in the slope of the donor dequenching profile for $\alpha6\mathrm{Y}\alpha6\mathrm{C}^*$ receptors when $\beta3$ was present (Table 1; Fig. 10E) and a decline in the FRET *E* for $\alpha6\mathrm{Y}\alpha6\mathrm{C}\beta2\beta3$ (21.7 ± 1.4%) versus $\alpha6\mathrm{Y}\alpha6\mathrm{C}\beta2$ (27.8 ± 1.7%) (Table 1; Fig. 10G). Thus, fluorescent $\alpha6^*$ receptors behave identically to $\alpha4^*$ receptors, and these results suggest that $\alpha6^*$ receptors are capable of forming either of two subunit stoichiometries: $(\alpha6)_2(\beta2)_3$ and $(\alpha6)_3(\beta2)_2$.

Several groups have reported the existence of $\alpha4\alpha6^*$ receptors in brain tissue (Zoli et al., 2002; Salminen et al., 2007), and $\alpha4\alpha6\beta2\beta3^*$ receptors (presumably $\alpha4_1\alpha6_1\beta2_2\beta3_1$) have high affinity for nicotine (Salminen et al., 2007). To learn about the subunit stoichiometry of $\alpha4\alpha6^*$ receptors, we expressed $\alpha6$-YFP and $\alpha4$-CFP along with $\beta2$ subunits in N2a cells. We noted a modest FRET signal, indicating that these subunits are present in some of the same nicotinic receptor pentamers (Fig. 8, B and C; Fig. 10F). In contrast to our results with $\alpha6\beta2\beta3$ and $\alpha4\beta2\beta3$ receptors, there was no difference between cells transfected with $\alpha6\mathrm{Y}/\alpha4\mathrm{C}/\beta2$ and $\alpha6\mathrm{Y}/\alpha4\mathrm{C}/\beta2/\beta3$ subunits (Fig. 10, F and G). This shows that addition of excess $\beta3$ subunits did not reduce FRET between $\alpha6\mathrm{Y}$ and $\alpha4\mathrm{C}$. Thus, this experiment is not informative regarding $\alpha4\alpha6\beta2\beta3$ receptors in N2a cells. For instance, the $\alpha{:}\beta$ subunit stoichiometry as measured by FRET may not change in the presence of $\beta3$.

TIRF Revealed $\alpha4^*$, $\alpha6^*$, and $\beta3^*$ Receptor Plasma Membrane Localization. Having confirmed that fluorescent $\alpha6$ and $\beta3$ subunits assemble to form nicotinic receptor pentamers, we probed the plasma membrane localization of nAChRs containing these subunits using TIRF microscopy. For nicotinic receptor subunits fused to fluorescent proteins, TIRF illumination selectively excites only receptors at or very close to the plasma membrane. We imaged live N2a cells expressing $\alpha4\beta2\beta3$-YFP, $\alpha6$-YFP$\beta2$, and $\alpha4$-YFP$\beta2$. In epifluorescence mode (Fig. 11, epi), these receptors exhibited an intracellular, endoplasmic reticulum-like localization identical to our confocal imaging data in Fig. 4. In TIRF mode, however, we noted robust plasma membrane fluorescence for all receptor combinations. We were surprised to find $\alpha4\mathrm{Y}\beta2$ receptors to be localized to distinct, filamentous structures protruding from the cell body (Fig. 11A, arrow). This specific filamentous pattern was seen for >90% of the plasma membrane fluorescence. These structures were reminiscent of filopodia, which are actin-dependent plasma membrane protrusions. To test whether these structures contain actin, a hallmark of filopodia, we imaged cells stained with rhodamine-phalloidin, a marker of polymerized actin. We noted distinct, actin-containing protrusions (Fig. 11B, arrow). These structures were actin-dependent, because they were destroyed by treatment with latrunculin B, an actin-disrupting agent (Fig. 11B, right). These data indicate that, in N2a cells, $\alpha4\mathrm{Y}\beta2$ nicotinic receptors are localized to membrane protrusions that strongly resemble filopodia.

Similar to $\alpha4\mathrm{Y}\beta2$, we imaged live N2a cells, in TIRF mode, expressing either $\alpha4\beta2\beta3\mathrm{Y}$ or $\alpha6\mathrm{Y}\beta2$. To our surprise, we noted a very different localization pattern compared with $\alpha4\mathrm{Y}\beta2$. $\beta3^*$ and $\alpha6^*$ receptors were well expressed on the plasma membrane, but there was no evidence of membrane

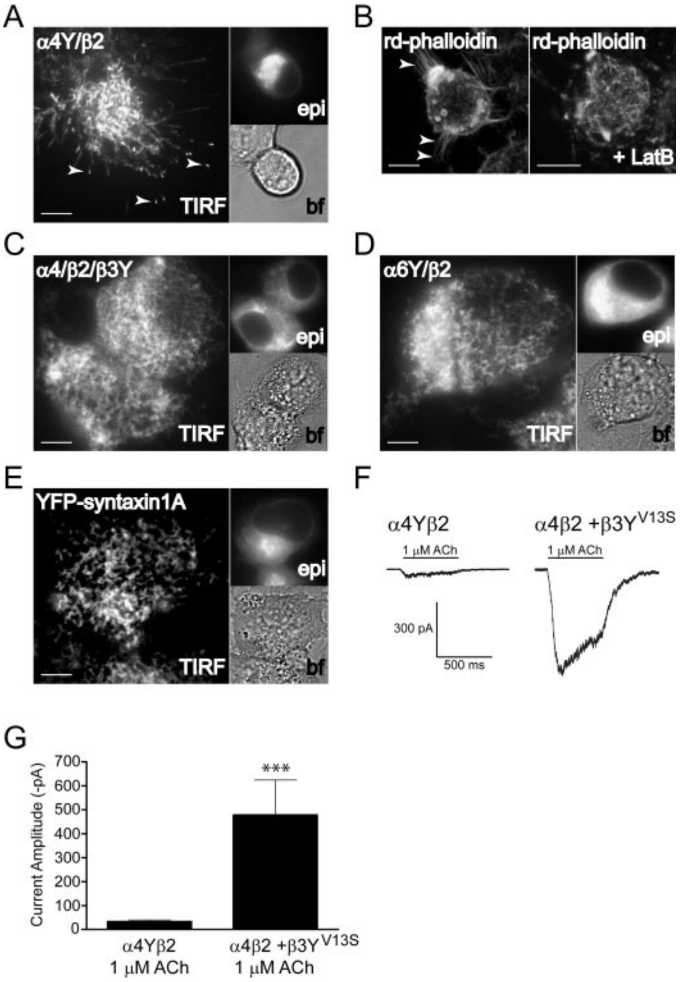

Fig. 11. Distinct plasma membrane localization for $\alpha4\beta2$ versus $\beta3^*$ and $\alpha6^*$ receptors. A, plasma membrane localization of $\alpha4\beta2$ receptors. N2a cells plated on polyethylenimine, expressing $\alpha4$-YFP$\beta2$ receptors were imaged live under TIRF illumination. Arrows indicate $\alpha4\beta2$ receptors in distal parts of membrane protrusions. Epifluorescence (non-TIRF) images and bright-field images are shown for reference. Scale bars, 10 μm. B, filopodia in N2a cells. N2a cells were plated as described in A and stained with rhodamine-phalloidin to mark actin filaments (left, arrows) in the cytoplasm and in filopodia-like protrusions. Cells were imaged with confocal microscopy. Cells were treated with latrunculin B to disrupt actin filaments (right). C and D, lattice-like and punctate localization of $\alpha4\beta2\beta3$-YFP and $\alpha6$-YFP$\beta2$ receptors on the plasma membrane. N2a cells expressing the indicated nAChR subunits were imaged in TIRF mode as described in A. Epifluorescence and bright-field images are shown for reference. E, syntaxin1A plasma membrane localization is similar to $\beta3$ and $\alpha6$ nicotinic receptors. N2a cells expressing YFP-syntaxin1A were imaged as described in A, C, and D. F, $\beta3$-YFP subunits on the plasma membrane are functional. N2a cells expressing either $\alpha4$-YFP$\beta2$ or $\alpha4\beta2\beta3$-YFP$^{\mathrm{V13S}}$ were studied using whole-cell patch-clamp electrophysiology. Voltage-clamped cells were stimulated with 1 μM ACh for 500 ms. A representative response from the indicated nAChR subtype is shown. Scale bar, 300 pA and 500 ms. G, quantification of electrophysiology data in F. Peak current responses from $\alpha4$-YFP$\beta2$ and $\alpha4\beta2\beta3$-YFP$^{\mathrm{V13S}}$ (1 μM stimulation) were averaged for four cells. ***, $p < 0.001$.

protrusion or filopodia localization for these receptors. Rather, these proteins exhibited a punctate, lattice-like localization pattern on the plasma membrane (Fig. 11, C and D). This pattern was consistently seen in other cells types such as HEK293 (data not shown), and it suggests that β3* or α6* receptors cluster in microdomains distinct from α4β2 receptors. Alternatively, some of these puncta could be clusters of assembled receptors adjacent to the plasma membrane within the 100-nm evanescent wave. We also recorded movies to monitor plasma membrane nAChRs, and we noted that although they exhibited localized, stochastic movements, most of these receptor clusters did not travel or translocate to any significant degree (data not shown). This localization pattern resembles that of the soluble *N*-ethylmaleimide-sensitive factor attachment protein receptor protein syntaxin1, which was localized to distinct granules or microdomains in the plasma membrane when observed in TIRF (Ohara-Imaizumi et al., 2004). Because soluble *N*-ethylmaleimide-sensitive factor attachment protein receptor proteins are important regulators of ion channel subcellular trafficking and function in neuronal soma and synaptic terminals (Bezprozvanny et al., 1995), we compared the plasma membrane localization pattern of YFP-syntaxin1A with β3-YFP* and α6-YFP* receptors in N2a cells. We observed a plasma membrane distribution pattern for syntaxin1A that was very similar to β3 and α6 subunits; syntaxin1A was also localized to distinct clusters adjacent to the plasma membrane or microdomains on the plasma membrane (Fig. 11E).

It is possible that the different plasma membrane localization pattern observed for α4Yβ2 versus α4β2β3Y reflects the localization pattern of functional versus nonfunctional nicotinic receptors, respectively. To address this, we used whole-cell patch-clamp electrophysiology to record voltage-clamped responses from functional, fluorescent nAChRs expressed in N2a cells. Because WT (Broadbent et al., 2006) or YFP-tagged β3 subunits (Fig. 2B) significantly attenuated nAChR responses, we used β3-YFP^{V13S} subunits to reverse this attenuation. We reasoned that, if coexpressed and coassembled with α4β2 receptors, β3-YFP^{V13S} subunits should 1) induce the high-sensitivity $(\alpha4)_2(\beta2)_2(\beta3)_1$ subunit stoichiometry similar to previous work (Broadbent et al., 2006); and 2) lower the EC_{50} for activation of this high-sensitivity form by approximately 1 order of magnitude (Fig. 3B). When voltage-clamped N2a cells expressing α4Yβ2 receptors were stimulated with 1 μM ACh, a dose that induces minimal (20–30 pA) responses in our previous work with HEK293 cells (Nashmi et al., 2003), we observed an identical phenotype (Fig. 11F). Responses to 300 μM ACh were robust (200–400 pA), indicating significant plasma membrane expression of these receptors (data not shown). However, cells expressing α4β2β3Y^{V13S} receptors exhibited robust responses to 1 μM ACh (Fig. 11F), which were significantly larger than the response size for α4β2 receptors (Fig. 11G). This is the expected result if β3-YFP^{V13S} subunits are incorporated into functional nAChRs in N2a cells, and it is consistent with our *X. laevis* oocyte experiments (Figs. 2 and 3), and with the work of others (Broadbent et al., 2006). These data confirm that both α4Yβ2 and α4β2β3Y receptors are functional in N2a cells and that the observed plasma membrane localization pattern for functional α4Yβ2 and α4β2β3Y receptors is significantly different.

Discussion

Subcellular Localization of Nicotinic ACh Receptors. α4β2 receptors were localized intracellularly in our previous studies in HEK293 cells and primary midbrain neurons (Nashmi et al., 2003), although enough receptors are expressed on the cell surface to record responses using electrophysiology. Furthermore, knockin mice with YFP-labeled α4 subunits show uniform intracellular and plasma membrane localization of α4* receptors (Nashmi et al., 2007). Other investigators have found a similar localization pattern for α4β2 (Xu et al., 2006), α3β4 (Grailhe et al., 2004), α7 (Xu et al., 2006), and 5-hydroxytryptamine$_{3A}$ (Grailhe et al., 2004) receptors. In light of these studies, it is not surprising that we found fully assembled β3* and α6* receptors in intracellular stores in N2a cells. This suggests that neurons produce more assembled nAChRs than they can use at any particular time and that they may require the ability to rapidly change either their total number or specific stoichiometry of receptor subtypes on the plasma membrane in response to different extracellular signals. The specific phenomenon of up- or down-regulation of nicotinic receptors occurs during chronic nicotine exposure (Marks et al., 1983; Nashmi et al., 2007) and in other neurological disorders including autism and Alzheimer's disease (for review, see Graham et al., 2002).

α4β2 receptors were localized to actin-dependent membrane protrusions akin to filopodia, whereas β3* and α6* receptors were not. Filopodia are critical sensory components of growth cones, influencing growth cone orientation and turning toward extracellular cues. Nicotinic receptors are required for growth cone orientation in some neuronal types (Zheng et al., 1994). Interestingly, α4 and β2 subunits are highly expressed during embryogenesis (Azam et al., 2007), suggesting a role for these subunits in neuronal development and in adult function. α6 and β3 subunits, in contrast, are not expressed at appreciable levels until after birth (Azam et al., 2007). We speculate that the differences we observe for α4β2 versus β3 or α6 receptors on the plasma membrane could reflect their involvement (or lack thereof) in neuronal development.

α6 Functional Expression. Although it remains unclear why it is very difficult to record functional responses from α6* receptors, this study advances our knowledge of this problem. In 20 different attempts, using several expression/assay systems, we could record no α6 functional responses (Supplemental Data; Table 1). This could be a result of many different problems, such as α6 mRNA stability, α6 protein production, proper assembly of α6* receptors, intracellular trafficking, or plasma membrane delivery. We (herein) and others have demonstrated that cells do not have an apparent problem synthesizing α6 subunits (Kuryatov et al., 2000; Tumkosit et al., 2006), and either partial or full assembly of α6* receptors occurs in mammalian tissue culture cells and *X. laevis* oocytes (Kuryatov et al., 2000; Tumkosit et al., 2006). We found robust ectopic expression of α6-YFP subunits in tissue culture cells and in primary neurons. Furthermore, based on our FRET measurements, α6 subunits are fully capable of assembling with α4, β2, and β3 subunits in a manner indistinguishable from that of α4 and β2. These are the presumptive subunits necessary for expression of α6* receptors in vivo (Salminen et al., 2007). Assembled α6* receptors are also localized identically to α4* receptors in our experiments. Finally, and most surprisingly, we ruled out the possibility that α6* receptors are not delivered to the plasma membrane. Plasma membrane localization for α6* receptors was identical to that of assembled, functional β3* receptors. From these data, we conclude that, although fully assembled and partially localized on the plasma membrane, α6* receptors do not yield responses in standard functional assays. This information should facilitate the design of new experimental approaches to develop robust, reproducible reconstitution of α6 function in vitro.

Because we found no difference in FRET between α4α6β2 receptors ± β3, the experiments probing the stoichiometry of α4α6β2β3 receptors are uninformative. It is possible that there are no assembled α4α6β2β3 receptors in N2a cells. We suggest that catecholaminergic or retinal ganglion cells, which are those cells in vivo that produce high levels of functional α6* receptors (Léna et al., 1999; Whiteaker et al., 2000; Champtiaux et al., 2002, 2003; Zoli et al., 2002; Gotti et al., 2005b), express a unique protein or factor that is essential for proper function of these receptors. It is also possible that these cells are specially suited to traffic α6* and/or β3* receptors to distal axons/presynaptic terminals. Our results probing α6 and β3 axonal targeting (Fig. 5B) may be negative as a result of differences in the cell trafficking machinery in hippocampal (α6-negative) versus catecholaminergic (α6-positive) neurons, and they highlight the need for a more detailed study of α6/β3 axonal targeting in α6-positive neurons. Perhaps there is an α6-associated protein similar to other nicotinic receptor-associated proteins, such as lynx1 (Miwa et al., 1999), which remains to be characterized.

α6* and β3* Receptor Assembly and Subunit Stoichiometry. We previously demonstrated that FRET between XFP-labeled nicotinic receptor subunits not only reveals proximity between subunits but that increased FRET efficiency correlates with increased assembled, functional receptors (Nashmi et al., 2003). Because we cannot measure functional responses from α6* receptors, we must draw conclusions about their behavior inferentially by comparing it to α4β2 receptors, which are functionally expressed. Using these criteria, we conclude that α6 subunits assemble with α4, β2, and β3 subunits. Furthermore, we conducted several specificity controls (FRET with GAT1C and GluCl β) that revealed that FRET between α6 or β3 and other nAChR subunits is robust and likely explained by pentameric assembly. These experiments also reveal that a subpopulation of α6 subunits may be contained in partially assembled receptors. It may be this feature that precludes routine measurement of functional responses, further supporting the notion of a special factor in vivo that promotes α6* nAChR assembly and function.

We noted a slightly higher FRET efficiency for α6* versus α4* receptors in all assays reported herein. Because FRET *E* depends on distance, we speculate that this is largely due to the smaller M3-M4 intracellular loop of α6 (~136 residues) versus α4 (~270 residues). When the same XFP-labeled β2 construct is expressed with α4 versus α6, the relative distance between fluorophores, and therefore the efficiency of FRET, will be different. Although the lack of structural information about these M3-M4 loops precludes us from making any quantitative predictions or correlations with our observed FRET *E* values, we assert that, at a qualitative level, the differences in FRET *E* for α4 versus α6 are likely explained by the differences in M3-M4 loop length.

In this study, we use FRET to describe α6 and β3 subunit stoichiometry in assembled pentamers containing these subunits. Based on our data, only one β3 subunit is able to incorporate into a nicotinic receptor pentamer with other α and β subunits. It is not clear whether β3 does so because it lacks residues required for formation of an α:β ligand-binding interface, or whether it is due to specific residues in the transmembrane segments or intracellular loops. What is clear is that β3 is able to displace one subunit in a pentamer, which affords the ability to alter the subunit stoichiometry of receptors containing this subunit. Although this has been assumed based on indirect experiments (Broadbent et al., 2006), the present study is the first to directly elucidate the stoichiometry of β3* receptors.

Based on our data, α6* receptors, like α4*, are stoichiometrically heterogeneous. Previous reports using immunoprecipitation or genetic techniques have identified the specific subunits coassembled with α6, but not their stoichiometry (Zoli et al., 2002; Salminen et al., 2007). For example, Salminen et al. (2007) demonstrated the existence of native α6β2, α6β2β3, and α4α6β2β3 subtypes, among others. But for α6β2 receptors, how many α6 and β2 subunits are present in a given pentamer? Our FRET results suggest that a mixture of stoichiometries exist for α6* receptors. We interpret the β3-induced decline in FRET between α6Y and α6C in α6β2 receptors to mean, at least in part, that β3 is displacing a third α6 subunit and stabilizing a stoichiometry of $(\alpha6)_2(\beta2)_2(\beta3)_1$. The alternative, that α6* receptors adopt a strict $(\alpha6)_2(\beta X)_3$ stoichiometry, is less likely. Such a scenario would require that β3 is able to significantly reduce FRET between α6Y and α6C without changing α6 stoichiometry. It is more reasonable to assume that α6 is behaving similar to α4, whose stoichiometry is varied and can be altered by β3 coexpression (Broadbent et al., 2006). α6 and β3 subunits are present in α4α6β2β3 receptors in striatum and nucleus accumbens, which have the highest affinity for nicotine of any nicotinic subtype yet reported (Salminen et al., 2007). Their localization on dopaminergic nerve terminals coupled with this high affinity for nicotine ensures that they are among the first nicotinic subtypes activated during a smoking-induced bolus of nicotine. These and other high-affinity receptors are important targets for smoking cessation and Parkinson's disease medications, so understanding their subunit stoichiometry is important for the rational design of small molecule modulators of nAChR function.

Acknowledgments

We thank members of the Lester laboratory for helpful advice and discussion, including Cagdas Son, Rigo Pantoja, and Fraser Moss. Special thanks to Fraser Moss and Monica Liu for help with molecular biology and Bruce Cohen for help with electrophysiology.

References

Azam L, Chen Y, and Leslie FM (2007) Developmental regulation of nicotinic acetylcholine receptors within midbrain dopamine neurons. *Neuroscience* **144:**1347–1360.

Bezprozvanny I, Scheller RH, and Tsien RW (1995) Functional impact of syntaxin on gating of N-type and Q-type calcium channels. *Nature* **378:**623–626.

Bierut LJ, Madden PA, Breslau N, Johnson EO, Hatsukami D, Pomerleau OF, Swan GE, Rutter J, Bertelsen S, Fox L, et al. (2007) Novel genes identified in a high-density genome wide association study for nicotine dependence. *Hum Mol Genet* **16:**24–35.

Boorman JP, Beato M, Groot-Kormelink PJ, Broadbent SD, and Sivilotti LG (2003) The effects of β3 subunit incorporation on the pharmacology and single channel properties of oocyte-expressed human $\alpha3\beta4$ neuronal nicotinic receptors. *J Biol Chem* **278:**44033–44040.

Boorman JP, Groot-Kormelink PJ, and Sivilotti LG (2000) Stoichiometry of human recombinant neuronal nicotinic receptors containing the $\beta3$ subunit expressed in *Xenopus* oocytes. *J Physiol* **529:**565–577.

Briggs CA, Gubbins EJ, Marks MJ, Putman CB, Thimmapaya R, Meyer MD, and Surowy CS (2006) Untranslated region-dependent exclusive expression of high-sensitivity subforms of $\alpha4\beta2$ and $\alpha3\beta2$ nicotinic acetylcholine receptors. *Mol Pharmacol* **70:**227–240.

Broadbent S, Groot-Kormelink PJ, Krashia PA, Harkness PC, Millar NS, Beato M, and Sivilotti LG (2006) Incorporation of the $\beta3$ subunit has a dominant-negative effect on the function of recombinant central-type neuronal nicotinic receptors. *Mol Pharmacol* **70:**1350–1357.

Buisson B and Bertrand D (2001) Chronic exposure to nicotine upregulates the human $\alpha4\beta2$ nicotinic acetylcholine receptor function. *J Neurosci* **21:**1819–1829.

Champtiaux N, Gotti C, Cordero-Erausquin M, David DJ, Przybylski C, Lena C, Clementi F, Moretti M, Rossi FM, Le Novere N, et al. (2003) Subunit composition of functional nicotinic receptors in dopaminergic neurons investigated with knock-out mice. *J Neurosci* **23:**7820–7829.

Champtiaux N, Han ZY, Bessis A, Rossi FM, Zoli M, Marubio L, McIntosh JM, and Changeux JP (2002) Distribution and pharmacology of $\alpha6$-containing nicotinic acetylcholine receptors analyzed with mutant mice. *J Neurosci* **22:**1208–1217.

Corry B, Jayatilaka D, and Rigby P (2005) A flexible approach to the calculation of resonance energy transfer efficiency between multiple donors and acceptors in complex geometries. *Biophys J* **89:**3822–3836.

Cui C, Booker TK, Allen RS, Grady SR, Whiteaker P, Marks MJ, Salminen O, Tritto T, Butt CM, Allen WR, et al. (2003) The $\beta3$ nicotinic receptor subunit: a component of α-conotoxin MII-binding nicotinic acetylcholine receptors that modulate dopamine release and related behaviors. *J Neurosci* **23:**11045–11053.

Drenan RM, Doupnik CA, Boyle MP, Muglia LJ, Huettner JE, Linder ME, and Blumer KJ (2005) Palmitoylation regulates plasma membrane-nuclear shuttling of R7BP, a novel membrane anchor for the RGS7 family. *J Cell Biol* **169:**623–633.

Fowler MJ, Flaskos J, McLean WG, and Hargreaves AJ (2001) Effects of neuropathic and non-neuropathic isomers of tricresyl phosphate and their microsomal activation on the production of axon-like processes by differentiating mouse N2a neuroblastoma cells. *J Neurochem* **76:**671–678.

Gotti C, Moretti M, Clementi F, Riganti L, McIntosh JM, Collins AC, Marks MJ, and Whiteaker P (2005a) Expression of nigrostriatal $\alpha6$-containing nicotinic acetylcholine receptors is selectively reduced, but not eliminated, by $\beta3$ subunit gene deletion. *Mol Pharmacol* **67:**2007–2015.

Gotti C, Moretti M, Zanardi A, Gaimarri A, Champtiaux N, Changeux JP, Whiteaker P, Marks MJ, Clementi F, and Zoli M (2005b) Heterogeneity and selective targeting of neuronal nicotinic acetylcholine receptor (nAChR) subtypes expressed on retinal afferents of the superior colliculus and lateral geniculate nucleus: identification of a new native nAChR subtype $\alpha3\beta2(\alpha5$ or $\beta3)$ enriched in retinocollicular afferents. *Mol Pharmacol* **68:**1162–1171.

Grady SR, Murphy KL, Cao J, Marks MJ, McIntosh JM, and Collins AC (2002) Characterization of nicotinic agonist-induced [^{3}H]dopamine release from synaptosomes prepared from four mouse brain regions. *J Pharmacol Exp Ther* **301:**651–660.

Graham AJ, Martin-Ruiz CM, Teaktong T, Ray MA, and Court JA (2002) Human brain nicotinic receptors, their distribution and participation in neuropsychiatric disorders. *Curr Drug Targets CNS Neurol Disord* **1:**387–397.

Grailhe R, de Carvalho LP, Paas Y, Le Poupon C, Soudant M, Bregestovski P, Changeux JP, and Corringer PJ (2004) Distinct subcellular targeting of fluorescent nicotinic $\alpha3\beta4$ and serotoninergic 5-HT$_{3A}$ receptors in hippocampal neurons. *Eur J Neurosci* **19:**855–862.

Groot-Kormelink PJ, Luyten WH, Colquhoun D, and Sivilotti LG (1998) A reporter mutation approach shows incorporation of the "orphan" subunit $\beta3$ into a functional nicotinic receptor. *J Biol Chem* **273:**15317–15320.

Kuryatov A, Olale F, Cooper J, Choi C, and Lindstrom J (2000) Human $\alpha6$ AChR subtypes: subunit composition, assembly, and pharmacological responses. *Neuropharmacology* **39:**2570–2590.

Léna C, de Kerchove D'Exaerde A, Cordero-Erausquin M, Le Novere N, del Mar Arroyo-Jimenez M, and Changeux JP (1999) Diversity and distribution of nicotinic acetylcholine receptors in the locus ceruleus neurons. *Proc Natl Acad Sci U S A* **96:**12126–12131.

Marks MJ, Burch JB, and Collins AC (1983) Effects of chronic nicotine infusion on tolerance development and nicotinic receptors. *J Pharmacol Exp Ther* **226:**817–825.

Miwa JM, Ibanez-Tallon I, Crabtree GW, Sanchez R, Sali A, Role LW, and Heintz N (1999) lynx1, an endogenous toxin-like modulator of nicotinic acetylcholine receptors in the mammalian CNS. *Neuron* **23:**105–114.

Miyazawa A, Fujiyoshi Y, Stowell M, and Unwin N (1999) Nicotinic acetylcholine receptor at 4.6 angstrom resolution: transverse tunnels in the channel wall. *J Mol Biol* **288:**765–786.

Nashmi R, Dickinson ME, McKinney S, Jareb M, Labarca C, Fraser SE, and Lester HA (2003) Assembly of $\alpha4\beta2$ nicotinic acetylcholine receptors assessed with functional fluorescently labeled subunits: effects of localization, trafficking, and nicotine-induced upregulation in clonal mammalian cells and in cultured midbrain neurons. *J Neurosci* **23:**11554–11567.

Nashmi R, Xiao C, Deshpande P, McKinney S, Grady SR, Whiteaker P, Huang Q, McClure-Begley T, Lindstrom JM, Labarca C, et al. (2007) Chronic nicotine cell specifically upregulates functional alpha4* nicotinic receptors: basis for both tolerance in midbrain and enhanced long-term potentiation in perforant path. *J Neurosci* **27:**8202–8218.

Nelson ME, Kuryatov A, Choi CH, Zhou Y, and Lindstrom J (2003) Alternate stoichiometries of $\alpha4\beta2$ nicotinic acetylcholine receptors. *Mol Pharmacol* **63:**332–341.

Ohara-Imaizumi M, Nishiwaki C, Nakamichi Y, Kikuta T, Nagai S, and Nagamatsu S (2004) Correlation of syntaxin-1 and SNAP-25 clusters with docking and fusion of insulin granules analysed by total internal reflection fluorescence microscopy. *Diabetologia* **47:**2200–2207.

Quick M and Lester HA (1994) Methods for expression of excitability proteins in *Xenopus* oocytes, in *Ion Channels of Excitable Cells* (Narahashi T ed) pp 261–279, Academic Press, San Diego, CA.

Quik M and McIntosh JM (2006) Striatal $\alpha6$* nicotinic acetylcholine receptors: potential targets for Parkinson's disease therapy. *J Pharmacol Exp Ther* **316:**481–489.

Rowell P (2002) Effects of nicotine on dopaminergic neurotransmission, in *Nicotinic Receptors in the Nervous System* (Levin ED ed) pp 51–80, CRC, Boca Raton, FL.

Salminen O, Drapeau JA, McIntosh JM, Collins AC, Marks MJ, and Grady SR (2007) Pharmacology of α-Conotoxin MII-Sensitive Subtypes of Nicotinic Acetylcholine Receptors Isolated by breeding of null mutant mice. *Mol Pharmacol* **71:**1563–1571.

Slimko EM, McKinney S, Anderson DJ, Davidson N, and Lester HA (2002) Selective electrical silencing of mammalian neurons in vitro by the use of invertebrate ligand-gated chloride channels. *J Neurosci* **22:**7373–7379.

Tapia L, Kuryatov A, and Lindstrom J (2007) Ca^{2+} permeability of the $(\alpha4)_3(\beta2)_2$ stoichiometry greatly exceeds that of $(\alpha4)_2(\beta2)_3$ human acetylcholine receptors. *Mol Pharmacol* **71:**769–776.

Tumkosit P, Kuryatov A, Luo J, and Lindstrom J (2006) $\beta3$ subunits promote expression and nicotine-induced up-regulation of human nicotinic $\alpha6$* nicotinic acetylcholine receptors expressed in transfected cell lines. *Mol Pharmacol* **70:**1358–1368.

Whiteaker P, McIntosh JM, Luo S, Collins AC, and Marks MJ (2000) [^{125}I]-α-Conotoxin MII identifies a novel nicotinic acetylcholine receptor population in mouse brain. *Mol Pharmacol* **57:**913–925.

Xu J, Zhu Y, and Heinemann SF (2006) Identification of sequence motifs that target neuronal nicotinic receptors to dendrites and axons. *J Neurosci* **26:**9780–9793.

Zheng JQ, Felder M, Connor JA, and Poo MM (1994) Turning of nerve growth cones induced by neurotransmitters. *Nature* **368:**140–144.

Zoli M, Moretti M, Zanardi A, McIntosh JM, Clementi F, and Gotti C (2002) Identification of the nicotinic receptor subtypes expressed on dopaminergic terminals in the rat striatum. *J Neurosci* **22:**8785–8789.

Address correspondence to: Dr. Henry A. Lester, California Institute of Technology, Division of Biology, M/C 156-29, 1200 E. California Blvd., Pasadena, CA 91125. E-mail: lester@caltech.edu